

Nicolas Loménie
Daniel Racoceanu
Alexandre Gouaillard (Eds.)

Advances in Bio-Imaging: From Physics to Signal Understanding Issues

 Springer

Advances in Intelligent and Soft Computing

Editor-in-Chief

Prof. Janusz Kacprzyk
Systems Research Institute
Polish Academy of Sciences
ul. Newelska 6
01-447 Warsaw
Poland
E-mail: kacprzyk@ibspan.waw.pl

Further volumes of this series can be found on our homepage: springer.com

Vol. 105. D. Jin and S. Lin (Eds.)
Advances in Computer Science, Intelligent System and Environment, 2011
ISBN 978-3-642-23755-3

Vol. 106. D. Jin and S. Lin (Eds.)
Advances in Computer Science, Intelligent System and Environment, 2011
ISBN 978-3-642-23752-2

Vol. 107. P. Melo-Pinto, P. Couto, C. Serôdio, J. Fodor, and B. De Baets (Eds.)
Eurofuse 2011, 2011
ISBN 978-3-642-24000-3

Vol. 108. Y. Wang (Ed.)
Education and Educational Technology, 2011
ISBN 978-3-642-24774-3

Vol. 109. Y. Wang (Ed.)
Education Management, Education Theory and Education Application, 2011
ISBN 978-3-642-24771-2

Vol. 110. L. Jiang (Ed.)
Proceedings of the 2011 International Conference on Informatics, Cybernetics, and Computer Engineering (ICCE 2011) November 19-20, 2011, Melbourne, Australia, 2011
ISBN 978-3-642-25184-9

Vol. 111. L. Jiang (Ed.)
Proceedings of the 2011 International Conference on Informatics, Cybernetics, and Computer Engineering (ICCE 2011) November 19-20, 2011, Melbourne, Australia, 2011
ISBN 978-3-642-25187-0

Vol. 112. L. Jiang (Ed.)
Proceedings of the 2011 International Conference on Informatics, Cybernetics, and Computer Engineering (ICCE 2011) November 19-20, 2011, Melbourne, Australia, 2011
ISBN 978-3-642-25193-1

Vol. 113. J. Altmann, U. Baumöl, and B.J. Krämer (Eds.)
Advances in Collective Intelligence 2011, 2011
ISBN 978-3-642-25320-1

Vol. 114. Y. Wu (Ed.)
Software Engineering and Knowledge Engineering: Theory and Practice, 2011
ISBN 978-3-642-03717-7

Vol. 115. Y. Wu (Ed.)
Software Engineering and Knowledge Engineering: Theory and Practice, 2011
ISBN 978-3-642-03717-7

Vol. 116. Yanwen Wu (Ed.)
Advanced Technology in Teaching - Proceedings of the 2009 3rd International Conference on Teaching and Computational Science (WTCS 2009), 2012
ISBN 978-3-642-11275-1

Vol. 117. Yanwen Wu (Ed.)
Advanced Technology in Teaching - Proceedings of the 2009 3rd International Conference on Teaching and Computational Science (WTCS 2009), 2012
ISBN 978-3-642-25436-9

Vol. 118. A. Kapczynski, E. Tkacz, and M. Rostanski (Eds.)
Internet - Technical Developments and Applications 2, 2011
ISBN 978-3-642-25354-6

Vol. 119. Tianbiao Zhang (Ed.)
Future Computer, Communication, Control and Automation, 2011
ISBN 978-3-642-25537-3

Vol. 120. N. Loménie, D. Racocanu, and A. Gouaillard (Eds.)
Advances in Bio-Imaging: From Physics to Signal Understanding Issues, 2012
ISBN 978-3-642-25546-5

Nicolas Loménie, Daniel Racoceanu,
and Alexandre Gouaillard (Eds.)

Advances in Bio-Imaging: From Physics to Signal Understanding Issues

State-of-the-Art and Challenges

Editors

Dr. Nicolas Loménie
Silesian University of Technology
IPAL, I2R & CNRS,
Republic of Singapore

Dr. Alexandre Gouaillard
Singapore Immunology
Network (SIgN),
Republic of Singapore

Dr. Daniel Racocanu
IPAL, I2R & CNRS,
Republic of Singapore

ISSN 1867-5662

e-ISSN 1867-5670

ISBN 978-3-642-25546-5

e-ISBN 978-3-642-25547-2

DOI 10.1007/978-3-642-25547-2

Springer Heidelberg New York Dordrecht London

Library of Congress Control Number: 2011941759

© Springer-Verlag Berlin Heidelberg 2012

This work is subject to copyright. All rights are reserved by the Publisher, whether the whole or part of the material is concerned, specifically the rights of translation, reprinting, reuse of illustrations, recitation, broadcasting, reproduction on microfilms or in any other physical way, and transmission or information storage and retrieval, electronic adaptation, computer software, or by similar or dissimilar methodology now known or hereafter developed. Exempted from this legal reservation are brief excerpts in connection with reviews or scholarly analysis or material supplied specifically for the purpose of being entered and executed on a computer system, for exclusive use by the purchaser of the work. Duplication of this publication or parts thereof is permitted only under the provisions of the Copyright Law of the Publisher's location, in its current version, and permission for use must always be obtained from Springer. Permissions for use may be obtained through RightsLink at the Copyright Clearance Center. Violations are liable to prosecution under the respective Copyright Law.

The use of general descriptive names, registered names, trademarks, service marks, etc. in this publication does not imply, even in the absence of a specific statement, that such names are exempt from the relevant protective laws and regulations and therefore free for general use.

While the advice and information in this book are believed to be true and accurate at the date of publication, neither the authors nor the editors nor the publisher can accept any legal responsibility for any errors or omissions that may be made. The publisher makes no warranty, express or implied, with respect to the material contained herein.

Printed on acid-free paper

Springer is part of Springer Science+Business Media (www.springer.com)

*This book is dedicated to the
French-Singaporean scientific and
technological collaboration and friendship.*

Foreword

We are delighted to have co-organized the 2011 edition of the Singaporean-French Bioimaging Workshop together with IPAL. This edition was held in Biopolis, and attracted 200 scientists mainly from the fields of image processing and biology. This interdisciplinary approach is dear to our heart for many reasons: first of all we believe that scientific innovations and discoveries come from bridging disciplines, as shown many years ago by Leonardo da Vinci. Second, this event has been an illustration of how successful a joint BMRC-SERC initiative can be in catalyzing shared interests in bio-imaging, from imaging to immunology, including image processing, physics etc. The complexity of the human immune system can only be addressed by a multidisciplinary approach. SIGN is planning to make more of such events happen in the future in order to foster communication between the two communities and enhance knowledge creation.

Singapore, September 2011

Paola Castagnoli, Alex Gouaillard,
Philippe Kourilsky

Preface

After more than ten years of passionate research work between Singaporean and French scientists within the Image and Pervasive Access Laboratory¹, a joint workshop about bio-imaging technologies has been held at Biopolis, Singapore in February 2011 in which the long-term scientific collaboration about computer vision issues and medical image analysis applications has been shaped again for the next couple of decades. This workshop was aimed at detecting the key technological partnerships to be promoted within the broad topic of bio-imaging. The workshop followed a multidisciplinary approach by sharing researchers' experience from the physics of acquisition [Athanasiou et al. 2008] to the numerical handling of the acquired data through cutting-edge research in biology and life sciences [Lutz et al. 2008].

As the current series is historically mostly oriented towards the numerical handling of visual data, we highlighted the image analysis challenges related to each contributed topic. However, this book is targeting an audience of students or researchers in the field of bio-imaging that are willing to get the big picture of the multi-(if possible trans-)disciplinary aspects of bio-imaging. Subsequently, contributions from physics and chemistry are given a large share of exposure while emerging research works in bio-engineering related to high-content screening are broached.

The workshop has been a great success with more than one hundred registered attendees mostly local Singaporeans working either within the Biopolis facilities or the National University of Singapore research units. A few collaborations have been set up so far between a French and a Singaporean team. For instance, a French research work about innovative chemical probes as described in this book (see p.37 *infra*) has been fostered by a collaboration with a Singaporean physics team expert in specific measure devices.

A specific range of papers deals with the emerging field of digitized histopathology building up a bridge between two communities: the one that handles real

¹ IPAL CNRS UMI France-Singapore 2955 (I2R/A*STAR, NUS, UJF, TELECOM, UPMC/Sorbonne).

matter and the one that deals with informational matter. By bringing together cognitive, mathematical, algorithmic and technological issues, this new field constitutes a perfect candidate to become a favourite playground for innovative integrated approaches for high-content, distributed monitoring of physiological biological processes as envisioned by the Virtual Physiological Human project².

We believe that this introduction to the latest developments in the broad field of bio-imaging will deliver as much as inspiration and willingness for the upcoming generation of researchers to tackle the new challenges of biology systems.

References

- [Athanasίου et al. 2008] Athanasίου, A., Deffieux, T., Gennisson, J.L., Montaldo, G., Muller, M., Tardivon, A., Fink, M.: Quantitative assessment of breast lesion viscoelasticity: initial clinical results using SuperSonic Imagine shear imaging. *Ultrasound Med. Biol.* (April 4, 2008)
- [Lutz et al. 2008] Lutz, C., Otis, T., DeSars, V., Charpak, S., DiGregorio, D.A., Emiliani, V.: Holographic photolysis of caged neurotransmitters. *Nature Methods* 5(9), 821–827 (2008)

Singapore,
May 2011,

Nicolas Loménie
Alexandre Gouaillard
Daniel Racoceanu

² <http://www.vph-noe.eu/>

Acknowledgments

We are very grateful to the Singaporean research agencies within A*STAR and in particular the Joint Council Organization (JCO) that funded the workshop to foster collaborations between the Biopolis and Fusionopolis research teams³ in Singapore. The French Embassy via the MERLION grant and University Paris Descartes⁴ made it possible to invite outstanding speakers from French research top institutes. The French National Center for Research (CNRS⁵) gave the first impulse to set up the event and be it earnestly acknowledged for the constant effort towards the French-Singaporean collaboration success over the years. Many thanks to the IPAL team⁶ and I2R⁷ for the organization and above all to the SIGN⁸ team for the strong support: Peggy and Cheryl, executive assistant managers and Paola Castagnoli, head of the department.

³ <http://www.a-star.edu.sg/tabid/860/default.aspx>

⁴ <http://www.sorbonne-paris-cite.fr/index.php/en>

⁵ <http://www.cnrs.fr/>

⁶ <http://ipal.i2r.a-star.edu.sg/>

⁷ <http://www.i2r.a-star.edu.sg/>

⁸ <http://www.sign.a-star.edu.sg/>

Contents

Part I Biology

| | |
|---|-----------|
| Intravital Multiphoton Imaging of Immune Cells | 3 |
| Jo Keeble, Chi Ching Goh, Yilin Wang, Wolfgang Weninger, and Lai Guan Ng | |
| 1 Introduction | 3 |
| 2 Multiphoton Microscopy | 4 |
| 3 Intravital Skin Imaging Model | 5 |
| 3.1 The Skin: An Important Immunological Site | 5 |
| 3.2 The Mouse Ear Skin Model | 6 |
| 3.3 Visualizing Immune Cells in the Vasculature and Skin | 6 |
| 3.4 Data Processing and Presentation | 9 |
| 3.5 Intravital Multiphoton Imaging Considerations | 10 |
| 4 The Missing Link in Multiphoton Microscopy: Software Development | 11 |
| 4.1 Image Acquisition and Data Management | 11 |
| 4.2 Spectral Unmixing | 11 |
| 4.3 Image Analysis | 12 |
| 4.4 Towards Standardized Imaging | 12 |
| 4.5 Data Interpretation and Presentation | 13 |
| 5 Concluding Remarks | 13 |
| Functional MRI of Neural Plasticity and Drug Effect in the Brain | 17 |
| Kai-Hsiang Chuang and Fatima A. Nasrallah | |
| 1 Introduction | 17 |
| 2 MRI of Neural Plasticity after Nerve Amputation | 18 |
| 3 MRI of Neural Plasticity after Learning | 20 |
| 4 MRI of Drug Effect | 22 |
| 5 Concluding Remarks | 23 |

| | |
|---|-----------|
| Automated Identification and Analysis of Visual Micro-experiments on Cellular Microarray | 27 |
| Auguste Genovesio | |
| 1 Background | 27 |
| 1.1 The High Throughput Screening | 27 |
| 1.2 The High Content Screening | 28 |
| 1.3 The High Content Screening in practice | 28 |
| 2 High Content Cellular Microarray | 30 |
| 3 Conclusion | 31 |

Part II Physics and Chemistry

| | |
|--|-----------|
| Persistent Luminescence Nanoparticles for Bioimaging | 37 |
| Cyrille Richard, Thomas Maldiney, Quentin le Masne de Chermont, Johanne Seguin, Nicolas Wattier, Gabriel Courties, Florence Apparailly, Michel Bessodes, and Daniel Scherman | |
| 1 Introduction | 38 |
| 2 Persistent Luminescence Nanoparticles from Silicate Host | 38 |
| 2.1 Synthesis of Enstatite-like Silicates: $MgSiO_3$, $ZnMgSi_2O_6$ and $Ca_{0.2}Zn_{0.9}Mg_{0.9}Si_2O_6$ doped with Eu^{2+} , Dy^{3+} and Mn^{2+} | 39 |
| 2.2 Characterization of Synthesized Nanomaterials | 40 |
| 3 Chemical Surface Functionalization of Silicates | 41 |
| 3.1 Obtention of Nanoparticles of Different Sizes | 41 |
| 3.2 Characterization of the Nanoparticles by DLS and TEM | 42 |
| 3.3 Surface Functionalization | 44 |
| 3.4 Characterization of the Functionalized PLNP | 44 |
| 4 Bioimaging with Persistent Luminescence Nanoparticles | 46 |
| 4.1 Principle | 46 |
| 4.2 Influence of Coating on the Biodistribution of 180nm PLNP | 46 |
| 4.3 Influence of Nanoparticle Diameter and PEG Chain Length on the Biodistribution in Healthy Mice | 47 |
| 4.4 Biodistribution of PEG-PLNP in Tumor Bearing Mice | 48 |
| 4.5 PLNP for Imaging Inflammation in a Mouse Model of Arthritis | 50 |
| 5 Conclusion | 51 |

| | |
|--|-----------|
| Bioimaging Probes Development by DOFLA (Diversity Oriented Fluorescence Library Approach) for in Vitro, in Vivo and Clinical Applications | 55 |
| Seong-Wook Yun and Young-Tae Chang | |
| 1 Visualizing Is Proving | 56 |
| 2 More Questions to Be Addressed in Post-Genomic Era | 57 |
| 3 Fluorescent Microscopy | 57 |
| 4 Fluorescent Small Molecules | 58 |

| | | |
|--|--|-----------|
| 5 | Diversity Oriented Fluorescence Library Approach | 59 |
| 5.1 | In Vitro Screening | 60 |
| 5.2 | Cell-Based Screening | 60 |
| 5.3 | Tissue-Based Screening | 61 |
| 5.4 | Whole Organism Screening | 62 |
| 6 | Multimodality Probe | 62 |
| 7 | Conclusion | 63 |
| | References | 64 |
| In Vivo Electron Paramagnetic Resonance and Imaging in Biomedical Science | | 67 |
| Yves-Michel Frapart | | |
| 1 | EPR and EPR Imaging | 67 |
| 2 | EPR and EPR Imaging Molecular Probes | 70 |
| 3 | In Vivo EPR and EPR Imaging Apparatus | 71 |
| 4 | In Vivo EPR Spectroscopy and Its Applications | 71 |
| 5 | EPR Imaging on Endogenous Radical | 72 |
| 6 | EPR Imaging Using Molecular Probes | 72 |
| 7 | Oxymetry | 73 |
| 8 | Mathematical Treatment of the EPR Signal to Get an EPR Image | 73 |
| 9 | EPR Imaging and Anatomical Repositioning | 74 |
| 10 | Conclusion | 75 |
| | References | 75 |
| Intra-Operative Ex-Situ and In-Situ Optical Biopsy Using Light-CT | | 77 |
| Martine Antoine, Brigitte Sigal, Fabrice Harms, Anne Latrive, Adriano Burcheri, Osnath Assayag, Bertrand de Poly, Sylvain Gigan, and A. Claude Boccara | | |
| 1 | Introduction: Virtual Pathology Using Light-CT | 77 |
| 2 | Proof of Concept: Fixed Tissues | 78 |
| 3 | Intra-Operative Studies: Fresh Tissues | 80 |
| 4 | Tomographic Light-CT Approach: Proof of Principle | 82 |
| 5 | Conclusion and Future Trends | 84 |
| | References | 84 |
| Photothermal Laser Material Interactions - From the Sledgehammer to Nano-GPS | | 85 |
| Jonathan Hobley, David Paramelle, Paul Free, David G. Fernig, Shinji Kajimoto, and Sergey Gorelik | | |
| 1 | Photothermal Fundamentals | 85 |
| 1.1 | Light Conversion to Heat | 85 |
| 1.2 | How Hot Does It Get? | 89 |
| 1.3 | Photothermal and Photoacoustic Effects | 90 |
| 1.4 | Photothermal Refractive Index Change and Lensing | 96 |

| | | |
|-----|---|------------|
| 2 | Photothermal Imaging | 99 |
| 2.1 | Overview | 99 |
| 2.2 | Fluorescent Probes | 99 |
| 2.3 | Nanoparticle Probes | 101 |
| 2.4 | Photothermal Heterodyne Imaging | 103 |
| 2.5 | Photothermal Tracking Microscopy | 104 |
| 3 | Conclusions and Future Vistas | 105 |
| | References | 108 |
| | Dual Axes Confocal Microendoscope | 113 |
| | Wibool Piyawattanametha | |
| 1 | Introduction | 114 |
| 2 | Single Axis Confocal Architecture | 115 |
| 2.1 | Configuration of Optics | 115 |
| 2.2 | Resolutions | 116 |
| 2.3 | Commercial Systems | 117 |
| 3 | Dual Axes Confocal Architecture | 118 |
| 3.1 | Configuration of Optics | 118 |
| 3.2 | Coordinates Definition | 119 |
| 3.3 | Point Spread Function | 120 |
| 3.4 | Dynamic Range | 122 |
| 3.5 | Post-Objective Scanning | 123 |
| 3.6 | Improved Rejection of Scattering | 124 |
| 4 | Tabletop Dual Axes Confocal Imaging Instruments | 128 |
| 4.1 | Horizontal Cross-Sectional Imaging Instrument | 129 |
| 4.2 | Vertical Cross-Sectional Imaging Instrument | 130 |
| 5 | MEMS-Scanner Based Dual Axes Confocal Imaging Instruments | 134 |
| 5.1 | MEMS Scanner Architecture | 134 |
| 5.2 | Theoretical Analysis | 135 |
| 5.3 | Device Fabrication | 136 |
| 5.4 | Device Characterization | 138 |
| 6 | Dual Axes Scanhead | 139 |
| 6.1 | Scanhead Design | 139 |
| 6.2 | Scanhead Alignment and Packaging | 140 |
| 6.3 | Instrument Control and Data Acquisition | 142 |
| 7 | Prototype Systems | 143 |
| 7.1 | Handheld Instrument | 143 |
| 7.2 | Endoscope-Compatible Instrument | 143 |
| 8 | Imaging Results | 145 |
| 8.1 | Reflectance Imaging | 145 |
| 8.2 | Ex Vivo Fluorescence Imaging | 146 |
| 9 | In Vivo Fluorescence Imaging | 147 |
| 10 | Conclusions and Future Directions | 149 |
| | References | 151 |

Part III Digitized Histopathology

Ontology-Enhanced Vision System for New Microscopy Imaging Challenges

| | |
|---|-----|
| Nicolas Lomenie and Daniel Racoceanu | |
| 1 Introduction | 157 |
| 2 Breast Cancer Grading | 158 |
| 2.1 Digitized Pathology | 158 |
| 2.2 Anatomical and Workflow Ontology: OWL | 160 |
| 3 Low-Level Signal Processing | 160 |
| 4 High-Level Processing | 161 |
| 4.1 Rules and Reasoning | 164 |
| 5 Results | 166 |
| 6 Conclusion | 171 |
| References | 171 |

Computational Approaches for the Processing of Cerebral Histological Images of Small Animals

| | |
|---|-----|
| Julien Dauguet | |
| 1 Introduction | 173 |
| 1.1 Brief History of Histology | 173 |
| 1.2 From Sections to Images | 175 |
| 1.3 Virtual Microscopy, Digital Microscopy | 176 |
| 2 3D Reconstruction of Series of Histological Slices | 177 |
| 2.1 3D Region of Interest | 177 |
| 2.2 Using 3D Atlases | 178 |
| 2.3 Voxel-wise Statistical Comparison | 179 |
| 3 Large Dimensions Microscopy Images | 180 |
| 3.1 Viewing Large Images | 180 |
| 3.2 Processing Large Images | 181 |
| 4 In Vivo / Post Mortem Correlation | 183 |
| 4.1 Estimation of a 3D Warping Transformation to Correct the Deformations | 184 |
| 4.2 Correlation for Comparison | 185 |
| 4.3 Correlation for Improved Information | 186 |
| 5 Conclusion | 187 |
| References | 187 |

Part IV Image Analysis

Liver Workbench: A Tool Suite for Liver and Liver Tumor Segmentation and Modeling

| | |
|--|-----|
| Jiayin Zhou, Wei Xiong, Feng Ding, Weimin Huang, Tian Qi, Zhimin Wang, Thiha Oo, and Sudhakar Kundapur Venkatesh | |
| 1 Introduction | 193 |
| 2 System Overview | 194 |

| | | |
|-----|--|------------|
| 3 | Segmentation of Liver and Liver Tumors | 195 |
| 3.1 | Flipping-free Mesh Deformation for Liver Segmentation | 195 |
| 3.2 | SVMs-Based Voxel Classification and Propagational Learning for Liver Tumor Segmentation | 199 |
| 3.3 | Implementation | 200 |
| 3.4 | Experiments and Evaluation Metrics | 201 |
| 4 | Probabilistic Liver Atlas Modeling | 202 |
| 5 | Experiments and Results | 203 |
| 5.1 | Liver and Tumor Segmentation Results | 203 |
| 5.2 | Probabilistic Liver Atlas Modeling Results | 205 |
| 6 | Conclusions | 207 |
| | References | 207 |
| | A Bag-of-Words Model for Cellular Image Segmentation | 209 |
| | Li Cheng, Ning Ye, Weimiao Yu, and Andre Cheah | |
| 1 | Introduction | 209 |
| 2 | Our Approach | 211 |
| 2.1 | Features | 211 |
| 2.2 | A Bag-of-words Model: Code, Superpixel-based Code | 212 |
| 3 | Datasets and Performance Evaluation | 214 |
| 3.1 | The Datasets | 214 |
| 3.2 | Performance Evaluation | 215 |
| 4 | Experiments | 216 |
| 5 | Outlook and Discussion | 216 |
| | References | 220 |
| | Knowledge Based and Statistical Based Approaches in Biomedical Image Analysis | 223 |
| | Florence Cloppet and Thomas Hurtut | |
| 1 | Introduction | 223 |
| 2 | Challenges | 225 |
| 3 | Knowledge-Based Approaches for Cell Extraction | 226 |
| 3.1 | Segmentation of Complex Nucleus Configurations | 227 |
| 3.2 | Extraction of Neurons Embedded in a Network | 229 |
| 4 | Statistical Modeling and Synthesis of Element-Based Biomedical textures | 230 |
| 5 | Conclusion | 234 |
| | References | 234 |
| | Glossary | 237 |
| | Index | 243 |

List of Contributors

Jo Keeble,
Chi Ching Goh,
Yilin Wang,
Singapore Immunology Network (SIGN), Agency for Science,
Technology and Research (A*STAR), Biopolis, Singapore.

Wolfgang Weninger,
The Centenary Institute, Newtown, NSW 2042, Australia &
Discipline of Dermatology, University of Sydney, Camperdown NSW 2050,
Australia &
Department of Dermatology, Royal Prince Alfred Hospital,
Camperdown, NSW 2050, Australia.

Auguste Genovesio,
Image Mining Group, Institut Pasteur Korea.

Kai-Hsiang Chuang,
Laboratory of Molecular Imaging, Singapore Bioimaging Consortium, Agency for
Science Technology and Research, Singapore &
Clinical Imaging Research Centre, National University of Singapore, Singapore &
Department of Physiology, Yong Loo Lin School of Medicine, National University
of Singapore, Singapore.

Cyrille Richard,
Thomas Maldiney,
Quentin le Masne de Chermont,
Johanne Seguin,
Nicolas Wattier,
Michel Bessodes,
Daniel Scherman,
Unité de Pharmacologie Chimique et Génétique et d'Imagerie; CNRS, UMR 8151,
&

Inserm, U1022 &
Université Paris Descartes, Faculté des Sciences Pharmaceutiques et Biologiques &
ENSCP, Chimie Paristech, Paris, France.

Gabriel Courties,
Florence Apparailly,
Inserm, U844, Montpellier &
Université Montpellier 1, UFR de Médecine &
Service d'immuno-rhumatologie, Hôpital Lapeyronie, Montpellier, France.

Seong-Wook Yun,
Young-Tae Chang,
Laboratory of Bioimaging Probe Development, Singapore Bioimaging Consortium,
Agency for Science, Technology and Research, Singapore; &
Department of Chemistry & NUS MedChem Program of Life Sciences Institute,
National University of Singapore, Singapore.

Yves-Michel Frapart,
UMR 8601 CNRS, Université Paris Descartes, 45, rue des Saints Pères, 75270
PARIS, France.

Martine Antoine,
Brigitte Sigal,
Hospital Tenon and Hospital Curie, Paris, France.

Fabrice Harms,
Anne Latrive,
Adriano Burcheri,
Osnath Assayag,
Bertrand de Poly,
Sylvain Gigan,
A. Claude Boccard,
Institut Langevin ESPCI-Paristech and LLTECH SAS, Paris, France.

James Hobley,
David Paramelle,
Paul Free,
David G. Fernig,
Shinji Kajimoto,
Sergey Gorelik,

Institute for Laser and Material Interactions, A*STAR, Singapore.

Wibool Piyawattanametha,
Head of Advanced Light Microscopy (ALM) Laboratory National Electronics and
Computer Technology Center (NECTEC) 112 Phahon Yothin Rd., Room 321,
Pathumthani 12120, Thailand &
Head of Advanced Imaging Research (AIR) Center Chulalongkorn University
Medical School, Thailand.

Nicolas Loménie,
Daniel Racoceanu,
IPAL CNRS UMI 2955 (I2R/A*STAR, NUS, UJF, TELECOM, UPMC/Sorbonne),
Singapore.

Julien Dauguet,
CEA-CNRS, MIRCen, Route du Panorama, 92265 Fontenay-aux-Roses, France.

Jiayin Zhou,
Wei Xiong,
Weimin Huang,
Tian Qi,
Zhimin Wang,
Thiha Oo,
Institute for Infocomm Research, A*STAR, Singapore.

Feng Ding,
Department of Diagnostic Radiology, School of Computing, National University of
Singapore, Singapore.

Sudhakar K Venkatesh,
Department of Diagnostic Radiology, National University of Singapore, Singapore.

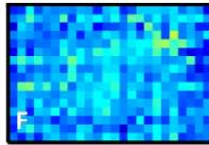
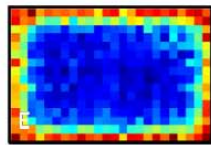
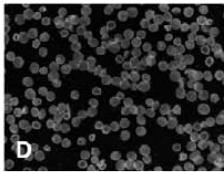
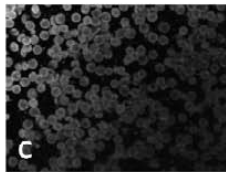
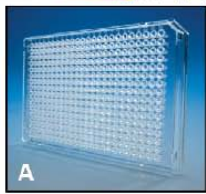
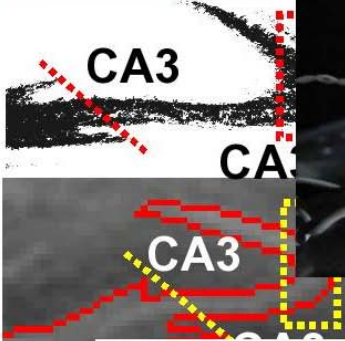
Li Cheng,
Ning Ye,
BioInformatics Institute, A*STAR, Singapore.

Weimiao Yu,
IMCB, A*STAR, Singapore.

Andre Cheah,
NUHS, Singapore.

Florence Cloppet,
Thomas Hurtut,
Laboratoire d'Informatique de Paris Descartes (LIPADE), Paris Descartes
University,
45, Rue des Saints Pères, 75006 Paris, France.

Part I
Biology



Intravital Multiphoton Imaging of Immune Cells

Jo Keeble, Chi Ching Goh, Yilin Wang, Wolfgang Weninger, and Lai Guan Ng

Abstract. Intravital multiphoton microscopy (MP-IVM) is a powerful imaging approach that allows direct visualization of cells within their native environment in real time. Multiphoton imaging of immune cells has been performed in different tissues, and these studies have revealed intriguing insights into the unique migratory and interactive behavior of immune cells in the steady-state and during disease conditions. Here we provide an overview of a MP-IVM model of the mouse ear skin, as well as the benefits, limitations and pitfalls of this approach. We also discuss the prospects of intravital imaging in the areas of image analysis, data management and standardization.

1 Introduction

One of the fundamental characteristics of the immune system lies in the highly dynamic nature of its cellular components. For instance, responses to a pathogen typically require long-range migration of cells, short-range communication by local chemotactic signaling, and direct cell-cell contact. Thus, direct visualization of these dynamic events by intravital microscopy is able to provide essential in-sights into how immune cells exert their functions in the context of intact organs or tissues. Several forms of intravital microscopy, including brightfield, epifluorescence and laser scanning confocal microscopy, have long been adopted by immunologists and have generated substantial insights into leukocyte trafficking. However, intravital

Jo Keeble · Chi Ching Goh · Yilin Wang · Lai Guan Ng
Singapore Immunology Network (SIgN), Agency for Science, Technology
and Research (A*STAR), Biopolis, Singapore

Wolfgang Weninger

The Centenary Institute, Newtown, NSW 2042, Australia & Discipline of Dermatology,
University of Sydney, Camperdown NSW 2050, Australia & Department of Dermatology,
Royal Prince Alfred Hospital, Camperdown, NSW 2050, Australia
e-mail: Ng_Lai_Guan@immunol.a-star.edu.sg

observations using these linear-absorption microscopy techniques have been limited to translucent tissues or superficial regions of non-translucent organs. These limitations are now overcome by intravital multiphoton microscopy (MP-IVM, also known as 2-photon microscopy), which provides greater depth penetration as the result of its localized nonlinear signal generation. Since the first application of multiphoton immune imaging in 2002 [Miller et al. 2002, Bousso et al. 2002], MP-IVM has rapidly evolved beyond merely an observational approach to address complex immunological questions at a quantitative level. MP-IVM is now routinely performed in a variety of tissues including lymph nodes, skin, brain, bone marrow, kidney, liver and even lung (reviewed in [Germain et al. 2006]). In this chapter, we first briefly introduce the methodology of MP-IVM, then provide an overview of a model for MP-IVM imaging of mouse ear skin ([Ng et al. 2008, Roediger et al. 2008]). Finally, we provide a broad overview of the future developments required to overcome some key challenges facing intravital imaging. Our intention is to use the skin model to make the practical aspects of MP-IVM more accessible to physicists, mathematicians and computer scientists, with the aim of facilitating inter-disciplinary interactions between immunologists and experts in the field of software development. We believe that the limitations and pitfalls of MP-IVM discussed in this chapter will provide a useful framework for developing algorithms and analysis tools that can be specifically applied to multiphoton imaging data.

2 Multiphoton Microscopy

Unlike conventional fluorescent microscopy, multiphoton microscopy relies on the near simultaneous absorption of two (or more) photons by a fluorophore, which together provide sufficient energy to excite and subsequently emit fluorescence (Figure 1). Given that the possibility of a fluorophore simultaneously absorbing more than one photon is extremely low at normal light intensity, multiphoton microscopy uses a high-powered femtosecond-pulsed laser beam that is focused through the objective lens to generate 'photon crowding' around the focal plane. Due to its non-linear excitation, multiphoton microscopy features the following advantages over conventional fluorescent microscopy: (1) Excitation is confined to a small volume around the focal point. This enables intrinsic optical sectioning and minimizes the effects of photobleaching and/or phototoxicity above and below the focal plane. (2) Longer wavelengths of multiphoton excitation result in less light scattering and absorption through tissues, thus enabling a deeper penetration of up to 1 mm depending on tissues; Excitation wavelengths used for multiphoton imaging are approximately double the wavelengths used for one photon microscopy (within the range of 700-1020 nm). The laser can also be coupled with a synchronously pumped optical parametric oscillator (OPO), which can tune the laser beam to even longer wavelengths (1080-1500 nm) for excitation of red and far-red fluorophores. (3) Due to the broad multiphoton excitation spectra, multiphoton microscopy enables simultaneous excitation and detection of several fluorophores using a single

wavelength; and (4) Due to the multiphoton generation of second and third harmonic signals (SHG and THG), components of the extracellular matrix, such as collagen and elastin, can be visualized without the need for fluorescent labeling ([Witte et al. 2011], [Zoumi et al. 2002]). This provides a useful reference, which facilitates the localization of fluorescent immune cells within the context of a whole organ or tissue.

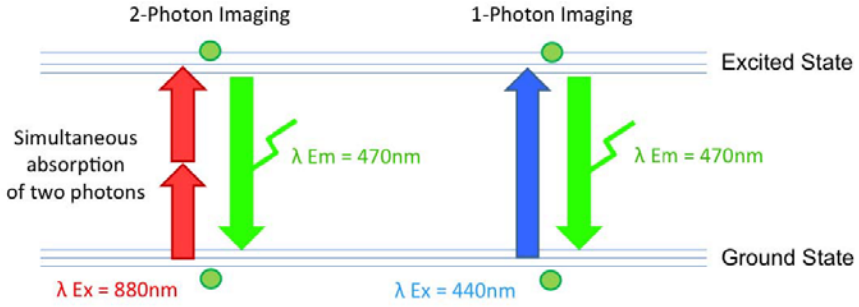


Fig. 1 Two-photon imaging versus one-photon imaging. Multi-photon microscopy relies on the simultaneous absorption of two photons that together provide the sufficient energy to excite the fluorophore of interest. In practical terms, this means that the wavelengths used for multi-photon imaging are approximately double the wavelengths used for conventional fluorescent microscopy. The wavelength of light emitted from an excited fluorophore as it returns to its ground state is identical for two-photon and one-photon imaging.

3 Intravital Skin Imaging Model

3.1 The Skin: An Important Immunological Site

The skin is the largest organ of the body and provides protection against the invasion of foreign pathogens by forming a physical barrier to the external environment, and is also home to several subsets of immune cells. The skin can be divided into two anatomical compartments: the epidermis, a relatively thin layer of cells composed primarily of keratinocytes, and the underlying dermis, which is rich in collagen-producing fibroblasts and contains a network of blood and lymphatic vessels. In the mouse skin, epidermal Langerhans cells [Banchereau et al. 1998] and dendritic epidermal T cells [Havran et al. 1988] are found in tight association with the surrounding keratinocytes in the epidermis. The dermis harbors macrophages, mast cells, dermal dendritic cells and memory T cells, and even scarce neutrophils that are dispersed throughout the collagen-rich interstitial space [Gebhardt et al. 2009], [Ng et al. 2008], [Sumaria et al. 2011]. Upon infection or injury, circulating inflammatory cells such as neutrophils are recruited in response to pro-inflammatory

cytokines released by skin resident cells. These inflammatory cells orchestrate innate immune responses to serve as first line of defense for eliminating invading pathogens [Nathan 2006]. Meanwhile, dendritic cells recognize and take up foreign antigens, and subsequently migrate to lymph nodes to initiate the adaptive immune response [Banchereau et al. 1998]. Maintaining the homeostasis of these immune cells is essential for the structural and functional integrity of the skin. Thus, a better understanding of these processes could lead to the identification of therapeutic targets for inflammatory diseases and may facilitate vaccine development.

3.2 *The Mouse Ear Skin Model*

The most commonly used sites for MP-IVM of the skin in mice are the ear and the hind footpad [Zinselmeyer et al. 2008, Ng et al. 2008, Matheu et al. 2008], [Peters et al. 2008, Sen et al. 2010]. Our laboratory mainly focuses on using the mouse ear skin. The mouse ear skin is an optimal imaging site as it is easily accessible and requires no surgical procedures prior to imaging, thereby preserving its physiological state. Its distal location also limits the effects of respiratory movements that can hinder imaging. Preparation for imaging starts with the removal of hair, which is highly auto-fluorescent and contributes to background signal. We have previously shown that hair removal does not interfere with the behavior of immune cells in the skin [Ng et al. 2008]. Albino mice are the best choice for imaging as the auto-fluorescent melanin, which is found in black-coated mice, may compromise the image quality. Although reducing laser power may dampen these background signals, this is sub-optimal as it results in reduced tissue penetration and decreased of signals when imaging deeper into the skin. For the actual experimental setup, after hair removal, the anesthetized mouse is placed onto a custom-built microscope stage (Figure 2) where the ear is immersed in PBS/glycerin (70:30 vol:vol) and covered with a glass cover slip. Care must be taken not to induce inflammation through the preparation, which may occur through physical trauma or dysregulated temperature. To ensure interstitial leukocyte activity is kept physiological, the temperature of the ear platform must be maintained around 35°C. The animal is kept at 37°C via a heating pad. In addition, adequate depth of anesthesia must be monitored closely to ensure that the animal is under a complete surgical anesthesia during the experiment (see [Roediger et al. 2008]).

3.3 *Visualizing Immune Cells in the Vasculature and Skin*

In order to visualize immune cells within the skin by MP-IVM, the cells of interest must be fluorescently tagged. This can be achieved by the endogenous expression

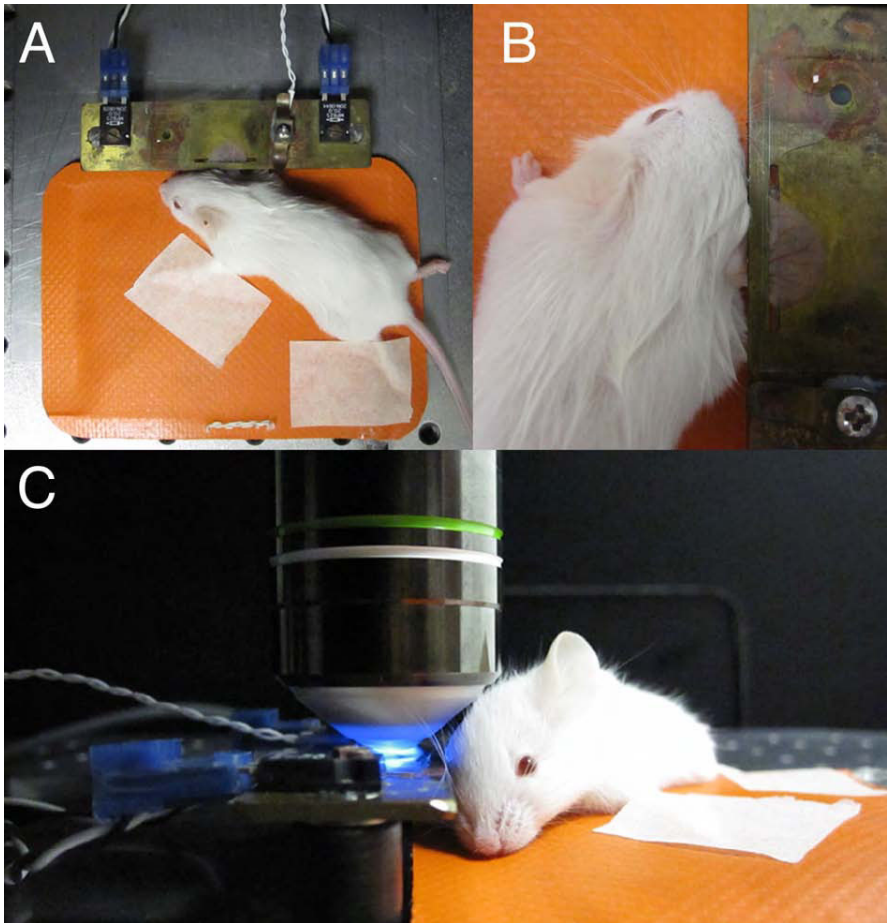


Fig. 2 Stage setup for intravital ear imaging. (A) The intravital imaging stage is a custom-built metal platform with a heating pad to maintain the body temperature of the anesthetized mouse at 37°C. The ear is positioned, dorsal surface up, on a metal strip with heating elements that maintains the temperature of the ear at 36°C. (B) Close up view of prepped ear on the metal strip. The ear is immersed in PBS/glycerin and covered with a glass cover slip. (C) The stage is placed on the microscope for imaging.

of a fluorescent protein under the control of an immune cell-specific gene promoter. The introduction of such an expression system into mice generates immune cell-specific fluorescent transgenic mice. Currently, there is a wide array of fluorescent transgenic mice available, for this chapter we only outlined the mouse strains that are useful for skin imaging (see Table I). Alternatively, fluorescently-labeled antibodies can be administered that recognize and bind to immune cells *in vivo*, or immune cells can be isolated and exogenously labeled with fluorescent compounds such as Cell Tracker Orange (CMTMR, invitrogen), before being adoptive transfer into

recipient mice [Bonasio et al. 2006][Mempel et al. 2004]. To visualize blood vessels, quantum dots, fluorescent dextrans or Evans blue dye can be used. As shown in Figure 3, using our ear skin model, we were able to visualize dendritic cells, collagen fibers and blood vessels in the ear dermis of a CD11c-YFP mouse (a fluorescent transgenic mouse expressing yellow fluorescent protein in all CD11c+ cells, which are the dendritic cells).

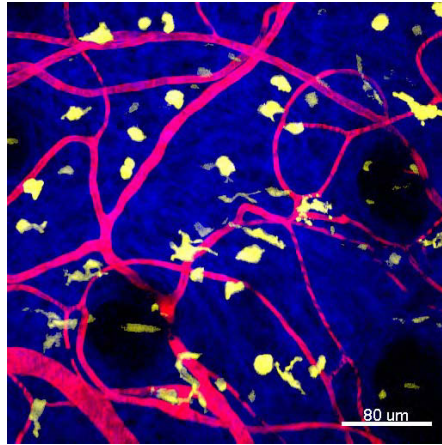


Fig. 3 Multiphoton imaging of the dermal dendritic cells within the ear skin of a CD11c-YFP mouse. Dermal dendritic cells (yellow) can be seen widely distributed within the highly vascularized (blood vessels shown in red), collagen-rich (blue, SHG) dermis.

Table 1 Immune Cell Specific Fluorescent Transgenic Mice.

| Mouse Strain | Fluorescent Immune Cells | References |
|---|--|-----------------------------|
| LysM-GFP | Neutrophils (GFPhi) Monocytes (GFPint) | [Faust et al. 2000] |
| CD41-YFP | Megakaryocytes and Platelets | [Varas et al. 2007] |
| CD11c-YFP | CD11c+ Dendritic Cells (DCs) | [Lindquist et al. 2004] |
| Langerin-GFP | Langerhans Cells | [Kissenpfennig et al. 2005] |
| CX3CR1-GFP | Monocytes Subsets of NK cells and DCs Microglial cells | [Jung et al. 2000] |
| FoxP3-IRES -mRFP (FIR) | Foxp3+ T regulatory cells | [Wan et al. 2005] |
| IL-4 GFP- enhanced transcript (4get) | IL-4 producing immune cells | [Mohr et al. 2001] |

Data acquisition and parameter extraction from intravital multiphoton imaging
The major strength of multiphoton imaging is the direct visualization of immune cell activities within intact organs and tissues. To understand the dynamics of the

immune system, three-dimensional (3D) image stacks are acquired longitudinally over time through time-lapse imaging (Figure 4). Special software is required to process and view the four-dimensionality (x, y, z and time) of these data. To date, the most widely used commercial software packages for data processing and analysis are Imaris (Bitplane) and Volocity (PerkinElmer). The output of these 4D datasets is most often presented as "extended focus view" movies, in which the information from multiple z -planes is compressed into one single plane. Visual inspection of the movie is the first step to examine the cellular behavior of the fluorescent objects in the image stacks. Although this can provide very useful information, it is still important to obtain quantitative information. Tracking analysis based on the extended focus view movies is not recommended because these data sets do not contain information from the z -axis. Ideally, to measure cell motility within an intact tissue/organ, 3D tracking should be performed. For optimal measurements, several aspects of image acquisition have to be carefully designed and recorded, these include: size and depth of the scan field, time interval between acquisition and the number of fluorochromes. In the end, various parameters (Table 2) can then be extracted from the tracking analysis to characterize cell motility and interactions.

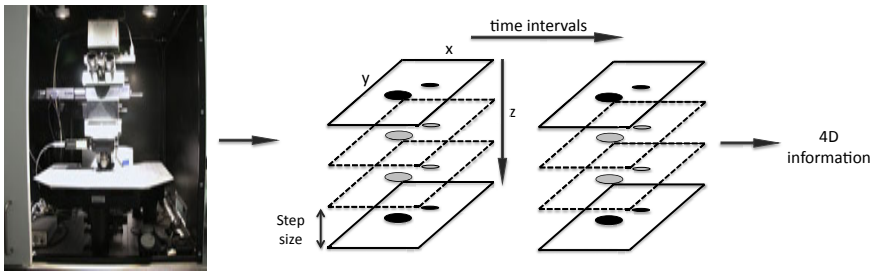


Fig. 4 Basics of Image Acquisition. Multi-photon imaging gives 4-D information (x, y, z plane over time, t) of cell morphology and motility. The area, depth, step size and imaging time can be determined prior to acquisition.

3.4 Data Processing and Presentation

Data sets generated from multiphoton imaging can be enormous in file sizes, as these files contain multi-dimensional information. The major challenge is how to best present dynamic cellular data in 2D print media such as articles in scientific journals. One possible way for such representation is to show snapshots of selected time-lapse images (Figure 5). This is often complemented with movie files up-loaded to the journal's website, which can provide a better dynamic view of the cellular activities. Although time-lapse images and movie files contain information for x - y dimensions, they lack the depth information on the z -axis. Because of this shortcoming,

Table 2 Parameters used to characterize cell motility and interaction (adapted from [Cahalan et al. 2008]).

| Parameters | Description | Unit |
|--------------------------------|--|----------------------------|
| Instantaneous velocity (v) | Velocity calculated as displacement/time during a single time step | $\mu\text{m}/\text{min}$ |
| Mean velocity (\bar{v}) | Mean velocity of a cell over several time steps (usually the entire imaging period) | $\mu\text{m}/\text{min}$ |
| Contact time | Time for which a cell is in contact with a defined cell or structure | sec:min |
| Path length | Cumulative distance traveled by a cell over a given time | μm |
| Displacement (D) | Straight-line distance of a cell from its starting point after any given time | μm |
| Motility coefficient (M) | $M = \text{displacement}^2/4t$ (for 2-D measurements) or $\text{displacement}^2/6t\mu\text{m}^2/\text{min}$ (for 3-D measurements); analogous to the diffusion coefficient for Brownian motion | $\mu\text{m}^2/\text{min}$ |

this can lead to incorrect visual perceptions, for instance the image may show that two objects are in close contact, but in reality they were only moving passed each other on different z-planes. Thus, it is important not to draw conclusions about cellular dynamics merely base on the visual inspection of images/movies. There is no question that dynamic imaging offers exciting ways to visualize immune cell behavior in vivo, however, results from extensive quantitative and statistical analyses must still form the basis for making conclusions.

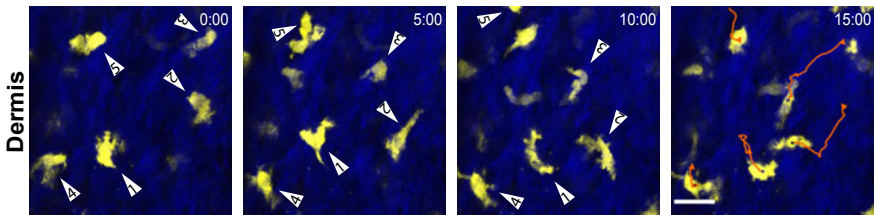


Fig. 5 Tracking cell motility using Imaris, a scientific 3-D/4-D Image Processing and Analysis Software. Five dermal dendritic cells (yellow, labeled 1 to 5) were tracked using Imaris (shown here are four consecutive, representative time frames). Orange lines indicate the 2-D tracking of these cells. Extracted from [Ng et al. 2008], [Roediger et al. 2008].

3.5 Intravital Multiphoton Imaging Considerations

In previous sections, we have outlined the benefits of using MP-IVM to study immune cells in the skin, as well as caveats and pit-falls associated with it. For the following section, we will provide a broad overview of MP-IVM areas requiring

software developments to overcome current challenges not only for skin imaging but also for other MP-IVM studies.

4 The Missing Link in Multiphoton Microscopy: Software Development

In the past few years, hardware development in multiphoton microscopy has accelerated to the point where it is now possible to purchase an off the shelf system that is highly reliable, compact and user friendly. As this technology slowly becomes common-place like conventional laser scanning confocal microscope, the main focus for future developments will be on bioinformatics tools. With the continuing efforts in hardware and optics developments, one can envision that future multiphoton imaging experiments will become more ambitious in terms of the numbers of the detection channels, resolution, acquisition speed, volume and duration. This multi-dimensional approach will no doubt generate large volumes of digital information, and special considerations should be given to find better solutions for storing, processing and analyzing these data. At the practical level, software that is capable of handling large volumes of image data sets to allow visualization, segmentation and quantification of multi-dimensional image sets, and provide methods for annotating raw and analyzed data in a standard format will be extremely useful. To date, no such widely functional software exists. In the following section, we will discuss several possible future developments that may help to achieve this goal.

4.1 *Image Acquisition and Data Management*

One challenging aspect for managing multi-dimensional images is keeping track of important contextual information related to these files. Currently, most acquisition software allows exportation of such information through Open Microscopy Environment (OME) or Metadata file formats [Swedlow et al. 2003]. However there is still no standardized metadata format for describing the hardware (e.g. objective lens and filter sets) or acquisition parameters (e.g. scan field and resolution) between microscope manufacturers. Implementations of standardization in the future will no doubt facilitate inter transferability of image-based data between different platforms and laboratories.

4.2 *Spectral Unmixing*

Given the advent of transgenic mice expressing fluorescent proteins as well as new techniques for labeling cells/structures *in vivo*, one would expect that multi-color

MP imaging be routinely performed. However, most of the MP imaging studies have only used 2 to 3 color detection. The limitation lies in the fact that most of the commonly used fluorescent proteins and/or dyes have overlapping emission spectra, leading to spectral bleed-through into multiple detection channels. As a result, it is then difficult to attribute a given color to a specific immune cell type or cellular structure. Spectral unmixing could be one approach to solve this problem [Dickinson et al. 2001, Hiraoka et al. 1991, Lansford et al. 2001]. However, it is important to note that current spectral unmixing algorithms were not designed for the separation and quantification of depth resolved spectra in complex biological tissues [Ducros et al. 2009]. Future efforts should focus on understanding how scattering and absorption effects in biological tissues may influence the emission spectra of various fluorophores. Such an understanding will be instrumental for the development of spectral unmixing algorithms that are suitable for the separation and quantification of spatially and spectrally over-lapping fluorophores in depth (within tissue) with high resolution.

4.3 Image Analysis

The principal challenge posed by analyzing images from multiphoton imaging is to translate pixel-based representation data to meaningful object-based (e.g. immune cells) data represented by the pixels. Recognizing and classifying cells in images, a process called segmentation, can be performed by software packages such as Imaris (Bitplane), Volocity (PerkinElmer) and ImageJ. Often this process is highly labor intensive, as it can only be done in a semi-automated manner. The difficulty of performing automated segmentation of images from intravital imaging lies in the multi-dimensionality of the data sets, i.e. cell volumes and movements over time. There is no common algorithm for segmenting cellular structures and cell tracks. Algorithms that work well for one application may not be good for another one. A major goal for future development should be providing a set of tools capable of extracting cell-based data from many different types of data sets generated by intravital imaging. One approach is to create organ- or tissue-specific sets of algorithms for image analysis. This approach, however, is possible only with the implementation of standardized imaging (see below).

4.4 Towards Standardized Imaging

Moving forward, one long-term goal of intravital imaging is to acquire and convert image-based data into a standardized, quantitative cell-based and anatomical format. If this goal is accomplished, it will allow direct comparison of data generated from different laboratories, and more importantly it can be used as a framework for cell- and anatomical-based databases. However to achieve this, major efforts need

to be made in standardizing several aspects of intravital multiphoton imaging, these include standardization of the imaging protocol, data extraction and presentation. If a universal system of standardized imaging is implemented, then one could imagine that data generated from MP-IVM can be digitized into a standard for-mat. This will form a powerful tool for immunologists to perform functional imaging, as comparison of normal and mutant phenotypes (e.g. genetically modified, gene-deletion or over-expression) could then be performed easily at cellular resolution.

4.5 Data Interpretation and Presentation

Although cell migration and interaction are major components of immune cell function, it remains a big challenge to "convince" non-imaging immunologists about the biological relevance of the numerical information extracted from imaging experiments. There is no best solution for this, however, if new methods can be implemented to better present the analytical data from these studies, it may help to bridge the perception gap. As mentioned above, cellular dynamics data are often represented by time-lapse images or movies, which lose most of their multi-dimensional information. Methods have been devised to provide more multi-dimensional information for the viewer. For instance, one scheme implemented was color coding of a cell based on its z-position in the tissue [Miller et al. 2002]. Future works should focus on how to create a simple intuitive interface that allows the viewer to perform rotation, zooming and simple 3D visualization of movie files without the need of specialized image analysis software.

5 Concluding Remarks

Intravital MP imaging is a powerful approach for investigating immune cell activities within their native environment. Although this is a relatively new field, it is now possible to perform dynamic, multi-dimensional imaging to simultaneously track cell populations at depths of up to several hundreds microns inside tissues over a long period of time (up to few hours). Despite its vast potential, there are still many limitations associated with MP imaging. We believe that interdisciplinary efforts from biologists, chemists, physicists, mathematicians and computer scientists will be needed in order to usher in a new era of functional immune imaging.

With the above-mentioned developments in mind, we hope that future software will be able to overcome major challenges for analyzing datasets obtained from in vivo imaging studies. These challenges include:

- A low signal-to-noise ratio due to the dynamics of the observation;

- The sharpness of the biological structure contours due to the similarity of the radiometry of the observed tissue;
- The variability of the shape and size of the biological structures.

We believe that overcoming these challenges is key to developing a software package that can automatically segment and track cells in a multidimensional manner.

Acknowledgements. We thank Jackson Li for critical reading of this book chapter. This work was supported by Agency of Science, Technology and Re-search (A*STAR), Singapore. This study work was also supported by NHMRC project grants 570769 and 632706 and a grant from OSMR to WW.

References

- [Banchereau et al. 1998] Banchereau, J., Steinman, R.M.: Dendritic cells and the control of immunity. *Nature* 392(6673), 245–252 (1998), doi:10.1038/32588
- [Bonasio et al. 2006] Bonasio, R., von Andrian, U.H.: Generation, migration and function of circulating dendritic cells. *Curr. Opin. Immunol.* 18(4), 503–511 (2006); doi:S0952-7915(06)00106-3 [pii] 10.1016/j.coi.2006.05.011
- [Bousso et al. 2002] Bousso, P., Bhakta, N.R., Lewis, R.S., Robey, E.: Dynamics of thymocyte-stromal cell interactions visualized by two-photon microscopy. *Science* 296(5574), 1876–1880 (2002); doi:10.1126/science.1070945 296/5574/1876 [pii]
- [Cahalan et al. 2008] Cahalan, M.D., Parker, I.: Choreography of cell motility and interaction dynamics imaged by two-photon microscopy in lymphoid organs. *Annu. Rev. Immunol.* 26, 585–626 (2008); doi:10.1146/annurev.immunol.24.021605.090620
- [Dickinson et al. 2001] Dickinson, M.E., Bearman, G., Tille, S., Lansford, R., Fraser, S.E.: Multi-spectral imaging and linear unmixing add a whole new dimension to laser scanning fluorescence microscopy. *Biotechniques* 31(6), 1272, 1274–1276, 1278 (2001)
- [Ducros et al. 2009] Ducros, M., Moreaux, L., Bradley, J., Tiret, P., Griesbeck, O., Charpak, S.: Spectral unmixing: analysis of performance in the olfactory bulb in vivo. *PLoS One* 4(2), e4418 (2009); doi:10.1371/journal.pone.0004418
- [Faust et al. 2000] Faust, N., Varas, F., Kelly, L.M., Heck, S., Graf, T.: Insertion of enhanced green fluorescent protein into the lysozyme gene creates mice with green fluorescent granulocytes and macrophages. *Blood* 96(2), 719–726 (2000)
- [Gebhardt et al. 2009] Gebhardt, T., Wakim, L.M., Eidsmo, L., Reading, P.C., Heath, W.R., Carbone, F.R.: Memory T cells in nonlymphoid tissue that provide enhanced local immunity during infection with herpes simplex virus. *Nat. Immunol.* 10(5), 524–530 (2009); doi:ni.1718 [pii] 10.1038/ni.1718
- [Germain et al. 2006] Germain, R.N., Miller, M.J., Dustin, M.L., Nussenzweig, M.C.: Dynamic imaging of the immune system: progress, pitfalls and promise. *Nat. Rev. Immunol.* 6(7), 497–507 (2006); doi:nri1884 [pii] 10.1038/nri1884
- [Havran et al. 1988] Havran, W.L., Allison, J.P.: Developmentally ordered appearance of thymocytes expressing different T-cell antigen receptors. *Nature* 335(6189), 443–445 (1988); doi:10.1038/335443a0

- [Hiraoka et al. 1991] Hiraoka, Y., Swedlow, J.R., Paddy, M.R., Agard, D.A., Sedat, J.W.: Three-dimensional multiple-wavelength fluorescence microscopy for the structural analysis of biological phenomena. *Semin. Cell. Biol.* 2(3), 153–165 (1991)
- [Jung et al. 2000] Jung, S., Aliberti, J., Graemmel, P., Sunshine, M.J., Kreutzberg, G.W., Sher, A., Littman, D.R.: Analysis of fractalkine receptor CX(3)CR1 function by targeted deletion and green fluorescent protein reporter gene insertion. *Mol. Cell. Biol.* 20(11), 4106–4114 (2000)
- [Kissenpfennig et al. 2005] Kissenpfennig, A., Henri, S., Dubois, B., Laplace-Builhe, C., Perrin, P., Romani, N., Tripp, C.H., Douillard, P., Leserman, L., Kaiserlian, D., Sae-land, S., Davoust, J., Malissen, B.: Dynamics and function of Langerhans cells in vivo: dermal dendritic cells colonize lymph node areas distinct from slower migrating Langerhans cells. *Immunity* 22(5), 643–654 (2005); doi:S1074-7613(05)00131-7 [pii] 10.1016/j.immuni.2005.04.004
- [Lansford et al. 2001] Lansford, R., Bearman, G., Fraser, S.E.: Resolution of multiple green fluorescent protein color variants and dyes using two-photon microscopy and imaging spectroscopy. *J. Biomed. Opt.* 6(3), 311–318 (2001); doi:10.1117/1.1383780
- [Lindquist et al. 2004] Lindquist, R.L., Shakhar, G., Dudziak, D., Wardemann, H., Eisenreich, T., Dustin, M.L., Nussenzweig, M.C.: Visualizing dendritic cell networks in vivo. *Nat. Immunol.* 5(12), 1243–1250 (2004); doi:ni1139 [pii] 10.1038/ni1139
- [Matheu et al. 2008] Matheu, M.P., Beeton, C., Garcia, A., Chi, V., Rangaraju, S., Safrina, O., Monaghan, K., Uemura, M.I., Li, D., Pal, S., de la Maza, L.M., Monuki, E., Flugel, A., Pennington, M.W., Parker, I., Chandy, K.G., Cahalan, M.D.: Imaging of effector memory T cells during a delayed-type hypersensitivity reaction and suppression by Kv1.3 channel block. *Immunity* 29(4), 602–614 (2008); doi:S1074-7613(08)00408-1 [pii] 10.1016/j.immuni.2008.07.015
- [Mempel et al. 2004] Mempel, T.R., Henrickson, S.E., Von Andrian, U.H.: T-cell priming by dendritic cells in lymph nodes occurs in three distinct phases. *Nature* 427(6970), 154–159 (2004); doi:10.1038/nature02238
- [Miller et al. 2002] Miller, M.J., Wei, S.H., Parker, I., Cahalan, M.D.: Two-photon imaging of lymphocyte motility and antigen response in intact lymph node. *Science* 296(5574), 1869–1873 (2002); doi:10.1126/science.1070051
- [Mohr et al. 2001] Mohrs, M., Shinkai, K., Mohrs, K., Locksley, R.M.: Analysis of type 2 immunity in vivo with a bicistronic IL-4 reporter. *Immunity* 15(2), 303–311 (2001); doi:S1074-7613(01)00186-8 [pii]
- [Nathan 2006] Nathan, C.: Neutrophils and immunity: challenges and opportunities. *Nat. Rev. Immunol.* 6(3), 173–182 (2006); doi:nri1785 [pii] 10.1038/nri1785
- [Ng et al. 2008] Ng, L.G., Hsu, A., Mandell, M.A., Roediger, B., Hoeller, C., Mrass, P., Iparraguirre, A., Cavanagh, L.L., Triccas, J.A., Beverley, S.M., Scott, P., Weninger, W.: Migratory dermal dendritic cells act as rapid sensors of protozoan parasites. *PLoS Pathog.* 4(11), 1000222 (2008), doi:10.1371/journal.ppat.1000222
- [Peters et al. 2008] Peters, N.C., Egen, J.G., Secundino, N., Debrabant, A., Kimblin, N., Kamhawi, S., Lawyer, P., Fay, M.P., Germain, R.N., Sacks, D.: In vivo imaging reveals an essential role for neutrophils in leishmaniasis transmitted by sand flies. *Science* 321(5891), 970–974 (2008); doi:321/5891/970 [pii] 10.1126/science.1159194
- [Roediger et al. 2008] Roediger, B., Ng, L.G., Smith, A.L., de St Groth, B.F., Weninger, W.: Visualizing dendritic cell migration within the skin. *Histochem. Cell Biol.* 130(6), 1131–1146 (2008); doi:10.1007/s00418-008-0531-7

- [Sen et al. 2010] Sen, D., Forrest, L., Kepler, T.B., Parker, I., Cahalan, M.D.: Selective and site-specific mobilization of dermal dendritic cells and Langerhans cells by Th1- and Th2-polarizing adjuvants. *Proc. Natl. Acad. Sci. USA* 107(18), 8334–8339 (2010); doi:0912817107 [pii] 10.1073/pnas.0912817107
- [Sumaria et al. 2011] Sumaria, N., Roediger, B., Ng, L.G., Qin, J., Pinto, R., Cavanagh, L.L., Shklovskaya, E., Fazekas de St Groth, B., Triccas, J.A., Weninger, W.: Cutaneous immunosurveillance by self-renewing dermal gammadelta T cells. *J. Exp. Med.* 208(3), 505–518 (2011); doi:jem.20101824 [pii] 10.1084/jem.20101824
- [Swedlow et al. 2003] Swedlow, J.R., Goldberg, I., Brauner, E., Sorger, P.K.: Informatics and quantitative analysis in biological imaging. *Science* 300(5616), 100–102 (2003); doi:10.1126/science.1082602
- [Wan et al. 2005] Wan, Y.Y., Flavell, R.A.: Identifying Foxp3-expressing suppressor T cells with a bicistronic reporter. *Proc. Natl. Acad. Sci. USA* 102(14), 5126–5131 (2005); doi:0501701102 [pii] 10.1073/pnas.0501701102
- [Witte et al. 2011] Witte, S., Negrean, A., Lodder, J.C., de Kock, C.P., Testa Silva, G., Mansvelder, H.D., Louise Groot, M.: Label-free live brain imaging and targeted patching with third-harmonic generation microscopy. *Proc. Natl. Acad. Sci. USA* (2011); doi:1018743108 [pii] 10.1073/pnas.1018743108
- [Varas et al. 2007] Zhang, J., Varas, F., Stadtfeld, M., Heck, S., Faust, N., Graf, T.: CD41-YFP mice allow in vivo labeling of megakaryocytic cells and reveal a subset of platelets hyperreactive to thrombin stimulation. *Exp. Hematol.* 35(3), 490–499 (2007); doi:S0301-472X(06)00714-4 [pii] 10.1016/j.exphem.2006.11.011
- [Zinselmeyer et al. 2008] Zinselmeyer, B.H., Lynch, J.N., Zhang, X., Aoshi, T., Miller, M.J.: Video-rate two-photon imaging of mouse footpad - a promising model for studying leukocyte recruitment dynamics during inflammation. *Inflamm. Res.* 57(3), 93–96 (2008); doi:10.1007/s00011-007-7195-y
- [Zoumi et al. 2002] Zoumi, A., Yeh, A., Tromberg, B.J.: Imaging cells and extracellular matrix in vivo by using second-harmonic generation and two-photon excited fluorescence. *Proc. Natl. Acad. Sci. USA* 99(17), 11014–11019 (2002); doi:10.1073/pnas.172368799

Functional MRI of Neural Plasticity and Drug Effect in the Brain

Kai-Hsiang Chuang and Fatima A. Nasrallah

Abstract. Recent advances in magnetic resonance imaging (MRI) have opened up new perspectives for understanding brain function and its plasticity after damage or even in the process of learning and memory. Using functional MRI (fMRI), reorganization of the cortical representation can be detected after the peripheral nerves deafferentation or digit amputation. To detect the more trivial changes during learning and memory, we established two techniques. One is to use manganese as a contrast agent to detect minute reorganization of hippocampal mossy fiber after training with hidden platform in Morris water maze. The other technique detects the synchrony in fMRI signal among neural areas that represents functional connectivity. We demonstrated the spatial memory network can be visualized in water maze trained animal. Furthermore, we showed that synchrony rather than activity in the brain can be modulated by receptor targeted pharmaceuticals, which indicate a different drug mechanism. The translation of these methods will facilitate our understanding of brain plasticity, early diagnosis of dementia, and evaluation of drug efficacy.

1 Introduction

Neural plasticity is the reorganization of neural circuit that continues throughout the lifetime [Johansen 2007, Berlucchi et al. 2009, Chopp et al. 2008], [Pascual et al. 2005]. It not only occurs in learning and memory, but also after damage in peripheral and central nervous system, such as stroke or

Kai-Hsiang Chuang

Laboratory of Molecular Imaging, Singapore Bioimaging Consortium,
Agency for Science Technology and Research, Singapore

e-mail: Chuang_Kai_Hsiang@sbic.a-star.edu.sg

Fatima A. Nasrallah

Clinical Imaging Research Centre, National University of Singapore,
Singapore & Department of Physiology, Yong Loo Lin School of Medicine,
National University of Singapore, Singapore

amputation [Calabresi et al. 2003, Doyon et al. 2005, Ramachandran et al. 1998], [Manning 2008]. The process involves changing in potentiation, synaptic transmission, synaptic/axonal density, large-scale connectivity and activity, and even neurogenesis. Understanding the mechanism and process in learning, memory, and the recovery from neural damage or degeneration will facilitate the development of approaches for improving or reversing these processes [Duffau 2006, Ward 2005]. Traditionally, it has been very difficult to study that in human. With the recent advance in non-invasive neuroimaging techniques, such as functional Magnetic Resonance Imaging (fMRI), we are able to observe the neural plasticity in the intact brain longitudinally for better diagnosis, prognosis and therapeutic development [van der Linden et al. 2009, Voss et al. 2009]. The most common fMRI technique is based on the so-called Blood Oxygenation Level Dependent (BOLD) contrast, which reflects the change in blood oxygenation, cerebral blood flow (CBF) and cerebral blood volume following neural activation that compensate for the increased glucose and oxygen utilization [Ogawa et al. 1990, Ogawa et al. 1998], [Ugurbil et al. 2000]. Since this method does not require injection of exogenous contrast agent nor involving ionizing radiation, it has been widely used to map neural activation under stimulation or performance of tasks in human to understand the neural circuits in perception, language, learning, memory, decision making and other high order cognitive function. Besides, clinical studies on pre-surgical planning, diagnosis and prognosis of neurological and psychological diseases, as well as evaluation of drug effects in the brain have been explored. However, the physiological change with neural plasticity, disease and drug could confound the BOLD fMRI signal [Logothetis et al. 2004, Poldrack 2000, Ekstrom 2010]. For example, long-term training or disease may change the vasculature, CBF and its reactivity to stimulation, and hence change the BOLD signal independent of the neural activity. In addition, both excitatory and inhibitory neural activity can increase metabolic demand and result in increased BOLD signal, making it difficult to interpret the underlying neural activity [Calford et al. 2005]. To better understand the neural mechanism of neural plasticity, we investigated several functional imaging techniques in rodent as a model system. We first applied BOLD fMRI to study the cortical plasticity after peripheral nerve deafferentation [Pelled et al. 2009, Pelled et al. 2007] and digit amputation [Weng et al. 2011]. Secondly, to visualize the plasticity in healthy animal after learning, we explored new technologies such as manganese-enhanced MRI (MEMRI) and resting-state functional connectivity MRI (fcMRI) in rats trained with Morris water maze. Lastly, the neural basis of fcMRI was investigated using a pharmacological approach.

2 MRI of Neural Plasticity after Nerve Amputation

It has been found that cortical reorganization occurs after peripheral nerve injury. It is also demonstrated in animal models that depriving the sensory input from a specific region of the adult neocortex can lead to large reorganization of cortical topography within the denervated area in subsequent months. For example, by

lesioning both sensory and motor afferents in rat's hindpaw, short-term and long-term plasticity in cortical and sub-cortical areas can be observed [Cusick 1996, Devor et al. 1979, Devor et al. 1981, Sjöberg et al. 1990, Wall et al. 1984]. To understand the underlying mechanism of the reorganization, we applied fMRI in the hindpaw deafferentation model. Three lesion groups were studied: 1) sciatic nerve, 2) sciatic and saphenous nerves, and 3) sham control. Both the sciatic and the saphenous nerves in the rat, contain sensory and motor fibers, thus lesioning them will remove both efferent and afferent components. The nerves were lesioned permanently to eliminate any possibility of regeneration. Two to three weeks following the surgery, BOLD fMRI was conducted on an 11.7T MRI by stimulating the right (operated) and the left (intact) hindpaws. Sham-operated rats showed similar activation in the contralateral SI hindpaw cortex as the intact side. No activation was observed when stimulating the lesioned hindpaw of the sciatic-deafferentiated or sciatic and saphenous- deafferentiated rats. However, bilateral activation was detected when stimulating the healthy hindpaw in the sciatic and saphenous- deafferentiated rats, indicating certain plasticity. Similar response can also be seen by lesioning the forepaw. To clarify whether the plasticity is through corticocortical or thalamocortical connection, the contralateral SI cortex to the intact hindpaw was lesioned. No bilateral activation was found when the left hindpaw was stimulated, suggesting the plasticity was not due to thalamocortical connection. To further elucidate the plasticity in the ipsilateral neural activity, local field potential at different layers of the cortex and single-unit recording was measured by stereotaxically inserting electrode in the ipsilateral SI cortex of the intact paw. Surprisingly, while BOLD activation was observed in the contralateral cortex of the lesioned paw, local field potential was not seen in any layer of the corresponding region. Instead, increased spiking activity with short duration was detected with single unit recording. With juxtacellular labeling of the active neurons, it shows that inhibitory interneurons but not pyramidal neurons are responsible for the increased activity in the denervated cortex. This also provides evidence that intracortical inhibitory activity can increase the CBF with minimal change in local field potential. To investigate intracortical plasticity, we explored another model where digit amputation was conducted at early age. The forepaw barrel subfield is an organized region in layer IV of the rodent primary somatosensory area. It consists of four centrally located bands of barrels orientated along a mediolateral plane. Each band consists of three to four barrels, which corresponds to digits from the 2nd digit (anterior) to the 5th digit (posterior) [Waltres et al. 1995, Woolsey et al. 1970, Welker 1976]. It has been reported that removal of a peripheral afferent input to the forepaw barrel subfield prior to postnatal day 5 or 6 results in a disorganized forepaw barrel subfield, whereas deafferentation at later times produces little or no alteration of the forepaw barrel subfield [Dawson et al. 1987, McCandlish et al. 1996]. Since each band is about 200 - 300 microns in width and 500 - 800 microns in length, it poses a challenge for non-invasive functional imaging like BOLD fMRI. High-resolution 3D fMRI with 300 micron isotropic resolution was implemented at 11.7T MRI. Data averaging was conducted to obtain fMRI with sufficient signal-to-noise ratio and resolution to detect the digit representation. By stimulating 2nd and 4th digit alternatively, the

corresponding representation of the digits can be clearly distinguished in the layer IV using a differential analysis that contrast between the digits rather than resting. The amputation of the 3rd digit was performed at postnatal day 3 and imaging was conducted at two and a half months old. The results showed reduced distance between the representation of 2nd and 4th while the width and area of the representation did not show significant increase (Figure 1). This demonstrates the potential of fMRI to resolve reorganization of digit barrels after amputation.

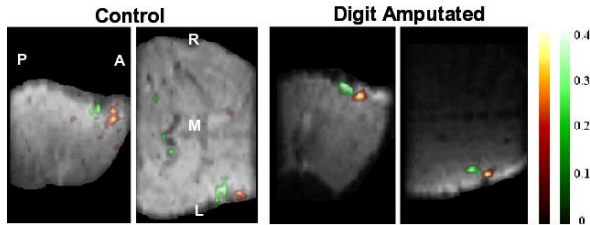


Fig. 1 High-resolution fMRI of 300 micron isotropic resolution shows digit representation in the primary somatosensory cortex of the rat. Cortical representations of digit 2 (red) and 4 (green) detected by fMRI is closer in the digit amputated animal (right) compared to the control (left) suggesting the brain area originally belongs to digit 3 was taken over. Adapted from [Weng et al. 2011].

3 MRI of Neural Plasticity after Learning

While large scale reorganization after damage can be observed by MRI, detection of plasticity after learning or day-to-day experience is still challenging. Memory employs a series of cognitive processes encompassing the acquisition of information and its subsequent consolidation, retention, and retrieval. Morris water maze has been widely used for studying spatial learning and memory and to evaluate memory impairment and treatment effects in rodent models [D’Hooge et al. 2001]. We explored detection of learning induced plasticity in hippocampal mossy fibers (MF) using MEMRI and the enhancement of memory network using fcMRI. It has been shown that MF undergo remodeling from the stratum lucidum into the stratum oriens after 5 days of Morris water maze training to find a hidden platform [Holahan et al. 2006]. This growth does not occur with visible platform training [Rekart et al. 2007] indicating that a specific mnemonic function, spatial memory, drives this structural plasticity. However, the relation between this structural plasticity and long-lasting memory remains unclear. To gain insight into this problem we explored MEMRI for noninvasive measurement of the MF remodeling. By using Mn^{2+} as a functional contrast agent, MEMRI allows visualization of neural structures of the brain in vivo especially in hippocampus [Aoki et al. 2004] (Figure 2). Because the remodeling is in the 100-200 micra range, we used high field MRI to

acquire high resolution image. Compared with naive control, the trained group showed increased CA3a region in each 100 micra slice with larger differences seen in the anterior sections, which is consistent with the Timm's staining [Chuang et al. 2010]. The results show that MEMRI has the potential to image the remodeling of the MF after learning. This non-invasive imaging allows longitudinal observation of MF to further elucidate the functional implications of this structural plasticity.

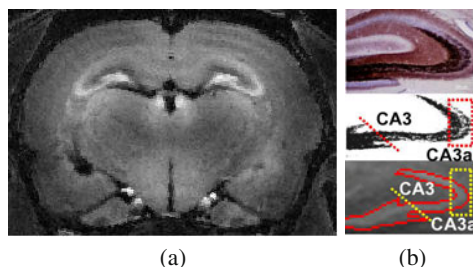


Fig. 2 (a) MEMRI acquired 1 day after Mn infusion shows intensified contrast in the hippocampus (arrow) of the rat brain. Particularly, the enhancement stems from dentate gyrus to CA3, which is similar to the distribution of (b) From top to bottom: the Timm's staining of the hippocampal mossy fiber, segmentation of Timm's staining, and MEMRI showing the CA3 and CA3a sub-regions in the hippocampus.

To understand how brain regions work together at each stage of memory, methods including cytochrome oxidase histochemistry, cFOS, and 2-deoxyglucose have been used to map functional changes after maze learning. However, these techniques are invasive and do not allow repeated measures. BOLD fMRI has been used to study brain activation under sensory stimulation in rodents, but probing cognitive function in rodent using this method is not possible due to physical restrictions of MRI and the use of anesthetics. Spontaneous, low frequency ($< 0.1\text{Hz}$) synchronous fMRI signal at resting state has been observed between functionally connected neural areas across the brain [Biswal et al. 1995, Vincent et al. 2006, Damoiseaux et al. 2006, Raichle et al. 2001, Greicus et al. 2003]. Moreover, abnormalities in such networks have been observed in the early stages of various neurological and psychiatric disorders [Greicus et al. 2004, Fleisher et al. 2009] and even in young adult carriers of a genetic risk factor of Alzheimer's disease [Filippini et al. 2009]. Recent studies using fcMRI have shown plasticity of the intrinsic brain network after intensive training in humans [Lewis et al. 2009]. To determine whether fcMRI can be used to detect plasticity in healthy rodent undergoing short period of training, we imaged rats at day 1 and day 7 after training in the Morris water maze. FcMRI of hidden-platform trained rat at 1 day after training revealed extensive connectivity across the brain especially in those regions related to spatial memory compared to the swim control. Significant increase of correlation was seen in the trained group in anterior hippocampus, posterior dentate gyrus, entorhinal cortex, visual cortex, retrosplenial cortex, and anterodorsal thalamus [Nasrallah et al. 2011]. Since fcMRI is a non-invasive method, it allows

plasticity to be detected longitudinally. The same animals were scanned again at 7 days after training. Functional connectivity was maintained at day 7 after training in both groups which the same regions still significant. This demonstrated, for the first time, memory network and its plasticity can be observed in intact brain in anesthetized animals.

4 MRI of Drug Effect

BOLD fMRI has been applied to study the drug activation or influence of a drug on task performance [Honey et al. 2004, Steward et al. 2005]. Besides neural activation, growing evidence show that connectivity could be modulated by drugs [Schwartz et al. 2009]. Here we applied fcMRI to study how connectivity changed by receptor-targeted pharmaceutical as well as to understand the neural mechanism of fcMRI.

To date, the relationship between spontaneous neural activity and the low frequency BOLD signal fluctuations that forms the basis for functional connectivity measurements using fMRI is still unclear. One source of the low frequency BOLD signal fluctuations is the physiological noise induced by respiratory and cardiac motions. Further studies have shown that with proper analysis and postprocessing, these artifacts can be eliminated to reveal the synchrony that would be related to neural activity. Perfusion imaging has been applied showing similar synchronous fluctuations in the cerebral blood flow (CBF) and hence the cerebral metabolic rate of oxygen (CMRO₂) [Chuang et al. 2008, Wu et al. 2009]. Electroencephalography (EEG) has been used to study the dynamics of brain; however, electrophysiological studies have yet to identify neural synchrony at a similar frequency ($< 0.1 Hz$) in the same subject.

To elucidate the neural mechanism of the hemodynamic change detected by fcMRI, our approach is to use receptor-targeted pharmacological manipulation to investigate the role of neuroreceptor systems in functional connectivity. The adrenergic system is a key modulator of numerous physiology and neural processes including attention, arousal, sleep, learning and memory [Pupo et al. 2001]. Especially, a study on attention and memory task in human showed changes in effective connectivity and suggested that noradrenergic system can mediate functional integration of those neurocircuits [Coull et al. 1999]. To understand the role of $\alpha 2$ -adrenergic system on the intrinsic brain network, the dose-dependent effects of an $\alpha 2$ -adrenergic receptor agonist, medetomidine, on brain activation and functional connectivity were investigated [Nasrallah et al. 2010]. Stimulation-induced activation and resting-state fluctuation in the rat somatosensory cortices and caudate putamen were measured. The results showed significant dose-dependent suppression of inter-hemispheric correlation but not the amplitude in the somatosensory areas, while the stimulation-induced activation in the same areas remained unchanged. To clarify the potential change in the hemodynamic response caused by the vasoconstrictive effect of medetomidine, the resting perfusion fluctuation was studied by

arterial spin labeling and showed similar results as the BOLD. This suggests that the oxygen metabolic rate and hence the neural activity may not be affected by medetomidine but only the synchrony between brain regions was suppressed. Furthermore, no change in functional connectivity with medetomidine dosages was seen in the caudate putamen, a region with much lower $\alpha 2$ adrenergic receptor density. These results indicate that resting-state signal correlation reflects underlying brain activity and a potential role of the adrenergic system in the functional connectivity. This approach will provide more insight to drug mechanism in the brain.

5 Concluding Remarks

Advances in MRI indicate potential for in vivo visualization of neural activity and connectivity after nerve damage, in the process of learning and memory, or under drug manipulation from system level down to individual barrel subfield or mossy fiber in the hippocampus. Further development is still ongoing to understand the neural mechanism through other techniques including electrophysiology, optical and radio-pharmaceutical. The establishment and application of these techniques will facilitate longitudinal study in disease models and clinical translation to understand the disease progression and evaluation of treatment efficacy.

Acknowledgements. The work on nerve amputation was supported by intramural research of National Institute of Neurological Disorder and Stroke, National Institutes of Health, USA. The rest of the work was supported by Agency of Science, Technology and Research (A*STAR), Singapore.

References

- [Aoki et al. 2004] Aoki, I., Wu, Y.J., Silva, A.C., Lynch, R.M., Koretsky, A.P.: *Neuroimage* 22, 1046–1059 (2004)
- [Berlucchi et al. 2009] Berlucchi, G., Buchtel, H.A.: *Exp. Brain Res.* 192, 307–319 (2009)
- [Biswal et al. 1995] Biswal, B., Yetkin, F.Z., Haughton, V.M., Hyde, J.S.: *Magnetic Resonance in Medicine* 34, 537–541 (1995)
- [Calabresi et al. 2003] Calabresi, P., Centonze, D., Pisani, A., Cupini, L., Bernardi, G.: *Lancet Neurol.* 2, 622–629 (2003)
- [Calford et al. 2005] Calford, M.B., Chino, Y.M., Das, A., Eysel, U.T., Gilbert, C.D., Heinen, S.J., Kaas, J.H., Ullman, S.: *Nature* 438 (2005); E3, discussion E3-4
- [Cusick 1996] Cusick, C.G.: *Prog. Brain. Res.* 108, 379–390 (1996)
- [Chopp et al. 2008] Chopp, M., Li, Y., Zhang, J.: *J. Neurol. Sci.* 265, 97–101 (2008)
- [Chuang et al. 2010] Chuang, K.H., Zhang, B.B., Chen, W., Sheu, F.S., Routtenberg, A.: In: 40th Annual Meeting of Society for Neuroscience, San Diego, USA (2010)
- [Chuang et al. 2008] Chuang, K.H., van Gelderen, P., Merkle, H., Bodurka, J., Ikonomidou, V.N., Koretsky, A.P., Duyn, J.H., Talagala, S.L.: *NeuroImage* 40, 1595–1605 (2008)
- [Coull et al. 1999] Coull, J.T., Buchel, C., Friston, K.J., Frith, C.D.: *Neuroimage* 10, 705–715 (1999)

- [Damoiseaux et al. 2006] Damoiseaux, J.S., Rombouts, S.A.R.B., Barkhof, F., Scheltens, P., Stam, C.J., Smith, S.M., Beckman, C.F.: *Proceedings of the National Academy of Sciences* 103, 13848–13853 (2006)
- [Dawson et al. 1987] Dawson, D.R., Killackey, H.P.: *J. Comp. Neurol.* 256, 246–256 (1987)
- [Devor et al. 1979] Devor, M., Schonfeld, D., Seltzer, Z., Wall, P.D.: *J. Comp. Neurol.* 185, 211–220 (1979)
- [Devor et al. 1981] Devor, M., Wall, P.D.: *J. Neurosci.* 1, 679–684 (1981)
- [D’Hooge et al. 2001] D’Hooge, R., De Deyn, P.P.: *Brain. Res. Brain. Res. Rev.* 36, 60–90 (2001)
- [Doyon et al. 2005] Doyon, J., Benali, H.: *Curr. Opin. Neurobiol.* 15, 161–167 (2005)
- [Duffau 2006] Duffau, H.: *J. Clin. Neurosci.* 13, 885–897 (2006)
- [Ekstrom 2010] Ekstrom, A.: *Brain Res. Rev.* 62, 233–244 (2010)
- [Filippini et al. 2009] Filippini, N., MacIntosh, B.J., Hough, M.G., Goodwin, G.M., Frisoni, G.B., Smith, S.M., Matthews, P.M., Beckmann, C.F., Mackay, C.E.: *Proceedings of the National Academy of Sciences*, 7209–7214 (2009)
- [Fleisher et al. 2009] Fleisher, A.S., Sherzai, A., Taylor, C., Langbaum, J.B.S., Chen, K., Buxton, R.B.: *NeuroImage* 47, 1678–1690 (2009)
- [Greicus et al. 2003] Greicius, M.D., Krasnow, B., Reiss, A.L., Menon, V.: *Proceedings of the National Academy of Sciences of the United States of America* 100, 253–258 (2003)
- [Greicus et al. 2004] Greicius, M.D., Srivastava, G., Reiss, A.L., Menon, V.: *Proceedings of the National Academy of Sciences of the United States of America* 101, 4637–4642 (2004)
- [Holahan et al. 2006] Holahan, M.R., Rekart, J.L., Sandoval, J., Routtenberg, A.: *Hippocampus* 16, 560–570 (2006)
- [Honey et al. 2004] Honey, G., Bullmore, E.: *Trends Pharmacol. Sci.* 25, 366–374 (2004)
- [Johansen 2007] Johansen-Berg, H.: *Curr. Biol.* 17, R141–R144 (2007)
- [Lewis et al. 2009] Lewis, C.M., Baldassarre, A., Comitteri, G., Romani, G.L., Corbetta, M.: *Proc. Natl. Acad. Sci. USA* 106, 17558–17563 (2009)
- [Logothetis et al. 2004] Logothetis, N.K., Wandell, B.A.: *Annu. Rev. Physiol.* 66, 735–769 (2004)
- [McCandlish et al. 1996] McCandlish, C., Li, C., Waters, R., Howard, E.: *Exp. Brain Res.* 108, 417–426 (1996)
- [Manning 2008] Manning, L.: *Behav. Brain Res.* 192, 143–148 (2008)
- [Nasrallah et al. 2011] Nasrallah, F.A., Chen, D.Y., Routtenberg, A., Chuang, K.H.: In: 19th Annual Meeting ISMRM, Montreal, Canada (2011)
- [Nasrallah et al. 2010] Nasrallah, F.A., Tan, J., Hennies, N., Chuang, K.H.: In: 18th Annual Meeting ISMRM-ESMRMB, Stockholm, Sweden (2010)
- [Ogawa et al. 1990] Ogawa, S., Lee, T.M., Kay, A.R., Tank, D.W.: *Proc. Natl. Acad. Sci. USA* 87, 9868–9872 (1990)
- [Ogawa et al. 1998] Ogawa, S., Menon, R.S., Kim, S.G., Ugurbil, K.: *Annu. Rev. Biophys. Biomol. Struct.* 27, 447–474 (1998)
- [Pascual et al. 2005] Pascual-Leone, A., Amedi, A., Fregni, F., Merabet, L.B.: *Annu. Rev. Neurosci.* 28, 377–401 (2005)
- [Pelled et al. 2009] Pelled, G., Bergstrom, D.A., Tierney, P.L., Conroy, R.S., Chuang, K.H., Yu, D., Leopold, D.A., Walters, J.R., Koretsky, A.P.: *Proc. Natl. Acad. Sci. USA* 106, 14114–14119 (2009)
- [Pelled et al. 2007] Pelled, G., Chuang, K.H., Dodd, S.J., Koretsky, A.P.: *Neuroimage* 37, 262–273 (2007)
- [Poldrack 2000] Poldrack, R.A.: *Neuroimage* 12, 1–13 (2000)
- [Pupo et al. 2001] Pupo, A., Minneman, K.: *CNS spectrums* 6, 656–662 (2001)

- [Raichle et al. 2001] Raichle, M.E., MacLeod, A.M., Snyder, A.Z., Powers, W.J., Gusnard, D.A., Shulman, G.L.: Proceedings of the National Academy of Sciences of the United States of America 98, 676–682 (2001)
- [Ramachandran et al. 1998] Ramachandran, V.S., Hirstein, W.: Brain 121(pt 9), 1603–1630 (1998)
- [Rekart et al. 2007] Rekart, J.L., Sandoval, C.J., Bermudez-Rattoni, F., Routtenberg, A.: Learn. Mem. 14, 416–421 (2007)
- [Sjoberg et al. 1990] Sjoberg, J., Kanje, M.: Brain Res. 529, 79–84 (1990)
- [Steward et al. 2005] Steward, C.A., Marsden, C.A., Prior, M.J., Morris, P.G., Shah, Y.B.: Psychopharmacology (Berl) 180, 687–704 (2005)
- [Schwartz et al. 2009] Schwarz, A.J., Gozzi, A., Bifone, A.: Neuroimage 47, 302–311 (2009)
- [Ugurbil et al. 2000] Ugurbil, K., Adriany, G., Andersen, P., Chen, W., Gruetter, R., Hu, X., Merkle, H., Kim, D.S., Kim, S.G., Strupp, J., Zhu, X.H., Ogawa, S.: Annu. Rev. Biomed. Eng. 2, 633–660 (2000)
- [van der Linden et al. 2009] Van der Linden, A., Van Meir, V., Boumans, T., Poirier, C., Baltazard, J.: Trends Neurosci. 32, 257–266 (2009)
- [Vincent et al. 2006] Vincent, J.L., Snyder, A.Z., Fox, M.D., Shannon, B.J., Andrews, J.R., Raichle, M.E., Buckner, R.L.: J. Neurophysiol. 96, 3517–3531 (2006)
- [Voss et al. 2009] Voss, H.U., Schiff, N.D.: Prog. Brain Res. 175, 483–496 (2009)
- [Wall et al. 1984] Wall, J.T., Cusick, C.G.: J Neurosci. 4, 1499–1515 (1984)
- [Waltres et al. 1995] Watres, R., Li, C., McCandlish, C.: Exp. Brain Res. 103, 183–197 (1995)
- [Ward 2005] Ward, N.S.: Prog. Brain Res. 150, 527–535 (2005)
- [Welker 1976] Welker, C.: J. Comp. Neurol. 166, 173–189 (1976)
- [Weng et al. 2011] Weng, J.C., Chuang, K.H., Goloshevsky, A., Dodd, S.J., Sharer, K.: Neuroimage 54, 1122–1129 (2011)
- [Woolsey et al. 1970] Woolsey, T.A., Van der Loos, H.: Brain Res. 17, 205–242 (1970)
- [Wu et al. 2009] Wu, C.W., Gu, H., Lu, H., Stein, E.A., Chen, J.H., Yang, Y.: NeuroImage 45, 694–701 (2009)

Automated Identification and Analysis of Visual Micro-experiments on Cellular Microarray

Auguste Genovesio

Abstract. This paper is an overview of the computer-based tools I designed at Institut Pasteur Korea in order to analyse a large quantity of microscopy cell based experiments. This development consisted in designing algorithms and software for automatically localize, identify and analyze cells on spots of cellular microarray at high resolution. We believe the applications of this work are numerous from genome wide loss of function screens to drug target deconvolution assays and diagnostic.

1 Background

To understand how the current biomedical research came to this automation and why it is important, a few concept and methods need to be recall first.

1.1 *The High Throughput Screening*

The High Throughput Screening (HTS) consists in the conduction of a massive amount of simple biological tests in an automated fashion. The same cellular function or process can be observed in the presence of a large variation of chemical compound such that to find stimulator or inhibitor of this function or process [Maloff et al. 1991]. The individual readout of a single experiment is often a fluorescent value using a fluorescent reader. The base material used to carry on those experiments is the microplate which is literally a plate that contains wells. There are various formats but most often microplate contains 96, 384 or 1536 wells. For instance, if the 384 format is used for a 50,000 compounds screen, about 130 plates will be necessary to conduct one pass. The HTS contains therefore a large part of

Auguste Genovesio
Image Mining Group, Institut Pasteur Korea

robotics and database managements to track all experiments, their content and their location. The HTS has been used by pharma-companies all over the world for the last 25 years as the method of choice for the first step in the identification of novel drug candidates. Recent advances has also largely increase the speed of this technology [Agresti et al. 2010]. For drug discovery, this technique rely mainly on the fact that prior to a screen and in order to create an assay, it is crucial to identify a cellular or pathogen function involved in an infectious process of interest and to understand it precisely because the HTS will bring up compounds that have potential effect on this specific process. It is nowadays perceived as a serious issue because this also mean that a screen will focus on a very specific part of an infectious process for exemple since our read out is narrow down to the process of interest. It does not allow for the discovery of a function but for the identification of compound having an effect on a known function.

1.2 The High Content Screening

The High Content Screening (HCS) appeared 15 years ago but really has emerged those last 5 years in research institutions [Liptrot 2001, Giuliano et al. 2003]. A HCS platform looks similar as a HTS platform except that the experiments are cell based and that the readout is not a fluorescent value but a whole microscopy image acquired by an automated microscope for each experiment. This is a large difference because it is a much slower platform but it increases dramatically the amount of information one can obtain from each experiment both because it concerns the whole cell-pathogen interaction and not only a cell function but also because image analysis algorithms can extract a dozen of numerical descriptions of the cell state. It is nothing less than the automation of a part of the cell biology research. This time the discovery of novel cellular functions appears possible with HCS assays. Furthermore, in combination to gene expression modulation at genome scale, we foresee its use for a possible inversion of the two first steps of the drug discovery pipeline namely the target identification and the lead molecule identification.

1.3 The High Content Screening in practice

When Institut Pasteur Korea started its activity in 2005, it has specialized in High Content Screening with a whole research group, the Image Mining Group, dedicated to the development of algorithms and software for the image analysis of specific image based assays. After one year of activity where we identified numerous compounds effective against several pathogens as Tuberculosis or HIV, we also realized that this large amount of information was contaminated by a lot of noise at many level when tackling genome wide assays. Some kinds of errors were known from HTS specialists while some other kinds were inherent to the microscopy readout. A major mistake HCS users first did and still do is often to consider HCS as a simple

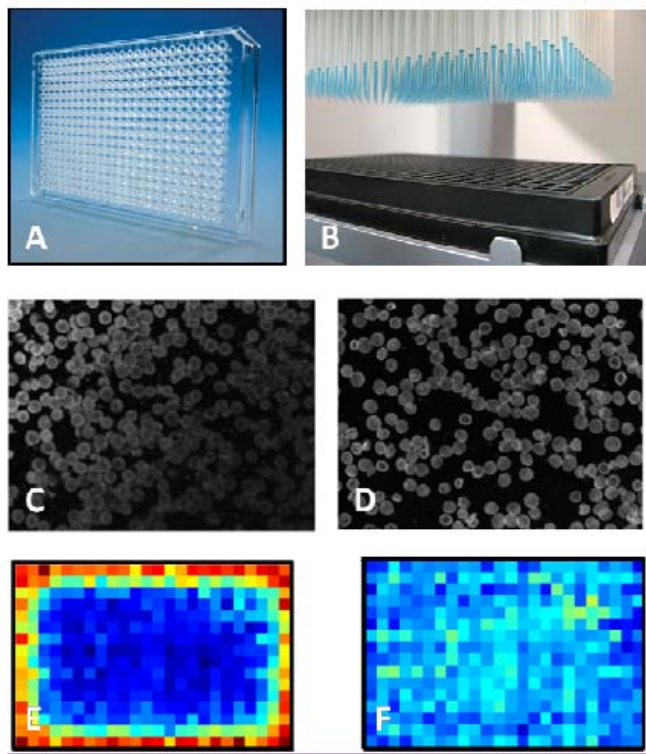


Fig. 1 A - A microplate with 384 wells commonly used in HTS and HCS. B - Most of the dispensing steps are subject to random errors that are difficult to quantify. C - Automated acquisition on those kind of plate often produce out of focus pictures and bias. D - Bias can be corrected by image processing steps but not the loss of focus. E - Bias issues also arise at the level of the whole plate since wells located on the border of the plate are affected by the difference of humidity level. F - Some signal processing methods can also be applied to correct this effect.

extension of HTS and therefore use the same tools for both while they are radically different. Several tools should be adapted along with most of the data analysis methods. For instance, a first point we noticed is that the microplate was responsible for a significant part of the reading errors. This is due to the fact that a much larger precision is required by a confocal microscope than by a fluorescent reader to obtain a reliable set of data (see Figure 1). Micro plates could be still largely used in the case where the expected readout was obvious and binary as for instance infected/none infected as for a reporter cell line screen on chemical compound. On the other hand, when the question became more complex as for classifying multiple phenotypes one can read from genome wide siRNA screens, the level of noise in microplate was so high that understanding became limited.

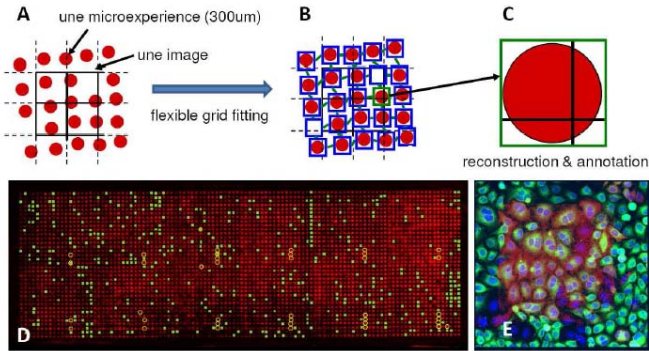


Fig. 2 High Content Cellular Microarray, a fast computational method to annotate and extract high resolution image of individual spotted micro-experiments. A. A high number of micro-experiments were printed by Discovery Cell Biology group at IPK and covered by a layer of cells. The whole slide can be scanned with an automated microscope. B - Thousands of pictures are miniaturized and re-assembled to obtain a broad vision of the whole microarray. A Robust, fully automated grid fitting algorithm was developed to identify the micro experiments on this miniaturized image. C - The pieces of pictures needed to construct each localized and annotated experiment were automatically reassembled to obtain an annotated high resolution picture per experiment/spot. D - A slide smaller than a finger contains about 4000 experiments. E - example of one experiment once automatically reconstructed.

2 High Content Cellular Microarray

To overcome those difficulties, Dr Neil Emans and Mr Yong Jun Kwon, biologists and myself, computer scientist have proposed and implemented a method to use cellular microarray as a fully automated high content screening platform. This platform has enabled to increase dramatically the number of experiment that one can possibly make with a visual platform to reinforce statistical significance and has also brought several major points of improvement in the quality of each experiment. Also the size and the cost of the platform was largely reduced due to the fact robotic coming along with a micro plate based platform became obsolete in our framework. The technology we developed at Institut Pasteur Korea uses cellular microarrays instead of wellplates. This means we address a grid of points printed on a slide instead of a grid of well in a plate. The cellular microarrays were first proposed in 2001 by Ziauddin and Sabatini [[Ziauddin et al. 2001](#)] when they proved that it was possible to reverse transfect a layer of cells onto a glass slide where spots containing cDNA were printed. Surprisingly, while this method appeared promising at first, in 2006 there was still no available platform on the market and few research efforts [[Carpenter et al. 2004](#), [Erfle et al. 2004](#), [Erfle et al. 2005](#)] that could bring researcher to effectively use cellular microarray to image a large amount of experiments at high resolution. A reason could be that going from a few tens or even hundreds of experiments to millions was not a simple step because it required a full automation of every single step involved. This is to the point where most of

the vast amount of pictures we generated would never be seen by anyone else than computers. This made a difference because then, no manual correction or tuning was possible and all steps had to be able to be automated. To achieve this goal, we relied on very clear and simple objectives: first reducing drastically the quantity of matter involved and the surface needed to create each of those experiments, second automating the identification, the analysis and the management of every experiment through the development of dedicated algorithms and software programs. We designed and implemented all the tools needed to cross this technological gap and finally obtained a prototype in mid-2006. This method replaced most robotic manipulations by computer analysis to locate and extract picture on a very large grid of image made of all the surface of a slide instead of acquiring images of experiments in wells one by one. This resulted in the miniaturization of the HCS technology to offer a real High Throughput to the High Content. Also performance was increase because, for instance, there was no more problem of out of focus picture which is a very common issue in HCS. This is due to the fact that the large slide picture is acquired continuously and the microscope head does not need to travel anymore between two consecutives experiments. It is also less expensive because the volume of each experiment was greatly reduced. We confirm our method can screen about 4000 experiments on an area that is smaller than a finger with a resolution that permit to observe about 100 cells for each experiment. It is fully automated which is to our knowledge unique as for today.

3 Conclusion

The benefit of such a method for cell biology research and drug development is important. This prototype alone made possible to answer important scientific question more precisely, quickly and for a much lower price. For instance, we identified in 2007 unknown human genes involved in HIV infection with a functional genome wide siRNA screen for which we had 7 independent replicates for each and every gene. This screen was made of about 200,000 visual experiments. Some of those factors could become therapeutic targets. We have repeated this process since then with different type of pathogens as *Trypanosoma Cruzi* and also cellular functions. It was also possible to observe a drug's dose response curve under the knock down of every single human gene which implied screening about half a million experiments, which we could do in only 3 weeks. We believe the possibility achieving a lot more experiments in a much shorter time with a higher precision will give the possibility to identify the target of a small compound in a systematic way soon but also it will open the door to new types of questions were system can be seen as a whole with a high level of information and within a reasonable level of noise.

We describe the development of a method to increase dramatically the speed of High Content Screen through miniaturization. We have also developed cell

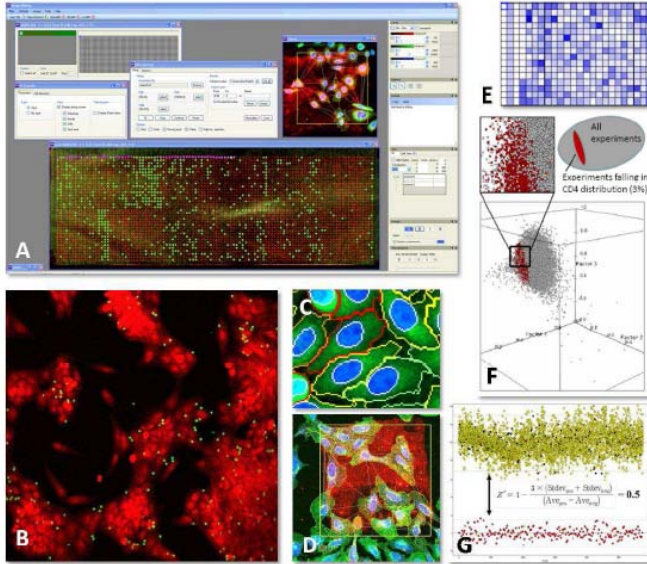


Fig. 3 The IM software is a software conceived and developed at Institut Pasteur Korea for High Content screening image analysis. We can see an opened cellular microarray being analyzed. It contains 3888 high resolution spotted experiments. B - Example screen where the number of cells (red) infected by a parasite (green) is estimated. C - Result of our cell detection algorithm. D - Analysis of a micro experiment. The few cells on the red spot are transfected with a specific siRNA and can possibly present a specific phenotype. E - Result of a microplate experiments. The color indicates the value taken by a descriptor. F - Example of a multidimensional analysis of a 200,000 experiments screen. G - Screen with a clear distinction of two phenotypes.

segmentation and description algorithm compatible with High Throughput. A remaining challenge will be to define and disseminate adapted data analysis methods for High Content Screening. Cell classification methods and software and examples of utilization of cell profiling data analysis were recently published but the community is still small. The increasing need of automated microscopy for cell biology and drug discovery should see the rise of an intense development of data analysis methods in this field of research in the coming years.

References

- [Agresti et al. 2010] Agresti, J.J., Antipov, E., Abate, A.R., Ahn, K., Rowat, A.C., Baret, J.-C., Marquez, M., Klibanov, A.M., Griffiths, A.D., Weitz, D.A.: Ultrahigh-throughput screening in drop-based microfluidics for directed evolution. *Proc. Natl. Acad. Sci. USA* 107(9), 4004–4009 (2010)
- [Carpenter et al. 2004] Carpenter, A.E., Sabatini, D.M.: Systematic genome-wide screens of gene function. *Nat. Rev. Genet.* 5(1), 11–22 (2004)
- [Erfle et al. 2005] Erfle, H., Pepperkok, R.: Arrays of transfected mammalian cells for high content screening microscopy. *Methods Enzymol.* 404, 1–8 (2005)
- [Erfle et al. 2004] Erfle, H., Simpson, J.C., Bastiaens, P.I.H., Pepperkok, R.: siRNA cell arrays for high-content screening microscopy. *Biotechniques* 37(3), 454–458, 460, 462 (2004)
- [Giuliano et al. 2003] Giuliano, K.A., Haskins, J.R., Lansing Taylor, D.: Advances in high content screening for drug discovery. *Assay Drug Dev. Technol.* 1(4), 565–577 (2003)
- [Liptrot 2001] Liptrot, C.: High content screening - from cells to data to knowledge. *Drug Discov. Today* 6(16), 832–834 (2001)
- [Maloff et al. 1991] Maloff, B.L., Delmendo, R.E.: Development of high-throughput radioligand binding assays for interleukin-1 alpha (IL-1 alpha) and tumor necrosis factor (TNF-alpha) in isolated membrane preparations. *Agents Actions* 34(1-2), 132–134 (1991)
- [Ziauddin et al. 2001] Ziauddin, J., Sabatini, D.M.: Microarrays of cells expressing defined cDNAs. *Nature* 411(5833), 107–110 (2001)

Part II
Physics and Chemistry

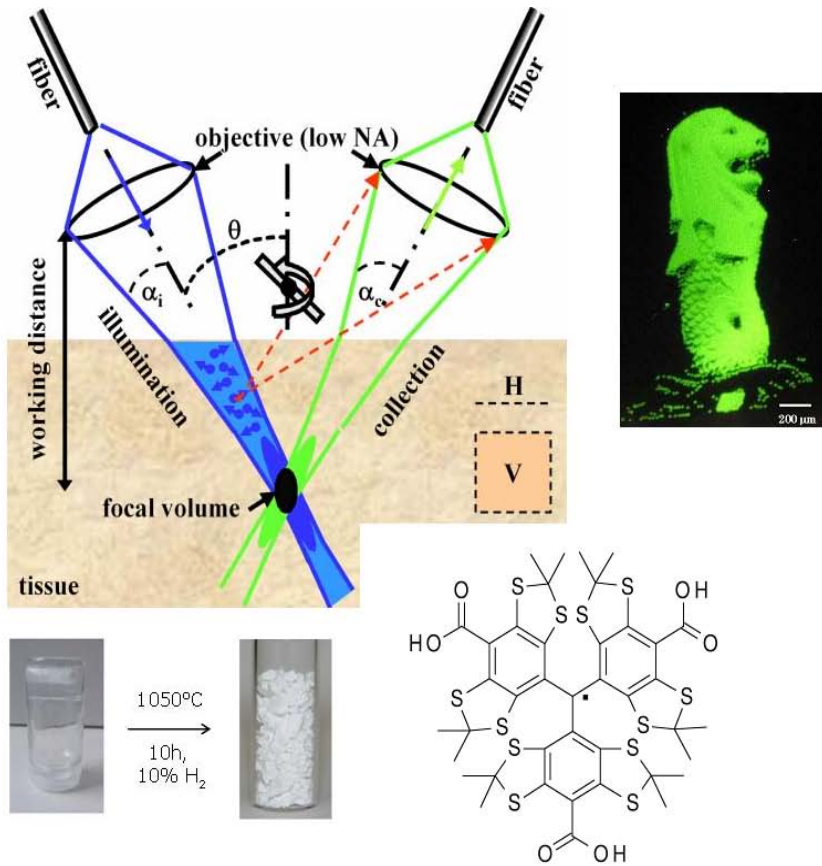
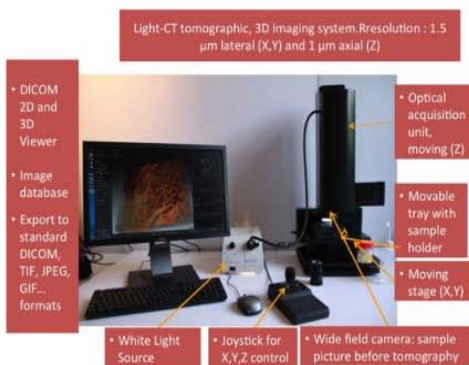


Figure 1: Formula of TAM
(tris-(p-carboxyltetra-thiaaryl)methyl radical)



Persistent Luminescence Nanoparticles for Bioimaging

Cyrille Richard, Thomas Maldiney, Quentin le Masne de Chermont, Johanne Seguin, Nicolas Wattier, Gabriel Courties, Florence Apparailly, Michel Bessodes, and Daniel Scherman

Abstract. Optical imaging is a rapidly developing field of research aimed at non-invasive monitoring of disease progression, evaluating the effects and pharmacokinetic of a drug, or identifying pathological biomarkers. To this end, it requires the development of targeting and highly specific contrast agents. In fluorescence imaging, an external light of appropriate wavelength is used to excite the fluorescent molecule, followed almost immediately by the release of longer wavelength, lower energy light for imaging. Fluorescence is increasingly used for imaging and has provided remarkable results. However this technique presents several limitations, especially due to tissue autofluorescence under external illumination and weak tissue penetration of low wavelength excitation light. To overcome these drawbacks, we have developed an innovative technique using persistent luminescence nanoparticles (PLNP) for optical imaging in small animal. Such nanoparticles can be excited before systemic injection, and their biodistribution monitored in real-time for dozen of minutes without the need for any external illumination source. This review article will focus on recent works undertaken in our laboratory on the synthesis of PLNP, their surface modifications and applications for bioimaging.

Keywords: Nanoparticle, Persistent luminescence, Silicate, Surface coating, Biodistribution, Tumor targeting, Inflammation; Biomedical imaging.

Cyrille Richard · Thomas Maldiney · Quentin le Masne de Chermont · Johanne Seguin · Nicolas Wattier · Michel Bessodes · Daniel Scherman
Unité de Pharmacologie Chimique et Génétique et d'Imagerie; CNRS, UMR 8151, Paris, F-75270 cedex France; Inserm, U1022, Paris, F-75270 cedex France;
Université Paris Descartes, Faculté des Sciences Pharmaceutiques et Biologiques, Paris, F-75270 cedex France; ENSCP, Chimie Paristech, Paris, F-75231 cedex France
e-mail: daniel.scherman@univ-paris5.fr

Gabriel Courties · Florence Apparailly
Inserm, U844, Montpellier, F-34091 France; Université Montpellier 1,
UFR de Médecine, Montpellier, F-34000 France ; Service d'immuno-rhumatologie,
Hôpital Lapeyronie, Montpellier, F-34295 France.

1 Introduction

From fluorescent organic dyes to luminescent nanocrystals, optical imaging raises growing interest for the understanding of physiological mechanisms or the development of new diagnosis and therapeutic applications [Weissleder et al. 2008]. Photonic probes offer not only practicable living sensors, but also rely on low-cost or affordable imaging devices and techniques. The semiconductor Quantum Dots (QDs) [Medintz et al. 2005] [Smith et al. 2008] exhibit high quantum yield, good photostability and tunable emission wavelength. Luminescent porous silicon nanoparticles can act as both diagnostic [Li et al. 2004] and therapeutic tools [Salonen et al. 2007]. At last, near-infrared fluorescent molecules [Chen et al. 2005] offer the possibility to work with very low autofluorescence from tissues under constant illumination.

Each of the above-mentioned probes displays characteristics that limit preclinical use or future therapeutic application. First, the emission wavelength of semiconductor QDs must be tuned by changing the particle diameter (ranging from 2 nm to 10 nm) or its composition. On the one hand, this opens alternatives for renal clearance [Choi 2007], but on the other hand it also shortens circulation time of the probe and impairs effective targeting, levying strict regulations on its design [Longmire et al. 2008]. Luminescent porous silicon nanoparticles show great promise as non-toxic, self-destructive, and traceable cargo for anti-cancer drugs, but they suffer from limited quantum yield [Park et al. 2009] ($\sim 10\%$) compared to QDs ($> 80\%$ in organic solvent). As for near-infrared fluorescent probes, it is now well established that organic dyes are susceptible to photobleaching, and are most often unstable under physiological conditions, which make them hardly the best candidate for a long-term biological or biomedical purpose [Resch-Genger et al. 2008].

To overcome these difficulties, we have recently developed persistent luminescence silicate nanoparticles [Le Masne de Chermont et al. 2007], referred to as PLNP, suitable for *in vivo* imaging, and specially designed to avoid most inherent problems encountered in classical optical systems. The key element of this technology is based on a new generation of long-luminescence nanoparticles, emitting in the near-infrared region, that can be optically excited before *in vivo* local or systemic injection. This long-lasting afterglow prevents residual background noise originating from *in situ* excitation and can last several hours. Thus, the significant signal-to-noise ratio improvement allows detection in rather deep organs and real-time biodistribution monitoring of active elements hours after injection.

2 Persistent Luminescence Nanoparticles from Silicate Host

Great progress have been made in long-lasting phosphorescence since the early 20th century. Long-lasting phosphors were widely used in emergency lighting, safety

indications, road signs and so on. Most of the long-lasting phosphors are based on sulfides and aluminates. Recently silicate phosphors have been paid considerable attention because of their bright phosphorescence, notably in blue and green regions [Jiang et al. 2003]. In 2003, Wang et al. reported the synthesis of MgSiO_3 enstatite, doped with Eu^{2+} , Dy^{3+} and Mn^{2+} luminescent ions, showing a long red persistent luminescence [Wang et al. 2003]. This article initiated in our laboratory the preparation of several luminescent silicates intended for bioimaging applications.

2.1 *Synthesis of Enstatite-like Silicates: MgSiO_3 , $\text{ZnMgSi}_2\text{O}_6$ and $\text{Ca}_{0.2}\text{Zn}_{0.9}\text{Mg}_{0.9}\text{Si}_2\text{O}_6$ doped with Eu^{2+} , Dy^{3+} and Mn^{2+}*

2.1.1 The Sol-Gel Process

Persistent luminescence materials are generally synthesized by a solid-state reaction, giving micrometer-sized particles. Such large particles would hardly circulate after systemic injection to small animals, thus limiting bioimaging applications. For this reason, we preferred a Sol-Gel approach to synthesize smaller particles [Brinker et al. 1990]. Raw materials used in our routine synthesis are: magnesium nitrate ($\text{Mg}(\text{NO}_3)_2 \cdot 6\text{H}_2\text{O}$), zinc chloride (ZnCl_2), calcium chloride ($\text{CaCl}_2 \cdot 2\text{H}_2\text{O}$), europium chloride ($\text{EuCl}_3 \cdot 6\text{H}_2\text{O}$), dysprosium nitrate ($\text{Dy}(\text{NO}_3)_3 \cdot 5\text{H}_2\text{O}$), manganese chloride ($\text{MnCl}_2 \cdot 4\text{H}_2\text{O}$), and tetraethoxysilane (TEOS). Depending on the desired nanomaterial (MgSiO_3 , $\text{ZnMgSi}_2\text{O}_6$ or $\text{Ca}_{0.2}\text{Zn}_{0.9}\text{Mg}_{0.9}\text{Si}_2\text{O}_6$) different amount of reagents were used [le Masne de Chermont et al. 2009]. For example, for the synthesis of $\text{Ca}_{0.2}\text{Zn}_{0.9}\text{Mg}_{0.9}\text{Si}_2\text{O}_6$ (where 10% of Zn and Mg atoms were substituted for Ca) doped with 0.5% Eu^{2+} , 1% Dy^{3+} , and 2.5% Mn^{2+} (the percentages are based on metallic cations content), we used: 125 mg of calcium chloride, 990 mg of magnesium nitrate, 525 mg of zinc chloride, 16 mg of europium chloride, 39 mg of dysprosium nitrate, 44 mg of manganese chloride, 4 mL of deionized water at pH 2 and 2 mL of TEOS. The mixture is vigorously stirred at room temperature for 1 hour and then for 2 hours at 70°C until the sol-gel transition occurred. The wet gel was then dried in an oven at 110°C for 20 h to remove water and ethanol (Figure 1).

2.1.2 Heating to Get Crystals

The resulting opaque dry gel is then calcined in a zirconium crucible under a weak reductive atmosphere using 10% H_2 , 90% Ar (Noxal 4, Air Liquide, Düsseldorf, Germany). Depending on the material we want, the final sintering temperature must be adapted. To prepare $\text{Ca}_{0.2}\text{Zn}_{0.9}\text{Mg}_{0.9}\text{Si}_2\text{O}_6$ (Eu^{2+} , Dy^{3+} , Mn^{2+}), the gel is fired at 1050°C for 10 h and slowly cooled down to room temperature to give white crystals (Figure 2).



Fig. 1 Hydrolysis of TEOS in the presence of the salts and sol-gel transition. Sol in the middle, gel on the right.

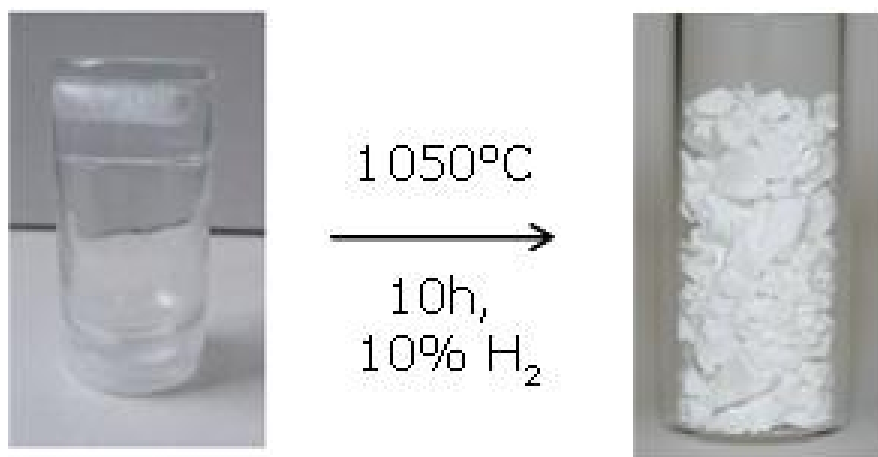


Fig. 2 Heating of the gel to get crystals.

2.2 Characterization of Synthesized Nanomaterials

2.2.1 Fluorescence Spectra

Optical spectra, shown in Figure 3, were recorded with a Varian (Palo Alto, CA) Cary-Eclipse Fluorescence spectrophotometer by using the phosphorescence mode with a delay and a gate time of 300 ms (for excitation spectrum: $\lambda_{em} = 690$ nm; excitation slit = 5 nm; emission slit = 20 nm) (for emission spectrum: $\lambda_{ex} = 340$ nm; excitation slit = 20 nm; emission slit = 5 nm). About 50 mg of each powder were deposited on a glass plate, stuck with a few drops of ethanol and inserted into the spectrophotometer.

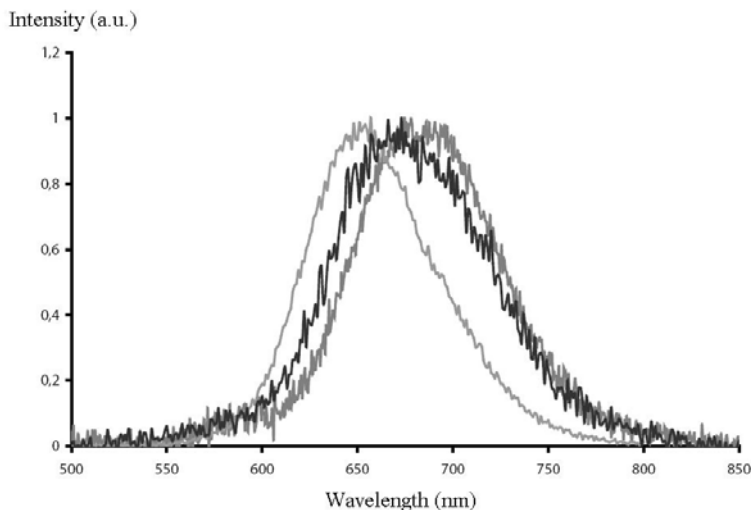


Fig. 3 Emission spectra of the three synthesized materials doped with Eu^{2+} , Dy^{3+} , Mn^{2+} . MgSiO_3 ($\lambda_{em} = 645$ nm), $\text{ZnMgSi}_2\text{O}_6$ ($\lambda_{em} = 660$ nm), $\text{Ca}_{0.2}\text{Zn}_{0.9}\text{Mg}_{0.9}\text{Si}_2\text{O}_6$ ($\lambda_{em} = 690$ nm).

2.2.2 Luminescence

To record persistent luminescence decline curves, 10 mg of each material were deposited on a 96-wells plate, excited for 2 min with a UV lamp, and placed under the photon-counting system consisting of a cooled GaAs intensified charge-coupled device (ICCD) camera (Photon Imager; Biospace Lab, Paris, France) without any external illumination system. Luminescence intensity was detectable for more than 24 h when kept in the dark. The decay kinetics (Figure 4) were found to be close to a power law $I \approx I_0 \cdot t^{-n}$ ($n = 0.96$, $R^2 = 0.996$) after the first 100 s.

For bioimaging application, we selected the $\text{Ca}_{0.2}\text{Zn}_{0.9}\text{Mg}_{0.9}\text{Si}_2\text{O}_6$ composition since it had the best characteristics in terms of emission wavelength (690 nm, which is located within the transparency window) and of luminescence intensity (the highest among all three synthesized silicates).

3 Chemical Surface Functionalization of Silicates

3.1 Obtention of Nanoparticles of Different Sizes

Nanometer-sized particles were obtained by basic wet grinding of the solid (500 mg) for 15 minutes with a mortar and pestle in a minimum volume of 5 mM NaOH solution. Hydroxylation was then performed overnight by dispersing the ground powder

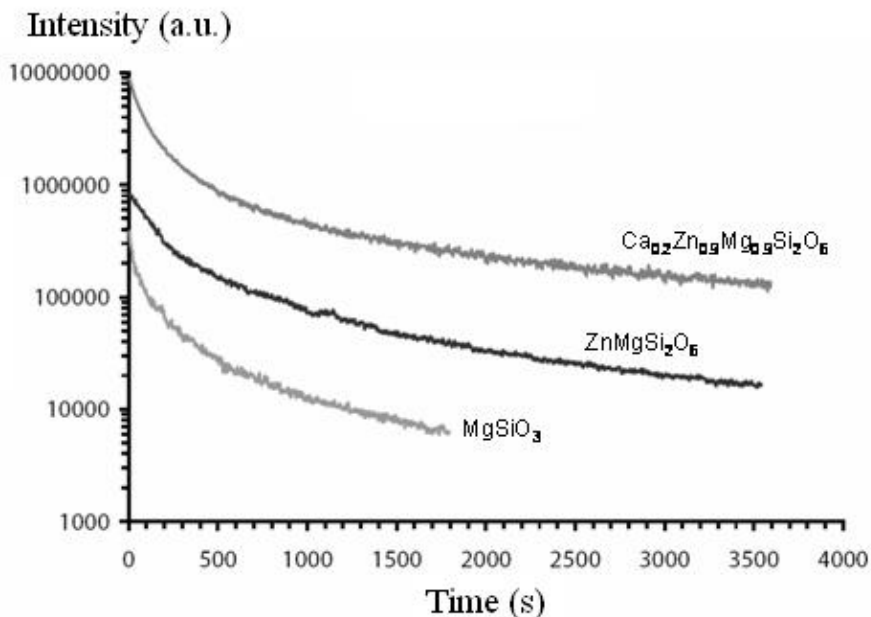


Fig. 4 Afterglow decays after UV excitation of the materials doped with Eu^{2+} , Dy^{3+} , Mn^{2+} . MgSiO_3 , $\text{ZnMgSi}_2\text{O}_6$, $\text{Ca}_{0.2}\text{Zn}_{0.9}\text{Mg}_{0.9}\text{Si}_2\text{O}_6$.

($\text{Ca}_{0.2}\text{Zn}_{0.9}\text{Mg}_{0.9}\text{Si}_2\text{O}_6$ doped with Eu^{2+} , Dy^{3+} , and Mn^{2+}) in 50 mL of the same NaOH solution to get hydroxyl-PLNP. Nanoparticles with a diameter of 180 nm were selected from the whole polydisperse colloidal suspension by centrifugation on a SANYO MSE Mistral 1000 at 4500 rpm for 5 minutes (centrifugation time was lengthened to 30 min in order to obtain 120 nm PLNP). They were located in the supernatant (assessed by Dynamic Light Scattering). The supernatants were gathered and concentrated to a final 5 mg/mL suspension. PLNP with a diameter of 80 nm were selected from the 120 nm concentrated suspension by centrifugation on an Eppendorf MiniSpin Plus at 8000 rpm for 5 minutes. Following a similar approach, centrifugation steps were repeated 4 times and the resulting suspension concentrated to a final amount of 5 mg/mL [Maldiney et al. 2011].

3.2 Characterization of the Nanoparticles by DLS and TEM

3.2.1 Dynamic Light Scattering Measurements

Photon correlation spectroscopy is a technique used to determine the diffusion coefficient of small particles in a liquid. The coefficient is determined by accurately

measuring the light scattering intensity of the particles as a function of time. Dynamic light scattering (DLS) was performed on a Nano ZS (Malvern Instruments, Southborough, MA) equipped with a 632.8 nm helium neon laser and 5 mW power, with a detection angle at 173° (noninvasive back scattering).

Intensity (%)

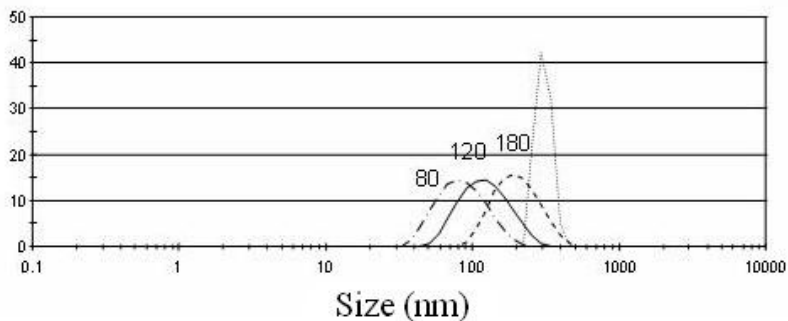


Fig. 5 Size of the different nanoparticles determined by dynamic light scattering.

3.2.2 Transmission Electron Microscopy

Electronic microscopy analysis was used to show both the shape and size of $\text{Ca}_{0.2}\text{Zn}_{0.9}\text{Mg}_{0.9}\text{Si}_2\text{O}_6$ nanoparticles doped with luminescent ions (Figure 6).

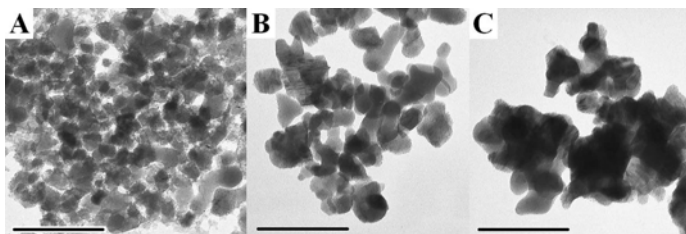


Fig. 6 TEM image of different size $\text{Ca}_{0.2}\text{Zn}_{0.9}\text{Mg}_{0.9}\text{Si}_2\text{O}_6$: Eu^{2+} , Dy^{3+} , Mn^{2+} . A: 80 nm. B: 120 nm. C: 180 nm. Scale bar = 100 nm. [\[Maldiney et al. 2011\]](#)

3.3 Surface Functionalization

In vivo biodistribution of nanoparticles highly depends on their charge and surface properties. Chemical modification of the surface of the probe is critical to better control its circulation and hope for a future targeting to a specific region of interest. For this reason, the PLNP were first reacted with 3-aminopropyl-triethoxysilane (APTES), in order to provide positively charged PLNP (referred to amino-PLNP) resulting from the presence of free amino groups at the surface. The APTES in excess was removed by several sedimentation washing procedures. The global surface charge of the amino-PLNP was reversed by condensation with diglycolic anhydride, which reacted with amines to give free carboxyl groups (carboxy-PLNP). As the use of polyethylene glycol (PEG) capping has already been shown to increase the circulation time of several colloidal systems [Moghimi et al. 2001], we also conducted coupling of different PEG moieties (either 5, 10 or 20 kDa) with the amino-PLNP (Figure 7).

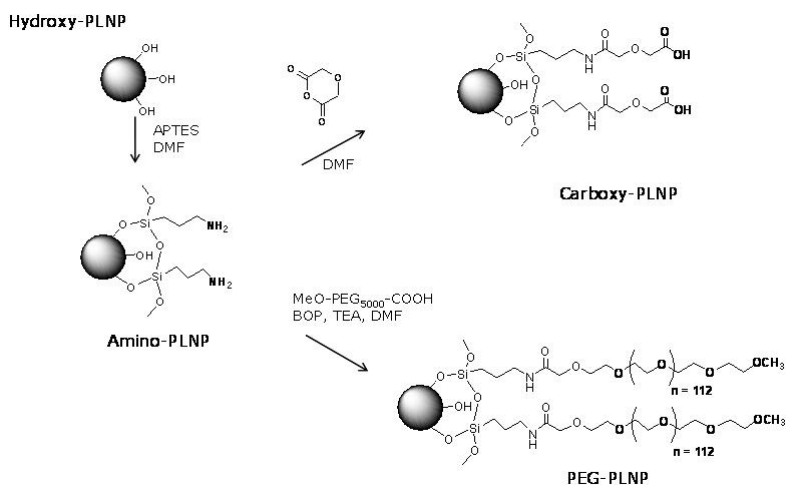


Fig. 7 PLNP surface modification with different molecules.

3.4 Characterization of the Functionalized PLNP

3.4.1 Zeta Potential

The success of the grafting procedure was assessed by zeta potential measurements (Figure 8). The zeta potential of amino-PLNP was positive (+35.8 mV at pH 7),

the zeta potential of carboxyl-PLNP was negative (-50.3 mV at pH 7). Finally as expected, PEGylation of PLNP led to neutral particles (+1 mV).

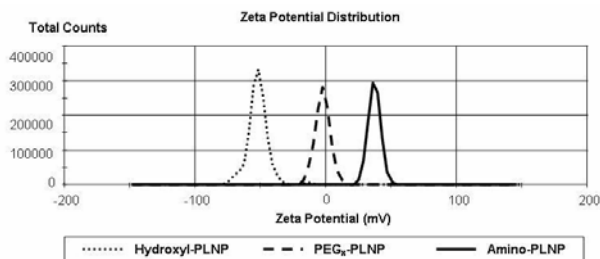


Fig. 8 Zeta potential of PLNP after each surface modification. [Maldiney et al. 2011]

3.4.2 Thermogravimetric Analysis

It exists several chemical methods to determine the amount of a given molecule grafted on nanoparticles. They usually rely on the reactivity of known chemical motifs on the ligand to dose, generally amines, carboxyl or carbonyl groups. In the case of PEG coverage, these methods could not be considered since the polymer lacked reactive functions. However, the relative high molecular weight of the chain opened alternative to a sensitive dosing of PEG moiety through thermogravimetric analysis (TGA). Briefly, TGA analysis was performed by gradually heating the sample from 20°C to 780°C under Argon atmosphere. Precision scales allowed to monitor the weight loss as a function of temperature. Weight loss curves for 120 nm PLNP were recorded after each functionalization step. From amino-PLNP to PEGylated PLNP we clearly distinguish two stages in surface decomposition. First, water trapped in the organic layer on the surface of PLNP evaporates before 325°C. The second stage begins after 325°C and corresponds to the decomposition of organic APTES and PEG coverage on the particles. When comparing TG curves for different PEG, we notice that the longer the PEG chain length, the fewer PEGylated chains remain grafted on the surface. Calculated values from weight loss percentages indicate that in the case of 5 kDa PEG, polymer concentration reaches about 15 nmol/mg of PLNP. This value drops significantly when increasing the size of the PEG to 9 nmol/mg for 10 kDa PEG and 3 nmol/mg for 20 kDa PEG. Despite the 20 fold molar excess of PEG (compared to the amount of free amino groups previously estimated on the surface: about 60 nmol/mg), it seems that steric hindrance hampers the approach of larger PEG near the particle, thus preventing quantitative reaction as well as equimolar loadings of the different PEG.

3.4.3 Colloidal Stability

Before any use of these nanoparticles for bioimaging, colloidal stability in biological media had to be checked. As shown in Figure 9, the addition of polyethylene glycol significantly changes the average value of hydrodynamic diameter, leading to particles from 40 to 70 nm larger than the initial hydroxyl-PLNP, and providing high colloidal stability in normal saline solution.

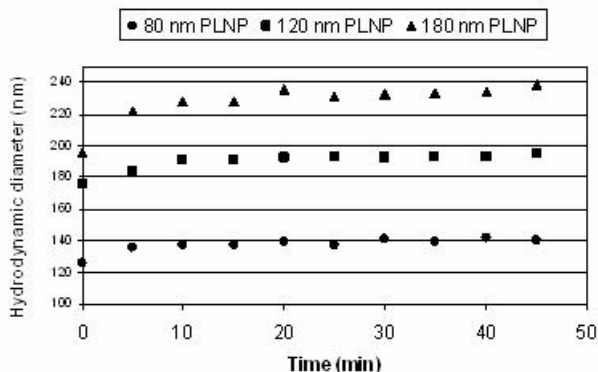


Fig. 9 Colloidal stability of 5 kDa PEG-PLNP: evolution of the hydrodynamic diameter in 150 mM NaCl for 45 minutes. [Maldiney et al. 2011]

4 Bioimaging with Persistent Luminescence Nanoparticles

4.1 Principle

As explained in the introduction, the major difference between our luminescent silicate and other classical optical probes (used for bioimaging) comes from the ability of PLNP to store excitation energy and to emit at higher wavelength from dozen of minutes to hours. This property allows to excite the probe before its systemic injection (Figure 10).

4.2 Influence of Coating on the Biodistribution of 180nm PLNP

Biodistribution of 180 nm PLNP with different surface coatings (either amino, carboxy, or PEG) was monitored 30 minutes after systemic injection in mice. Acquired images are shown in Figure 11. For positive amino-PLNP, an important lung retention was observed (Figure 11a). During the first hour, there was little change in this

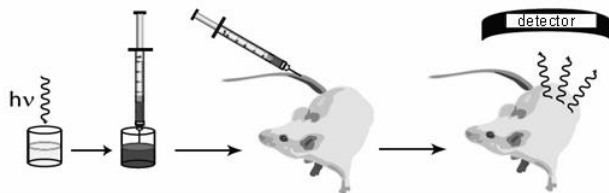


Fig. 10 Bioimaging with PLNP: the principle.

distribution, except a progressive PLNP release from lungs to liver and spleen. Two reasons can explain this biodistribution pattern [Song et al. 1998]. The first one is a nonspecific electrostatic interaction of amino-PLNP with the negative charges displayed by plasmatic membranes of capillary endothelial cells, such as sulfated proteoglycans and glycosylaminoglycans. Another explanation could be provided by aggregation of amino-PLNP with negatively charged blood components, leading to trapping agglomerates of increased size in the narrow lung capillaries. Negative carboxy-PLNP were rapidly cleared from blood flow by liver uptake (Figure 11b). This biodistribution pattern presumably resulted from a rapid opsonisation and an uptake by endothelial and Kupffer cells of the reticuloendothelial system (RES), as is generally observed for nanoparticles or liposomes [Kamps et al. 1997] [Krieger et al. 1994]. Neutral PEG-PLNP were able to circulate longer, as assessed by a diffuse signal throughout the mouse body that lasted for the rest of the acquisition time (Figure 11c). However, biodistribution images clearly show liver accumulation after 60 minutes. When Kupffer cells were saturated by prior administration of anionic liposomes, the neutral PEG-PLNP circulation time increased further (images not shown).

4.3 Influence of Nanoparticle Diameter and PEG Chain Length on the Biodistribution in Healthy Mice

The biodistribution of PLNP was studied in function of nanoparticle diameter (80, 120 and 180 nm) and PEG chain length (5, 10 and 20 kDa). Relative long-term biodistribution in healthy mice was achieved six hours after systemic injection to validate a potential use of this probe for in vivo applications. Delayed fluorescence from europium ions trapped in the core of the nanoparticles allowed an ex vivo quantitative analysis through tissue homogenates after animal sacrifice. As shown in Figure 12, similarly to several classes of nanoparticles, and regardless of surface coverage, long term PLNP biodistribution occurs predominantly within liver and spleen [Minchin et al. 2010]. Combined uptake in the kidneys and lungs remains

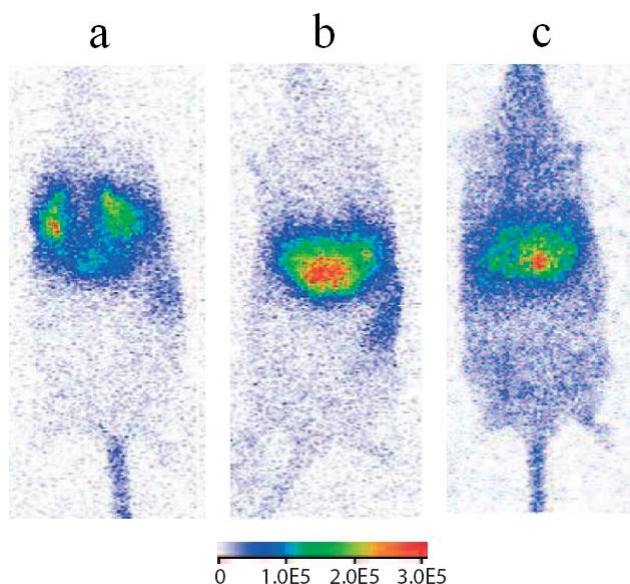


Fig. 11 Biodistribution of PLNP 30 minutes after tail vein injection. a: amino-PLNP. b: carboxy-PLNP. c: PEG-PLNP. [Le Masne de Chermont et al. 2007]

below 5 % of the injected dose. The PEG chain length seems to have little influence on the global RES accumulation (combined uptake in liver and spleen), and is only responsible for a slight change in the liver/spleen ratio (only noticeable for 120 nm PLNP). On the contrary, the nanoparticle core diameter appears to be critical. As shown in Figure 12, decreasing the particle core diameter from 180 nm to 80 nm causes a much lower combined RES uptake of PEG-PLNP from 100 % down to around 35 % of the injected dose [Maldiney et al. 2011].

4.4 Biodistribution of PEG-PLNP in Tumor Bearing Mice

Malignant tumors display both increased angiogenesis and chaotic microenvironment growth, mainly responsible for hypervascularization, leaky vasculature, and poor lymphatic drainage [Maeda et al. 2000]. The pore size in the vasculature ranges from 200 to 600 nm in diameter, leading to an enhanced permeability and retention (EPR) effect [Brannon-Peppas et al. 2004]. It was reported that long-circulating nanoparticles with PEG modifications on their surface were able to conduct passive tumor targeting [Moghimi et al. 2001] [Greenwald 2001]. The injection of our 180 nm PEG-PLNP to C57BL/6 mouse bearing an s.c. implanted Lewis lung carcinoma (3LL) tumour in the inguinal region, allowed us to detect the tumor vasculature the first 2 minutes after injection (Figure 13a). However no passive accumulation of our

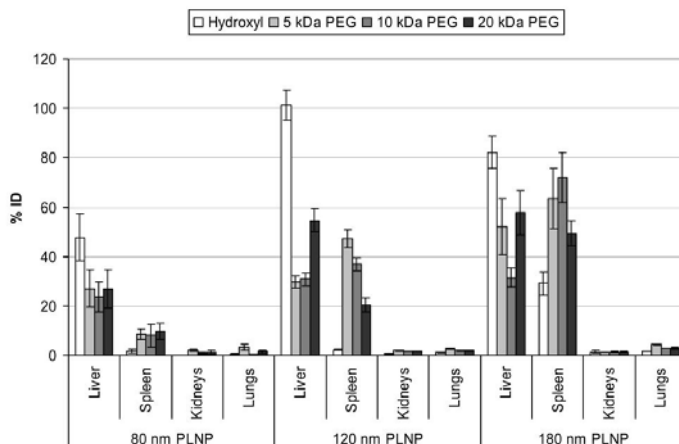


Fig. 12 PLNP tissue distribution 6 hours after systemic injection to healthy mice (n=6). Error bars correspond to standard deviation. [Maldiney et al. 2011]

PLNP-PEG could be observed at longer time (Figure 13b). In order to favor a passive accumulation of PEG-PLNP in the tumour area we have recently reported the influence of both the diameter of the PLNP (80, 120 and 180 nm) and the length of the PEG chain (5, 10 and 20 kDa). This study revealed that after intravenous injection of 80 nm PLNP-PEG_{10kDa} in 3LL tumor bearing mice, 5.9 ± 2.8 % of the injected dose were located within the tumour micro-environment 6 hours after the injection [Maldiney et al. 2011].

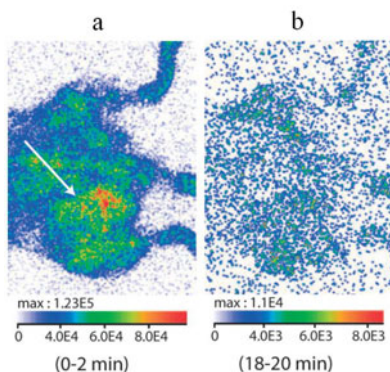


Fig. 13 Images of PLNP-PEG injected to a mouse bearing an s.c. implanted Lewis lung carcinoma (3LL) tumor. a: image obtained 2 minutes after injection. b: image obtained 20 minutes after injection of PLNP. [Le Masne de Chermont et al. 2007]

Another way to target tumor vasculature is to use nanoparticles coated with targeting ligands [Richard et al. 2008] [Byrne et al. 2008] [Loomis et al. 2011]. Efforts in our laboratory are actually directed towards surface functionalization of PLNP with ligands able to target receptors of interest.

4.5 *PLNP for Imaging Inflammation in a Mouse Model of Arthritis*

Rheumatoid synovium is characterized by hyperplasia of the synovial lining layer and marked infiltration by lymphocytes, macrophages and plasma cells. Locally produced inflammatory mediators and subsequent up-regulation of adhesion molecules within inflammation sites are both pivotal to the development of rheumatoid arthritis [Choy et al. 2001] [Tak et al. 1996].

Neovascularization is also a vital component of pannus formation. The early diagnosis of rheumatoid arthritis is made problematic by heterogeneity in its clinical presentation and uncertainty about which patients will respond to treatment. Sensitive and specific imaging methods are required for the detection of early inflammatory changes to the synovium in patients with arthritis and for monitoring response to treatment.

We have evaluated the capacity of carboxy and PEG-PLNP to reveal inflammatory sites in an experimental mouse model of arthritis. The pathology was induced in the DBA/1 mice by immunization with 100 μg of bovine collagen type II at the base of the tail on day 0 and day 21 [Courties et al. 2009]. Thirty days after immunization, 100 μg of PLNP (carboxy or PEG) previously excited with a UV lamp for 5 min were injected in the tail vein. Their biodistribution was then monitored under the photon-counting system (Figure 14).

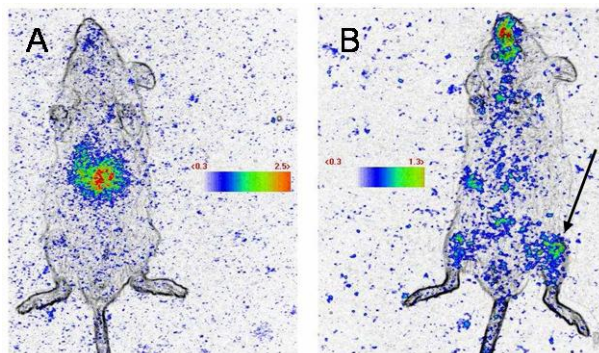


Fig. 14 PLNP for imaging inflammation sites. A: image obtained with carboxy-PLNP 30 minutes after injection. B: image obtained with PEG-PLNP. In both cases GdCl_3 was injected before PLNP to increase the circulation time of the nanoparticles. The black arrow indicates the site of inflammation.

As shown in Figure 14-A, carboxy-PLNP were quickly trapped in liver, even in the presence of GdCl_3 (generally used to saturate liver macrophages). In contrast, PEGylated PLNP evade liver (Figure 14-B) to accumulate in the hind legs, at sites of inflammation, and in the oral cavity which is a highly vascularized area. Surface and diameter of the PLNP are key elements that we are actually modifying to improve these results.

5 Conclusion

We described the synthesis of several persistent luminescence nanoparticles from silicate host. Among them, $\text{Ca}_{0.2}\text{Zn}_{0.9}\text{Mg}_{0.9}\text{Si}_2\text{O}_6$ doped with Eu^{2+} , Dy^{3+} , and Mn^{2+} appeared as the most interesting material for bioimaging applications in terms of emission wavelength and intensity of luminescence. We extracted different monodisperse nano-sized distributions (from 80 to 180 nm) and showed that surface functionalization could not only drastically improve their biodistribution in healthy and tumor-bearing mice, but could also allow to monitor inflammation in a mouse model of arthritis. These results are encouraging, and additional works are actually in progress to heighten image analysis of the acquired data by the means of more reliable softwares and computational tools, but also to improve PLNP optical performances, biodegradability and targeting capabilities.

From the automatic image analysis side, there remain several challenges associated with this innovative technique.

- First, as luminescence decreases with time, background signal becomes predominant. After approximately one hour, signal from PLNP is not detectable anymore. This first limitation requires to focus on persistent luminescence materials, and to find new compositions with improved optical properties.
- Then, two-dimensional optical detection raises the problem of photons diffusion, depth-dependent, that blurs biological structures contours and hampers organs distinction.
- Therefore, we sometimes observe distorted organs (such as liver or spleen) with variable shape and size. To circumvent this last issue, valuable efforts are being made to work on three-dimensional acquisition systems that would permit combined acquisition in several plans, as well as image reconstruction of the organ through highly developed softwares designed to return the corrected shape and size of the organ from acquired data.

References

- [Brannon-Peppas et al. 2004] Brannon-Peppas, L., Blanchette, J.O.: Nanoparticle and targeted systems for cancer therapy. *Adv. Drug Deliv. Rev.* 56, 1649–1659 (2004)
- [Brinker et al. 1990] Brinker, C.J., Scherer, G.W.: *Sol-Gel Science: The physics and the chemistry of sol-gel processing* (1990) (academic London)
- [Byrne et al. 2008] Byrne, J.D., Betancourt, T., Brannon-Peppas, L.: Active targeting schemes for nanoparticle systems in cancer therapeutics. *Adv. Drug Deliv. Rev.* 60, 1615–1626 (2008)
- [Chen et al. 2005] Chen, W., Mahmood, U., Weissleder, R., Tung, C.: Arthritis Imaging Using a Near-Infrared Fluorescence Folate-Targeted Probe. *Arthritis Res. Ther.* 7, R310–317 (2005)
- [Choi 2007] Choi, H.S.: Renal Clearance of Quantum Dots. *Nat. Biotechnol.* 25, 1165–1170 (2007)
- [Choy et al. 2001] Choy, E.H., Panayi, G.S.: Cytokine pathways and joint inflammation in rheumatoid arthritis. *N. Engl. J. Med.* 344, 907–916 (2001)
- [Courties et al. 2009] Courties, G., Presumey, J., Duroux-Richard, I., Jorgensen, C., Apparailly, F.: RNA interference-based gene therapy for successful treatment of rheumatoid arthritis. *Expert Opin. Biol. Ther.* 9, 535–538 (2009)
- [Greenwald 2001] Greenwald, R.B.: PEG drug: an overview. *J. Controlled Release* 74, 159–171 (2001)
- [Jiang et al. 2003] Jiang, L., Chang, C., Mao, D.: Luminescent properties of $\text{CaMgSi}_2\text{O}_6$ and $\text{Ca}_2\text{MgSi}_2\text{O}_7$ phosphors activated by Eu^{2+} , Dy^{3+} and Nd^{3+} . *J. Alloys Comp.* 360, 193–197 (2003)
- [Kamps et al. 1997] Kamps, J.A., Morselt, H.W.M., Swart, P.J., Meijer, D.K.F., Scherphof, G.L.: Massive targeting of liposomes, surface-modified with anionized albumins, to hepatic endothelial cells. *Proc. Natl. Acad. Sci. USA* 94, 11681–11685 (1997)
- [Krieger et al. 1994] Krieger, M., Herz, J.: Structures and functions of multiligand lipoprotein receptors: macrophage scavenger receptors and LDL receptor-related protein. *Annu. Rev. Biochem.* 63, 601–637 (1994)
- [le Masne de Chermont et al. 2007] Le Masne de Chermont, Q., Chanac, C., Seguin, J., Pelle, F., Matrejean, S., Jolivet, J.P., Gourier, D., Bessodes, M., Scherman, D.: Nanoprobes with Near-Infrared Persistent Luminescence for In Vivo Imaging. *Proc. Natl. Acad. Sci. USA* 104, 9266–9271 (2007)
- [le Masne de Chermont et al. 2009] le Masne de Chermont, Q., Richard, C., Seguin, J., Chanac, C., Bessodes, M., Scherman, D.: Silicates doped with luminescent ions: useful tools for optical imaging applications. In: *Proc of SPIE*, vol. 7189, 71890B/1-71890B (2009)
- [Li et al. 2004] Li, Z.F., Ruckenstein, E.: Water-soluble poly(acrylic acid) grafted luminescent silicon nanoparticles and their use as fluorescent biological staining labels. *Nano. Lett.* 4, 1463–1467 (2004)
- [Longmire et al. 2008] Longmire, M., Choyke, P.L., Kobayashi, H.: Clearance properties of nano-sized particles and molecules as imaging agents: considerations and caveats. *Nanomedicine* 3, 703–717 (2008)
- [Loomis et al. 2011] Loomis, K., McNeeley, K., Bellamkonda, R.V.: Nanoparticles with targeting, triggered release, and imaging functionality for cancer applications. *Soft Matter* 7, 839–856 (2011)
- [Maeda et al. 2000] Maeda, H., Wu, J., Sawa, T., Matsumura, Y., Hori, K.: Tumor vascular permeability and the EPR effect in macromolecular therapeutics: a review. *J. Controlled Release* 65, 271–284 (2000)

- [Maldiney et al. 2011] Maldiney, T., Richard, C., Seguin, J., Wattier, N., Bessodes, M., Scherman, D.: Effect of core diameter, surface coating and PEG chain length on the biodistribution of persistent luminescent nanoparticles in mice. *ACS Nano* 5, 854–862 (2011)
- [Medintz et al. 2005] Medintz, I.L., Uyeda, H.T., Goldman, E.R., Mattoussi, H.: Quantum dot bioconjugates for imaging, labelling and sensing. *Nat. Mater* 4, 435–446 (2005)
- [Minchin et al. 2010] Minchin, R.F., Martin, D.J.: Nanoparticles for molecular imaging - an overview. *Endocrinology* 151, 474–481 (2010)
- [Moghimi et al. 2001] Moghimi, S.M., Hunter, C., Murray, J.C.: Long-circulating and target-specific nanoparticles: theory to practice. *Pharmacol Rev.* 53, 283–318 (2001)
- [Park et al. 2009] Park, J.H., Gu, L., von Maltzahn, G., Ruoslahti, E., Bhatia, S.N., Sailor, M.J.: Biodegradable luminescent porous silicon nanoparticles for in vivo applications. *Nat. Mater* 8, 331–336 (2009)
- [Resch-Genger et al. 2008] Resch-Genger, U., Grabolle, M., Cavaliere-Jaricot, S., Nitschke, R., Nann, T.: Quantum dots versus organic dyes as fluorescent labels. *Nat. Methods* 5, 763–775 (2008)
- [Richard et al 2008] Richard, C., le Masne de Chermont, Q., Scherman, D.: Nanoparticles for imaging and tumor gene delivery. *Tumori* 94, 264–270 (2008)
- [Salonen et al. 2007] Salonen, J., Kaukonen, A.M., Hirvonen, J., Lehto, V.P.: Mesoporous silicon in drug delivery applications. *J. Pharm. Sci.* 97, 632–653 (2007)
- [Smith et al. 2008] Smith, A.M., Duan, H., Mohs, A.M., Nie, S.: Bioconjugated quantum dots for in vivo molecular and cellular imaging. *Adv. Drug. Deliver Rev.* 60, 1226–1240 (2008)
- [Song et al. 1998] Song, Y.K., Liu, F.: Liu Enhanced gene expression in mouse lung by prolonging the retention time of intravenously injected plasmid DNA. *Gene. Ther.* 5, 1531–1537 (1998)
- [Tak et al. 1996] Tak, P.P., Taylor, P.C., Breedveld, F.C., Smeets, T.J.M., Daha, M.R., Kluin, P.M., Meinders, A.E., Maini, R.N.: Decrease in cellularity and expression of adhesion molecules by anti-tumor necrosis factor alpha monoclonal antibody treatment in patients with rheumatoid arthritis. *Arthritis Rheum* 39, 1077–1081 (1996)
- [Wang et al. 2003] Wang, X.J., Jia, D., Yen, W.M.: Mn²⁺ activated green, yellow, and red long persistent phosphors. *J. Lumin* 103, 34–37 (2003)
- [Weissleder et al. 2008] Weissleder, R., Pittet, M.J.: Imaging in the era of molecular oncology. *Nature* 452, 580–589 (2008)

Bioimaging Probes Development by DOFLA (Diversity Oriented Fluorescence Library Approach) for in Vitro, in Vivo and Clinical Applications

Seong-Wook Yun and Young-Tae Chang

Abstract. Due to the remarkable development of bioimaging probes and equipment during the last decades, we are able to see a variety of biological systems with a resolution ranging from centimeters to subnanometers. Bioimaging is now an indispensable tool for basic research and clinical diagnosis. Particularly, the application of fluorescence in optical imaging has enabled us to investigate molecular events as well as the structures in living cells and tissues. Among the fluorescent molecules, low molecular weight chemicals have great potentials to be developed as highly specific and versatile bioimaging probes. Target-specific fluorescent probes have been developed conventionally by a hypothesis-driven approach in which fluorophores are conjugated to already developed molecules such as antibody, peptide or small molecule drug. However, the fluorescence-labeled macromolecules may not be used for the detection of intracellular molecules in living cells and tagging small molecule without affecting its property is relatively challenging. To overcome these problems, we have developed Diversity Oriented Fluorescence Library (DOFL) by exploring the diverse chemical space directly around fluorophores using combinatorial chemistry. By screening DOFL in various platforms such as in vitro, cell, tissue and whole organism, we have successfully developed bioimaging probes which interact specifically with the targets. In this article, we discuss how bioimaging contributes to the development of biomedical science, why the development of new bioimaging probes is necessary and what can be achieved by DOFL approach (DOFLA).

Seong-Wook Yun

Laboratory of Bioimaging Probe Development,
Singapore Bioimaging Consortium, Agency for Science,
Technology and Research, Singapore 138667, Republic of Singapore
e-mail: yunseongwook@sbic.a-star.edu.sg

Young-Tae Chang

Department of Chemistry & NUS MedChem Program of Life Sciences Institute,
National University of Singapore, Singapore 117543, Republic of Singapore
e-mail: chmcyt@nus.edu

1 Visualizing Is Proving

Visualizing in a reproductive way is proving. Robert Hooke's discovery of the cell using a compound microscope in 1665 led to the discovery of bacteria, fungi and protozoa, thus opening up the microbial world. The development of the electron microscope in 1930s has enabled us to explore inside a single cell with nanometer resolution contributing to the discovery of thousands of different viruses. Since the discovery of X-ray and its application to skeletal imaging by Wilhelm Röntgen in 1895, non-invasive imaging using radiation has become a pivotal technology for the diagnosis and prognosis of a wide range of diseases. Imaging modalities such as computed tomography (CT), magnetic resonance imaging (MRI), positron emission tomography (PET), and single photon emission computed tomography (SPECT) are now capable of providing both structural and functional information in health and disease. Some representative imaging tools for biomedical science are depicted in Figure 1 with their applications and resolutions [5]. In addition to the examples briefly mentioned above, various imaging technologies are being developed to meet the increasing demand of accurate and target-specific imaging in the post-genomic era.

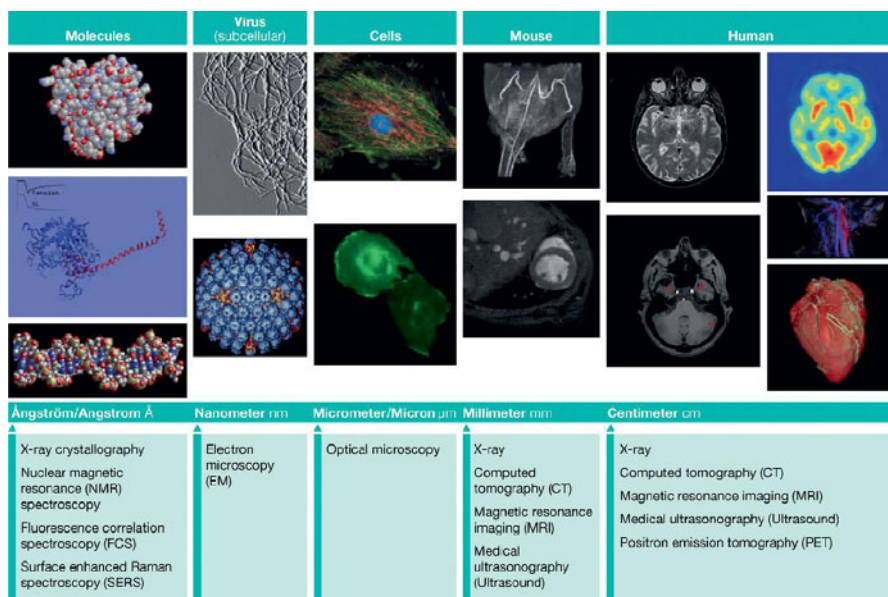


Fig. 1 Imaging modalities, their spatial resolution and applications. Bioimaging encompasses a range of imaging modalities that provide spatial and functional analysis of molecules from angstrom level to centimeter level. NMR, nuclear magnetic resonance; SERS, surface-enhanced Raman scattering; CT, computed tomography; MRI, magnetic resonance imaging; PET, positron emission tomography. Han et al., Imaging metabolic syndrome. *EMBO Mol. Med.* 2010, 2, 196-210. Copyright Wiley-VCH Verlag GmbH & Co. KGaA. Reproduced with permission.

2 More Questions to Be Addressed in Post-Genomic Era

The quest to understand the fundamentals of living organism by sequencing whole genomes finally led to a completion of human genome project in 2003 after 13 years of collaboration of many international research centers [3]. In parallel, the whole genome sequences of various organisms ranging from virus to vertebrates have been identified, hence leading to the era of genomics. One unexpected finding of the genome project is that the number of genes in the human genome is approximately 25,000 which is comparable to the 20,000 genes of a nematode *C.elegans* [7]. This finding implies that the complexity of organisms is determined by the different functions and regulations of gene products rather than the gene number. After transcription, complex processing steps including splicing, translational regulation and post-translational modification are involved in the production of proteins, the final product of gene expression. The activities of proteins endow the cells with specific properties that determine their structure, function and metabolic status. Due to the various processes and modifications during the protein production, the number of proteins is much more than the number of genes. Proteomics, which is the study about the behavior of entire set of proteins, is emerging as the next challenge to genomics to understand the mechanisms of life and disease [?]. The function and structure of many proteins have been revealed by diverse in vitro analyses and the information saved as a database has provided valuable clues about their roles in biological system. However, the results of those in vitro studies need to be confirmed in the in vivo system for the biological function of protein to be properly interpreted. The in vivo function of proteins is affected by many conditions that cannot be reproduced in the in vitro experimental settings and the behavior of proteins can be different in different cells and environments. Therefore, the information obtained through genomics and proteomics studies raised more questions than before. The development of sophisticated bioimaging probes and their applications in various imaging modalities will be a way to address those questions.

3 Fluorescent Microscopy

Technical advancement in the development of optical imaging instruments is especially stunning in the fluorescence-based technology along with the development of various fluorophores and their applications to cell biology. Confocal microscopy collects fluorescence images of a plane at different depths of specimen eliminating blurry out-of-focus background. Two-photon microscopy uses long-wavelength e.g., infra-red light which easily penetrates several hundred micrometer thick living tissue to excite the fluorophores that absorb and emit in much shorter wavelength region than that of the light source [?]. OPT (Optical Projection Tomography) and LSM (Light Sheet Fluorescence Microscopy) are used for 3D images of millimeter-size specimens [10,23]. Super-resolution microscopes such as PALM (Photo-Activated Localization Microscopy), STORM (Stochastic

Optical Reconstruction Microscopy), STED (Stimulated Emission Depletion Microscopy), and SIM (Structured Illumination Microscopy) provide images with 10 to 20 times higher resolution than the resolution limit of conventional optical microscopes which is approximately 200 nm [?]. Last, small animal whole-body fluorescence imaging, especially by using near infrared dyes, makes it possible to investigate pathophysiological changes non-invasively in live animal models [22].

4 Fluorescent Small Molecules

The fluorescence, which has been used for lighting since the middle of 19th century, is now an indispensable tool for biomedical research and clinical diagnosis. The most common uses of fluorescence in these fields are for chemical sensing and labeling of molecules of interest. Among the fluorescence materials, small molecules are the most versatile in these applications. Although numerous fluorescent molecules have been developed, most of them are synthesized from dozens of common cores as illustrated in Figure 2. By changing side chains or substituting elements of a core, many different compounds with different properties can be synthesized [11].

Calcium indicators such as FLUO-3 and -4, Calcium Green-1 and Oregon Green 488 BAPTA-1 have been widely used [21] for high throughput drug screening to discover antagonist, agonist or allosteric modulator of G-protein-coupled receptors which are targets of 30 % of marketed small-molecule drugs [8]. Antibodies and peptide ligands have been labeled with fluorescent dyes such as Cy or Alexa Fluor series dyes to visualize the localization or distribution of their targets in live or dead cells. If an enzyme is highly expressed in a certain cell or tissue, its substrate can be labeled with a quenched fluorescent probe which is activated only by the enzymatic reaction at the location of interest. Peptide substrates of several disease-related enzymes such as matrix metalloproteinases, cathepsins, caspases, and dipeptidyl peptidases have been used to make activatable fluorescent probes [14]. Although the labeled peptides or antibodies are highly specific to their targets, they are not stable in vivo, their delivery to the target site is often limited by biological barriers e.g., blood-brain-barrier, and the cost of production is high. Fluorescent small molecule itself can also be a substrate of a specific enzyme. BODIPY aminoacetaldehyde, a fluorescence substrate of aldehyde dehydrogenase, passively diffuses into the cells and converts to negatively charged BODIPY- aminoacetate by the enzyme. Because the charged product is retained inside the cells, cells that express high level of aldehyde dehydrogenase e.g., hematopoietic stem cells are brightly stained [?]. Compared to the antibody or peptide, small molecules allow easy manipulation of their properties according to the requirements of application and are cheaper to produce. Some fluorescent small molecules have been used to stain specific organelles such as mitochondria, lysosome, endoplasmic reticulum, and Golgi apparatus in living cells, although they are not cell type-specific [6]. The functions and activities of biological small molecules such as nucleotides, amino acids, lipids, carbohydrates, vitamins, and neurotransmitters are precisely regulated in vivo. Synthetic small molecules are

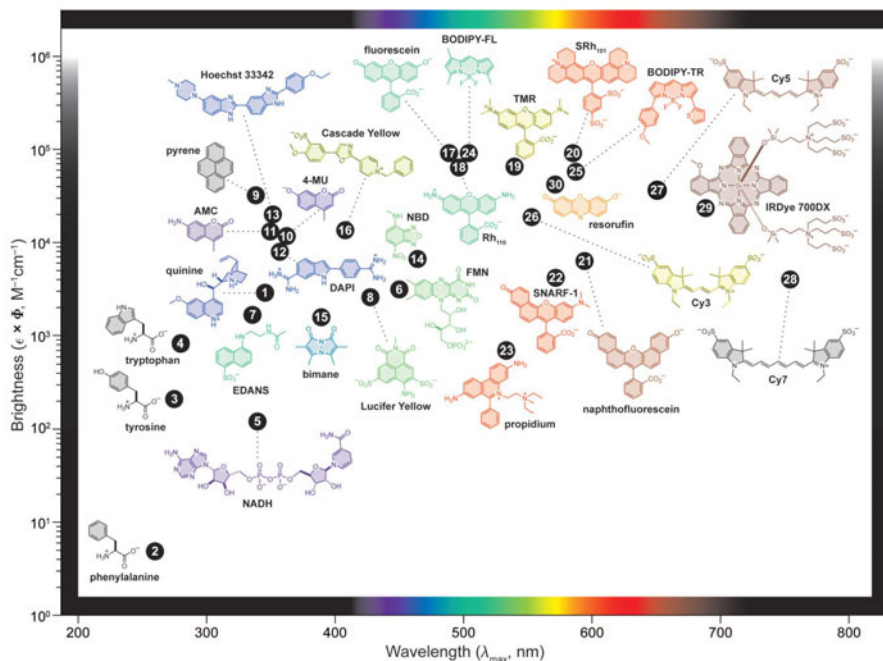


Fig. 2 Plot of fluorophore brightness ($\epsilon \times \Phi$) vs the wavelength of maximum absorption (λ_{max}) for the major classes of fluorophores. The color of the structure indicates its wavelength of maximum emission (λ_{em}). For clarity, only the fluorophoric moiety of some molecules is shown. Lavis and Raines, *Bright Ideas for Chemical Biology*. ACS Chem. Biol. 2008, 3, 142-155. Copyright American Chemical Society. Reproduced with permission.

also the majority of drugs prescribed to inhibit, stimulate or modulate specific biological activities. These facts suggest that fluorescent organic small molecules have enough potential to be developed as more target-specific bioimaging probes.

5 Diversity Oriented Fluorescence Library Approach

Fluorescent organic imaging probes may be developed either by hypothesis-driven approach or diversity-driven approach. In the hypothesis-driven approach, a recognition motif is designed based on the structure and property of a known target; a fluorophore is then conjugated as a reporter to the recognition motif through a linker. Although this method can be straightforward if the target is determined, designing a recognition motif and tagging it with a fluorophore without affecting its property are a challenge. On the other hand, diversity-driven approach relies on the structural diversity of the probe library which are constructed by combinatorial chemistry as a tool box for unbiased screening. This approach is very well-suited for the

development of probes with novel recognition motifs when the target molecule is not known, provided that the tool box library contains a broad enough structural diversity. To meet the need of molecular bioimaging that employs highly sophisticated small molecular weight imaging probes, we have developed a chemical compound library comprising of several thousand fluorescence small molecules by combinatorial synthesis. This Diversity Oriented Fluorescence Library (DOFL) has been applied for the development of specific bioimaging probes in our studies [?]. Depending on the final application of the imaging probes, the screening methods are determined. The details of each method and examples of imaging probes are listed in the following section and in Figure 3.

5.1 *In Vitro* Screening

The fluorescence intensity or emission wave length of fluorophores may change by binding to molecules or due to environmental changes. A diverse set of inorganic and organic compounds, such as metal ions, neurotransmitters, metabolites, nucleic acid, proteins and sugars are incubated with DOFL in a microplate to identify the compounds that increase or decrease their fluorescence intensity or change colors. Because the analytes are usually stable and exact conditions are reproducible, the screening technique is simple. However, for real applications of the discovered probe, several factors should be taken into consideration in designing the screening format. First, the concentration of analytes should be within the detection range. Because the detection range of a probe can be determined only after the discovery of the probe, the concentrations of analytes for the screening should be determined prior to screening. Usually, a range covering the concentrations of analytes in the real sample of interest is applied, although concentration or dilution of the samples can be considered, if necessary. Second, screening should be carried out in a similar environmental condition of the assay system. For example, albumin is known to bind many small molecules non-selectively. If the probe is to detect an element in the serum, the potential hit molecules which have higher affinity also to albumin could be eliminated by adding albumin in the screening system. Last, the hit compounds discovered from the primary screening should be validated using real samples for further screening. Viscosity, pH, impurities and other unexpected factors may affect the behavior of probe, especially in the biological samples such as urine and serum where chemically similar components compete with the target.

5.2 *Cell-Based* Screening

Compared to the in vitro screening, the outcome of live cell-based screening is affected by many unknown factors and unpredictable conditions. For the hypothesis-driven approach, this complexicity is a big obstacle because it is very difficult to

predict how the modification of the original probe affects the probe's properties in the *in vivo* condition. On the other hand, diversity-oriented approach can benefit from this complexity because the probe is developed by screening of diverse compounds directly in live cells. The combination of many *in vivo* factors can generate unique characteristics of a specific cell type that increase the chance of specific probe discovery. The primary screening format consists of a set of cell types which are linked to each other. For example, embryonic stem (ES) cells are usually cultured on fibroblast feeder cells. And the fibroblasts can be reprogrammed into induced pluripotent stem (iPS) cells which are similar to embryonic stem cells. To develop pluripotent stem cell selective probe, Im et al. added DOFL in the mouse fibroblast and mouse ES cell culture prepared side by side on a microplate [9]. The images of fluorescently stained living cells were acquired using an automated high throughput microscopy system at different incubation time points. The primary hit compounds which stained mouse ES cells much more brightly than fibroblast were further screened by flow cytometry to discover the most ES cell-selective compound CDy1. Once the final hit is identified, it should be tested in various types of cells to validate its application potential. Because CDy1 does not stain ES cells differentiated into ectoderm, endoderm and mesoderm lineages but stain iPS cells at early stage of reprogramming, an application of CDy1 would be to isolate undifferentiated ES cells and early stage iPS cells from heterogeneous cell population.

5.3 *Tissue-Based Screening*

Tissue sections have been examined to understand the nature of life and disease by analyzing the distribution of certain types of cells in tissues. Several micrometer-thick sections can be prepared for incubation with DOFL on a slide glass from the tissues processed by embedding in paraffin or freezing. If the screening sample is prepared from an organotypic slice culture which is a couple of hundred micrometer thick, it may take several hours or longer for the dye compounds to penetrate deep enough into the tissue. The screening throughput is lower compared to the *in vitro* or cell-based screening because of the difficulty in sample preparation and data analysis. Due to the heterogeneity of tissue components the fluorescence images need to be analyzed manually based on structural information. However, this screening method is particularly useful for the targets which cannot be mimicked by a cell culture model or an artificial *in vitro* system. Li et al. screened second generation styryl-based neutral compounds directly in human Alzheimer's disease patient's brain sections to develop STB-8, which was later proved to cross blood-brain barrier and stain beta-amyloid plaques in the brain [18].

5.4 Whole Organism Screening

For the clinical application of imaging probes, they should be validated preclinically in animal models. Once the final hit imaging probes are identified based on optical imaging, the adsorption, distribution, metabolism and excretion of their derivatives converted to nuclear imaging probes are investigated using small animals such as mouse and rat before testing on primate or human. While screening dozens of imaging probes in mice or rats to test their in vivo applicability and specificity has been commonly performed, screening thousands of probes in thousands of these animals is not realistic. Zebrafish is one of the well-characterized small animal models together with the nematode *C.elegans* and fruit fly for research. Because its larvae is transparent and is a few millimeters in size, the larvae has been widely used for high throughput optical screening [19]. For imaging probe development, Li et al. screened 320 rosamine compounds in live zebra fish larvae to develop two neural tracers with different colors named ZeN (Zebrafish Neurotracer)-Green and Red which were applied to test gentamicin ototoxicity [15].

6 Multimodality Probe

Each optical and nuclear imaging modality has its own advantage and disadvantage depending on the purpose of the study. Although fluorescent imaging provides a power tool for ex vivo analysis and in vivo experiments using small animals, its application to deep tissue imaging in human is limited by light penetration depth in tissues which is at best several centimeters. The small molecule optical imaging probe, however, can be easily modified by attaching an MRI-, PET- or SPECT-compatible functional group or a single atomic radioisotope which would render them suitable for deep tissue imaging. To convert an optical imaging probe into a PET probe an introduction of iodine-124, fluorine-18 or carbon-11 into the probe is required whereas iodine-123, iodine-131 or technetium-99 is required for SPECT probe. These isotopes can be introduced by chemical replacement of reactive functional groups or by chelation to multifunctional ligands. Because most of these modifications require minimal chemical changes within the molecular structure, the resulting PET and SPECT probes generally maintain the biological properties of the original optical imaging probes. For MR imaging, the optical imaging probe needs to be combined with gadolinium chelate. An example of possible strategies to make various nuclear imaging probes using a pancreatic alpha cell selective fluorescent probe, Glucagon Yellow is illustrated in Figure 4.

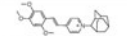
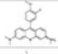
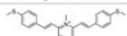
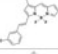
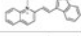
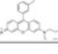
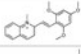
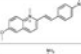
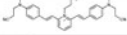
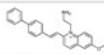
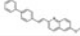
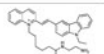
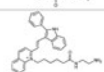
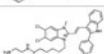
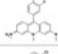
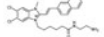
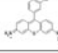

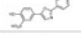
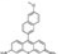
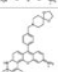
| Probes developed by in vitro screening | | | | Probes developed by cell-based screening | | | |
|--|----------------------|---|-----------|---|-----------------|---|-----------|
| Probing target | Probe Name | Structure | Reference | Probing target | Probe Name | Structure | Reference |
| DNA | A41B2 |  | [13] | Muscle cell state | E26 |  | [29] |
| | C61 |  | [4] | Glucagon | Glucagon Yellow |  | [12] |
| RNA | E36 |  | [17] | Pluripotent stem cells | CDy1 |  | [9] |
| | E144 |  | [17] | | | | |
| | F22 |  | [17] | Probes developed by tissue-based screening | | | |
| β -Amyloid peptide | 2C40 |  | [16] | Probing target | Probe Name | Structure | Reference |
| | 2E10 |  | [16] | β -Amyloid peptide | STB-8 |  | [18] |
| Chymotrypsin | QN-33 |  | [32] | Probes developed by whole organism screening | | | |
| | QN-49 |  | [32] | Probing target | Probe Name | Structure | Reference |
| GTP | GTP green (G49) |  | [30] | Nervous system | Zen-Green |  | [15] |
| Heparin | Heparin Blue (G45) |  | [31] | | Zen-Red |  | [15] |
| | Heparin Orange (G26) |  | [31] | | | | |
| Human Serum Albumine (HSA) | A41-S |  | [20] | | | | |
| | G13 |  | [2] | | | | |
| Glutathione (GSH) | H22 |  | [1] | | | | |

Fig. 3 Probe development

7 Conclusion

Despite the remarkable advancement in biomedical science these days, we still suffer from a lot of diseases. Continuous development of techniques for early diagnosis of diseases and drugs with high efficacy will lead to a better life. Bioimaging which requires close collaborations among chemists, biologists, physicist, computer scientist, and clinicians is rapidly emerging as an essential technology for the diagnosis and drug development. The starting point of this comprehensive technology is the development of bioimaging probes. The examples shown here demonstrate the high efficiency of DOFLA in the development of bioimaging probes. It is anticipated that more highly specific and versatile bioimaging probes will be developed by DOFLA.

From the automatic image analysis side, the application of fluorescent imaging probes might be limited by:

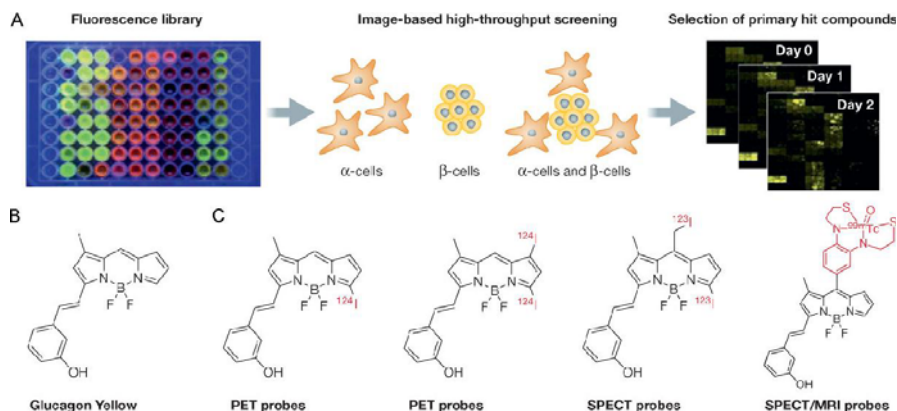


Fig. 4 Schematic work flow of DOFLA in alpha- and beta-cell screening and its application for in vivo imaging. A. DOFL preparation and high throughput screening in alpha- and beta-cells to identify a probe specific for each of the cell types. B. Structure of an alpha-cell selective probe Glucagon Yellow. C. Examples of some potential modifications to convert Glucagon Yellow into PET, SPECT and MRI probes. Han et al., *Imaging metabolic syndrome*. *EMBO Mol. Med.* 2010, 2, 196-210. Copyright Wiley-VCH Verlag GmbH & Co. KGaA. Reproduced with permission.

- Short penetration depth of excitation/ emission light;
- A few distinguishable colors;
- Photobleaching of the organic fluorophore.

Acknowledgements. We thank Emmiline Ang for assistance in editing the manuscript.

References

1. Ahn, Y.H., Lee, J.S., Chang, Y.T.: Combinatorial rosamine library and application to in vivo glutathione probe. *J. Am. Chem. Soc.* 129, 4510–4511 (2007)
2. Ahn, Y.H., Lee, J.S., Chang, Y.T.: Selective human serum albumin sensor from the screening of a fluorescent rosamine library. *J. Comb. Chem.* 10, 376–380 (2008)
3. Buller, F., Steiner, M., Frey, K., Mircsof, D., Scheuermann, J., Kalisch, M., Buhlmann, P., Supuran, C.T., Neri, D.: Selection of Carbonic Anhydrase IX Inhibitors from One Million DNA-Encoded Compounds. *ACS Chem. Biol.* (2010)
4. Feng, S., Kim, Y.K., Yang, S., Chang, Y.T.: Discovery of a green DNA probe for live-cell imaging. *Chem. Commun. (Camb)* 46, 436–438 (2010)
5. Hillier, L.W., Miller, R.D., Baird, S.E., Chinwalla, A., Fulton, L.A., Koboldt, D.C., Waterston, R.H.: Comparison of *C. elegans* and *C. briggsae* genome sequences reveals extensive conservation of chromosome organization and synteny. *PLoS Biol.* 5, e167 (2007)

6. Hopkins, A.L., Groom, C.R.: The druggable genome. *Nat. Rev. Drug Discov.* 1, 727–730 (2002)
7. Im, C.N., Kang, N.Y., Ha, H.H., Bi, X., Lee, J.J., Park, S.J., Lee, S.Y., Vendrell, M., Kim, Y.K., Lee, J.S., Li, J., Ahn, Y.H., Feng, B., Ng, H.H., Yun, S.W., Chang, Y.T.: A fluorescent rosamine compound selectively stains pluripotent stem cells. *Angew Chem. Int. Ed. Engl.* 49, 7497–7500 (2010)
8. Keating, S.M., Clark, K.R., Stefanich, L.D., Arellano, F., Edwards, C.P., Bodary, S.C., Spencer, S.A., Gadek, T.R., Marsters Jr., J.C., Beresini, M.H.: Competition between intercellular adhesion molecule-1 and a small-molecule antagonist for a common binding site on the alpha subunit of lymphocyte function-associated antigen-1. *Protein Sci.* 15, 290–303 (2006)
9. Lee, J.S., Kang, N.Y., Kim, Y.K., Samanta, A., Feng, S., Kim, H.K., Vendrell, M., Park, J.H., Chang, Y.T.: Synthesis of a BODIPY library and its application to the development of live cell glucagon imaging probe. *J. Am. Chem. Soc.* 131, 10077–10082 (2009)
10. Lee, J.W., Jung, M., Rosania, G.R., Chang, Y.T.: Development of novel cell-permeable DNA sensitive dyes using combinatorial synthesis and cell-based screening. *Chem. Commun. (Camb)*, 1852–1853 (2003)
11. Lee, S., Park, K., Kim, K., Choi, K., Kwon, I.C.: Activatable imaging probes with amplified fluorescent signals. *Chem. Commun. (Camb)*, 4250–4260 (2008)
12. Li, J., Ha, H.H., Guo, L., Coomber, D., Chang, Y.T.: Discovery of novel zebrafish neural tracers by organism-based screening of a rosamine library. *Chem. Commun. (Camb)* 46, 2932–2934 (2010)
13. Li, Q., Lee, J.S., Ha, C., Park, C.B., Yang, G., Gan, W.B., Chang, Y.T.: Solid-phase synthesis of styryl dyes and their application as amyloid sensors. *Angew Chem. Int. Ed. Engl.* 43, 6331–6335 (2004)
14. Li, Q., Kim, Y., Namm, J., Kulkarni, A., Rosania, G.R., Ahn, Y.H., Chang, Y.T.: RNA-selective, live cell imaging probes for studying nuclear structure and function. *Chem. Biol.* 13, 615–623 (2006)
15. Li, Q., Min, J., Ahn, Y.H., Namm, J., Kim, E.M., Lui, R., Kim, H.Y., Ji, Y., Wu, H., Wisniewski, T., Chang, Y.T.: Styryl-based compounds as potential in vivo imaging agents for beta-amyloid plaques. *Chem. Biochem.* 8, 1679–1687 (2007)
16. Lieschke, G.J., Currie, P.D.: Animal models of human disease: zebrafish swim into view. *Nat. Rev. Genet.* 8, 353–367 (2007)
17. Min, J., Lee, J.W., Ahn, Y.H., Chang, Y.T.: Combinatorial dapoxyl dye library and its application to site selective probe for human serum albumin. *J. Comb. Chem.* 9, 1079–1083 (2007)
18. Oksvold, M.P., Skarpen, E., Widerberg, J., Huitfeldt, H.S.: Fluorescent histochemical techniques for analysis of intracellular signaling. *J. Histochem. Cytochem.* 50, 289–303 (2002)
19. Storms, R.W., Trujillo, A.P., Springer, J.B., Shah, L., Colvin, O.M., Ludeman, S.M., Smith, C.: Isolation of primitive human hematopoietic progenitors on the basis of aldehyde dehydrogenase activity. *Proc. Natl. Acad. Sci. USA* 96, 9118–9123 (1999)
20. Wagner, B.K., Carrinski, H.A., Ahn, Y.H., Kim, Y.K., Gilbert, T.J., Fomina, D.A., Schreiber, S.L., Chang, Y.T., Clemons, P.A.: Small-molecule fluorophores to detect cell-state switching in the context of high-throughput screening. *J. Am. Chem. Soc.* 130, 4208–4209 (2008)

21. Wang, S., Chang, Y.T.: Combinatorial synthesis of benzimidazolium dyes and its diversity directed application toward GTP-selective fluorescent chemosensors. *J. Am. Chem. Soc.* 128, 10380–10381 (2006)
22. Wang, S., Chang, Y.T.: Discovery of heparin chemosensors through diversity oriented fluorescence library approach. *Chem. Commun. (Camb)*, 1173–1175 (2008)
23. Wang, S., Kim, Y.K., Chang, Y.T.: Diversity-oriented fluorescence library approach (DOFLA) to the discovery of chymotrypsin sensor. *J. Comb. Chem.* 10, 460–465 (2008)

In Vivo Electron Paramagnetic Resonance and Imaging in Biomedical Science

Yves-Michel Frapart

Abstract. Electron Paramagnetic Resonance (EPR) is aiming to non-destructively and non-invasively characterize and quantify paramagnetic species such as superoxide, nitric oxide, dioxygen, ascorbyl radical, or metallo-enzymes. Due to the growing interest in these molecules in biomedical science, EPR and EPR imaging are important tools that are used to obtain information on paramagnetic species, molecules which can not be directly studied using other conventional spectroscopy or imaging methods used in biology.

1 EPR and EPR Imaging

As depicted by the name, EPR is a magnetic method. As paramagnetic species have free electrons, which have a magnetic moment (electronic spin), a magnetic field is applied to the sample to split the energy level between the spin states of the free electron. Applying a microwave of the same energy, one can then observe an energy absorption corresponding to the energy associated with the electronic spin passing from the $m_S = -1/2$ to $m_S = +1/2$ energy states. Typically, EPR spectroscopy is done on a sample of a few microliters placed in a capillary or a flat cell at room temperature, which is then placed in a 4 mm diameter tube at freezing temperature to combat micro-wave absorption by water. This technique does not allow in vivo EPR experiments. Since the 90's, scientists have been using lower micro-wave frequencies (1 GHz or less), which allow the study of bigger lossy samples and open the way to EPR imaging. Technically, an EPR spectrum is observed making the magnetic field vary (abscissa of the spectrum) and recording the absorption of the electromagnetic micro-wave. Due to the utilization of a magnetic field modulation synchronized with the detection to amplify the signal, one observes the derivative (modulated) signal. This signal appears at the resonant field where the energy between the two electronic spin sublevels created by the magnetic field ($g\beta H$, where

Yves-Michel Frapart

UMR 8601 CNRS, University Paris Descartes, 45, rue des Saints-Peres, 75270 PARIS, France

g is the lande factor, β the Bohr magneton and H the magnetic field applied to the sample containing radicals with spin $S=1/2$ for instance) is equal to the energy of the fixed microwave ($h\nu$, where h is the Planck constant and ν the microwave frequency). This equality is the fundamental equation in EPR:

$$h\nu = g\beta H \text{ or } g = h\nu/\beta H \quad (1)$$

From this equation one can deduce the g factor of the absorption line, which, with the splitting of this line in different lines due to the interaction of the electronic spin with the nuclear spin of the molecules, is giving the EPR spectrum characteristic of the molecule. EPR spectroscopy is using a homogeneous magnetic field applied to the sample, and allows the characterization of the paramagnetic species in the sample. The spectrum allows identification of the radical observed and its behavior in the middle (concentration determination, fluidity, interaction with other radicals).

The principle of EPRI is based on the application of tomography in EPR spectroscopy in order to encode the position R of a paramagnetic species into the resonance field.

This is achieved by adding a spatially varying field $B(\vec{R}) = \vec{G}\vec{R}$, where \vec{G} is the field gradient, to the uniform magnetic field \vec{B}_0 conventionally used in EPR. This additional field is parallel to the uniform field but changes in magnitude along a selected direction of space corresponding to the direction of vector \vec{G} . The value of the uniform field at which resonance is observed is then:

$$B_{res}(\vec{R}) = \frac{h\nu}{g\beta} - \vec{G}\vec{R} = \frac{h\nu}{g\beta} - GX \quad (2)$$

where G is the magnitude of the field gradient and X is the abscissa of the paramagnetic species along the field gradient direction. In the equation above ν is the microwave frequency, h the Planck constant, g the g -factor of the paramagnetic species and β the electron Bohr magneton. Let $\rho_{\vec{G}}(X)$ represent the density profile along the field gradient direction \vec{G} i.e. the density of paramagnetic species located in a plane perpendicular to the field gradient direction at abscissa X , then the EPR spectrum obtained under a given field gradient G is:

$$S_{\vec{G}}(B_0) = \int \rho(X)f(B_0 - \frac{h\nu}{g\beta} - GX)dx \quad (3)$$

with $f(B_0 - \frac{h\nu}{g\beta} - GX)$ being the EPR line shape function of the paramagnetic species with abscissa X .

The density profile $\rho_{\vec{G}}(X)$ can then be obtained by a deconvolution process, provided the line-shape function f is known. The latter is obtained by recording an EPR spectrum of the sample with no field gradient. This process assumes that the EPR spectrum contains signals arising from only one type of paramagnetic species and that the line shape function is independent of the position. In the case of our experiments, a deconvolution process based on Fourier transform (FT) provided in Xepri (Bruker) can be used.

A low-pass window function W was applied in the Fourier space to avoid high-frequency noise enhancement due to the division by nearly zero values of $FT(f)$ at high frequencies. Due to the window function W , the density profile $\rho'_{\vec{G}}(X)$ differs from the actual profile $\rho_{\vec{G}}(X)$. Both profiles are linked by: $\rho'_{\vec{G}}(X) = \rho_{\vec{G}}(X) * Ft(W)$ where the symbol $*$ stands for the convolution product. The convolution of the actual profile by the Fourier transform of the window function generally induces a decrease in spatial resolution since a single point in the sample is represented in the image by a more or less extended spot corresponding to the point-spread-function (PSF) $FT(W)$. In our case, the window function was chosen to be Gaussian so that the width of the PSF is $1/\Delta k$. The spatial resolution is thus given by: $\Delta X = 1/\Delta k \cdot G$.

Generally, a reasonable choice of the width Δk of the window function achieving good compromise between resolution and signal-to-noise ratio is: $\Delta k \approx 1/\Delta B_{pp}$ where B_{pp} is the peak-to-peak linewidth of the zero-gradient EPR signal. The width of $FT(W)$ is therefore $\Delta k \approx \Delta B_{pp}$ so that the spatial resolution is roughly $\Delta X \approx \Delta B_{pp}/G$. This points out the importance of ΔB_{pp} for the resolution of the image. Two dimensional (2D) images corresponding to the projection of the spin density onto a selected plane or three dimensional (3D) images are then obtained from a series of profiles $\rho'_{\vec{G}}(X)$ with different gradient directions often called sinogram. In the case of 2D images, the field gradient direction is rotated in the selected plane only, while for 3D images the field gradient directions span the whole 3D space. A filtered back-projection reconstruction process implemented in Xepi (Bruker) with an image from a set of profiles $\rho'_{\vec{G}}(X)$.

In vivo EPR and EPR imaging are not competitive to any other modality; they are aiming at the mapping of radical species which are not easily observable using other modalities (radicals derived from oxygen, dioxygen, nitric oxide), radicals produced in solid parts of the body (especially in bones and teeth under ionizing radiation exposure), and constitutive free radicals (melanoyl). Radicals derived from dioxygen and nitric oxide need molecular probes to get the information.

As EPR is a molecular spectroscopy, it brings to the biologist molecular information and often needs an anatomical co-imaging modality. EPR imaging is bringing challenging research in the fields of chemistry of the molecular probes, methodological and technical progress, and mathematical and informatics treatment of the data and the image. Also, correlation of the measurements with physiological or pathological events brings accurate information for researchers and clinicians for diagnosis. It also concerns polymer material research, material aging, paleontology.

This article presents an overview of the research developed on in vivo EPR and imaging. After a short presentation of the chemical used in EPR and the apparatus that has been developed for imaging and hybrid imaging, we will focus on a few applications which are already developed.

2 EPR and EPR Imaging Molecular Probes

For different reasons such as relaxation properties, or concentration, the paramagnetic species that the EPR spectroscopist is trying to observe are not visible. In such a situation the EPR spectroscopist can use molecular probes, which modify the magnetic properties of specific radicals to observe them. One can distinguish two kinds of molecular probes for EPR.

- Free radicals that have an EPR signal which vary with an external parameter (dioxygen concentration, pH, redox potential),
- Spin traps (diamagnetic molecules which react selectively with a radical of interest to stabilize a paramagnetic form of it the spin adduct) and those that have a characteristic spectrum (oxygen derived radical, nitric oxide).

For in vivo EPR or imaging the molecules used have to be relatively stable (at least one hour stability) and nontoxic. The synthesis of suitable molecular probes for EPR imaging is a key point for the development of this methodology in living animals.

- Spin-Traps: Reactive oxygen species are currently observed using cyclic nitrones, such as BocMPO (5-tert-butoxycarbonyl-5-methyl-1-pyrroline N-oxide). Up-to-date, the spin traps that we have tested do not give any stable spin adducts to be used in vivo or for imaging. Swartz et al published the EPR spectrum of a spin trapping adduct in living mice. However, it has been shown [1] that the spin adduct is reduced to amine, or can be oxidized in its diamagnetic form too rapidly to be observed using in vivo EPR. Nitric oxide is studied with iron diethylthiocarbamate, which together make a paramagnetic complex. The complexation of nitric oxide has been extensively used for spectroscopy; this complex is subject to different equilibriums in solution, but never-the-less it is useful for nitric oxide imaging and in vivo detection in stressed or pathological situations [2].
- Molecular probes: Dioxygen is usually measured using triarylmethyl radicals (Figure 1), which are very stable in buffer solution, but turn out to be unstable in biological media [3]. Nevertheless, due to a magnetic interaction with dioxygen, the line width of their spectrum is linearly correlated to dioxygen concentration in the vicinity of the radical. These radicals are very interesting for imaging due to their very small line width (ca $10 \mu T$ at 0% O_2) which increases to ca $20 \mu T$ at 21% O_2 . Indian ink is utilized for oximetry but gives a very broad spectrum; when one does not need the spatial information, indian ink can even be used in humans [4]. Lithium phthalocyanine crystals present the advantage of being stable over time and very sensitive to oxygen concentration ($1 \mu T$ at 0% O_2 and $300 \mu T$ at 21% O_2).

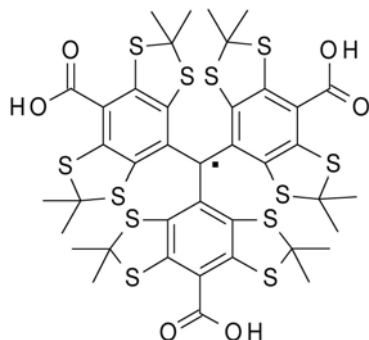


Fig. 1 Formula of TAM (tris-(p-carboxyltetra-thiaaryl)methylradical)

3 In Vivo EPR and EPR Imaging Apparatus

Commercial equipment for in vivo EPR imaging for small animals are available from Bruker Biospin or Jeol. This equipment works at 1 GHz allowing a whole body experiment on 36 mm diameter lossy sample (animal). In vivo EPR spectroscopy on humans is possible using a surface coil which allows EPR in regions of interest of a few millimeters under the surface coil, about 1 cm diameter. Many EPR imaging apparatus are home built, operating at micro-wave frequencies from 0,2 to 1 GHz. The lower the frequency, the deeper the penetration of the micro-wave in the body (a few millimeters at 10 GHz, up to 3 or 4 centimeters at 1 GHz; a few decimeters at lower frequency which are close to the one used in MRI). EPR and relative methods are not invasive on a radiation point of view- the frequencies are the ones used in cellular phone technology, working at very low power (from 1 to 100 mW), and the magnetic field applied on the subject is about 50 mT (MRI is working at 1 to 4 T). These considerations made EPR spectroscopy reasonable to investigate for human applications in the USA.

4 In Vivo EPR Spectroscopy and Its Applications

Some valuable information can be obtained using EPR spectroscopy on living systems. A Dartmouth College group, lead by Harold Swartz [5], is the leading EPR group in the world, and the only one to have an EPR spectrometer dedicated to humans.

One of the most important applications for EPR is dosimetry. As mentioned, ionizing radiation such as X-rays, nuclear radiation, and extracted electrons induce the production of radicals in soft tissue. However, these radicals rapidly disappear. When an electron is extracted from a bond in a solid, this leaves a paramagnetic defect, which can be considered as a $S=1/2$ paramagnetic species. The intensity of

the EPR signal is relative to the spin quantity, so the number of defects which have been created is proportional to the intensity. These radicals can be observed in nails, teeth or bones. The signal in teeth is particularly interesting because the intensity of the signal is linearly correlated to the radiation dose received by the person. This method is currently being developed as a standard in the USA to determine the radiation received in a large population. Hundreds of people have had an EPR spectrum taken of their teeth on a simplified EPR spectrometer developed by Swartz's team. It seems that this method can detect dosimetry from about 0,1 Gy to over 20 Gy.

Other applications need the utilization of a contrast agent; currently used is Indian ink applied as a tattoo. As mentioned, the EPR signal of Indian ink is dependent on oxygen concentration in its surrounding environment. This characteristic is used by the Dartmouth team to determine oxygen recuperation in the foot, as a prevention method for arthritis in diabetic patients [5].

5 EPR Imaging on Endogenous Radical

As mentioned before, some radicals are naturally observed in living system (endogenous radical). The melanin radical which is derived from melanine naturally exists in skin and hair. White skin does not have a large enough concentration of this radical to be observable by EPR, but the dark-colored beauty mark does, and thus is observable. From this finding, Bernard Gallez's group in Brussels (Belgium, Université Catholique de Louvain) has tried to observe melanin in melanoma, deposited on the heads of rats. He succeeded to image the melanoma using a surface coil [6].

Under UV irradiation the ascorbyl radical can be observed in skin. So far the observation of this radical has not lead to any application in EPR imaging.

6 EPR Imaging Using Molecular Probes

As specified before, spin trapping of the oxygen derived radical has lead to spin adducts which are not stable enough to be used in EPR imaging. Three kinds of experiments are commonly used in EPR imaging: detection of nitric oxide in situations leading to a large over-production of this radical; Oxymetry using soluble molecular probes, and redox status imaging using hydroxylamine probes which are oxidized to the corresponding aminoxyl radical at a certain redox potential.

Detection and quantification of nitric oxide: Nitric oxide over-produced in mice is observed using complexation with a iron(II) complexes. Typically a solution of diethylthiocarbamate is injected subcutaneously into a mouse, and iron(II) (Mohr salt or iron citrate) is injected into the mouse 30 minutes before imaging. This method has been applied on whole body imaging of mice for detection of NO after ISDN injection [7], LPS treatment [8] with a 3 to 6 mm resolution. Recently we studied

the apparition and imaging of the repartition of the $[\text{Fe}(\text{DETC})_2]\text{NO}$ after injection of the diethylthiocarbamate, and the NO donor PAPANONOate in mice. The complex was mainly detected in the liver, but repositioning is needed to confirm these results (figure). We managed to obtain a 1 mm resolution.



Fig. 2 a : Dissection of a mice in the area of the liver after EPR imaging, b : EPR imaging of $[(\text{FETC})_2\text{FeNO}]$ complexe in mice.

7 Oxymetry

The line-width of a radical species is dependent on the oxygen concentration in its surroundings. This has been demonstrated using Tris(p-carboxyltetraarylyl)methyl radical (TAM), for which the line-width is varying from 8 to 18 μT from 0 to 21 % of dioxygen. Making a spatial spectral EPR image, where a spectrum is recorded in each voxel, allows oxygen mapping [9]. Oxymetry applications have been published [10] in many cases for the determination of oxygen concentration in tumors for instance [11].

8 Mathematical Treatment of the EPR Signal to Get an EPR Image

When one applies a magnetic field gradient to an EPR sample during an EPR experiment, one obtains the convolution of the EPR spectrum of the sample with the spatial repartition of the paramagnetic species in the field of view. Then he can obtain the image from this experiment making a deconvolution of this image spectrum with a reference spectrum. To get a multidimensional image, the gradient is turned around the sample, and the image is obtained adding a back projection operation after the deconvolution. Commercial EPR Imaging software uses deconvolution procedures based on Fourier Transform, while some groups are trying to get better results using other kind of transformations (Radon Transform [12]).

9 EPR Imaging and Anatomical Repositioning

EPR imaging allow image of radicals inside a space volume. There is no anatomical information in an EPR image. Different groups are using MRI to get the anatomical information [13]. We are using X-ray micro-computed tomography. The repositioning is done manually, but this technique works quite well. Figure 3 shows the repositioning of a 3 mm inner diameter tube containing plastic balls, in a 2mM TAM solution. Two capillaries are positioned on the side to allow the alignment of the central tube.

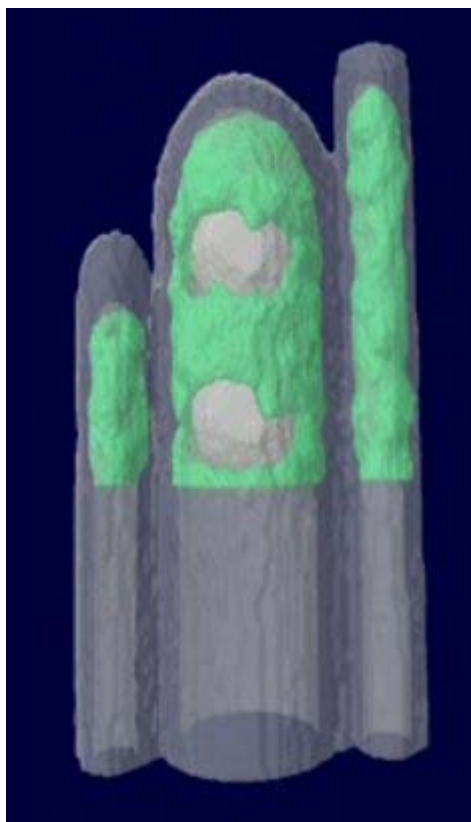


Fig. 3 a : Dissection of a mice in the area of the liver after EPR imaging, b : EPR imaging of $[(FETC)_2FeNO]$ complexe in mice.

10 Conclusion

EPR imaging is an emerging non invasive complementary molecular imaging modality, which aim at the detection of free radical species, which are not imaged by other modalities. Free radicals (O_2 , NO, etc.) are involved in many different physiological and pathological situations (cancer, degenerative disease, ischemia) so that EPR imaging can be an important tool in biomedical science. Before some progress has to be done in chemistry to get accurate, specific stable molecular probes, in technology to have more sensitive apparatus, in signal and image processing to get fast and accurate information from the EPR signal acquired.

References

1. Beziere, N., Frapart, Y.-M., Rockenbauer, A., Boucher, J.-L., Peyrot, F.: Metabolic stability of superoxide and hydroxyl radical adducts of a cyclic nitron toward rat liver microsomes and cytosol: A stopped-flow ESR spectroscopy study. *Free Radical in Biology and Medicine* 49(3), 437–446 (2010)
2. Berliner, L.J., Fujii, H.: In Vivo Spin Trapping of Nitric Oxide. *Antioxydant and Redox Signaling* 6(3), 649–656 (2007)
3. Decroos, C., Li, Y., Soltani, A., Frapart, Y., Mansuy, D., Boucher, J.-L.: Oxidative and reductive metabolism of tris(p-carboxyltetraaryl)methyl radicals by liver microsomes. *Chem. Res. Toxicol.* 22, 1342–1350 (2009)
4. Swartz, H.M., Khan, N., Buckey, J., Comi, R., Gould, L., Grinberg, O., Hartford, A., Hopf, H., Hou, H., Hug, E., Iwasakik, A., Lesniewski, P., Salikhov, I., Walczak, T.: Clinical applications of EPR: overview and perspectives. *NMR in Biomedicine* 17, 335–351 (2004)
5. Salikhov, I., Walczak, T., Lesniewski, P., Khan, N., Iwasaki, A., Comi, R., Bucjkey, J., Swartz, H.M.: EPR Spectrometer for Clinical Applications. *Magnetic Resonance in Medicine* 54, 1317–1320 (2005)
6. Vanea, E., Charlier, N., DeWever, J., Dinguizli, M., Feron, O., Baurain, J.-F., Gallez, B.: Rapid Communication: Molecular electron paramagnetic resonance imaging of melanin in melanomas: a proof-of-concept. *NMR in Biomedicine* (2008)
7. Nagano, T., Yoshimura, T.: *Chemical Review* (2002)
8. Hirayama, et al.: *Molecular and Cellular Biochemistry* (2003)
9. Velan, S.S., Spencer, R.G.S., Zweier, J.L., Kuppusamy, P.: Electron Paramagnetic Resonance Oxygen Mapping (EPRM): Direct Visualization of Oxygen Concentration in Tissue. *Magnetic Resonance in Medicine* 43, 804–809 (2000)
10. Gallez, B., Baudelet, C., Jordan, B.F.: Assesment of tumor oxygenation by electron paramagnetic resonance: principle and application. *NMR in Biomedicine* 17, 240–262 (2004)
11. Matsumoto, K.-I., Subramanian, S., Devasahayam, N., Aravalluvan, T., Murugesan, R., Cook, J.A., Mitchell, J.B., Krishna, M.C.: Electron Paramagnetic Resonance Imaging of Tumor Hypoxia: Enhanced Spatial and Temporal Resolution for In Vivo pO₂, Determination. *Magnetic Resonance in Medicine* 55, 1157–1163 (2006)

12. Williams, B., Pan, X., Halpern, H.J.: EPR imaging: The relationship between CW spectra acquired from an extended sample subjected to fixed stepped gradients and the Radon transform of the resonance density. *Journal of Magnetic Resonance* 174, 88–96 (2005)
13. Samouilov, A., Caia, G.L., Kesselring, E., Petryakov, S., Wasowicz, T., Zweier, J.L.: Development of a Hybrid EPR/NMR Coimaging System. *Magnetic Resonance in Medicine* 58, 156–166 (2007)

Intra-Operative Ex-Situ and In-Situ Optical Biopsy Using Light-CT

Martine Antoine, Brigitte Sigal, Fabrice Harms, Anne Latrive, Adriano Burcheri, Osnath Assayag, Bertrand de Poly, Sylvain Gigan, and A. Claude Boccara

Abstract. The field of digital pathology is evolving very quickly: there is an increasing implication of laboratories and imaging companies in the biomedical field of histology. For our part we propose a digital imaging tool based on optical interferometry with short coherence length light sources (OCT). This instrument provides, without preparation or contrast agents, virtual sections of biological tissues with a field of view (1cm^2) and spatial resolution (approximately 1 micron in 3-D) suitable for histology. We show the relevance of this approach by comparing our images obtained in minutes during surgery with histological sections obtained after a few days. In these studies we worked on fixed tissue, fresh tissue in vivo or ex vivo. Finally, an endoscopic probe based on the same principle has been validated ex-vivo for use inside the bodies of patients.

1 Introduction: Virtual Pathology Using Light-CT

Virtual pathology is now widely used by taking advantage of optical sectioning. Among the methods that had been used we can emphasize on:

- Confocal Microscopy (CM) with a lateral and axial resolution has mainly been coupled with fluorescent exogenous contrast agents but an interesting approach has been used by the group of Memorial Sloan and Kettering for Moss surgery using acetic acid or aluminum chloride as backscattering contrast agent. The penetration depth of (CM) is moreover much more limited than the Optical Coherence Tomography one.

Martine Antoine · Brigitte Sigal
Hospital Tenon and Hospital Curie (Paris, France)

Fabrice Harms · Anne Latrive · Adriano Burcheri · Osnath Assayag ·
Bertrand de Poly · Sylvain Gigan · A. Claude Boccara
Institut Langevin ESPCI-Paristech (Paris, France) and LLTECH SAS (France)
e-mail: boccara@espci.fr

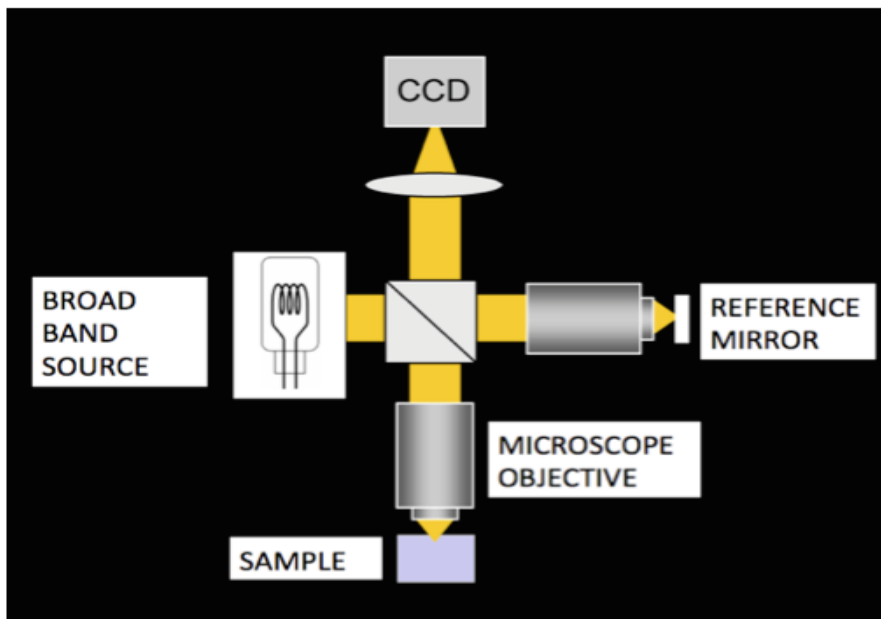
- Optical Coherence Tomography (OCT) is the equivalent of ultrasonography in the optical domain. OCT uses low coherence interferometry to section in-depth. A large number of commercial setups are now available mainly for eye examination. Although the penetration depth of OCT is about 1 mm the resolution is rather limited (5 to 15 micrometers axial or lateral) to reveal cellular structures.
- Multiphoton microscopy is also a powerful technique that sections tissues; using an IR wavelength it exhibits a larger penetration depth than confocal microscopy. This technique requires the use of expensive ultrashort high peak power lasers. Multiphoton microscopy that has been able to image rat brains at a few hundred micrometers depth has not proven to pass the 100 micrometers limit in dense, high refractive index tissues.
- Full field OCT uses the very short coherence length of thermal sources or of LEDs to provide en face sections of less than 1 micrometer with a transverse resolution in the 0.7 to 1.5 micrometer range. LLTech Inc. has recently improved this technique in its Light-CT scanner design by introducing real time corrections that insure optimal image quality. The basic principle of this approach has been describes in many papers, a basic scheme of the setup is given on Figure 1. It is based on a Linnik interferometer with a white light source. This simplified scheme shows that the light reflected from a pixel of the reference arm interferes with the light backscattered by a voxel in the sample depth only when the path difference between the two arms of the interferometers are equal within the coherence length of the source. The camera allows recording simultaneously mega pixels at a rate typically in the 100 Hz range (some experiments have been done at 4 kHz using high image rate cameras). The software program is user friendly, a non-specialized person can use it; moreover it allows compensating from the mismatch of refractive index between the sample and the water used as immersion medium for the objectives.

2 Proof of Concept: Fixed Tissues

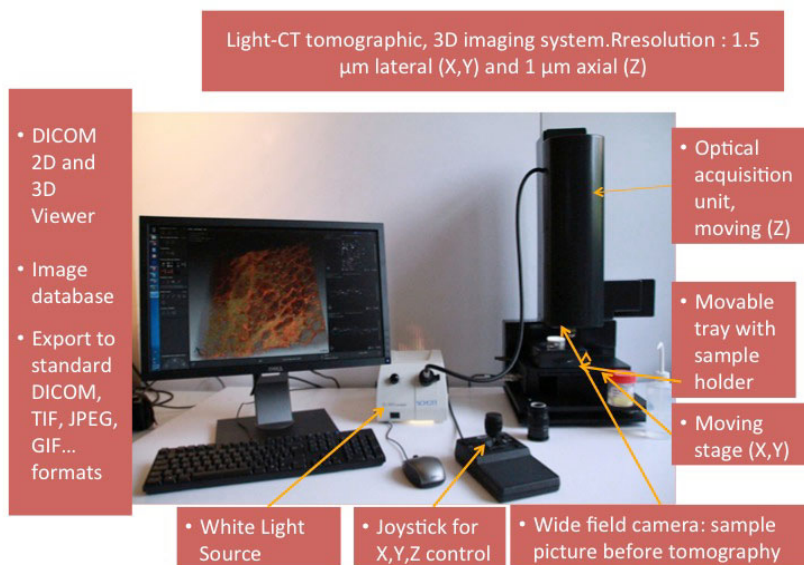
Because fresh human tissues can only be observed in hospitals we started comparisons in our laboratory with histology using fixed tissues. The fixation makes sometimes the scattering strong enough to prevent us to reach structures at depths larger than 150-200 microns in dense tissues. On the contrary the increased rigidity of the tissues allow easy an sectioning and the images are more easily compared with histology slices.

The discussions between the physicists and the pathologists quickly led to the fact that:

- Large fields of view are necessary so that the pathologist can follow up the morphology, and focus to the suspect area. The typical field being about 1 mm^2 (with 10x objectives) a 10x10 stitching is used to display the images.



(a)



(b)

Fig. 1 (a) Principle of the Linnik interferometer used in these studies; (b) Picture of the Light-CT scanner with informations explaining the role of the different parts.

- The resolution of the 10x objective is about 1.3 micrometers and is suitable to observe in detail cellular structures.
- It takes about 5 minutes to record such images; less if we record large signals close to the surface, more when the light penetration depth damps the signals.

Figure 2 and 3 show our first studies on gastrointestinal track (colon).

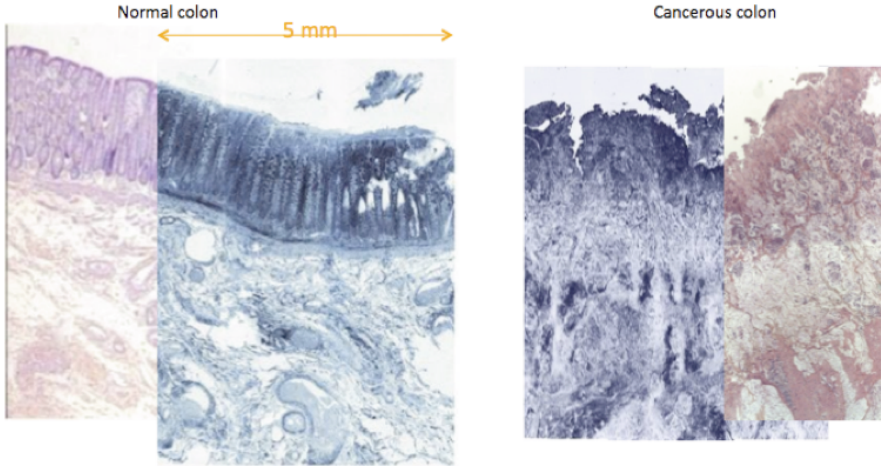


Fig. 2 Colon: large field of view of colon tissues normal (left) and cancerous (right) and the corresponding histology.

Figure 4 shows the images of breast cancer tumors fixed tissues and the comparison with histology. One can easily recognize all the important structures that aim to lead to the diagnostic such as lobules, galactophoric channels, fat cells (adipocytes), membranes and vessels.

3 Intra-Operative Studies: Fresh Tissues

Being able to get a quick reliable diagnostic without waiting for a few days the results of the traditional histopathology process should be able to reduce the reoperation rate (15 to 40% in the case of breast).

The Light-CT scanner has been installed in various hospitals in France and in the USA, so it has been possible to work on fresh tissues. These very soft tissues are sometimes difficult to slice and for the comparison with histology more difficult to get images of the exact same zone without deformation. Nevertheless it is clear that we can identify the same kinds of structures than on fixed tissues and achieve a diagnostic from such images. As an example Figure 5 shows a lobular carcinoma and the comparison with histology. The lesion is characterized by distention of the

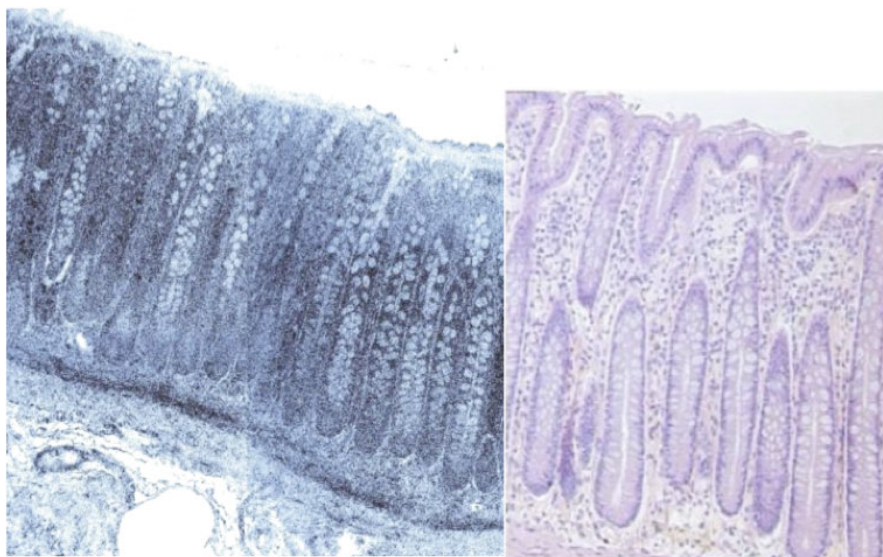


Fig. 3 Colon: Zoom on the upper part of the normal colon image showing a more detailed view of the epithelium.

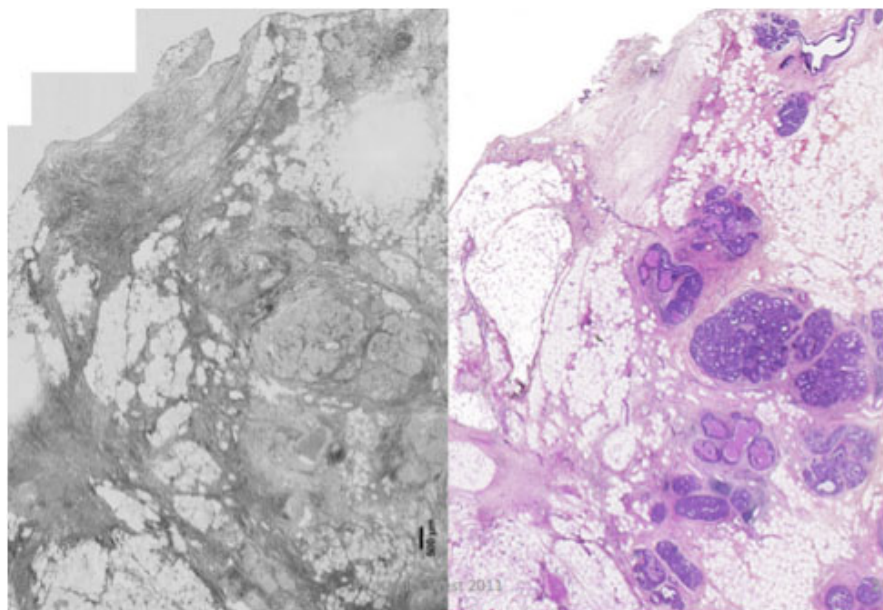


Fig. 4 Breast (fixed tissue): Ductal carcinoma in situ. Light-CT (left) and comparison with Histology (right).

tubules within a lobule. Tubules are characterized by the presence of epithelial cells called apocrine metaplasia.

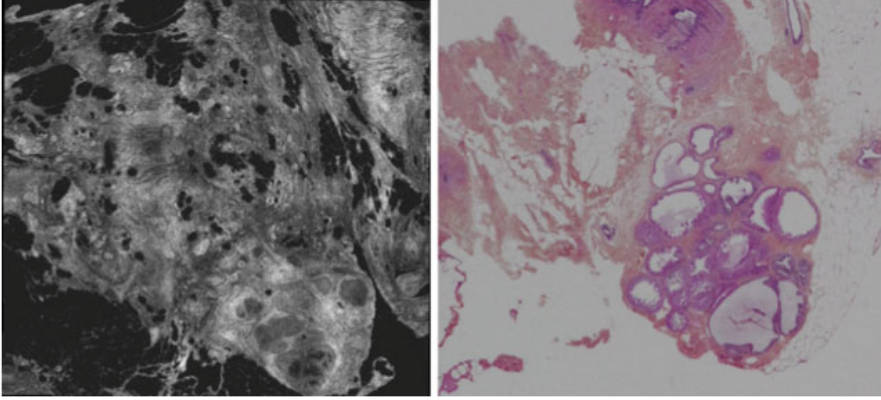


Fig. 5 Breast: Lobular Carcinoma (fresh tissue, hospital experiment) Light-CT image and comparison with histology.

4 Tomographic Light-CT Approach: Proof of Principle

Most of the OCT systems with probe are optical fiber versions of the Michelson interferometer, where 2D images are acquired with point-to-point scanning at the tip of the probe. Such scanning systems require advanced miniaturized mechanical systems at the tip of the probe, which are likely to increase the diameter of the probe, as well as electric supply, which raises the issue of medical safety. Last but not least they do not provide both the axial (sectioning) and lateral resolution.

The advantage of full field OCT is that en face images are directly taken without any transversal scanning. Our laboratory setup, built for the proof of principle, is however different from the standard Full Field OCT setup in the sense that all the signal processing that allows the sectioning at different depth is made by a first interferometer while the imaging is performed by a second one at the tip of the probe in contact with the sample.

To our knowledge no FF-OCT setup with probe suitable for in vivo biomedical endoscopic imaging (meaning with a small end diameter of 1 or 2 mm) has already been demonstrated.

The principle of our system is represented on Figure 6. We use a spatially and temporally incoherent light source such as a Xenon arc lamp. It illuminates the processing interferometer, for instance a Michelson interferometer, which modulates the spectrum. Light is then injected into the probe to the distal interferometer that is common-path: interferences occur between the reference light reflected at the tip of

the probe and light backscattered by structures at a certain depth within the tissue. The external and distal interferometers are coupled: a maximum signal is detected when both path length differences match, so that by setting the path length difference of the external interferometer one sets the imaging depth within the sample. Eventually, a 3D image can be reconstructed by performing a one-dimensional depth scan using the processing interferometer.

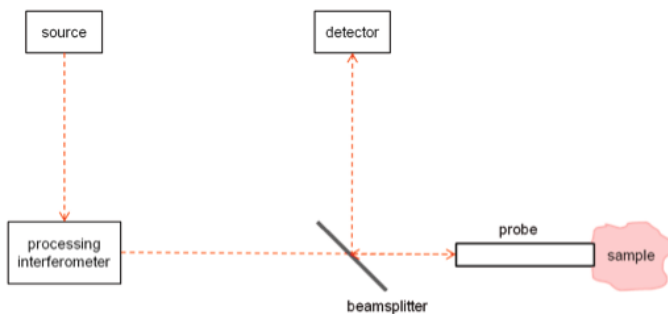


Fig. 6 Principle of the Full-Field OCT setup with a distal probe



Fig. 7 The 2mm distal probe

We have explored ex vivo fixed tissues at various depth in the range 0 to 100 microns. The probe was simply applied in contact with the sample (Figure 7). As an example Figure 8 was taken on an human breast tissue 60 microns below the surface. One can distinguish in this area fat cells as well as collagen fibers.

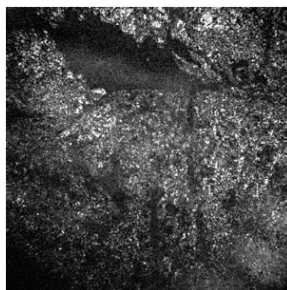


Fig. 8 Breast tumor tissue (fixed)

5 Conclusion and Future Trends

We have shown through a number of examples that the back-scattering signal imaged with a Light-CT scanner, that we call non-destructive virtual sections, matches the morphology revealed through pathologic sections. In order to make this diagnostic more secure we have a number of paths that should lead to a more complete diagnostic:

- Tissue elasticity maps could be obtained by applying a stress to the sample.
- In addition to back scattering we can deduce from measurements a map of the scattering coefficient that is another kind of contrast.
- At a smaller scale, one knows that the density of nuclei, their size or shape carry informations dealing with the tumor state.

We have started [Fujimoto et al. 1995] to get such new complementary imaging tools. Some are in the process of being implemented on the light-CT scanner. We would like to thank the Fondation Pierre-Gilles de Gennes and the Cancéropole Ile de France for their support.

Imaging the inner structure of tumors with a cellular resolution is a challenge. From an automatic image analysis side, the difficulties to overcome are:

- The very high light scattering level of the tissue.
- The low ballistic light level backscattered from the tissue structures.
- The noise of megapixel cameras.

Reference

[Fujimoto et al. 1995] Fujimoto, J.G., Brezinski, M.E., Tearney, G.J., Boppart, S.A., Bouma, B.E., Hee, M.R., Southern, J.F., Swanson, E.A.: Optical biopsy and imaging using optical coherence tomography. *Nature Med.* 1, 970–972 (1995)

Photothermal Laser Material Interactions - From the Sledgehammer to Nano-GPS

Jonathan Hobley, David Paramelle, Paul Free, David G. Fernig,
Shinji Kajimoto, and Sergey Gorelik

Abstract. In this chapter we will summarize the main photothermal, photoacoustic and photomechanical effects of coupling a laser beam into a material from the absorption of the laser light to the deactivation of vibrationally and electronically excited states. Some methods to estimate the resulting temperature rise will be discussed and the resulting pressure increase in the heated area explained. The relaxation of both pressure and thermal transients will be explored and several methods described, such as pump-probe spectroscopy and imaging techniques, which can be used to investigate the dynamics of the relaxation pathways. We will explain how photothermal effects can manifest as optical effects. Finally, we will describe how we can harness photothermally induced optical changes to provide a new methodology in bioimaging involving *indestructible* 5-10 nm noble metal nanoparticles that can be observed using photothermal tracking microscopy for unprecedented periods of time in live cell imaging.

1 Photothermal Fundamentals

1.1 Light Conversion to Heat

The intense monochromatic and polarized photon flux generated by a laser makes it a versatile tool in many laboratories. The high intensity of light can melt metals, force explosive boiling of liquids and even generate x-rays and plasma [3,4]. However, when using lasers we can also take a more gentle approach by simply turning down the laser power. The possibility to attenuate the power of a laser down is also a powerful means of controlling the outcomes in many laser materials interactions (Figure 1). This is simply because the outcome of a laser material interaction is

Jonathan Hobley · David Paramelle · Paul Free · David G. Fernig ·
Shinji Kajimoto · Sergey Gorelik
Institute for Laser and Material Interactions, A*STAR, Singapore

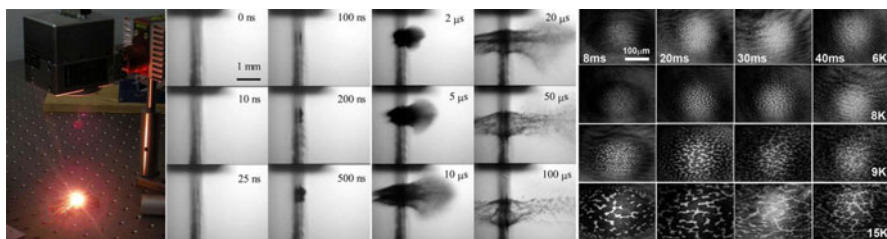


Fig. 1 Varying degrees of laser interactions. Left - Black body radiation emitted during CO_2 -laser treatment of ceramic (Temperature increase ~ 1500 K); Middle - Water boiling after IR nanosecond laser heating (Temperature increase ~ 100 K) [1]; Right - De-mixing butoxyethanol-water induced by nanosecond laser heating of a liquid surface (Temperature increase ~ 15 K) [2].

totally dependent on the incident energy. In fact with a high power laser, melting boiling and phase explosions are all easy to achieve, however more subtle results may be desirable in a well designed experiment.

To interact with a material a laser must first be absorbed or coupled into the material. This can happen in several ways depending on the wavelength of the light and the intensity of the laser beam. Low intensity infra-red laser light can cause vibrational excitation of a molecule or bulk medium, whereas low intensity visible and near UV light excites electronic transitions. The formation and deactivation pathways of molecules excited with single photons can be summarized in a Jablonski diagram as shown in Figure 2. In this diagram energy increases vertically. On the left hand side we see the singlet (S) states and on the right the triplet (T) states. The triplet and singlet states have electronically excited states denoted subscript 1, 2, 3, etc. Between the electronic states there are vibrational levels (v) with increasing energy also denoted with subscripts 1,2,3 etc. The energy between the successive states decreases the higher the energy. The singlet states and triplet states are named due to their multiplicity (M). This is not critical to the discussion but, for completeness, it is given by $M = 2|S| + 1$ where S is the sum of the spins of the electrons in the molecular orbitals of a molecule which can have values of $+1/2$ or $-1/2$ depending on whether the electrons spin is up or down. Singlets have one electron up and one down so $|S| = 0$ and $M = 1$, whereas triplets have two electrons up or two electrons down, so for triplets $|S| = 1$ and $M = 3$.

In the diagram there are several different scenarios (excluding a host of possible photochemical reactions) for light absorption and deactivation marked with numbers 1 to 8. There is a 9th possibility that will also be discussed. We will discuss each in turn.

1. Light is absorbed driving the molecule from its ground state S_0 in its lowest vibrational level v_0 to the first excited state S_1 in its lowest vibrational level v_0 . The $S_1 v_0$ state deactivates by emission back to $S_0 v_0$. This process gives virtually no heating as the molecule went directly between vibrationally cold states by absorption and emission of light. We put light in and we got light out. There is a

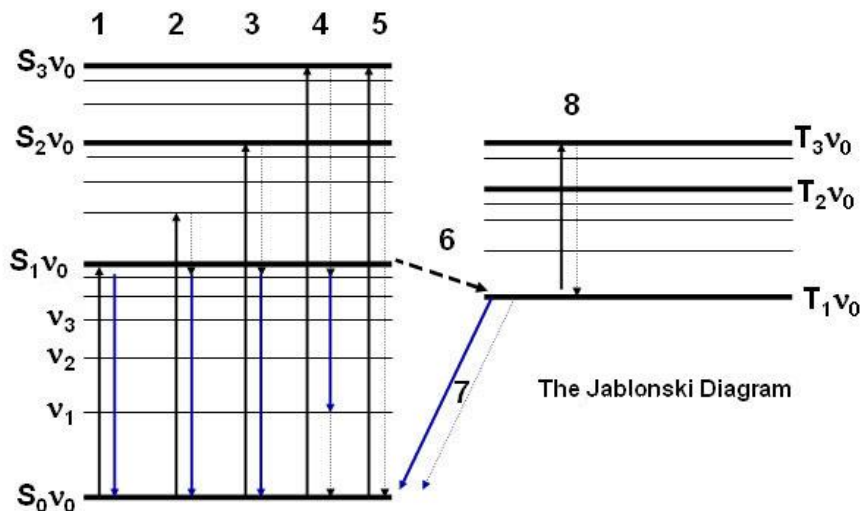


Fig. 2 The Jablonski Diagram. Light absorption is denoted by vertical solid arrows going up, light emission is denoted by solid arrows going down and heat generating processes are denoted by dashed arrows.

tiny amount of heating in this case due to the equilibration and solvation of the excited state. This results in a small energy gap between the excited state that forms initially and the equilibrated excited state from which emission occurs, however, as this results in very little heating this small effect will be ignored in subsequent discussions.

2. Light is absorbed driving the molecule from S_0v_0 to the S_1v_1 . Rapidly S_1v_1 relaxes by vibrational cascade to S_1v_0 giving heat (the thin dotted lines are heat generating processes called vibrational cascade). Next it goes back to S_0v_0 by emitting light. The only process giving heat in this case is the vibrational cascade.
3. Light is absorbed driving the molecule from S_0v_0 to the S_2v_0 . The excited state deactivates firstly by internal conversion, where it changes (isoenergetically) from vibrationally cold S_2v_0 to vibrationally hot S_1v_4 (numbers for v levels not shown in this case and the exact numbers will vary from system to system). From S_1v_4 the molecule undergoes vibrational cascade giving out heat until it arrives at S_1v_0 . In this case, from S_1v_0 , the molecules returns back to S_0v_0 by emission which gives light but no heating. So in this case the only process generating heat is the vibrational cascade from S_1v_4 to S_1v_0 .
4. Light is absorbed driving the molecule from S_0v_0 to S_3v_0 . The molecule internally converts from S_3v_0 to S_2v_3 and then vibrationally cascades down to S_2v_0 giving out heat. From S_2v_0 it internally converts to S_1v_4 which vibrationally cascades down to S_1v_0 , again giving out heat. From S_1v_0 the molecule emits light.

However here we will show another possible way to get down from $S_1 v_0$ which can happen in many cases. The molecule again emits, but this time it goes only to $S_0 v_1$ (it is also possible to go to any vibrational level in S_0). From $S_0 v_1$ the molecule returns to its lowest state $S_0 v_0$ by vibrational cascade giving out heat. In this case heat is generated from all three vibrational cascade events.

5. Light is absorbed driving the molecule from $S_0 v_0$ to $S_3 v_0$. The molecule internally converts from $S_3 v_0$ to $S_2 v_3$ and then vibrationally cascades down to $S_2 v_0$ giving out heat. From $S_2 v_0$ it internally converts to $S_1 v_4$ which vibrationally cascades down to $S_1 v_0$ giving out heat. From $S_1 v_0$ the molecule internally converts to $S_0 v_6$ which vibrationally cascades down to $S_0 v_0$ giving out heat. In this case no light is produced by emission and the full energy of the initial transition from $S_0 v_0$ to $S_3 v_0$ is given back as heat.
6. The molecule can go from the excited singlet state S_0 to the triplet state T_1 in a process called intersystem crossing, which does not give emission so it generates heat since T_1 is lower in energy than S_1 .
7. The molecule can return from $T_1 v_0$ to $S_0 v_0$, or upper vibrational levels in S_0 , by giving emission called phosphorescence. Heat is only given out if the transition goes via upper vibrational levels and not directly to $S_0 v_0$, or more usually for organic molecules at room temperature the system returns to $S_0 v_0$ without giving light thereby generating heat.
8. Whilst in the excited state (either S_1 or T_1) the molecule may absorb a second photon and get excited to S_n or T_n (in this case T_3). From there it will internally convert from $T_3 v_0$ to $T_2 v_3$ then vibrationally cascade to $T_2 v_0$, then internally convert to $T_1 v_4$ and then vibrationally cascade to $T_1 v_0$. From $T_1 v_0$ it will return to the ground state with or without phosphorescence, or it may absorb another photon in the excited state and cycle round again generating heat [5].
9. A 9^{th} possibility (not shown) is that the exciting light does not have enough energy to excite the molecule to an electronically excited state and can only change the system from $S_0 v_0$ to $S_0 v_n$, where n is the number of the vibrational level. In this case the molecule returns to $S_0 v_0$ giving heat [11,3].

So there are many possibilities for molecules to generate heat in excited states and we can summarize the main points here.

1. All processes which lower energy without light emission will result in heat.
2. Nearly all of the excitation at room temperature occurs from $S_1 v_0$ as $S_0 v_1$ and higher levels are not heavily populated at room temperature.
3. In the vast majority of cases, upper excited states return to $S_1 v_0$ generating heat before anything else happens such as light emission or photochemistry. This generally happens on the timescale of tens of picoseconds [6-8].

In conclusion, low intensity irradiation leads to single photon absorption and low photochemical conversions to excited states and products. Deactivation of these states subsequently leads to mild photothermal heating and as we shall explore later, photoacoustic effects in the bulk. We can also detect thermal and acoustic effects due to vibrational deactivation of excited states [9-14]. In contrast higher power excitation can lead to multiphoton absorption, ionization, field ionization and eventually

plasma generation [4]. Plasma generation is accompanied by light emission extending from THz to x-rays and this light emission can be enhanced by devising ways for the incoming photons to interact with the plasma through a variety of mechanisms such as resonance absorption. A whole science in itself is dedicated to laser plasma interactions, due to the possibility of generating laser induced fusion reactions and of making pulsed-x-ray lasers. The scope of this discussion will, however, be limited to more simple low power laser material interactions, where we heat the sample by up to ~ 100 K and less. As we will show, with laser ablation, although the flash bang of high-power laser interactions can be attention drawing, in fact sometimes less can be more.

1.2 How Hot Does It Get?

In the field of laser material interactions one of the most commonly asked and yet hardest questions to answer is how do we know how much a laser has heated a material? Or put another way - how hot does it get? The usual answer to this is that the T-jump is calculated based on the laser fluence (I_0), the Napierian absorption coefficient of the material (α), the materials density (ρ), and the heat capacity (C) of the material. The surface T-jump for a system in thermal confinement is given by equation [1] below [5]

$$\Delta T = I_0 \alpha / \rho C \quad (1)$$

Where ΔT is the T-jump. C can be either C_p or C_v depending on whether the material has expanded to its equilibrium volume or not (respectively). However, this is a little less than satisfactory. The T-jump does not result in a system at equilibrium since volume changes can change the magnitude of the T-jump [1]. More seriously phase transitions will also use up heat and can reduce the magnitude of the T-jump [3]. Additionally exothermic processes will add to the magnitude of the T-jump [5]. For this reason many prefer some direct measurement, which is rarely possible. We will show later that one experimental way to determine the magnitude of ΔT is using Raman spectroscopy [1,3]. After the light is absorbed the system may or may not be in thermal confinement. This is determined by whether the heated volume can loose its temperature excess during the duration of the excitation process [15]. The critical time t_{th} the thermal relaxation time given by:

$$t_{th} = d^2 / 4\Delta \quad (2)$$

Where d is the characteristic length (either $1/\alpha$ or ρ radius of the laser beam in the case of bulk heating or the effective absorbing radius in the case of a small particle in the bulk), Δ is the thermal diffusivity. If t_{th} is much longer than the laser pulse, then the system is under thermal confinement and maximum heating occurs. If not, then the system is loosing heat even as the light is heating it and the maximum temperature achievable will be less.

1.3 Photothermal and Photoacoustic Effects

Next we will discuss what happens once a material is suddenly heated up with a bright light source such as a laser. To do this we will consider laser T-jump experiments. Laser T-jump experiments have been on the laboratory bench since the 1970's as a method of conducting relaxation experiments for systems that have fast kinetics [1, 2, 3, 16, 17]. Since materials generally expand upon heating, laser T-jumps also lead to volumetric expansion of the heated medium that cause positive and negative pressure transients, and ultimately the relaxation of these transients leads to zones of lower refractive index (thermal lens) acoustic waves and sometimes acoustic cavitations [1, 15, 17, 18, 19]. In fact photoacoustics had even been noted by Alexander Graham Bell in the 1880's using a chopper and sunlight and his ear as a detector [20]. Photothermal and photoacoustic spectroscopy have both developed into mature fields in photochemistry as a way to make measurements of the deactivation time of dark states such as triplets [9-14]. Additionally photoacoustic and photothermal effects can be important modes of damage during laser surgery, since acoustic cavitation can occur even with very mild T-jumps. Material can even be ejected from a surface at T-jumps of ~ 1 K due to photomechanical effects of pressure transients well below the materials boiling point [1]. Immediately after a laser beam is absorbed the system may or may not be in a pressure confinement regime. This is determined by whether the heated volume can lose its pressure excess during the duration of the laser excitation [1, 15]. The critical time is t_{ac} , which is the acoustic relaxation time,

$$t_{ac} = d/c \quad (3)$$

Where d is the characteristic length (either the laser beam or effective absorbing radius or $1/\alpha$), Δ is the thermal diffusivity and c is the speed of sound in the medium. As for t_{th} , if t_{ac} is much longer than the laser pulse then the system is under pressure confinement. Next we will describe the sequence of events when a nanosecond (10ns) laser beam is absorbed by a material, causing heating. Just after the light is absorbed some of the molecules will have become vibrationally or electronically excited. Sometimes they are both electronically and vibrationally excited and in this case they will lose their initial heat excess to the medium in less than 100 ps [6, 7, 8] to form their thermally equilibrated first excited S_1 states. This S_1 state will give up its excess energy either as heat to the medium (internal conversion and vibrational cascade) or as light (fluorescence). Fluorescence will not result in heating unless the molecule returns to a vibrationally excited form of the S_0 or ground state, which would then relax giving heat. Excited state molecules may also absorb the laser light [5], because those that form in the early part of the pulse will be able to absorb more photons from the remaining part of the pulse before they decay to the ground state. Deactivated ground state molecules may also reabsorb light and re-form excited states. The net result of all non-radiative processes described above is that heat will be produced in the irradiated volume.

Let us simplify the discussion a bit and look at nanosecond infra-red heating of water using a 10 ns, 1.9 μm wavelength laser beam, where only vibrational heating and the system is well understood [1]. First question - how long do the molecules

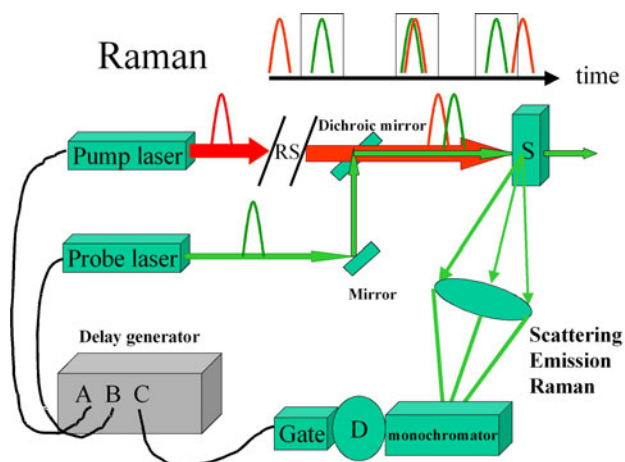


Fig. 3 Apparatus for nanosecond pump-probe Raman / emission measurement. The timing of arrival of pump and probe pulses is controlled by a delay generator and the Raman spectrometer has an electronic gate that opens in synchronization with the arrival of the probe pulse and hence the Raman signal.

in this bulk medium take to respond to the T-jump? Is it during the pulse or after the laser pulse? We have studied this using pump-probe Raman spectroscopy with applied T-jumps provided by the pump pulse (apparatus shown in Figure 3). In this way we can determine Raman spectra at any time delay before or after pulsed laser heating with nanosecond time-resolution. Since pump-probe [1,2,3] is an important method with wide application related to this chapter we will consider it in detail. The method relies on the timed synchronization of two lasers. These are the pump (excitation laser) and the probe (measurement) laser. The pump creates an effect in a few nanoseconds and the probe investigates the effect at any time before or after the arrival of the pump. The arrival times of the pump and probe at the sample are governed by a delay generator which nowadays can be stepped in 500 ps steps. The full kinetics of a process can therefore be acquired by making a series of measurements with different time delays. In the case of aqueous systems, we know that the ratios of OH stretching bands $\sim 3500\text{cm}^{-1}$ are temperature sensitive [1,3] because they are comprised of a range of strong and weak H-bonded OH bands. At lower temperature stronger H-bonding peaks, at lower frequencies, are relatively more represented than weaker H-bonding peaks at higher frequencies. We can therefore determine two factors in a single experiment, these being both the experimentally determined T-jump and the rate of attainment of the molecular structure of the T-jumped form (albeit at confined pressure). This is shown below in Figure 4. We can see that the major changes in the water vibrational spectral ratios occur within the nanosecond laser pulse and that no changes can be detected from after this time until beyond 400ns.

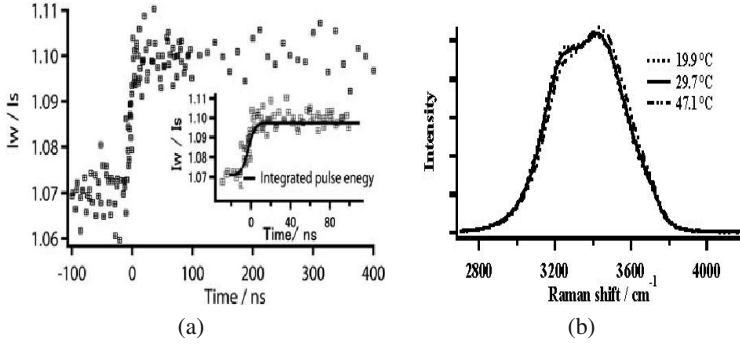


Fig. 4 Dynamics of vibrational H-bond re-structuring for a surface T-jump of 30 K (this can be averaged to T-jump to 200 nm depth 9 K taking into account that the intensity of the light decays exponentially into the sample). Left: Dynamics of spectral ratio changes. Inset shows the earliest times before and after the laser pulse with the integrated pulse energy deposition overlaid. Right: Shows actual spectral changes with temperature.

Furthermore we can establish that calculated T-jumps are very close to the experimentally measure T-jumps by comparing the intensity ratios of the dynamic experiment with those measured under equilibrium conditions. So the laser energy has been absorbed and the system is hot but as it is in pressure confinement it has not yet expanded. How high is the pressure in the heated volume V and what will happen in order to relieve this pressure? The heated volume is given by the expression below [11]:

$$V = A/\alpha \quad (4)$$

where A is the heated area. If the beam radius is taken to be $150 \mu\text{m}$, V is $11 \times 10^{-6} \text{cm}^3$. For a laser fluence $\sim 0.9 \text{J.cm}^{-2}$, surface T-jumps of $\sim 33 \text{K}$ would be produced ($\sim 10 \text{K}$ averaging to a depth of $200 \mu\text{m}$). The total laser pulse energy required to create this magnitude of T-jump is $\sim 6.4 \times 10^{-4} \text{J}$. Typical expected volume changes can be estimated to be $\sim 3 \times 10^{-8} \text{cm}^3$ from:

$$\Delta V = E\beta/\rho Cp \quad (5)$$

where E is the pulse energy and β is the coefficient of volumetric expansion (taken to be $207 \times 10^6 \text{K}^{-1}$) [18]. Furthermore the expected pressure jump can be estimated for these conditions to be $\sim 6 \times 10^6 \text{Pa}$ from [18]:

$$\Delta P = c^2 \beta I \alpha / Cp \quad (6)$$

Note that atmospheric pressure is $\sim 1.01 \times 10^5 \text{Pa}$ so the system must release its pressure as soon as it can, which it does by expanding. We have monitored the rate at which the volume expands using a pump-probe Michelson interferometer (Figure 5).

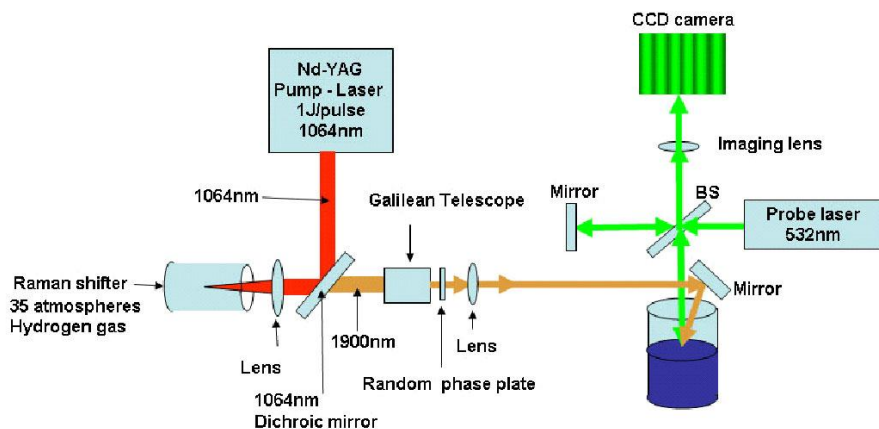


Fig. 5 Apparatus for nanosecond pump-probe interferometry.

In this experiment the water is again heated in a beaker using a ~ 10 ns pulse duration laser with a wavelength of $1.9 \mu\text{m}$. The heated volume expands and pushes against its incompressible water surroundings as well as on the air above. It is easier to push the air above so the water level rises upwards as the pressure is released by the expansion of the liquid. The interferometer is used to monitor the rate of the height increase and from this the rate of volume change can be known or inferred. Data from the interferometer for water heating is shown in Figure 6. We can see that the initial volume change is a little slower than the time it takes for the laser pulse energy to be absorbed confirming pressure confinement. After the temperature of the water is jumped by a few Kelvin the volume of the liquid begins to increase. The initial increase in the liquid height takes 80 ns which corresponds well with the acoustic relaxation time for this system. The initial height increase is slightly greater than expected based on the volumetric expansion coefficient for water at equilibrium and this suggests that at $\sim 80\text{ns}$ the liquid height has overshot the equilibrated height for that T-jump implying that a low pressure zone might form below the liquid surface. After the initial rise in height the height drops slightly until $\sim 1\mu\text{s}$. After this the height again increases. We link this second rise to the formation of cavities inside the liquid that form in the low pressure zone below the liquid surface.

Pump-probe time resolved shadowgraphy was used to look for any evidence of cavitation in similarly heated water samples. The apparatus for time resolved shadowgraphy is shown in Figure 7 and data acquired using this apparatus is shown in Figure 8. Interestingly, we could only detect visible evidence for cavitation at T-jumps much greater than those used in the interferometry experiments as shown in Figure 6. This means that in the interferometry experiment whatever cavities formed were sub-micron in size and collapsed after $\sim 20\mu\text{s}$. Let's next estimate the drop in pressure below the liquid surface.

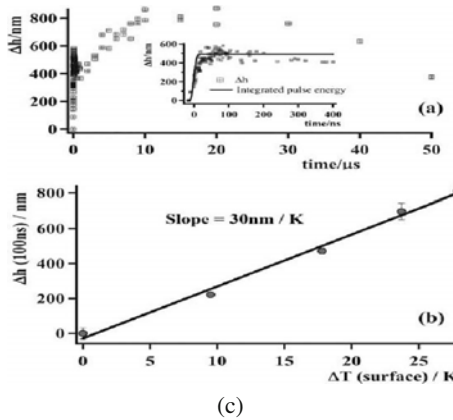
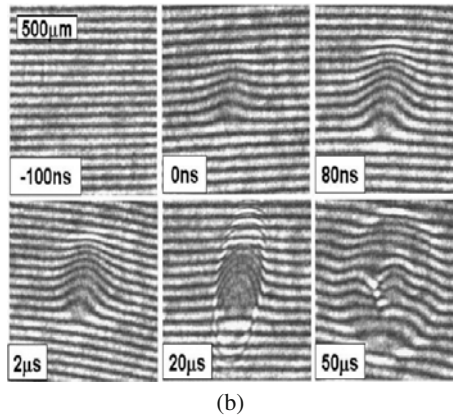
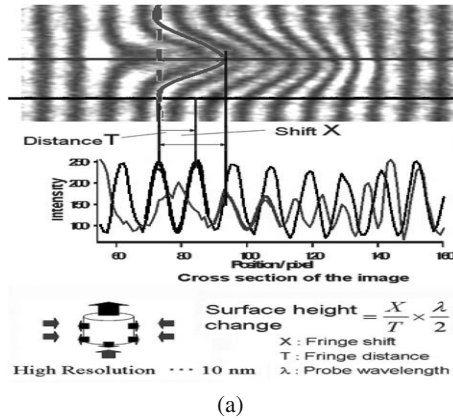


Fig. 6 Volume changes lead to an increase in the height of water at the surface in a laser heated area, which can be evaluated using interferometry. The rate of increase in the height of water is also shown for a 6 K T-jump.

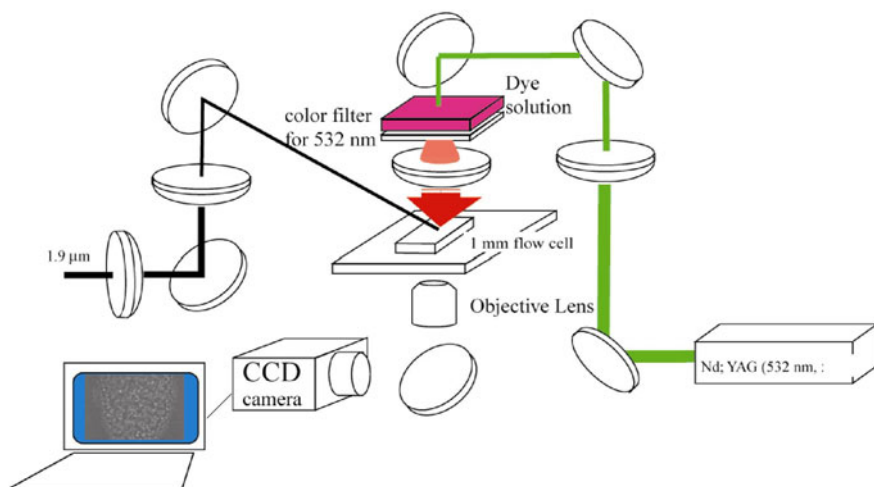


Fig. 7 The apparatus for time resolved shadowgraphy.

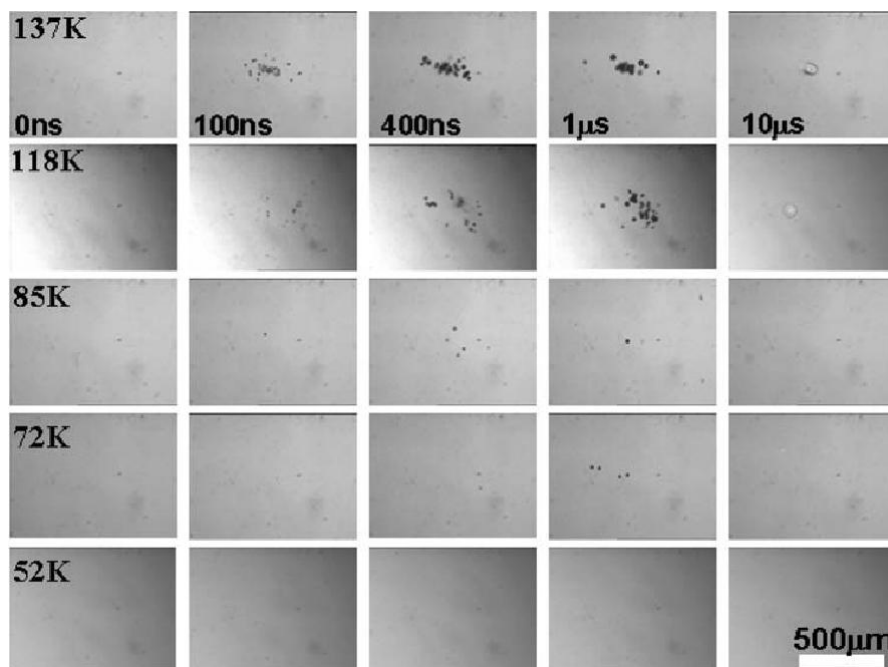


Fig. 8 Photoacoustic cavitation at different T-jumps observed using time resolved pump probe shadowgraphy.

The linear coefficient of the height increase with temperature could be estimated from Figure 6 to be 30 nm K^{-1} . This gives an experimentally determined volumetric expansion coefficient β of $200 \times 10^{-6} \text{ K}^{-1}$ based on the estimated volume change and the heated volume of $11 \times 10^{-6} \text{ cm}^3$ using the surface T-jump value. This is the same as the expected value of β . However, the average T-jump estimated to a depth of 200 mm is approximately 0.3 times the surface T-jump. This means that values for the linear coefficient for the height increase of $\sim 100 \text{ nm K}^{-1}$ with $\beta \sim 600 \times 10^{-6} \text{ K}^{-1}$ are more representative, since the measured expansion is produced to some depth in the sample. Hence, the experimentally determined dynamic value of β is larger than the expected equilibrium value. This can be interpreted to mean that the liquid surface expands more than the equilibrium value and that the over-expanded liquid must exist in stress at a reduced pressure. We can estimate the pressure drop using the following expression [18]:

$$B = \Delta P / (\Delta V / V) \quad (7)$$

where B is the bulk modulus ($2.2 \times 10^9 \text{ Nm}^{-2}$) and ΔV can be taken to be the expected volume change minus the experimentally determined volume change ($1.9 \times 10^{-8} - 3.2 \times 10^{-8} = \sim 1.3 \times 10^{-8} \text{ cm}^3$) and V is $11 \times 10^{-6} \text{ cm}^3$. This gives a pressure drop of $\sim 27 \text{ bar}$ ($\sim 2.7 \times 10^6 \text{ Pa}$). These are ball-park figures that give some insight into the conditions below the liquid surface. In this case we can expect cavities to form where there are weaknesses in the liquid cause by microscopic impurities or ions.

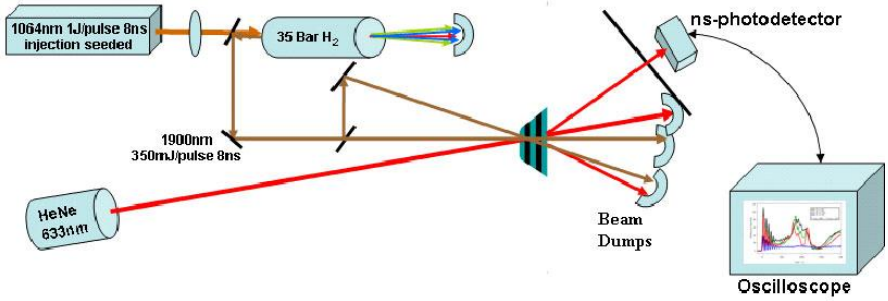
In further support of the hypothesis that *invisible* bubbles form, it has been reported that in order for bubble nuclei to develop into full-blown bubbles they must achieve a certain radius given by [19]:

$$R_b > 2\sigma / (P_v - P_{ext}) \quad (8)$$

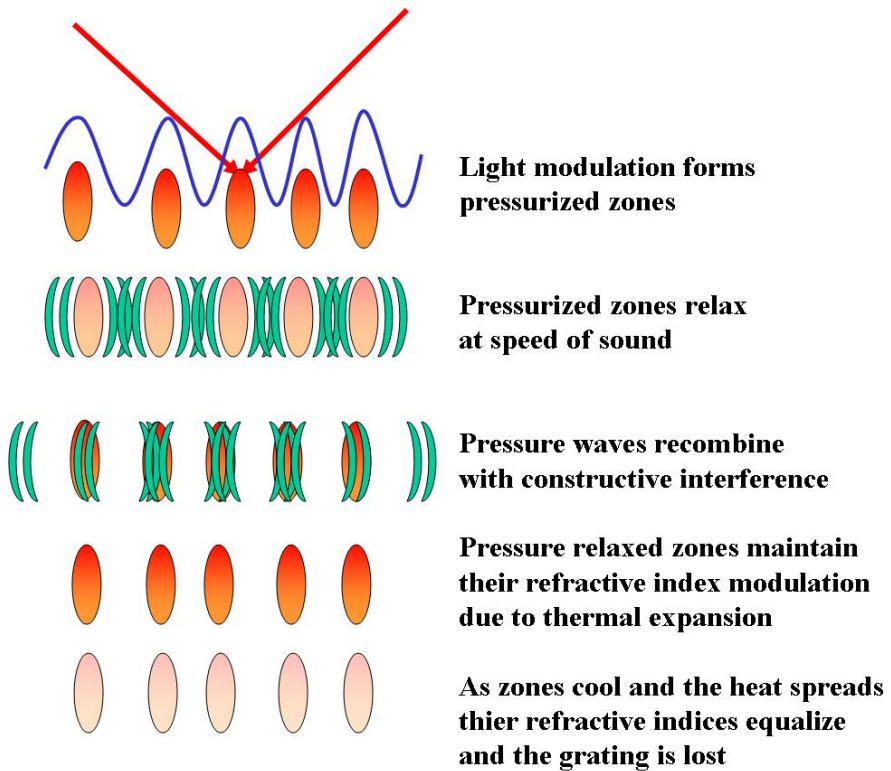
where R_b is the minimum size of nucleation bubble that can expand above the critical size, σ is the surface tension coefficient for water ($7.26 \times 10^{-2} \text{ J.m}^{-2}$) and P_v is the vapor pressure inside the bubble (say 0.03 bar at room temperature [19], 1 bar = $1.01 \times 10^5 \text{ Pa}$). P_{ext} is the pressure in the surrounding liquid, which may be around -27 bar experimentally. This would give a critical stable bubble size of $\sim 50 \text{ nm}$. Hence, stable nucleated bubbles would not necessarily be observable using optical means.

1.4 Photothermal Refractive Index Change and Lensing

The fact that the initial height increase is observed for modest T-jumps, before cavitation effects became evident is in fact the manifestation of the volume change that results in a laser induced transient thermal lens. This is because the volume change will manifest as a change in refractive index. The refractive index becomes lower than the surroundings and the change depends on spatial distribution of the laser energy so we would expect for a Gaussian beam to get a diverging lens forming at the laser irradiated area.



(a)



(b)

Fig. 9 A nanosecond time-resolved transient grating experiment using a CW probe laser (top) with a schematic of the thermal grating formation and decay process (bottom).

Another way to visualize refractive index changes in a medium is using the method of transient grating [21, 22] where the pump-laser beam is split and recombined to form a grating at the sample surface with interference causing high and

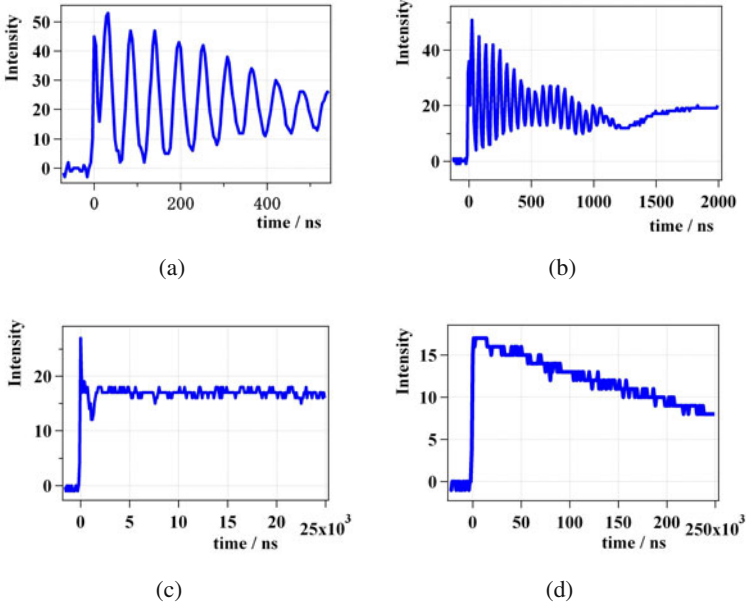


Fig. 10 Transient grating data (grating spacing $80 \mu\text{m}$) for water T-jumped by $\sim 10\text{K}$ from 0 ns to $250 \mu\text{s}$. The intensity is that of a diffracted spot formed by a thermal grating. The formation of low pressure transients is also evident in the transient grating experiment as a signal drop until $\sim 1 \mu\text{s}$.

low intensity laser light as shown in Figure 9. Typical transient grating data for 10 K T-jump in water are shown in Figure 10. In these data we can see that initially the laser heats the liquid forming high pressure zones in a grating pattern causing diffraction of the probe laser beam. The pressurized zones relax acoustically at the speed of sound, thermally expanding, leading to the diffraction intensity dropping. However the pressure waves emanating from adjacent zones recombine, after they have traveled equal distances through the liquid, re-pressurizing the initially pressurized zones and once again increasing the diffracted light intensity. This effect oscillates until the acoustic waves have fully relaxed and by this time the medium has reached its final T-jumped volume. Note that t_{th} is slower than t_{ac} . This volume is maintained until thermal diffusion equalizes the temperature over the whole irradiated volume, or until the system returns to room temperature.

This is a clear example of the optical effects, which can be expected for photoacoustic phenomena and the detection of the thermal effect using a probe light.

2 Photothermal Imaging

2.1 Overview

Photothermal and photoacoustic analysis has been developed over several years independently by many groups and for a range of applications. For example Braslavsky et al. [8,9] Harata et al. [12,13,14] and many others developed photoacoustic and thermal lens techniques to examine the dynamics of excited states of molecules. Sawada et al. [21] and Terizima et al. [23] developed transient grating methods to study photothermal signals from excited states. Thermal lens microscopy capable of detecting sub-yoctomolar solutes was developed by Kitamori et al. [11]. Photothermal imaging has been developed to look at both biological [24-26] and non-biological samples [27-30]. More recently photothermal heterodyne Imaging, tracking microscopy, as well as absorption correlation spectroscopy, have both been developed by Lounis et al. and Orrit et al. [31-36] have even detected single molecule photothermal signals [37]. In photoacoustic methods the detector is a microphone and the rate of production of sound or the spectral response of the sound output by the system is determined to examine the kinetics and spectra of the excited states being monitored. In thermal lensing experiments it is the divergence of a probe beam that is evaluated, as the photothermal signal generates a diverging lens in the sample. Transient grating has been explained previously. Photothermal microscopy uses two lasers, one heating laser and one probe laser. The heating laser generates a thermal lens around the heated object transiently increasing its scattering cross section and the scatter of the probe laser is determined for every point on the sample by raster scanning the microscope sample stage, keeping the sample in a constant position. Parameters such as position and thermal diffusivity can be derived from such measurements. However photothermal heterodyne imaging and tracking will be the main subject in the rest of this chapter. Although thermal lens and similar techniques have been around for some time there is continued interest in the method especially in the field of bioimaging. The reason for this will be described in the next section.

2.2 Fluorescent Probes

Fluorescence microscopy has formed the backbone to bioimaging for the last few decades, and with the advent of laser scanning confocal microscopy this field has become very well established. There are now commercial industries dedicated to the provision of the microscopes and the probes to use in the microscopes. The fluorescence techniques have developed in time to deliver a broad range of methodologies with which a biologist can examine living systems. For example there are techniques such as FRAP (fluorescence recovery after photobleaching - for measuring molecular diffusion) FCS (fluorescence correlation spectroscopy - for measuring molecular or particle diffusion) FLIM (fluorescence lifetime imaging - for determining local environmental conditions by their effect on a fluorophores lifetime) TIRF (total

internal reflection fluorescence microscopy - for looking at interfaces) FRET (Forster resonant energy transfer - to measure the proximity of a donor molecule to a receptor molecule with nanometer precision). Moreover, with increased sensitivity leading to single molecule detection in the last 20 years, the old Abbe diffraction limit has been broken. This has enabled us to see 20 nm resolved optical images using a range of methods such as STED (stimulated emission depletion microscopy) PALM (photoactivated localization microscopy) STORM (stochastic optical reconstruction microscopy) and dSTORM (direct storm). The list goes on and will doubtless keep growing. In addition there is a very wide range of fluorescent probes that can be obtained commercially and newer dyes such as perylene tetracarboxylic acid diimides appear to more robust to light than ever. So what can photothermal microscopy possibly hope to deliver that fluorescence microscopy has not already or very soon will deliver? The answer is that fluorescent molecules emit from photochemically excited states that are inherently unstable in harsh environments such as living cells. We can strengthen them at the cost of adding more and more functional groups, but this increases their size, the number of their chemical interactions and often limits their solubility unless we add more solubilizing groups to them (Figure 11). In the end the resulting probes still photobleach or blink so that they cannot be tracked for long periods of time ($> 10s$) in live cells, this is the Achilles heel of fluorescent probes.

Enter the noble metal nanoparticle probe. They cannot be photobleached, they can be functionalized and they can be modified with ligands and it is very easy to see them when they are large (50 to 100 nm in diameter) even using conventional darkfield imaging. However, at these sizes they are larger than most biomolecules, including the ones that they label. Consequently, there is a substantial degree of uncertainty with such large probes as to their effect on the biomolecule they label and the functions of the cell. So ideally we would like to have much smaller nanoparticle probes (of the same dimensions of a medium-sized protein ~ 5 nm diameter), protected from the environment with a thin ($< 2nm$) non-biologically interacting shell 1:1 liganded to a biomolecule of interest. Obviously we need to be able to detect the probe in some way. Unfortunately, scattering from a nanoparticle of $\sim 5nm$ is virtually impossible to detect, since this decreases as the sixth power of the particle's radius.

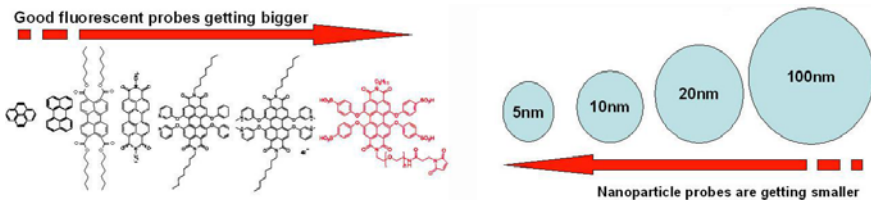


Fig. 11 The future direction of fluorescent probes and nanoparticle probes

2.3 Nanoparticle Probes

Small 5 to 10 nm gold nanoparticles can be bought commercially, however in their initial form they are not very useful for bioimaging. The approach used for the introduction of the key properties to make them useful is by the formation of a self-assembled monolayer of thiolated ligands onto the nanoparticles surface [38]. They follow a basic design starting with a thiol group for bonding to the metal, a hydrophobic core, allowing packing of the monolayer, and a hydrophilic terminus exposed to solvent to enable solubility in physiological environments. A popular method to synthesis gold nanoparticles in aqueous solution uses the citrate molecule to reduce Au⁺ and stabilize the nanoparticles [39]. The weakly bound citrate allows for a more stable monolayer to be introduced. Traditionally, thiol molecules have been used to provide strong binding to gold nanoparticles, such as alkanethiols [40], thioalkylated tetraethylene glycol [41], mercaptoalkyl-oligonucleotides [42] or cysteine containing peptides [43] or peptidols [44]. It is possible to use molecules that bind more weakly to gold than thiols, such as an amino group, if one is using a polymer to stabilize the nanoparticles. Such an approach has been used to provide reversible binding of the ligand shell to the nanoparticles surface [45]. Other molecules that form stronger binding to gold surfaces have also been used, including isocyanide ligands [46] or metal-carbon covalent bonds formed by reductive grafting of diazonium compounds [47]. Stabilized nanoparticles don't just need a strong affinity for its bound ligand, they also require a high grafting density of ligand on the surface. This later property is important to shield the nanoparticles' surface from its biological environment that contains many molecules that can bind to the nanoparticles' surface. These include thiol-containing peptides or proteins, and small molecules such as glutathione that can ligand-exchange with the monolayer on the nanoparticle, replacing it altogether. Colloidal stability must also be maintained in complex biological environments that contain both electrolytes and a high concentration of macromolecules (of the order of several 100 mg/mL). A comparison between two highly passivated polyethylene glycol (PEG) ligand shells bound to gold nanoparticles (thioalkyl-PEG600 and thiolated PEG3000) showed the importance of a dense ligand grafting of the alkyl containing ligand to limit undesirable place-exchange reactions [48]. The surface grafting density of monolayers formed on gold nanoparticles can be probed using the effect of cyanide on its reaction with the gold core. The gold core of susceptible monolayers will be dissolved by a cyanide solution. The kinetics of dissolution by cyanide are thus related to the density and packing of the monolayer. It has been shown previously that shorter length alkyl thiolateprotected gold nanoparticles are more susceptible to etching of the gold core than longer length alkyl thiolates [49]. The grafting density of the peptide-alkanethiol ethylene glycol monolayer matrix as used by Duchesne et al. [44] have been tested with cyanide solutions and found to be highly resistant over a long time [50]. Silver nanoparticles are better absorbers and scatterers of light than gold nanoparticles, yet they have been overshadowed, partly due to their ease of oxidation [51]. However, silver nanoparticles protected from oxidation by a high surface grafting density of appropriate ligands such as the mixed

peptide - alkanethiol ethylene glycol mixed monolayers [44] prove to be highly resistant to cyanide attack and are stable on a time-scale of months without any change in their UV-visible absorption spectra. The use of ligand shells that provide solubility in an aqueous or physiological environment requires a surface chemistry that is essentially hydrophilic. [52, 53, 43] Water soluble passivated ligands often rely on the use of polyethylene glycol (PEG) ligands [54]. PEG has been shown to reduce the interactions with serum proteins, or the uptake of PEG-containing nanoparticles by cells [55]. Gold nanoparticles must be stabilized against van der Waals attractive forces to prevent aggregation. The methods to do this can generally be classified as either electrostatic stabilization, steric stabilization, or electrosteric stabilization [56]. These methods have been used successfully with peptide ligands for binding to gold (and silver [57]) nanoparticles [43, 44, 50]. Using the monolayer approach, the ligand shell is thin (1.3 nm) compared to polymers, such that the hydrodynamic diameter of the nanoparticles probe is comparable to that of a protein. Sterically it is important to minimize the effect of the probe on the surrounding environment. For example, the use of block-copolymers and high molecular weight PEG groups can significantly increase the hydrodynamic size of nanoparticles by as much as 25 nm [58]. A key point is that stabilization and functionalisation of these materials are independent of each other, but achieved in the same preparative step. Therefore, the number of recognition functions present on each nanoparticle can be controlled and reduced to a single moiety without compromising their stability. This allows the labeling of individual biomolecules with nanoparticle probes in a one-to-one ratio [44]. Current methods of conjugation of optical probes to proteins are limited. These include: genetically encoded fluorophores (GFP, etc.), which do not possess optimal optical properties; a small number of tags, e.g., FIAsh, a biarsenical compound reacting with a sequence of four, genetically encoded, cysteines [59], Tris-NTA, interacting with a genetically encoded hexahistidine tag [44] and so-called *snap tags*. The methods to conjugate nanoparticles at 1:1 stoichiometry to biomaterials, such as proteins, or other materials, are even more limited. Worden et al. [60] used a method of solid-phase place exchange reactions to introduce a single carboxylic acid functional group onto the surface of an alkylthiol protected gold nanoparticles. With an extensive array of commercially available polyhistidine-tagged proteins and protein expression systems, an alternative methodology to incorporate multiple nitrilotriacetic acid (NTA) molecules [61] into gold nanoparticles for binding to hexahistidine-containing proteins, is an attractive approach. One such approach to incorporate a single Tris-NTA group into the monolayer of gold nanoparticles has been achieved using immobilized metal ion affinity chromatography [62]. At low probabilities of incorporation of functional Tris-NTA ligand, when the proportion of labeled nanoparticles tends towards zero, all affinity-bound nanoparticles will have a single Tris-NTA label. Hence we can produce 5-10nm gold nanoparticles with high density peptide and PEG shells with a 1:1 ligand of Tris-NTA, so using a polyhistidine tag we can 1:1 label a molecule of interest. This is schematically shown in Figure [12]

Once we have a good nanoparticle probe that is biologically inert, 1:1 functionalized with a biomolecule and small enough that it does not drag the biomolecule

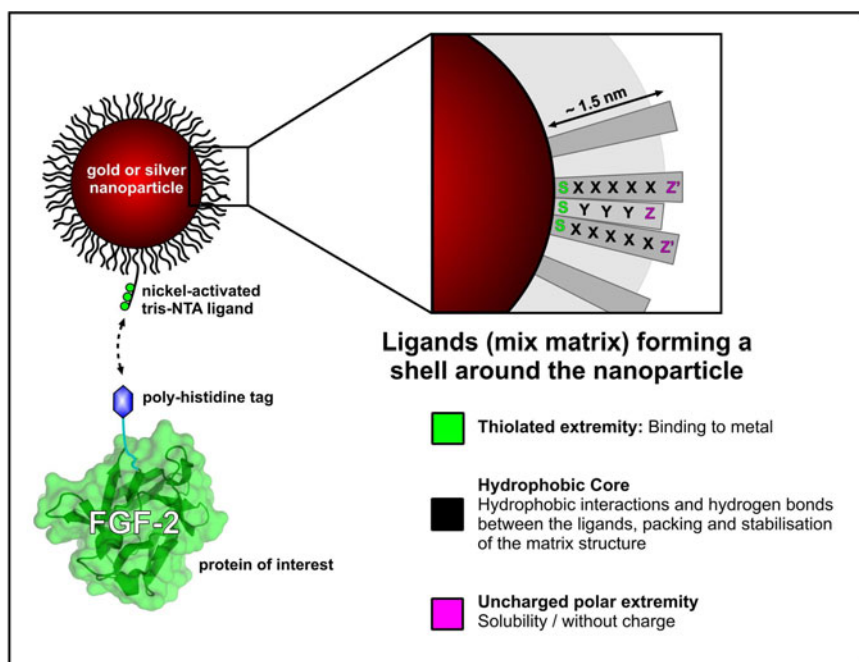


Fig. 12 A probe for photothermal tracking microscopy.

around, how are we actually going to see it, and how are we going to be able to locate it and track it? The answer to that comes in the form of photothermal tracking microscopy developed by Lounis et al. [33].

2.4 Photothermal Heterodyne Imaging

Small noble metal (gold) nanoparticles have plasmon resonances in the visible and have large absorbance cross sections. Furthermore they decay back to their initial state in picoseconds. This means that noble metal nanoparticles absorb light with great efficiency and their fast non-radiative relaxation leads to efficient generation of heat. The heat that is generated then can dissipate to the surroundings causing a spherical thermal lens that increases the ability of the particle to scatter light by increasing its effective size. The thermal lens will increase its size with time as the heat dissipates to the surroundings governed by the thermal diffusivity and as it does the refractive index gradient will become reduced until eventually the system is back to or closer to the starting condition. Small 5-10 nm gold particles can be effectively heated by a green laser (e.g Nd-YAG 532 nm) close to their plasmon band. In the photothermal experiment the green heating laser is made co-linear with a second probe laser (e.g. a HeNe at 633 nm) that is not resonant with the plasmon band and the beams are expanded and made to back-fill the high NA objective in a microscope. In this way both beams are combined at a small focal point at the focus

- | | | |
|-----------------------------|--------------------------|---------------------|
| 1) Polarizing beam splitter | 5) Sample on piezo stage | 8) Telescope |
| 2) 1/4 plate | 6) x80 NA 0.8 Objective | 9) AO Modulator |
| 3) Dichroic mirror | 7) MHz Detectors | 10) Red-pass filter |
| 4) x100, 1.4 NA Objective | | |

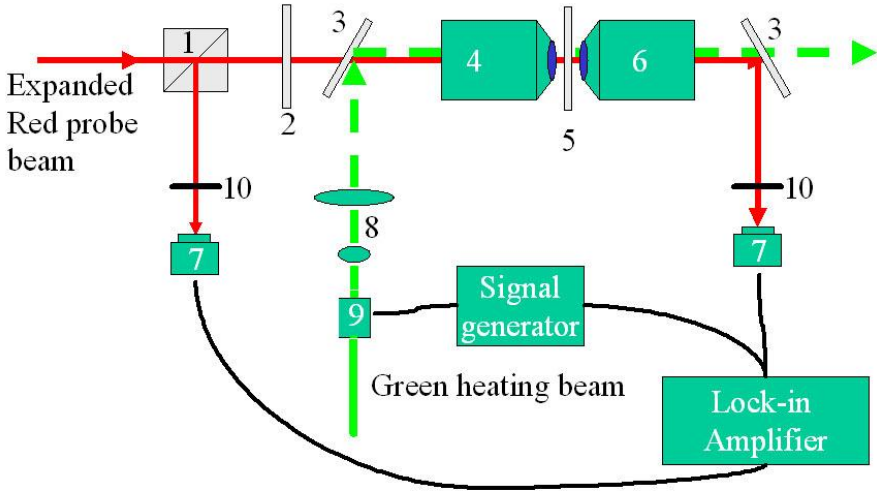


Fig. 13 Photothermal heterodyne imaging

of the objective. The green laser beam is modulated so that the thermal lens from any nanoparticle at or close to the focal point modulates thereby giving modulation of the scattered beam. The scattered signal is detected with a MHz photodetector using lock in amplification. The most sensitive form of this method is photothermal heterodyne imaging (Figure 13) [33]. In this case the probe light interacts with the time dependent modulation in the refractive index around the heated nanoparticle producing a modulated scattered field that is frequency shifted. This produces a beatnote with the probe beam which is acting as a local oscillator. The measurement can be made in either forward detection or reverse detection modes. By raster scanning the sample the photothermal signal can be mapped in the x and y planes.

2.5 Photothermal Tracking Microscopy

The photothermal signal, generated by the convoluted nanoparticle position and its interaction with the heating and probe beams, has a point spread function. In other words the size of the signal depends on the position of the nanoparticle relative to the overlapping laser beams at the focal point of the objective. This means that by taking three data points around a particle and determining the relative intensities of the three signals it is possible to determine the point at which the nanoparticle sits (Figure 13). The piezo stage can then be centered to that position and the

triangulated measurement can be made again to determine if and where the particle moved to. This can be repeated over and over and a track of the particle can be derived over very long timescales (Figure 14).

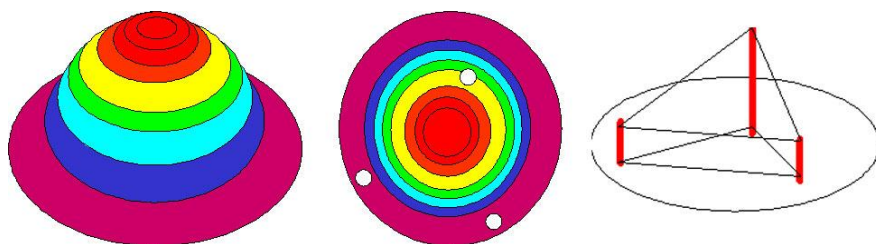


Fig. 14 Triangulation (nm-GPS) to determine the position of the nanoparticle.

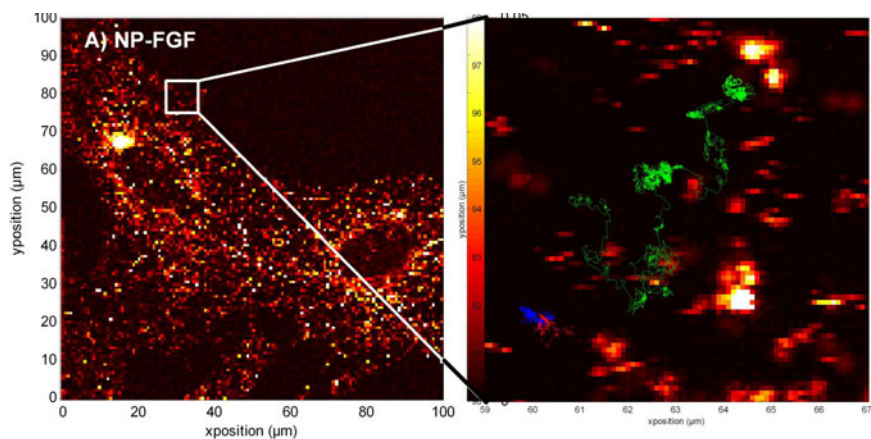


Fig. 15 A photothermal image of fibroblasts (Left) with photothermal tracks (Right) in green, blue and red.

3 Conclusions and Future Vistas

In this chapter we have described the origin of photothermal optical effects and we have explored means of making measurements based on them. We have looked at the effects of heating a bulk material with a laser and we have traveled through to heating discrete particles. Furthermore we have described the development of a new range of nanoparticle probes that have been proven as powerful agents in bioimaging using photothermal tracking microscopy. But what is the future vista for this technique, or range of techniques? We envisage that photothermal tracking systems can be coupled with more conventional microscopies like differential interference

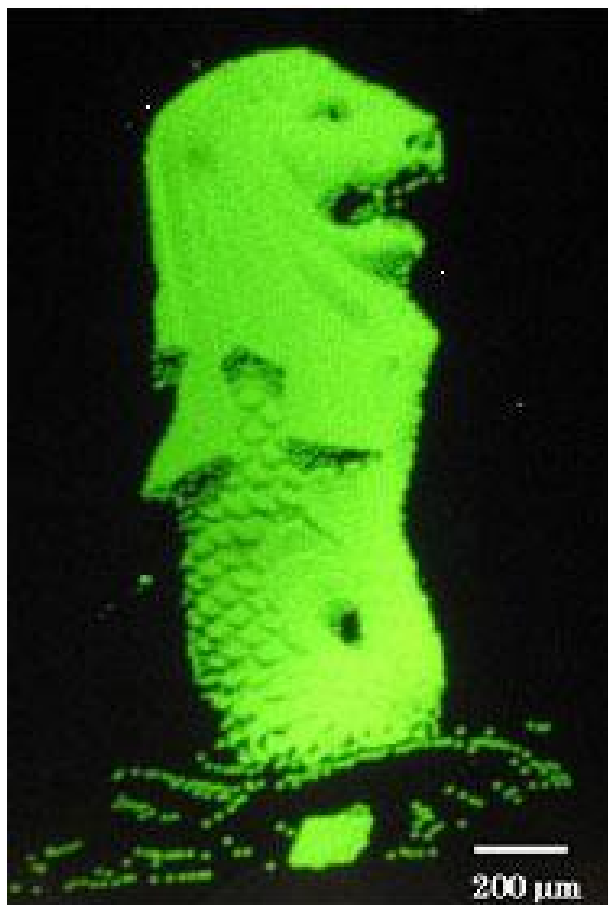


Fig. 16 A mm-Merlion (the symbol of Singapore where our team has a base) made by pulsed laser implantation of coumarin molecules into a polymer. Although peak temperatures are above the temperatures required to decompose C-C bonds the molecule survives as can be seen by its fluorescence (courtesy of Masahiro Goto, National Institute of Materials Science (NIMS) Tsukuba Japan) [65].

contrast (DIC) phase contrast and epi-fluorescence. Furthermore there is no reason why they cannot be used with confocal or super-resolution systems. Already absorption correlation spectroscopy has been demonstrated and with time, just as for fluorescence, we expect the number of acronyms applicable to the photothermal techniques to grow. Current photothermal systems are laser scanning systems, however Zharov et al. [64] have also predicted that wide field systems may also be built in the future. Interestingly these may be pump-probe shadowgraphic systems using nanosecond lasers. Intuitively people may shy away from the high peak powers of nanosecond pulsed lasers for biological imaging and it is true that peak temperatures

for these systems would need to exceed continuous wave (CW or non-pulsed) peak powers by orders of magnitude to see a signal. However, it has been demonstrated time and again that organic materials and biological materials can be transferred in a fully functional form, maintaining their exact chemistry and photochemistry, using pulsed laser ablation. This is true even when the initial temperatures that they endure are $> 1000K$ (Figure 16) [65-67]. The one thing that saves the molecules is that when they are discretely heated they lose their thermal energy to the surroundings before they can denature or decompose. In principle this means that when a particle is heated discretely it can lose its heat before the heat causes damage. This means that biomolecules heated by a nanoparticle irradiated with a pulsed laser may endure more violent heating than when a CW laser is used for the brief period of time during which they are heated.

Finally we will highlight some key challenges in the development of photothermal imaging and tracking. Firstly the biological context to photothermal tracks could be improved significantly if the photothermal track were to be overlaid over a conventional fluorescence, or better still a confocal fluorescence image. Especially with different labels labeling different parts of the cell and if the photothermal track could be viewed by the experimenter, overlaid onto the fluorescence image, in real time. However this is non-trivial. Cells move so it may not be as simple as taking a fluorescence image before starting a tracking sequence. Interleaving of the fluorescence and tracking image may be required and this may require some predictive analysis of the particle motion so that we do not lose it during the measurement of the fluorescence image. Currently tracking in 3-dimensions needs to be developed. This is a well known problem in microscopy and adds another level of complexity to the tracking of a particle. Biological molecules do not function alone. Sometimes they may recruit partner molecules to produce dimers and tetramers. It is notable that, during the acquisition of a nanoparticle track, the intensity of the signal often jumps in a quantized manner. This occurs when two or more nanoparticle labeled biomolecules come together. When the biomolecules, and their nanoparticles, separate again the signal dims to the original level of a single nanoparticle scattering. The problem is that we cannot be sure if we are tracking the original particle or the particle that it attached to. Finally analysis of the diffusion constants will be very useful in order to establish the expression that describes mean squared displacement: $msd(t) \sim Dt^\alpha$, Where D is the diffusion coefficient. In other words analysis is required to determine if the exponent α in the power law is greater than, less than or equal to one.

Interpretation of data will be improved by:

- Tracking the particles with an improved biological context e.g. a fluorescence image corresponding to the position of the various parts and functions of the cell;
- Tracking a particle in x, y and z dimensions - currently we have shown data for x and y only;
- Keeping track of the same particle when its biomolecule forms dimmers, trimers etc with other labeled nanoparticles and then dissociates;
- Understanding the anomalous diffusion of biomolecules attached to nanoparticles based on biological function and morphology change

Acknowledgements. The authors are grateful to A-STAR Joint Council Office for funding their bioimaging research. They are also grateful to Brahim Lounis and his group for images of photothermal tracking.

References

1. Hobley, J., Kuge, Y., Gorelik, S., Kasuya, M., Hatanaka, K., Kajimoto, S., Fukumura, H.: Water expansion dynamics after pulsed IR laser heating. *Phys. Chem. Chem. Phys.* 10, 5256–5263 (2008)
2. Hobley, J., Oori, T., Gorelik, S., Kajimoto, S., Fukumura, H., Honig, D.: Time-Resolved Brewster angle microscopy for photochemical and photothermal studies on thin-films and monolayers. *J. Nanosci. Nanotech.* 8, 1–10 (2009)
3. Takamizawa, A., Kajimoto, S., Hobley, J., Hatanaka, K., Ohta, K., Fukumura, H.: Explosive boiling of water after pulsed IR laser heating 5, 888–895 (2003)
4. Hatanaka, K., Yomogihata, K.I., Ono, H., Nagafuchi, K., Fukumura, H., Fukushima, M., Hashimoto, T., Juodkazis, S., Misawa, H.: Hard X-ray generation using femtosecond irradiation of PbO glass. *J. Non-Crystalline Solids* 354, 5485–5490 (2008)
5. Fukumura, H., Hatanaka, K., Hobley, J.: Laser light interactions with solids and their surfaces. *J. Photochem. Photobiol. C Photochemistry Reviews* 2, 153–167 (2001)
6. Iwata, K., Hamaguchi, H.: Microscopic mechanism of solute-solvent energy dissipation probed by picosecond time-resolved Raman spectroscopy. *J. Phys. Chem. A* 101, 632–637 (1997)
7. Iwata, K., Hamaguchi, H.: Vibrational cooling process in solution probed by picosecond time-resolved Raman spectroscopy. Analysis of the cooling kinetics. *J. Mol. Liq.uids* 65/66, 417–420 (1995)
8. Deak, J.C., Rhea, S.T., Iwaki, L.K., Dlott, D.D.: Vibrational energy relaxation and spectral diffusion in water and deuterated water. *J. Phys. Chem. A* 104, 4866–4875 (2000)
9. Heinhoff, K., Braslavsky, S.E.: Triplet lifetime determination by laser-induced optoacoustic spectroscopy. Benzophenone/iodide revisited. *Chem. Phys. Lett.* 131(3), 183–188 (1986)
10. Bilmes, G.M., Tocho, J.O., Braslavsky, S.E.: Photophysical processes of polymethine dyes. An absorption, emission and optoacoustic study on 3,3-diethylthiadicarbocyanine iodide. *J. Phys. Chem.* 93, 6696–6699 (1989)

11. Tokeshi, M., Uchida, M., Hibara, A., Sawada, T., Kitamori, T.: Determination of sub-yoctomole amounts of non-fluorescent molecules using a thermal lens microscope: Subsingle-molecule determination. *Anal. Chem.* 73, 2112–2116 (2001)
12. Harata, A., Yamaguchi, N.: Photothermal lensing signal enhancement by the transient absorption of photoexcited states in liquid solutions. *Anal. Sci.* 16, 743–749 (2000)
13. Harata, A., Fukushima, K., Hatano, Y.: Magnification in excess of 100-times of the photothermal lensing signal from solute molecules by two-color excitation with continuous-wave lasers. *Anal. Sci.* 18, 1367–1373 (2002)
14. Hirashima, S., Harata, A.: Ultraviolet excitation photothermal spectroscopy of non-labeled amino acids and visible-light induced signal enhancement. *J. Appl. Phys.* 47, 3970–3973 (2008)
15. Paltauf, G., Dyer, P.E.: Photomechanical processes and effects in ablation. *Chem. Rev.* 103, 487–518 (2003)
16. Ballew, R.M., Sabelko, J., Reinier, C., Grubeke, M.: A single-sweep nanosecond time resolution laser temperature-jump apparatus. *Rev. Sci. Instrum.* 67(10), 3694–3699 (1996)
17. Wray, W.O., Aida, T., Dyer, R.B.: Photoacoustic cavitation and heat transfer effects in the laser-induced temperature jump in water. *Appl. Phys. B* 74, 57–66 (2002)
18. Kim, D., Ye, M., Grigoropoulos, C.P.: Pulsed laser-induced ablation of absorbing liquids and acoustic-transient generation (1998)
19. Oraevsky, A.A., Jacques, S.L.: Mechanism of laser ablation for aqueous media irradiated under confined-stress conditions. *J. Appl. Phys.* 78(2), 1281–1290 (1995)
20. Lscher: Photoacoustic Effect in Condensed Matter Historical Development. In: Lscher, Edgar, et al. (eds.) *Photoacoustic Effect: Principles and Applications*, p. 1. Friedr. Vieweg & Sohn, Braunschweig (1984)
21. Harata, A., Shen, Q., Sawada, T.: Photothermal applications of lasers: Study of fast and ultrafast photothermal phenomena at metal-liquid interfaces (1999)
22. Sawada, T.: Ultrafast dynamics at solid/liquid interfaces as investigated by photothermal spectroscopy. *Pure Appl. Chem.* 73(10), 1613–1623 (2001)
23. Terazima, M.: Ultrafast rise of translational temperature after photoexcitation to electronic excited state in solution: Transient lens study of Ni^{2+} aqueous solution. *J. Chem. Phys.* 105(16), 6587–6595 (1996)
24. Harata, A., Matuda, T., Hirashima, S.: Ultraviolet-laser excitation microscopic photothermal lens imaging for observing biological cells. *J. Appl. Phys.* 46(7B), 4561–4563 (2007)
25. Harada, M., Shibata, M., Kitamori, T., Sawada, T.: Application of coaxial beam photothermal microscopy to the analysis of a single biological cell in water. *Anal. Chim. Acta* 299, 343–347 (1995)
26. Kimura, H., Mukaida, M., Kitamori, T., Sawada, T.: *Anal. Sci.* 13, 729–734 (1997)
27. Tao, C., Zhao, Y., He, H., Li, D., Shao, J., Fan, Z.: Imaging photothermal microscopy for absorption measurements of optical coatings. *Chin. Optics Lett.* 7(11), 1061–1064 (2009)
28. Savignat, G., Boch, P., Pottier, L., Vandembroucq, D., Fournier, D.: Non-destructive characterization of refractories by mirage effect and photothermal microscopy. *J. De Physique IV Colloque C7 Supplement of J. De Physique III* 3, 1267–1272 (1993)
29. Studenmund, W.R., Fishman, I.M., Kino, G.S., Giapintzakis, J.: Progress in photothermal microscopy of $\text{Yb}_2\text{Cu}_3\text{O}_{7-x}$. *J. Phys. Chem. Solids* 10–12, 2012–2014 (1998)
30. Commandre, M., Natoli, J.-Y., Gallais, L.: Photothermal microscopy for studying the role of nano-sized absorbing precursors in laser-induced damage of optical materials. *Eur. Phys. J. Special topics* 153, 59–64 (2008)

31. Oceau, V., Cognet, L., Duchesne, L., Lasne, D., Schaeffer, N., Fernig, D.G., Lounis, B.: Photothermal Absorption Correlation Spectroscopy. *ACS Nano* 3(2), 345–350 (2009)
32. van Dijk, M.A., Tchegotareva, A.L., Orrit, M., Lippitz, M., Berciaud, S., Lasne, D., Cognet, L., Lounis, B.: Absorption and scattering microscopy of single metal nanoparticles. *Phys. Chem. Chem. Phys.* 8, 3486–3495 (2006)
33. Lasne, D., Blab, G.A., Berciaud, S., Heine, M., Groc, L., Choquet, D., Cognet, L., Lounis, B.: Single Nanoparticle Photothermal Tracking (SNaPT) of 5-nm Gold Beads in Live Cells. *Biophys. J.* 91, 4598–4604 (2006)
34. Berciaud, S., Cognet, L., Tamarat, P., Lounis, B.: Observation of Intrinsic Size Effects in the Optical Response of Individual Gold Nanoparticles. *Nano Lett.* 5(3), 515–518 (2005)
35. Berciaud, S., Cognet, L., Blab, G.A., Lounis, B.: Photothermal Heterodyne Imaging of Individual Nonfluorescent Nanoclusters and Nanocrystals. *Phys. Rev. Lett.* 93, 257402-1 – 257402-4 (2004)
36. Berciaud, S., Lasne, D., Blab, G.A., Cognet, L., Lounis, B.: Photothermal heterodyne imaging of individual metallic nanoparticles: Theory versus experiment. *Phys. Rev. B* 73, 045424-1– 045424-8 (2006)
37. Gaiduk, I.A., Yorulmaz, M., Ruijgrok, P.V., Orrit, M.: Room-Temperature Detection of a Single Molecules Absorption by Photothermal Contrast. *Science* 330(6002), 353–356 (2010)
38. Love, J.C., Estroff, L.A., Kriebel, J.K., Nuzzo, R.G., Whitesides, G.M.: Self-assembled monolayers of thiolates on metals as a form of nanotechnology. *Chem. Rev.* 105, 1103–1169 (2005)
39. Frens, G.: Controlled nucleation for the regulation of the particle size in monodisperse gold suspensions. *Nature. Phys. Sci.* 241, 20–22 (1973)
40. Brust, M., Walker, M., Bethell, D., Schiffrin, D.J., Whyman, R.J.: Synthesis of thiol-derivatized gold nanoparticles in a twophase liquid-liquid system. *J. Chem. Soc. Chem. Commun.*, 801–802 (1994)
41. Kanaras, A.G., Kamounah, F.S., Schaumburg, K., Kiely, C.J., Brust, M.: Thioalkylated tetraethylene glycol: a new ligand for water soluble monolayer protected gold clusters. *Chem. Commun.*, 2294–2295 (2002)
42. Elghanian, R., Storhoff, J.J., Mucic, R.C., Letsinger, R.L., Mirkin, C.A.: Selective colorimetric detection of polynucleotides based on the distance-dependent optical Properties of Gold Nanoparticles. *Science* 277, 1078–1081 (1997)
43. Lvy, R., Thanh, N.T.K., Doty, R.C., Hussain, I., Nichols, R.J., Schiffrin, D.J., Brust, M., Fernig, D.G.: Rational and combinatorial design of peptide capping ligands for gold nanoparticles. *JACS* 126, 10076–10084 (2004)
44. Duchesne, L., Gentili, D., Comes-Franchini, M., Fernig, D.G.: Robust ligand shells for biological applications of gold nanoparticles. *Langmuir* 24, 13580–13752 (2008)
45. Sardar, R., Bjorge, N.S., Shumaker-Parry, J.S.: pH-Controlled assemblies of polymeric amine-stabilized gold nanoparticles. *Macromolecules* 41, 4347–4352 (2008)
46. Kim, K., Shin, D., Kim, K.L., Shin, K.S.: Electromagnetic field enhancement in the gap between two Au nanoparticles: the size of hot site probed by surface-enhanced raman scattering. *Phys. Chem. Chem. Phys.* 12, 3747–3752 (2010)
47. Mirkhalaf, F., Paprotny, J., Schiffrin, D.J.: Synthesis of metal nanoparticles stabilized by metal-carbon bonds. *JACS* 128, 7400–7401 (2006)
48. Maus, L., Dick, O., Bading, H., Spatz, J.P., Fiammengio, R.: Conjugation of peptides to the passivation shell of gold nanoparticles for targeting of cell-surface receptors. *ACS Nano*. 4, 6617–6628 (2010)
49. Templeton, A.C., Hostetler, M.J., Kraft, C.T., Murray, R.W.: Reactivity of monolayer-protected gold cluster molecules: steric effects. *JACS* 120, 1906–1911 (1998)

50. Free, P., Shaw, C.P., Lvy, R.: PEGylation modulates the interfacial kinetics of proteases on peptide-capped gold nanoparticles. *Chem. Commun.*, 5009–5011 (2009)
51. Henglein, A.: Colloidal silver nanoparticles: photochemical preparation and interaction with O₂, CCl₄, and some metal ions. *Chem. Mater.* 10, 444–450 (1998)
52. Templeton, A.C., Wuelfing, M.P., Murray, R.W.: Monolayer-protected cluster molecules. *Acc. Chem. Res.* 33, 27–36 (2000)
53. Pengo, P., Polizzi, S., Battagliarin, M., Pasquato, L., Scrimin, P.J.: Synthesis, characterization and properties of water-soluble gold nanoparticles with tunable core size. *Mater Chem.* 13, 2471–2478 (2003)
54. Bartz, M., Kuther, J., Nelles, G., Weber, N., Seshadri, R., Tremel, W.: Monothiols derived from glycols as agents for stabilizing gold colloids in water: synthesis, self-assembly and use as crystallization templates. *J. Mater Chem.* 9, 1121–1125 (1999)
55. Zahr, A.S., Davis, C.A., Pishko, M.V.: Macrophage uptake of core-shell nanoparticles surface modified with poly (ethylene glycol). *Langmuir* 22, 8178–8185 (2006)
56. Zhao, W., Brook, M.A., Li, Y.: Design of gold nanoparticles-based colorimetric bio sensing assays. *Chembiochem.* 9, 2363–2371 (2008)
57. Doty, R.C., Tsikhudo, T.R., Brust, M., Fernig, D.G.: Extremely stable water-soluble Ag nanoparticles. *Chem. Mater.* 17, 4630–4635 (2005)
58. Budijono, S.J., Shan, J., Yao, N., Miura, Y., Hoye, T., Austin, R.H., Ju, Y., Prudhomme, R.K.: Synthesis of stable block-copolymer-protected NaYF₄:Yb³⁺, Er³⁺ up-converting phosphor nanoparticles. *Chem. Mater.* 22, 311–318 (2010)
59. Griffin, B.A., Adams, S.R., Tsien, R.Y.: Specific covalent labeling of recombinant protein molecules inside live cells. *Science* 281, 269–272 (1998)
60. Worden, J.G., Dai, Q., Shaffer, A.W., Huo, Q.: Monofunctional group-modified gold nanoparticles from solid phase synthesis approach: solid support and experimental condition effect. *Chem. Mater.* 16, 3746–3755 (2004)
61. Lata, S., Reichel, A., Brock, R., Tamp, R., Piehler, J.: High-affinity adaptors for switch able recognition of histidine-tagged proteins. *JACS* 127, 10205–10215 (2005)
62. Lvy, R., Wang, Z., Duchesne, L., Doty, R.C., Cooper, A.I., Brust, M., Fernig, D.G.: A Generic approach to monofunctionalized protein-like gold nanoparticles based on immobilized metal ion affinity chromatography. *Chembiochem.* 7, 592–594 (2006)
63. Zharov, V.P.: Far-field photothermal microscopy beyond the diffraction limit. *Optics Lett.* 28(5), 1314–1316 (2003)
64. Chrisey, D.B., Pique, A., McGill, R.A., Horwitz, J.S., Ringeisen, B.R., Bubb, D.M., Wu, P.K.: Laser deposition of polymer and biomaterial films. *Chem. Rev.* 103, 553–576 (2003)
65. Goto, M., Pihosh, Y., Kasahara, A., Tosa, M., Hogley, J., Oishi, T.: Pulsed Laser Writing of Coumarin 6 Molecular Micro Patterns on a Poly(ethyl-methacrylate) Film. *J. Adv. Mater.* 41(1), 13–17 (2009)
66. Hogley, J., Nakamori, T., Kajimoto, S., Kasuya, M., Hatanaka, K., Fukumura, H., Nishio, S.: Formation of 3,4,9,10-perylene-tetracarboxylic dianhydride nanoparticles with perylene and polyne byproducts by 355 nm nanosecond pulsed laser ablation of microcrystal suspensions. *J. Photochem. Photobiol. A* 189(1), 105–113 (2007)

Dual Axes Confocal Microendoscope

Wibool Piyawattanametha

Abstract. Biomedical research truly needs new advances in imaging. Existing modalities of in vivo imaging, such as magnetic resonance imaging or ultrasound, lack the spatiotemporal resolution required to image the fundamental building block of living tissue. By contrast, existing high-resolution techniques for imaging cells and their sub-cellular features are technologies that are best suited for in vitro experiments in tissue slices. Yet, the ability to make direct connections between human pathological symptoms/behavior and the underlying cells and molecules responsible for such behavior requires in vivo techniques that can image cellular constituents. Our group research aim is to develop novel high-resolution optical endoscopes to satisfy unmet needs in the clinical environment. These differ from medical endoscopes, which are generally larger and designed to image macroscopic abnormalities. Most importantly, this novel optical endoscopic imaging might suggest new approaches to disease diagnosis and treatment. This talk will be focused on the development a novel confocal imaging modality integrated with microelectromechanical systems (MEMS) technology and their imaging applications. Confocal microscopy is an attractive tool for three-dimensional (3-D) imaging due to its optical sectioning property. Conventional single-axis confocal (SAC) microscopes have a tradeoff between resolution, field of view, and objective lens size, since a high numerical aperture (NA) lens is needed for sufficient resolution, and a long focal length is needed for a large FOV and working distance. A dual-axes confocal (DAC) microscope architecture has been proposed utilizing two overlapping low NA beams, which effectively decouples these tradeoffs. The other important advantage is the ability to achieve a much superior optical sectioning compared to the SAC design. The microscopes are miniaturized into two form factors (5 mm and 10 mm

Wibool Piyawattanametha

Head of Advanced Light Microscopy (ALM) Laboratory National Electronics and Computer Technology Center (NECTEC) 112 Phahon Yothin Rd., Room 321, Pathumthani 12120, Thailand & Head of Advanced Imaging Research (AIR) Center Chulalongkorn University Medical School, 104 Rajdamri Rd., Patayapat Bldg., Room 805 Pathumwan, Bangkok 10330, Thailand

e-mail: wibool@gmail.com

diameter). The imaging demonstrations of the probes were on both *ex vivo* and *in vivo* from mice and human for cancer oncology and genetic research.

1 Introduction

Interpretation of the diseased tissue is generally diagnosed by visual inspection of excised specimens under microscope. Even though this technique has been formally used for over half of century, many limitations of the technique are time consumption, interpretive variability processing artifact, and sampling error [1]. Furthermore, the understanding of the underlying biology is far from complete. Light can achieve spatial resolution that is far superior to that of other imaging modalities, including positron emission tomography (PET), single photon emission computed tomography (SPECT), computed tomography (CT), magnetic resonance imaging (MRI), and ultrasound. Recently, tremendous progress has been made in the development of microendoscopes that can be used inside the human body to directly visualize tissue *in vivo*. These advances have been made possible by significant technological advancements in flexible optical fibers, micro-optics, and compact scanning mechanisms. For instance, confocal microscope is a powerful optical imaging tool that can achieve sub-cellular resolution in real-time *in vivo*. The technique of optical sectioning provides clear images from "optically thick" biological tissues that have previously been collected with large, tabletop instruments that occupy the size of a table [2,3]. They can be used to collect either reflectance or fluorescence images to identify morphological or molecular features of cells and tissues, respectively. Moreover, images in both modalities can be captured simultaneously with complete spatial registration. This approach uses a "pinhole" placed in between the objective lens and the detector to allow only the light that originates from within a tiny focal volume below the tissue surface to be collected. For miniature instruments, the core of an optical fiber is used as the "pinhole." Recently, significant progress has been made in the development of endoscope-compatible confocal imaging instruments for visualizing inside the human body. This direction has been accelerated by the availability, variety and low cost of optical fibers, scanners, and light sources, in particular, semiconductor lasers. These methods are being developed for use in the clinic as well as in small animal imaging facilities. The addition of a miniature real-time, high resolution imaging instrument can help guide tissue biopsy and reduce pathology costs. However, these efforts are technically challenging because of the demanding performance requirements for small instrument size, high image resolution, deep tissue penetration depths, and fast frame rates. The performance parameters for miniature *in vivo* confocal imaging instruments are governed by the specific application. An important goal is the early detection and image guided therapy of disease in hollow organs, including colon, esophagus, lung, oropharynx, and cervix. Applications can also be found for better understanding of the molecular mechanisms of disease in small animals. In particular, localization of pre-malignant (dysplastic) lesions in the digestive tract can guide tissue biopsy for early

detection and prevention of cancer. In addition, visualization of over expressed molecular targets in small animal models can lead to the discovery of new drugs.

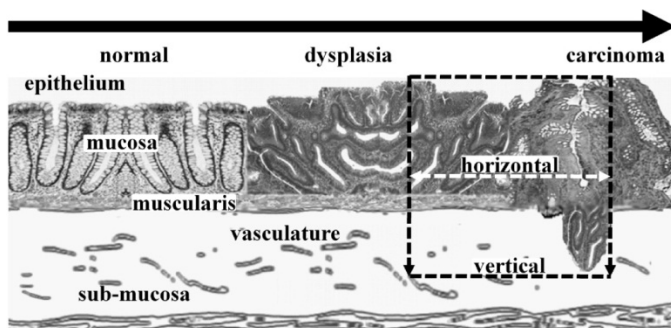


Fig. 1 Dysplasia represents a pre-malignant condition in the epithelium of hollow organs, such as the colon and esophagus. The dual axes confocal architecture has high dynamic range that is suitable for imaging in the vertical cross-sectional plane to visualize disease processes with greater tissue penetration depths.

As shown in Figure 1, dysplasia originates in the epithelium and represents an important step in the transformation of normal mucosa to carcinoma. Dysplasia has a latency period of approximately 7 to 14 years before progressing onto cancer and offers a window of opportunity for evaluating patients by endoscopy who are at increased risk for developing cancer. The early detection and localization of dysplastic lesions can guide tissue resection and prevent future cancer progression. Dysplastic glands can be present from the mucosal surface down to the muscularis. Thus, an imaging depth of $\sim 500\mu\text{m}$ is sufficient to evaluate most early epithelial disease processes. On reflectance imaging, sub-cellular resolution (typically $< 5\mu\text{m}$) is needed to identify nuclear features, such as nuclear-to-cytoplasm ratio. On fluorescence imaging, high contrast is needed to distinguish between the target and background. With both modalities, a fast imaging frame rate ($> 4\text{ Hz}$) is necessary to avoid motion artefact.

2 Single Axis Confocal Architecture

2.1 Configuration of Optics

Advances in the development of microlenses and miniature scanners have resulted in the development of fiber optic coupled instruments that are endoscope compatible with high resolution, including single [4,5,6,7,8], and multiple fiber [7,9] strategies. Different methods of scanning are also being explored [10, 11, 12, 13, 14]. All of these endoscope compatible designs use a single axis design, where the pinhole (fiber) and objective are located along one main optical axis. A high NA objective

is used to achieve sub-cellular resolution and maximum light collection, and the same objective is used for both the illumination and collection of light. In order to scale down the dimension of these instruments for endoscope compatibility, the diameter of the objective must be reduced to ~ 5 mm or less. As a consequence, the working distance (WD) as well as the field-of-view (FOV) is also decreased, as shown by the progression of the 3 different objectives in Figure 2. The tissue penetration depth also decreases, and is typically inadequate to assess the tissue down to the muscularis, which is located at a depth of $\sim 500\mu\text{m}$ and is an important landmark for defining the early presence of epithelial cancers.

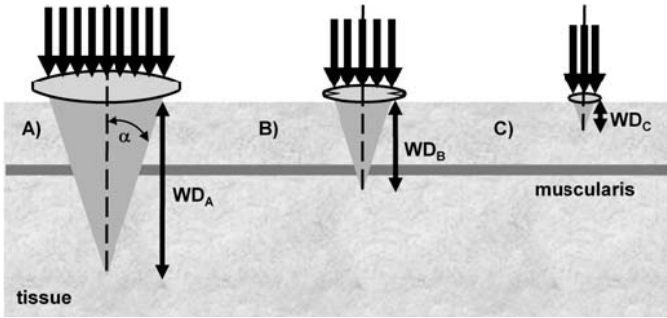


Fig. 2 For endoscope compatibility, the diameter of a single axis confocal microscope must be scaled down in size ($A \rightarrow B \rightarrow C$), resulting in a reduced working distance and limited tissue penetration depth.

2.2 Resolutions

For the conventional single axis architecture, the transverse, Δr_s , and axial, Δz_s , resolution between full-width-half-power (FWHP) points for uniform illumination of the lenses are defined by the following equations [3]:

$$\Delta z_s = \frac{0.89\lambda}{n(1 - \cos \alpha)} \sim \frac{1.78\lambda}{n\alpha^2} \quad (1)$$

where λ is the wavelength, n is the refractive index of the medium, α is the maximum convergence half-angle of the beam, $NA = n \sin \alpha$ is the numerical aperture, and $\sin \alpha \sim \alpha$ for low NA lenses. Eq. (1) implies that the transverse and axial resolution varies as $1/NA$ and $1/NA^2$, respectively. A resolution of less than $5 \mu\text{m}$ is adequate to identify sub-cellular structures that are important for medical and biological applications. To achieve this resolution in the axial dimension, the objective lens used requires a relatively large NA (> 0.4). The optics can be reduced to the millimeter scale for in vivo imaging, but requires a sacrifice of resolution, FOV, or

WD. Also, a high NA objective limits the available WD, and requires that the scanning mechanism be located in the pre-objective position, restricting the FOV and further increasing sensitivity to off-axis aberrations.

2.3 Commercial Systems

Two endoscope compatible confocal imaging systems are commercially available for clinical use. The EC-3870K (Pentax Precision Instruments, Tokyo, Japan) has an integrated design where a confocal module (Optiscan Pty Ltd, Victoria, Australia) is built into the insertion tube of the endoscope, and results in an overall diameter of 12.8 mm, as shown in Figure 3(a) [15]. This module uses the single axis optical configuration where a single mode optical fiber is aligned on-axis with an objective that has an $NA \approx 0.6$. Scanning of the distal tip of the optical fiber is performed mechanically by coupling the fiber to a tuning fork that vibrates at resonance. Axial scanning is performed with a shape memory alloy (nitinol) actuator that can translate the focal volume over a distance of 0 to 250 μm below the tissue surface. Excitation is provide at 488 nm (peak absorption of fluorescein) by a semi-conductor laser, and a transverse and axial resolution of 0.7 and 7 m, respectively, has been achieved. The images are collected at a frame rate of either 0.8 or 1.6 Hz to achieve a FOV of either 1024x1024 or 1024x512 pixels, respectively. The dimension of the confocal instrument by itself is 5 mm. When a suspicious lesion is identified, the confocal window located on the distial tip is placed into contact with the tissue to collect images. A separate instrument channel can be used to obtain pinch biopsies of tissue.

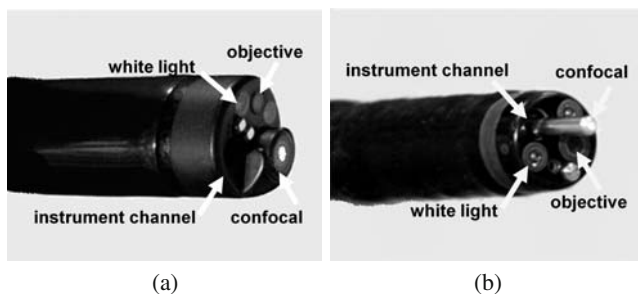


Fig. 3 (a) The EC-3870K (Pentax) has a confocal module (Optiscan) integrated into the endoscope insertion tube. (b) The Cellvizio GI is a confocal miniprobe that passes through the instrument channel of the endoscope.

The Cellvizio GI (Mauna Kea Technologies, Paris, France) uses a set of miniprobes that range in diameter from 1.5 to 2.5 mm, and passes through the standard instrument channel of medical endoscopes, as shown in Figure 3(b). This instrument moves independently of the endoscope, and its placement onto the tissue surface can be guided by the conventional white light image [8,15]. This miniprobe consists of a fiber bundle with 30,000 individual fibers that is aligned on-axis with

an objective that has an $NA \approx 0.6$. The core of each individual fiber acts as a collection pinhole to reject out-of-focus light. Scanning is performed at the proximal end of the bundle in the instrument control unit with a 4 kHz oscillating mirror for horizontal lines and a 12 Hz galvo mirror for frames. In this design, axial scanning cannot be performed. Instead, separate miniprobes that have different working distances are needed to optically section at different depths. Excitation is provided at 488 nm, and the transverse and axial resolution of these instruments ranges from 2.5 to 5 μm and 15 to 20 μm , respectively. Images are collected at a frame rate of 12 Hz with a FOV of either 600x500 μm^2 or 240x200 μm^2 .

3 Dual Axes Confocal Architecture

3.1 Configuration of Optics

From the above, the aforementioned miniaturization techniques in the previous section deploy a conventional single-axis confocal architecture that has the objective and optical fiber aligned along the same optical axis. In order to overcome some of these limitations for endoscope compatibility and in vivo imaging, we have developed the novel dual axes confocal configuration, shown in Figure 4. We use two fibers oriented along separate optical axis of different low NA objectives to spatially separate the light paths for illumination and collection [16, 17]. The region of overlap between the two beams (crossed at a half angle from the midline) defines the focal volume, hence the resolution, and can achieve sub-cellular dimensions. A very low probability exists for light scattered by tissue along the illumination path (blue cone) to enter the low NA collection objective (green cone), thus significant improvement in the dynamic range of detection can be achieved.

Furthermore, the low NA objectives enable an increased working distance so that the scanning mirror can be placed on the distal (tissue) side of the lens (post-objective position), resulting in less sensitivity to off-axis aberrations [17]. In this configuration, the beams always pass through the low NA objectives on axis, resulting in a diffraction-limited focal volume that can then be scanned over a large FOV, limited by the performance of the scanner rather than by the optics. This design feature allows for the instrument to be scaled down in size to millimeter dimensions for compatibility with medical endoscopes without loss of performance. We first develop the theory to explain the unique performance features of the dual axes confocal architecture by characterizing the point-spread function (PSF) and dynamic range. Then, we demonstrate the scaled down implementation of this configuration in miniature prototypes. Because of the challenges of packaging in such a small form factor, we first demonstrate a handheld (10 mm diameter) instrument and then an endoscope-compatible (5.5 mm diameter) prototype, using the same MEMS mirror and scanhead optics.

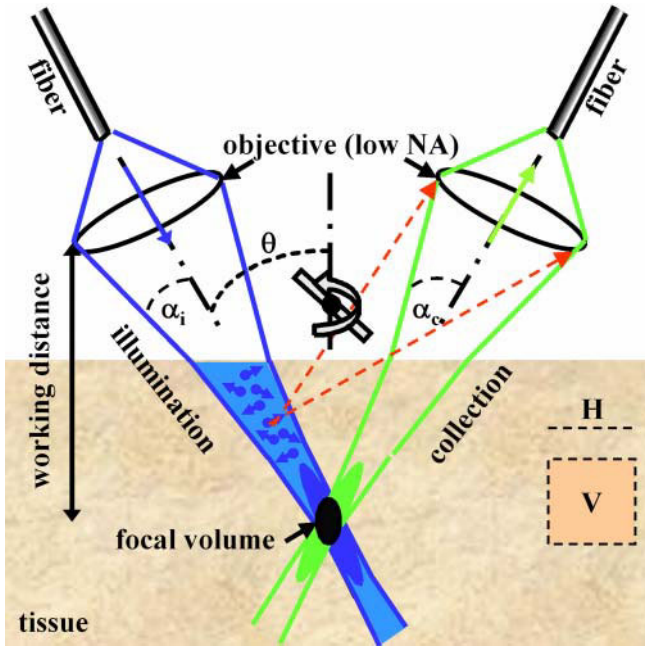


Fig. 4 Novel dual axes confocal architecture uses separate optical fibers and low NA lenses for off-axis light collection, achieving long working distance, high dynamic range, and scalability while preserving resolution.

3.2 Coordinates Definition

The coordinates for the dual axes confocal configuration are shown in Figure 5. The illumination (IO) and collection (CO) objectives represent separate low NA lenses. The maximum convergence half-angles of the illumination and collection beams are represented by α_i and α_c , respectively. The separate optical axes are defined to cross the z-axis (z_d) at an angle θ . The main lobe of the PSF of the illumination objective is represented by the light gray oval. This lobe has a narrow transverse but a wide axial dimension.

Similarly, the main lobe of the PSF of the collection objective is similar in shape but symmetrically reflected about z_d , as represented by the dark gray oval. For dual axes, the combined PSF is represented by the overlap of the two individual PSF's, represented by the black oval. This region is characterized by narrow transverse dimensions, Δx_d and Δy_d (out of the page), and by a significantly reduced axial dimension, Δz_d , which depends on the transverse rather than the axial dimension of the individual beams where they intersect.

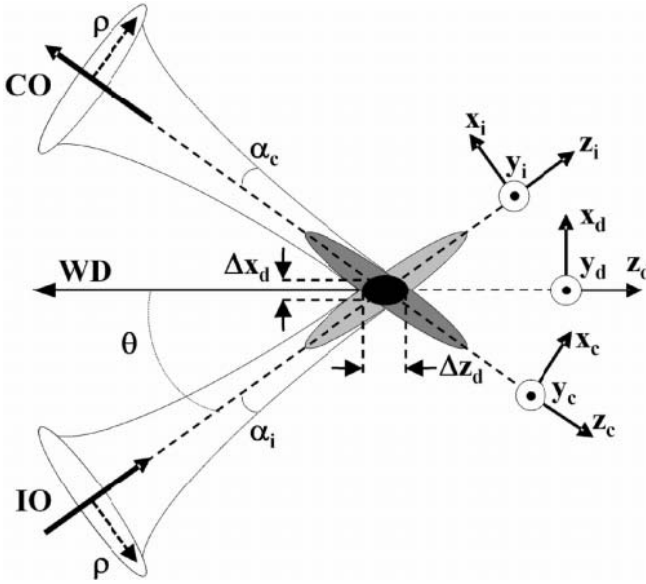


Fig. 5 Coordinates for dual axes confocal configuration.

3.3 Point Spread Function

The dual axes PSF can be derived using diffraction theory with paraxial approximations [18]. The coordinates for the illumination (x_i, y_i, z_i) and collection (x_c, y_c, z_c) beams are defined in terms of the coordinates of the main optical axis (x_d, y_d, z_d) , and may be expressed as follows:

$$\begin{aligned}
 x_i &= x_d \cos \theta - z_d \sin \theta & x_c &= x_d \cos \theta + z_d \sin \theta \\
 y_i &= y_d & y_c &= y_d \\
 z_i &= x_d \sin \theta + z_d \cos \theta & z_c &= -x_d \sin \theta + z_d \cos \theta
 \end{aligned} \tag{2}$$

The maximum convergence half-angles of the focused illumination and collection beams in the sample media are represented as α_i and α_c , respectively. The angle at which the two beams intersect the main optical axis is denoted as θ . A set of general dimensionless coordinates may be defined along the illumination and collection axes, as follows [19]:

$$\begin{aligned}
 u_i &= k_i n z_i \sin^2 \alpha_i & u_c &= k_c n z_c \sin^2 \alpha_c \\
 v_i &= k_i n \sqrt{x_i^2 + y_i^2} \sin \alpha_i & v_c &= k_c n \sqrt{x_c^2 + y_c^2} \sin \alpha_c
 \end{aligned} \tag{3}$$

The wave numbers for illumination and collection are defined as $k_i = 2\pi/\lambda_i$ and $k_c = 2\pi/\lambda_c$, respectively, where λ_i and λ_c are the wavelengths, and n is the index of refraction of the media. The amplitude PSF describes the spatial distribution of the electric field of the focused beams. Diffraction theory may be used to show that the PSF of the illumination and collection beams is proportional to the Huygens-Fresnel integrals below [18]:

$$U_i(v_i, u_i) \propto \int_0^1 W_i(\rho) J_0(\rho v_i) e^{-ju_i \rho^2/2} \rho d\rho \quad (4)$$

$$U_c(v_c, u_c) \propto \int_0^1 W_c(\rho) J_0(\rho v_c) e^{-ju_c \rho^2/2} \rho d\rho \quad (5)$$

where J_0 is the Bessel function of order zero, and ρ is a normalized radial distance variable at the objective aperture. The weighting function, $W(\rho)$, describes the truncation (apodization) of the beams. For uniform illumination, $W(\rho) = 1$. For Gaussian illumination, the objectives truncate the beams at the $1/e^2$ intensity, resulting in a weighting function of $W(\rho) = e^{-\rho^2}$. In practice, the beams are typically truncated so that 99 % of the power is transmitted. For a Gaussian beam with a radius ($1/e^2$ intensity) given by w , an aperture with diameter πw passes 99 % of the power. In this case, the weighting function is given as follows:

$$W(\rho) = e^{-\pi\rho^2/2} \quad (6)$$

For the single axis configuration, the illumination and collection PSF's at the focal plane ($u_i = u_c = 0$) are identical functions of the radial distance ρ , and can both be given by U_s using the substitution $v = knr \sin \alpha$, as follows:

$$U_s(v) \propto \int_0^1 W_i(\rho) J_0(\rho v) \rho d\rho \quad (7)$$

The resulting signal at the detector V from a point source reflector in the media is proportional to the power received, and is given by the square of the product of the overlapping PSF's as follows:

$$V = A |U_i U_c|^2 \quad (8)$$

where A is a constant.

Similarly, since the depth of focus for each individual beam, described within the exponential term in the integral product of Eqs. (3) and (4), is much larger than that of the transverse width, the exponential term may be neglected. As a result, the detector output v_d for the dual axes configuration for uniform illumination ($W = 1$), is given as follows:

$$U_s(v) \propto \int_0^1 W_i(\rho) J_0(\rho v) \rho d\rho \quad (9)$$

This expression can be combined with Eqs. (2) and (3) to derive the result for transverse and axial resolution with uniform illumination as follows [16]:

$$V_d \propto \left(\frac{2J_1(v_i)}{v_i} \right)^2 \left(\frac{2J_1(v_c)}{v_c} \right)^2 \quad (10)$$

$$\Delta x_d = \frac{0.37\lambda}{n\alpha \cos \theta}; \Delta y_d = \frac{0.37\lambda}{n\alpha}; \Delta z_d = \frac{0.37\lambda}{n\alpha \sin \theta}; \quad (11)$$

Note that for the dual axes configuration, the axial resolution is proportional to $1/NA$, where $NA = n \sin \alpha \approx n\alpha$, rather than $1/NA^2$, as is the case for the single axis design [3]. For example, with uniform illumination and the following parameters: $\alpha = 0.21$ radians, $\theta = 30^\circ$, $\lambda = 0.785\mu\text{m}$ and $n = 1.4$ for tissue, Eq. (10) reveals a result for the dual axes configuration of $\Delta x_d = 1.1\mu\text{m}$, $\Delta y_d = 1.0\mu\text{m}$, and $\Delta z_d = 2\mu\text{m}$ for the transverse and axial resolutions, respectively. Thus, sub-cellular resolution can be achieved in both the transverse and axial dimensions with the dual axes configuration using low NA optics but not with the single axis architecture. For an endoscope-compatible instrument, delivery of the illumination and collection light is performed with use of optical fibers and is more appropriately modeled by a Gaussian rather than a uniform beam. With this apodization, the detector response for the dual axes configuration from a point source reflector in the media, given by Eq. (9), may be solved numerically as a function of transverse (x_d and y_d) and axial (z_d) dimensions. The integrals are calculated in Matlab, and use the weighting function with 99 % transmission. In comparison, this model reveals a result of $\Delta x_d = 2.4\mu\text{m}$, $\Delta y_d = 2.1\mu\text{m}$, and $\Delta z_d = 4.2\mu\text{m}$ for the transverse and axial resolutions, respectively. Thus, the use of optical fibers, modeled by a Gaussian beam, produces results that are slightly worse but still comparable to that of uniform illumination [19].

3.4 Dynamic Range

Differences in the dynamic range between the single and dual axes confocal configurations can also be illustrated with this model [18]. The calculated axial response for the single axis design with Gaussian illumination is shown by the dashed line in Figure 6(a), where optical parameters are used that achieve the same axial resolution (FWHM) of $4.2\mu\text{m}$. The result reveals that the main lobe falls off in the axial (z -axis) direction as $1/z^2$, and reaches a value of approximately -25 dB at a distance of $10\mu\text{m}$ from the focal plane ($z = 0$). In addition, a number of side lobes can be appreciated.

In comparison, the response for the dual axes configuration, shown by the solid line in Figure 6(a), reveals that the main lobe rolls off in the axial (z -axis) direction as \exp^{-kz^2} , and reaches a value of -60 dB at a distance of $10\mu\text{m}$ from the focal plane ($z = 0$). Thus, off-axis illumination and collection of light in the dual axes architecture results in a significant improvement in dynamic range and in an exponential rejection of out-of-focus scattered light in comparison to that for single axis.

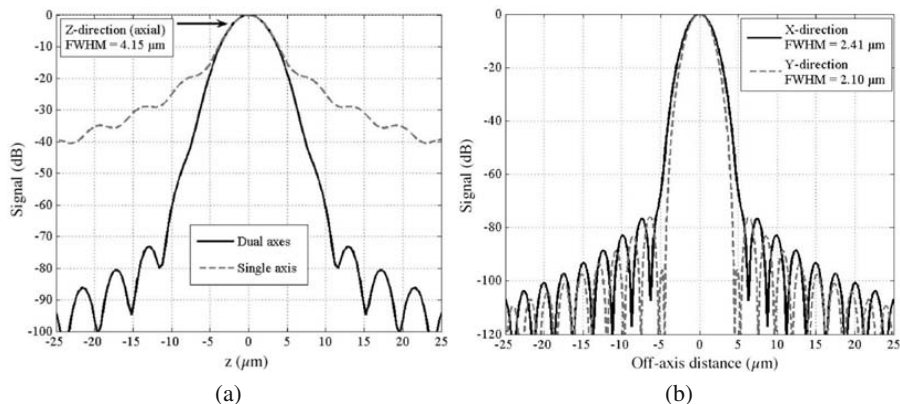


Fig. 6 Dynamic range of novel dual axes confocal architecture. a) The axial response of the single axis (dashed line) configuration falls off as $1/z^2$ and that for the dual axes (solid line) design falls off as \exp^{-kz^2} , resulting in a significant improvement in dynamic range, allowing for vertical cross-sectional imaging to be performed. b) Transverse (X-Y direction) response.

This advantage allows for the dual axes configuration to collect images with deeper tissue penetration and with a vertical cross-section orientation. The transverse response with Gaussian illumination is shown in Figure 6(b).

3.5 Post-objective Scanning

In confocal microscopes, scanning of the focal volume is necessary to create an image. In the single axis architecture, the high NA objectives used limit the working distance, thus the scan mirror is by convention placed on the pinhole (fiber) side of the objective, or in the pre-objective position, as shown in Figure 7(a). Scanning

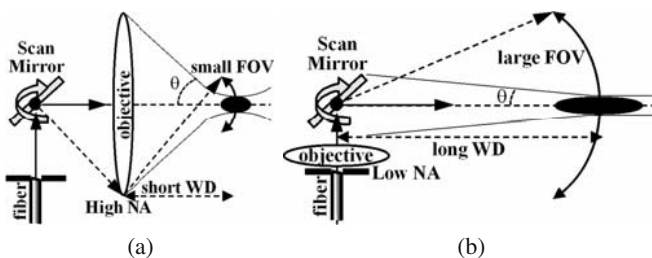


Fig. 7 a) For pre-objective scanning, illumination light is incident on the objective off-axis, resulting in more sensitivity to aberrations and limited FOV. b) With post-objective scanning, the incident light is on-axis, less sensitivity to aberrations, and large FOV. Post-objective scanning is made possible by the long WD produced by the low NA objectives used in the dual axes architecture.

orients the beam at various angles to the optical axis and introduces off-axis aberrations that expand the focal volume. In addition, the FOV of pre-objective scanning systems is proportional to the scan angle and the focal length of the objective. The diameter of the objective limits the maximum scan angle, and as this dimension is reduced for endoscope compatibility, the focal length and FOV are also diminished. In the dual axes configuration, the low NA objectives used creates a long working distance that allows for the scanner to be placed on the tissue side of the objective, or in the post-objective position [17]. This design feature is critical for scaling the size of the instrument down to millimeter dimensions for in vivo imaging applications without losing performance. As shown in Figure 7(b), the illumination light is always incident on-axis to the objective. In the post-objective location, the scan mirror can sweep a diffraction-limited focal volume over an arbitrarily large FOV, limited only by the maximum deflection angle of the mirror. Moreover, the scanner steers the illumination and collection beams together with the intersection of the two beams oriented at a constant angle and with the overlapping focal volume moving without changing shape along an arc-line. This property can be conceptualized by regarding the dual axes geometry as being equivalent to two separate beams produced from two circles in the outer annulus of a high NA lens containing a central obstruction (or a large central hole). A flat scan mirror deflects both beams equally, and thereby preserves the overlapping region without introducing aberrations to the beams.

3.6 Improved Rejection of Scattering

In the dual axes confocal architecture, the off-axis collection of light significantly reduces the deleterious effects of tissue scattering on the dynamic range of detection and allows for deeper ballistic photons to be resolved [20]. These features provide the unique capacity to collect vertical cross-sectional images in the plane perpendicular to the tissue surface. This is the preferred view of pathologists because differences from the normal patterns of tissue differentiation are revealed in the direction from the lumen to the sub-mucosa.

3.6.1 Optical Configurations

The improvement in rejection of light scattered by tissue can be illustrated by comparing the dynamic range of detection between the single and dual axes optical configurations with equivalent axial resolution, as shown in Figure 8(a) and 8(b). The incident beams are modeled with a Gaussian profile because this is representative of light delivered through an optical fiber. For the single axis configuration, this beam is focused into the tissue by an ideal lens (L1). A mirror (M) is embedded in the tissue at the focal plane (parallel to the x-y plane) of the objective lens. In this scheme, the rays that reflect from the mirror pass back through the lens L1,

deflect at an angle off the beam splitter, and are focused by an ideal lens (L2) on to a pinhole detector. For the dual axes set-up, the incident Gaussian beam is focused into the tissue by an ideal lens (L3) with its axis oriented at an angle $\theta = 30^\circ$ to the z-axis, and an ideal lens (L4) focuses the backscattered beam, with its axis z at an angle -30° to the z-axis, onto the pinhole detector. As before, a mirror (M) with its plane perpendicular to the z-axis and passing through the coincident focuses of the lenses is embedded in the tissue to reflect the incident light to the detector. In both configurations, the lens system has a magnification of 1 from the focal plane to the pinhole detector.

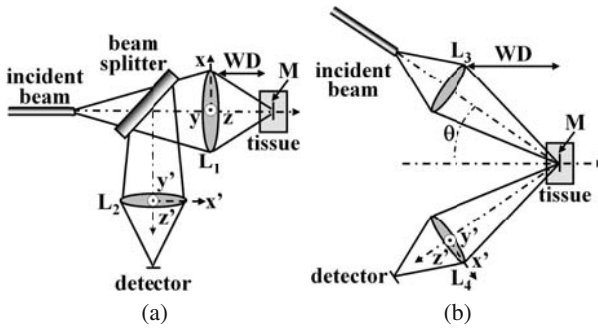


Fig. 8 a) Single axis and b) dual axes optical configurations are used to evaluate the axial response at the detector.

In order to achieve an equivalent -3 dB axial resolution (FWHM), the NA's for the single and dual axes configurations are defined to be 0.58 and 0.21, respectively. From diffraction theory, discussed above, the theoretical transverse and axial resolutions for the PSF for dual axes at a wavelength $\lambda_0 = 633\text{nm}$ with an average tissue refractive index of 1.4 and $\text{NA} = 0.21$ are found to be $\Delta x = 1.16\mu\text{m}$, $\Delta y = 1.00\mu\text{m}$, and $\Delta z = 2.00\mu\text{m}^3$. The mirror is placed at a distance of $200\mu\text{m}$ below the tissue surface in the focal plane of the objective lenses for both the single and dual axes configurations. This depth is representative of the imaging distance of interest in the epithelium of hollow organs. The calculations performed to analyze the effects of tissue scattering on light are based on Monte Carlo simulations using a non-sequential ray tracing program (ASAP 2006 Breault Research Organization, Tucson, AZ). Three assumptions are made in this simulation study: 1) multiple scattering of an incoherent beam dominates over diffraction effects, 2) the non-scattering optical medium surrounding the lenses and the tissue (the scattering medium) is index matched to eliminate aberrations, and 3) absorption is not included to simplify this model and because there is much larger attenuation due to the scattering of ballistic photons.

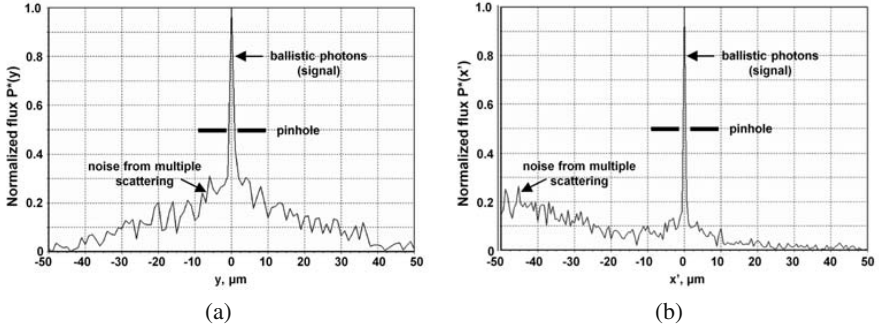


Fig. 9 Distributions of photon flux in tissue scattering model. The peak value of multiple scattered photons for A) single axis is co-located with the confocal pinhole while that for B) dual axes is separated by $\sim 50\mu m$. As a consequence, the ballistic photons for dual axes result in a greater signal-to-noise ratio.

3.6.2 Mie Scattering Analysis

We use Mie theory with the Henyey-Greenstein phase function $p(\theta)$ to model the angular dependence of tissue scattering, as follows [21,22]:

$$p(\theta) = \frac{1}{4\pi} \frac{1 - g^2}{(1 + g^2 - 2g \cos \theta)^{3/2}} \quad (12)$$

where g , the anisotropy factor, is defined as

$$g = \langle \cos \theta \rangle = \int_0^{2\pi} \int_0^\pi \cos(\theta) \cdot p(\theta) \sin \theta d\theta d\phi \quad (13)$$

Given the average scatterer size, refractive index, and concentration, the attenuation coefficient μ_s and anisotropy g are determined and provided to the ASAP program as simulation parameters. For a tissue phantom composed of polystyrene spheres with a diameter of $0.48 \mu m$, refractive index 1.59, and a concentration of $0.0394 \text{ spheres}/\mu m^3$ in water, the values $g = 0.81$ and $\mu_s = 5.0 \text{ mm}^{-1}$ at $\lambda = 633 \text{ nm}$ are calculated from Mie theory [23]. For single axis, $P(y')$ is defined as the photon flux distribution along the y' -axis at the detector. The photon flux can be normalized by defining $P^*(y') = P(y')/P_{max}$, where P_{max} is the maximum flux. The normalized flux $P^*(y')$ consists of ballistic (signal) and multiple scattered (noise) photons, as shown in Figure 9(a) [24]. The maximum flux for both the signal and noise components arrive at center of the detector. A confocal pinhole placed in front of the detector can filter out some but not all of this "noise," resulting in a reduced signal-to-noise ratio (SNR). For dual axes, the detector is angled off the optical axis by 30° . $P(x')$ is defined as the photon flux distribution along the x' -axis at the detector. The photon flux can be normalized by defining $P^*(x') = P(x')/P_{max}$, where P_{max} is the maximum flux at the detector. Figure 9(b) shows that normalized photon flux distribution for dual axes also exhibits a ballistic and multiple scattered components.

However, for dual axes, the peak flux of multiple scattered photons arrives $\sim 50\mu\text{m}$ lateral to the center of the detector where the ballistic photons arrive, a consequence of off-axis collection. Thus, there is much less "noise" for the confocal pinhole (diameter $1\mu\text{m}$) to filter out, resulting in a higher SNR and dynamic range.

3.6.3 Improvement in Dynamic Range

An implication of this result is that the dual axes configuration has improved dynamic range compared to that of single axis. This difference can be quantified by determining the axial response at the detector. This can be done by calculating the photon flux $f(\Delta z)$ as the mirror is displaced along the z -axis in the tissue. The flux is calculated using Monte-Carlo simulations in ASAP with the mirror at positioned in the range $-10\mu\text{m} \leq \Delta z \leq 10\mu\text{m}$ with respect to the focal plane at $z = 0$, which is located at $200\mu\text{m}$ below the tissue surface. The flux is then normalized according to $F(\Delta z) = f(\Delta z)/f(0)$. The axial response is shown in Figure 10(a) for various pinhole diameters D , including 1, 2 and $3\mu\text{m}$, which correspond to typical fiber core dimensions. Note that for each pinhole diameter, the dual axes (DA) configuration has significantly better dynamic range than that of single axis (SA). Note that the introduction of tissue scattering results in a reduction of the dynamic range compared to that found in free space, as shown by Figure 6(a).

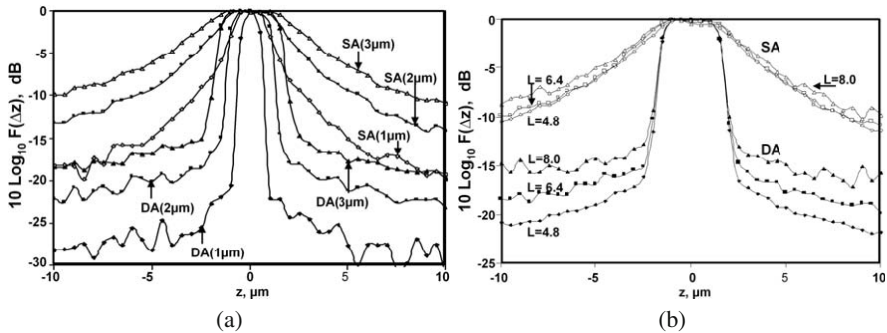


Fig. 10 Axial response for single and dual axes geometries. The dual axes (DA) configuration has a much greater dynamic range than that for single axis (SA) given different a) pinhole diameters (1, 2, and 3 m) and b) optical lengths L (4.8, 6.4 and 8.0).

We can also determine the axial response of the detector for various optical lengths in tissue. This analysis reveals differences in the dynamic range between the single and dual axes configuration for tissues with various scattering properties. The total optical length L is defined as twice the product of the scattering coefficient s and the tissue depth t , or $L = 2\mu_s t$. The factor of two originates from the fact that the total path length is twice the tissue depth. The axial response is shown in Figure 10(b) for various optical lengths L , including 4.8, 6.4, and 8.0. Note that for each optical length L , the dual axes (DA) configuration has significantly better

dynamic range than that of single axis (SA). These values of L are typical parameters of gastrointestinal epithelium. At $\lambda = 633nm$, s is about $7mm^{-1}$ for esophagus tissue [24] and about $20mm^{-1}$ for normal colon mucosa [25]. The range of tissue depths spanned by $L = 4.8$ to 8 for esophagus and colon is $340 \mu m$ to $570 \mu m$ and $120 \mu m$ to $200 \mu m$, respectively. In addition, these results shows that for single axis only minimal changes occur in the dynamic range with approximately a factor of 2 difference in optical thickness L , while for dual axes significant changes occur over this thickness range. Furthermore, scattering does not appear to alter the FWHM of the axial response for either single or dual axes over this range of lengths.

3.6.4 Geometric Differences Produced by Off-Axis Detection

The superior axial response of the dual axes confocal architecture has a simple geometric explanation. When the mirror moves away from the focal plane by Δ , the centroid of the beam is steered away from the optical axis by $2\Delta \sin \theta$ from where the center of the pinhole is located [20]. Even taking into consideration diffraction and the broadening of the out-of-focus beam, the beam intensity decreases exponentially when $\Delta \geq D/2$ (for $\theta = 30^\circ$). But in the single axis case, many of the photons scattered near the vicinity of the focal plane (Δ) are collected by the detector through the pinhole. Thus, the spatial filtering effect by a pinhole for the single axis configuration is not as effective as that for dual axes. The implication of this effect for imaging deep in tissue is evident. In the single axis case, many of the multiple scattered photons that arrive from the same direction as that of the ballistic photons, starting from the surface to deep within the tissue, are collected by the detector despite the presence of a pinhole to filter the out-of-focus light. This explains why in Figure 9(a) the single axis configuration has a large noise component alongside the ballistic component. Thus, the dual axes confocal architecture provides optical sectioning capability that is superior to that of the conventional single axis design in terms of SNR and dynamic range, and this result can be generalized to a range of relevant pinhole sizes. As a result, the dual axes architecture allows for imaging with greater tissue penetration depth, thus is capable of providing images in the vertical cross-section with high contrast. The implementation of the dual axes confocal configuration to an endoscope compatible instrument for collection of both reflectance and fluorescence has significant implications for in vivo imaging by providing both functional and structural information deep below the tissue surface.

4 Tabletop Dual Axes Confocal Imaging Instruments

The dual axes confocal architecture was first implemented as a tabletop instrument using readily available optical components to demonstrate the proof of concept of off-axis illumination and collection with post-objective scanning. In particular, the primary advantages of the dual axes configuration including high dynamic range and

deep tissue penetration are revealed by vertical cross-sectional images with either reflectance or fluorescence. The combination of these two imaging modes forms a powerful strategy for integrating structural with functional information. The dual axes optical design incorporates a solid immersion lens (SIL) made from a fused-silica hemisphere at the interface where the two off-axis beams meet the tissue. This refractive element minimizes spherical aberrations that occur when light undergoes a step change in refractive index between two media. The curved surface of the SIL provides a normal interface for the two beams to cross the air-glass boundary. Fused silica is used because its index of refraction of $n = 1.45$ is closely matched to that of tissue. Note that as the beams are scanned away from their neutral positions, they will no longer be incident to the surface of the SIL and small aberrations will occur. Another feature of the SIL is that its curved surface increases the effective NA of the beams in the tissue by a factor of n , the index of refraction, and produces higher resolution and light collection efficiency. On the other hand, the SIL acts to reduce the scanning displacement of the beams in the tissue by a factor of $1/n$ so that larger deflections are needed to achieve the desired scan range.

4.1 Horizontal Cross-Sectional Imaging Instrument

Reflectance imaging takes advantage of subtle differences in the refractive indices of tissue micro-structures to generate contrast. The backscattered photons can provide plenty of signal to overcome the low NA objectives used for light collection in the dual axes configuration. The first reflectance images were collected with a

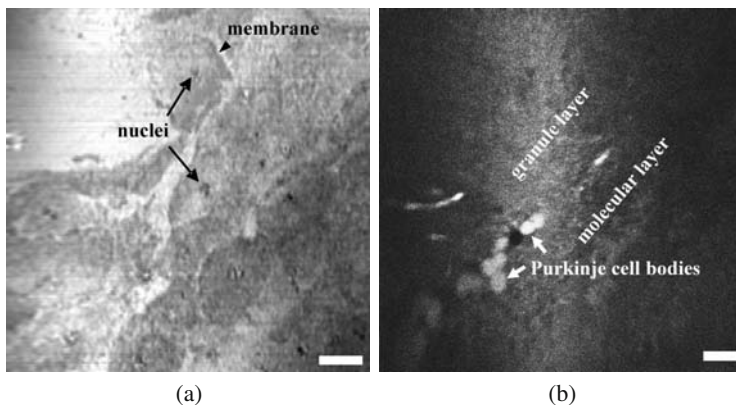


Fig. 11 Horizontal cross-sectional dual axes images ex vivo. a) Squamous esophageal mucosa collected at $z = 0 \mu\text{m}$ with $\lambda = 488 \text{ nm}$ reveals sub-cellular features, including cell nuclei (arrows) and membrane (arrowhead), scale bar $20 \mu\text{m}$. b) Normal colonic mucosa at $z = 150 \mu\text{m}$ with $\lambda = 1.3 \mu\text{m}$ illumination reveals circular crypts with colonocytes surround the lumen and lamina propria (LP) filling space in between the crypts, scale bar $50 \mu\text{m}$.

tabletop system that used a 488 nm semiconductor laser that delivered illumination into a single mode optical fiber that was focused by a set of collimating lenses with $NA = 0.16$ to a spot size with $\sim 400\mu W$ of power [16]. These parameters produced a transverse and axial resolution of 1.1 and 2.1 μm , respectively. The reflected light was collected by a complementary set of optics. The off-axis illumination and collection was performed at $\theta = 30^\circ$ to the main optical axis. Reflectance images were collected in horizontal cross-sections of freshly excised specimens of esophagus *ex vivo*. As shown in Figure 4.1(a), the cell membrane and individual nuclei of squamous (normal) esophageal mucosa can be appreciated in the image collected at $z = 0 \mu m$, scale bar 20 μm . Much greater image contrast can be achieved with fluorescence imaging where the use of optical reporters, such as GFP, and exogenous probes can reveal over expression of molecular targets. The same tabletop dual axes microscope was also used to collect fluorescence images with a long pass filter to block the excitation light and photomultiplier tube (PMT) for detection [26]. In Figure 4.1(b), a fluorescence image of the cerebellum of a transgenic mouse that constitutively expresses GFP under the control of a β -actin promoter at a depth of $z = 30 \mu m$ is shown, scale bar 50 μm . Purkinje cell bodies (arrows) can be seen as large round structures aligned side by side in a row, separating the granule layer and the molecular layer.

4.2 Vertical Cross-Sectional Imaging Instrument

4.2.1 Reflection Imaging Mode

In order to collect vertical cross-sectional images, heterodyning can be used to provide a coherence gate that filters out illumination photons that are multiply-scattered and travel over longer optical paths within the tissue [17]. This approach is demonstrated with a fiber optic Mach-Zehnder interferometer, shown in Figure 4.2(a). A broadband near-infrared source produces light centered at $\lambda_0 = 1345nm$ with a 3 dB bandwidth of 35 nm and a coherence length in tissue of $\sim 50\mu m$. A fiber coupler directs $\sim 99\%$ of the power to the illumination path, which consists of a single mode optical fiber (SMF1) with a collimating (CL1) and focusing lens (FL1) with $NA = 0.186$. The axes of illumination and collection are oriented at $\theta = 30^\circ$ to the midline. Light reflected from the tissue is collected by the second set of focusing (FL2) and collimating (CL2) lenses into another single mode fiber (SMF2). The lens and fiber parameters are the same for both the illumination and collection beams. The fiber optic coupler directs $\sim 1\%$ of the source into a reference beam which is frequency shifted by an acousto-optic modulator at 55 MHz for heterodyne detection. An adjustable optical delay is used to increase the signal by matching the optical path length of the reference beam to that of the ballistic photons. An adjustable optical delay is used to increase the signal. In addition, a polarization controller consisting of two half-wave plates and a single quarter-wave plate is used to maximize the signal. The reference and collection beams are combined by a 50/50

coupler and the resulting heterodyne signal is detected by a balanced InGaAs detector (D1, D2) with a bandwidth of 80 MHz. The resulting electronic signal is then processed with a band pass filter (BPF) with a 3 MHz bandwidth centered at 55 MHz, then demodulated (DM), digitized by a frame grabber (FG), and displayed (D). In this heterodyne detection scheme, the reference beam essentially provides amplification of the weak collection beam via coherent optical mixing, and enables the measurement of reflected light with a dynamic range larger than 70 dB. Post-objective scanning is performed with the scan mirror (SM) placed distal to the objective lenses. Reflectance images were collected from fresh biopsy specimens taken from the squamo-columnar junction of subjects with Barrett's esophagus. Specimens with dimensions of $\sim 3\text{mm}$ were resected with jumbo biopsy forceps, and the mucosal surface was oriented normal to the z-axis. Vertical cross-sectional images were collected with depth of 1 mm. From Figure 12(b), squamous (normal) mucosa is present over the left half of the image with an intact epithelium (EP). The other structures of normal esophageal mucosa, including the muscularis mucosa (MM), sub-mucosa (SM), and muscularis propria (MP), can also be identified. Columnar mucosa consistent with intestinal metaplasia is seen over the right half of the image, and reveals the presence of pit epithelium (PE) [17]. These findings correlate with the tissue micro-structures seen on histology.

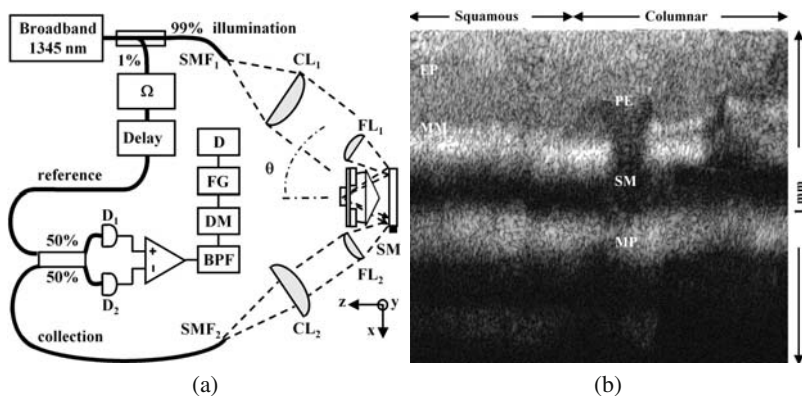


Fig. 12 Vertical cross-sectional dual axes confocal reflectance images ex vivo. a) Schematic of optical circuit for heterodyne detection, details discussed in the text. b) Reflectance image of squamo-columnar junction in esophagus with vertical depth of 1 mm. Squamous (normal) mucosa reveals epithelium (EP) and muscularis mucosa (MM) over left half. Columnar (intestinal metaplasia) mucosa shows pit epithelium (PE) over right half. Submucosa (SM) and muscularis propria (MP) are seen on both sides.

4.2.2 Fluorescence Imaging Mode

Fluorescence detection adds an entirely new dimension to the imaging capabilities of the dual axes architecture. Detection in this mode offers an opportunity to achieve much higher image contrast compared to that of reflectance and is sensitive to labeled molecular probes that can identify specific tissue and cellular targets. These features provide a method to perform functional as well as structural imaging, and allows for the study of a wide variety of molecular mechanisms. Although the use of low NA objectives in the dual axes configuration reduces the collection efficiency of the optics by a factor of $\sim NA^2$, this deficit can be overcome by the use of bright fluorophores. In order to achieve the deep tissue penetration depths possible with the off-axis collection of light, a near-infrared laser at 785 nm is used as the source and a PMT with a long pass filter to block the excitation light is used as the detector [27]. The large dynamic range ($\geq 40dB$) of the dual axes confocal architecture encountered with collection of vertical cross-sectional images requires modulation of the PMT gain to compensate for the rapid decrease in fluorescence signal with axial depth due to tissue absorption and scattering.

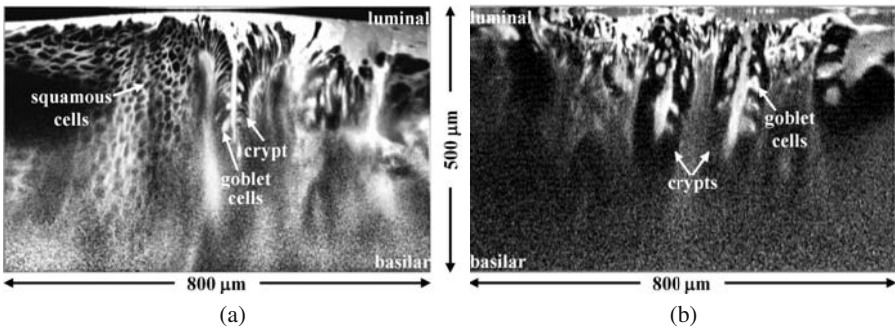


Fig. 13 Vertical cross-sectional dual axes confocal fluorescence images ex vivo. a) Squamo-columnar junction in esophagus with vertical depth of $500\ \mu\text{m}$. Squamous mucosa present over left half. Columnar (intestinal metaplasia) mucosa over right half shows crypts with goblet cells. b) Colon. Many goblet cells can be seen in dysplastic crypts from a flat colonic adenoma.

In Figure 13, vertical cross-sectional fluorescence images of a) esophagus and b) colon collected with a tabletop dual axes confocal microscope are shown [27]. These specimens were incubated with a near-infrared dye, LI-COR IRDye 800 CW NHS Ester (LI-COR Biosciences, Inc) prior to imaging after being freshly excised during endoscopy. These images were collected at 2 frames per second with a transverse and axial resolution of 2 and 3 μm , respectively. With use of post-objective scanning, a very large FOV of $800 \times 500\ \mu\text{m}^2$ deep was achieved. In Figure 13(a), the specimen was collected from the squamo-columnar junction of a patient with Barrett's esophagus. Over the left half of the image, the individual squamous cells from normal esophageal mucosa can be seen in the luminal to the basilar direction

over a depth of $500\ \mu\text{m}$. Over the right half of the image, vertically oriented crypts with individual mucin-secreting goblet cells associated with intestinal metaplasia can be appreciated as brightly stained vacuoles. This diseased condition is associated with greater than 100 fold relative risk of developing cancer in the esophagus. In Figure 13(b), the specimen was collected from a flat colonic adenoma, and the image reveals vertically oriented dysplastic crypts with individual goblet cells. Volume rendering can also be performed with the dual axes confocal microscope to illustrate three-dimensional (3D) imaging capabilities. These views are important for tracking cell movements, observing protein-protein interactions, and monitoring angiogenic development. A xenograft mouse model of glioblastoma multiforme has been developed by subcutaneously implanting 107 human U87MG glioblastoma cells in the flank of a nude mouse. Horizontal cross-sectional fluorescence images were collected with a tabletop instrument when the tumors reached $\sim 1\text{ cm}$ in size. The mice were anesthetized for the in vivo imaging session, and indocyanine green (ICG) at a concentration of $0.5\ \text{mg/ml}$ was injected intravenously to produce contrast. A skin flap overlying the tumor was exposed, and horizontal cross-sectional images were collected with a FOV of $400 \times 500\ \mu\text{m}^2$. A fluorescence image collected at $50\ \mu\text{m}$ below the tissue surface, shown in Figure 14(a), reveals that the glioblastoma has developed a dense, complex network of tortuous vasculature. A total of 400 horizontal cross-sectional images acquired at $1\ \mu\text{m}$ increments were used to generate the 3D volumetric image, shown in Figure 14(b). Volume rendering was performed using AmiraTM modeling software.

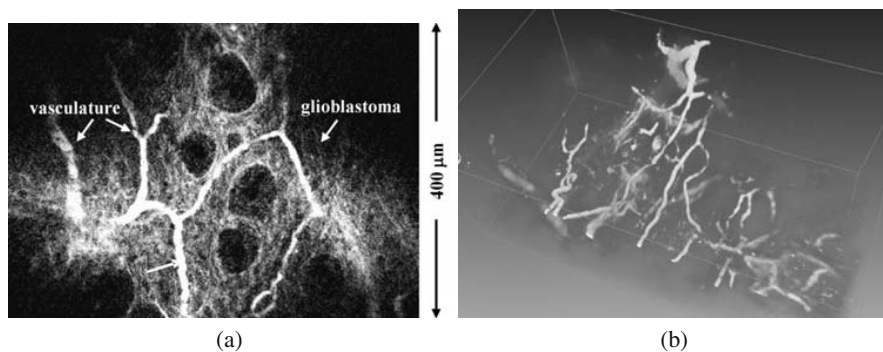


Fig. 14 Dual axes confocal fluorescence images in small animal models. a) A horizontal cross-sectional fluorescence image of a human U87MG xenograft glioblastoma tumor implanted subcutaneously in the flank of a nude mouse was collected in vivo at $50\ \mu\text{m}$ depth using i.v. indocyanine green (ICG). b) A 3D volumetric image is generated from a z-stack of 400 sections collected at $1\ \mu\text{m}$ intervals.

5 MEMS-Scanner Based Dual Axes Confocal Imaging Instruments

The long working distance created by the low NA objectives in the dual axes architecture provides space for a scanning mechanism to be placed in the post-objective position. This location is a key feature of the design that allows for scaling down of the optics to millimeter dimensions. Moreover, for in vivo imaging, a fast scan rate is needed to overcome motion artifacts introduced by organ peristalsis, heart beating, and respiratory activity, typically requiring a frame rate of > 4 per second. As a result, we have developed a MEMS-scanner based miniature and endoscope compatible imaging instruments without loss of performance. This strategy is much more complex than other approaches being developed, but is well suited to meet the size and speed requirements for in vivo imaging in a compact package [28,29].

5.1 MEMS Scanner Architecture

The schematic of the 2-D MEMS scanner is shown in Figure 15(a). It has a gimbal structure, and is electrostatically actuated by self-aligned, vertical combdrives to give large deflection. The mirror can be actuated with respect to the frame by rotating around the springs that define the inner axis. The frame supporting the mirror can be actuated with respect to the substrate by rotating around the springs that define the outer axis. Figure 2(b) shows the cross-sections of various structures of the device, which is made in double-stacked silicon-on-insulator (SOI). The two device layers are each $30\ \mu\text{m}$ thick with an oxide layer of $0.38\ \mu\text{m}$ in between. The substrate thickness is $530\ \mu\text{m}$, while the oxide layer between the lower device layer and substrate has a thickness of $1\ \mu\text{m}$. The thick device layers increase the tilt range of the mirror by deeper comb engagement, and lead to a larger FOV. The mirror, movable combteeth, and inner torsional springs are fabricated in the upper device layer. The fixed combteeth, outer torsional spring, and frame consist of double-stacked layers. A backside window is located below the gimbal structure to release the device and allow large-range motion. Four actuation voltages are supplied to the lower layer to actuate both sides of each axis (outer: V1 and V2, inner: V3 and V4, in Figure 15(a)). The upper layer and substrate are both grounded. Electrical isolation between the device layers and the substrate is provided by buried oxide layers, as seen in Figure 15(b). The double-stacked layers of the outer torsional spring and frame deliver actuation voltages and ground to the inner combdrives. Alignment of the off-axis illumination and collection are achieved with two mirrors connected together by a strut. The size of the mirrors ($600\ \mu\text{m} \times 650\ \mu\text{m}$) and the distance between them ($1.51\ \text{mm}$) enable an off-axis half-angle, θ , of 24.3° . The inner combdrives are placed on the connecting beam between the two mirrors and the inner springs are recessed into the mirror sides, to allow the die size to be reduced to $3.4\ \text{mm} \times 2.9\ \text{mm}$ to fit inside the scanhead package. The frame width is designed to be $150\ \mu\text{m}$ to prevent stress-induced curvature of the gimbal. In order to increase the torque with the same

number of combs, the moment arm is lengthened by placing the outer combdrives further away from the outer torsional spring.

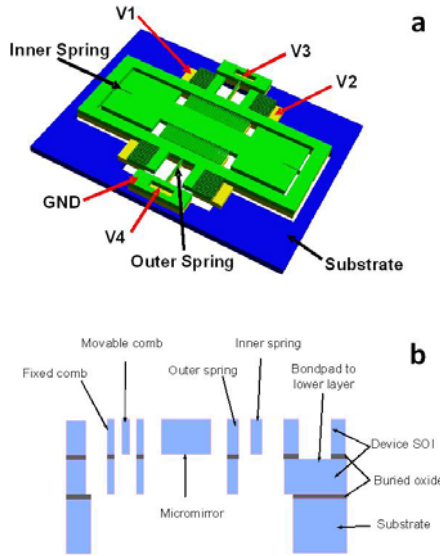


Fig. 15 (a) Schematic drawing of the 2-D MEMS scanner. (b) Cross-sectional view of various structures of the scanner.

5.2 Theoretical Analysis

The outer spring consists of two silicon device layers (each $30 \mu\text{m}$ thick) with an oxide layer ($0.38 \mu\text{m}$) in between, and delivers three different voltages to the inner frame. Its dimensions are $60.38 \mu\text{m}$ thick and $350 \mu\text{m}$ long. The inner spring consists of one silicon layer and is therefore $30 \mu\text{m}$ thick. The mechanical torque of the torsional spring can be expressed as

$$T_{\Phi}(\Phi) = k_{\Phi}\Phi, \quad (14)$$

where k_{Φ} is the torsional spring constant, and Φ is the mechanical deflection angle. Both torsional springs are rectangular, so k_{Φ} is given as follows [30].

$$k_{\Phi} = \frac{2Gtw^3}{3l} \left[1 - \frac{192w}{\pi^5 t} \tanh\left(\frac{\pi t}{2w}\right) \right] \text{ for } w \leq t, \quad (15)$$

Here G is the shear modulus given by $G = E/2(1 + \nu)$, where E is the Young's modulus, and ν is Poisson's ratio. The parameters l, w, t represent the length, width, and thickness of the spring, respectively. When an electrical voltage, V , is applied between the fixed and movable combs, the electrical torque, T_e , is given as follows.

$$T_e(\Phi, V) = NV^2 \frac{\partial C_{unit}(\Phi)}{\partial \Phi}, \quad (16)$$

Here N is the number of comb pairs, and C_{unit} is the capacitance of a comb pair. In steady-state, the mechanical torque of the spring is balanced by the electrostatic torque of the combdrives, and torques expressed by equations (13) and (15) are equal. A hybrid program which combines a 2-D finite element method (FEM) with analytical calculation [31] is used for generating the simulated DC transfer curves of Figure 16.

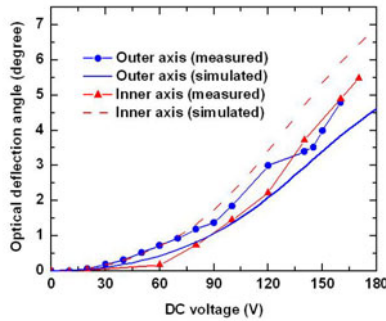


Fig. 16 Static optical deflection curve of MEMS scanner.

5.3 Device Fabrication

The design of this mirror uses a gimbal geometry to perform scanning in the horizontal (X-Y) plane, and rotation around an inner and outer axes defined by the location of the respective springs. The overall structure has a barbell shape with two individual mirrors that have active surface dimensions of $600 \times 650 \mu\text{m}^2$. A 1.51 mm long strut connects these two mirrors so that the illumination and collection beams preserve the overlapping focal volume in the tissue. The fabrication process flow, shown in Figure 17, starts with a SOI wafer composed of a silicon substrate, buried oxide, and silicon lower device layers that are 530, 0.38, and $30 \mu\text{m}$ thick, respectively [32]. A deep-reactive-ion-etch (DRIE) of coarse patterns, including the combdrives and trenches, is performed on the SOI wafer with Mask 1 (step 1). Next,

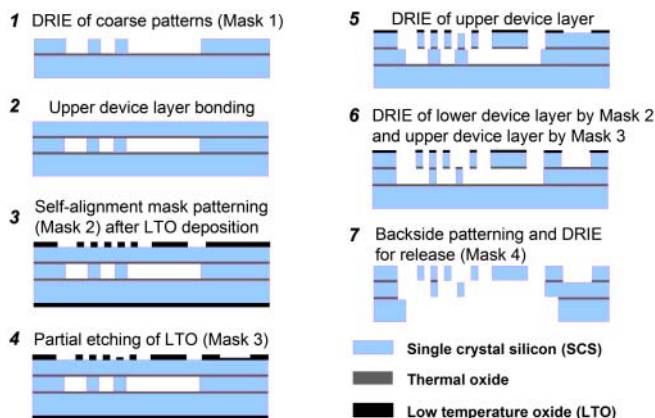


Fig. 17 MEMS scanner fabrication process flow.

an oxide layer is grown on a plain silicon wafer using a wet oxidation process. This wafer is then fusion bonded onto the etched surface of the SOI wafer (step 2). The yield is increased by bonding in vacuum, and the bonded plain wafer is ground and polished down to $30\ \mu\text{m}$ thickness, forming the upper device layer.

The two oxide layers between the silicon layers provide electrical isolation, and act as etch stops, allowing for precise thickness control. The front side of the double-stacked SOI wafer is patterned and DRIE etched to expose the underlying alignment marks in the lower device layer. Then, a low temperature oxide (LTO) layer is deposited on both sides of the wafer. The front side layer is patterned by two masks. The first mask (Mask 2) is the self-alignment mask (step 3), and is etched into the full thickness of the upper LTO layer. The second mask (Mask 3) is mainly for patterning the electrodes for voltage supplied to the lower device layer (step 4). It goes through a partial etch leaving a thin layer of LTO. The alignment accuracy of each step needs to be $> g/2$, where g is the comb gap. Since most devices have $6\ \mu\text{m}$ comb gaps, this leads to a required alignment accuracy of better than $3\ \mu\text{m}$.

Alignment accuracy ($\leq 3\ \mu\text{m}$) is important to minimize failures due to electrostatic instability during actuation. These three masks eventually define the structures in the upper, lower, and double-stacked layers. After the front side patterning is done, the LTO layer on the wafer back side is stripped (step 5). The wafer is cleaned and photoresist is deposited on the back side. Then, front side alignment marks are patterned. Next, the upper silicon layer is etched with the features of Mask 2 in DRIE. Then, a thin LTO and buried oxide layer is anisotropically dry-etched. Finally, the lower and upper silicon layers are etched (DRIE) simultaneously with features patterned by Mask 2 and 3, respectively (step 6). For backside processing, the wafer is bonded to an oxidized handle wafer with photoresist. The back side trenches are patterned with Mask 4 on photoresist (step 7). The back side trench should etch through the substrate to release the gimbal structure, so handle wafer bonding and thick resist is required for DRIE. Alignment to the front side features are

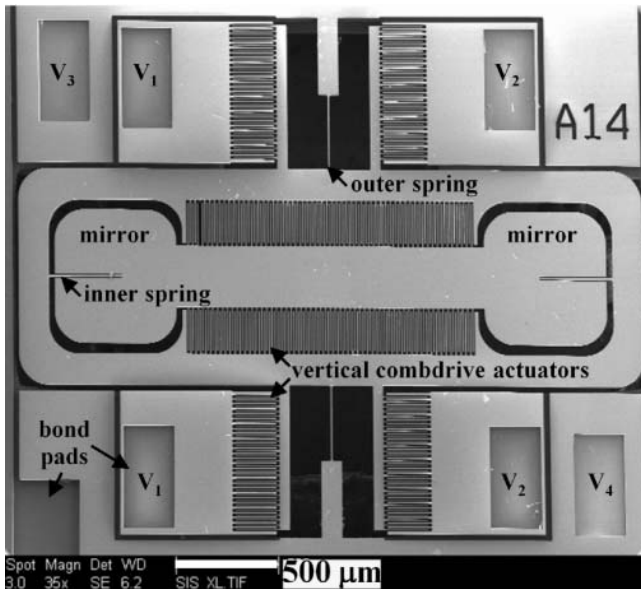


Fig. 18 SEM of 2D gimbaled MEMS scanner, scale bar 500 μm .

accomplished by aligning to the previously etched patterns. After the substrate (530 μm) is etched by DRIE, the process wafer is separated from the handle wafer with acetone. After wafer cleaning, the exposed oxide layer is directionally dry-etched from the back side. Finally, the remaining masking LTO and exposed buried oxide layer is directionally etched from the front side.

5.4 Device Characterization

The two-dimensional (2D) MEMS scanner is actuated by electrostatic vertical combdrive actuators [33]. Electrostatic actuation in each direction is provided by two sets of vertical comb actuators that generate a large force to produce sizable deflection angles. The scanning electron micrograph (SEM) of the scanner is shown in Figure 18. There are 4 actuation voltages (V_1 , V_2 , V_3 , and V_4) that power the device. The parameters of the scanner are characterized for quality control purposes prior to use in the miniature dual axes confocal microscope. First, the flatness of the mirror is measured with an interferometric surface profiler to identify micro-mirrors that have a peak-to-valley surface deformation $\leq 0.1\mu\text{m}$. The scanner is metalized with 10 nm thick aluminum (reflectivity = 67 % at 785 nm wavelength) to increase reflectivity.

The radius of curvature of the mirror is greater than 60 cm with an average surface roughness of 7 nm. Static optical deflections of 1.5° at 180 volts and 4.25° at 150

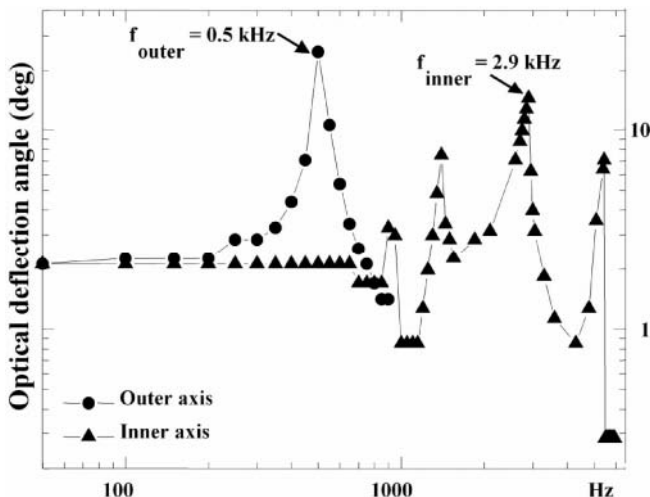


Fig. 19 Frequency response of MEMS mirror shows resonant peaks at 0.5 kHz (outer axis) and 2.9 kHz (inner axis) to achieve real time operation.

volts are achieved for the outer and inner axis, respectively. The resonant frequencies are 0.5 kHz with 10° optical angle at resonance for the outer axis and 2.9 kHz with 17° optical angle at resonance for the inner axis. The frequency response of the device is shown in Figure 19. The parametric resonances can sometimes be observed in the inner axis near frequencies of $2f_0/n$, where n is an integer ≥ 1 [34]. This phenomenon is caused by the non-linear response of the torsional combdrives, which leads to sub-harmonic oscillations.

6 Dual Axes Scanhead

6.1 Scanhead Design

The design and integration of the miniature dual axes scanhead is a very challenging part of the development of this novel imaging technique because of the small size required for compatibility with medical endoscopes. This process requires a package that allows for precise mounting of the following optical elements: 1) two fiber-coupled collimators, 2) 2D MEMS scanner, 3) parabolic focusing mirror, and 4) hemispherical index-matching solid-immersion-lens (SIL) [35]. The basic design of the miniature scanhead is shown in Figure 20. Two collimated beams are focused at an inclination angle θ to the z -axis by a parabolic mirror with a maximum cone half-angle α to an overlapping focal volume below the tissue surface after being deflected by the 2D MEMS scanner. The flat side of the SIL is placed against the tissue, and the curve surface accommodates the incident beams at normal incidence to minimize aberrations. The parabolic mirror is fabricated using a

replicated molding process that provides a surface profile and smoothness needed for diffraction-limited focusing of the two collimated beams. Once the beams are aligned parallel to each other, the parabolic mirror then provides a "self-aligning" property that forces the focused beams to intersect at a common focal point below the tissue surface. Focusing is performed primarily by the parabolic mirror which is a non-refractive optical element with an NA of 0.12. This feature allows for the optical design to be achromatic. That is, light over a broad spectral regime can be focused to the same point below the tissue surface simultaneously, allowing for future multi-spectral imaging to be performed.

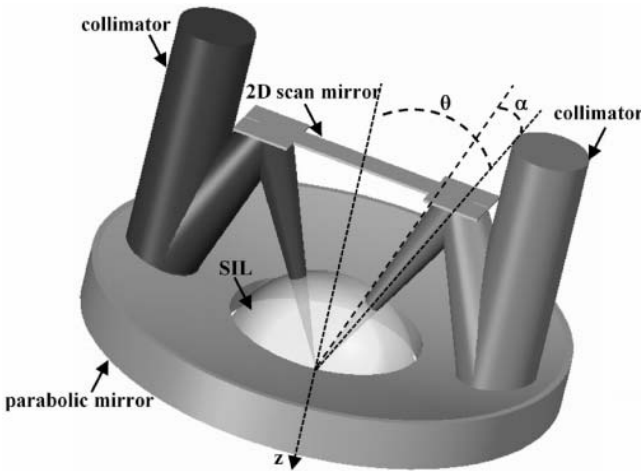


Fig. 20 Miniature dual axes scanhead. Two collimated beams that are focused by a parabolic mirror at angle θ to the z-axis for en face scanning by the 2D MEMS mirror. The solid-immersion lens (SIL) minimizes aberrations to the incident beams.

6.2 Scanhead Alignment and Packaging

Alignment of the two beams in this configuration is a key step to maximizing imaging performance. This step is accomplished by locating the two fiber-pigtailed collimators in a pair of v-grooves that are precision machined into the housing, as shown in Figure 21(a) [35]. An accuracy of 0.05° can be achieved in aligning the two beams parallel to one another using the v-grooves with pre-assembled fiber collimators. Additional precision in alignment can be attained with use of Risley prisms (optical wedges) introduced into the light paths to provide fine steering of the collimated beams to bring the system into final alignment. These prisms are angled at 0.1° , and can be rotated to steer the collimated beam in an arbitrary direction over a maximum range of $\sim 0.05^\circ$. This feature maximizes the overlap of the two beams after they are focused by the parabolic mirror. Two wedges are used in each beam

so that complete cancellation of the deflection by each can be achieved, if needed, to provide maximum flexibility.

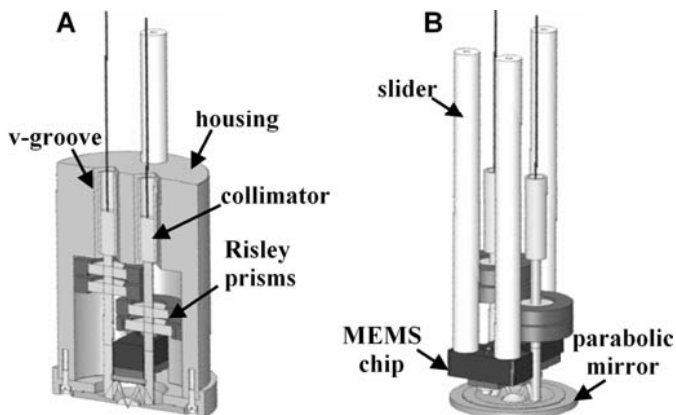


Fig. 21 Alignment and assembly of dual axes scanhead. a) Precision machined v-grooves and Risley prisms provide coarse and fine alignment, respectively, of the two beams. b) Axial (z-axis) displacement of the MEMS chip is made with a slider mechanism.

Axial (z-axis) displacement of the MEMS chip is performed with a computer-controlled piezoelectric actuator (Physik Instrumente GmbH, P-783.ZL actuator, and E-662.LR controller) that moves a slider along 3 mechanical supports, shown in Figure 21(b). This feature adjusts the imaging depths to collect a stack of en face images to produce the 3D volume rendered images. The distal end of the slider has a mounting surface to attach the printed circuit board (PCB), which supports the MEMS chip, wire bonding surfaces, and soldering terminals.

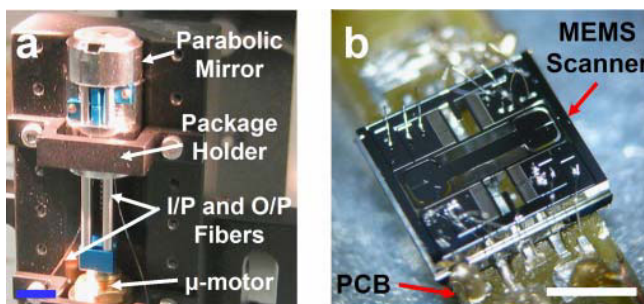


Fig. 22 a) Assembly of the dual axes confocal scanhead mounted on a V-block. b) Gimbaled 2D MEMS scanner wire bonded onto the PCB, scale bar 2 mm.

A mixture of conductive epoxy (adhesive resin ECCOBOND Solder 56 C and Catalyst 9, Emerson & Cuming, Inc.) is used to attach aluminum-1 % silicon bonding wire (Semiconductor Packaging Materials, Inc.) from the bond pads on the MEMS die to that on the PCB. Electrical power is delivered to the mirror via wires that run through the middle of the housing, and are soldered onto the PCB terminals. The z-axis translational stage consists of a closed-loop piezoelectric linear actuator. Finally, the scanhead assembly is covered and sealed from the environment using UV-curing glue to prevent inward leakage of bodily fluids. Packaging of the 10 mm diameter scanhead mounted on a V-block stage is shown in Figure 22(a). A piezoelectric micro-motor is used to perform vertical depth translation (z-axis). The MEMS scanner (die size is 3.2 (w) 2.9 (h) mm^2) mounted on the PCB is shown in Figure 22(b).

6.3 Instrument Control and Data Acquisition

Both the data acquisition and MEMS actuation systems are controlled using LabVIEWTM with Vision Acquisition software package and two National Instruments data acquisition (DAQ) boards (PXI-6711 and PXI-6115). The frequency and amplitude of the actuation signals control the frame rate and FOV of the MEMS scanner. There are 4 live and 1 ground wires that provide voltage to the device and are connected to the wirebond pads on the PCB via an ultrasonic wedge bonding technique. For each 2D en face image, the MEMS scanner is resonantly driven at 180° phase difference to maximize the linear region of the angular deflection [14, 29] around the outer axis (V1 and V2) at 1.22 kHz with a unipolar sine wave at a maximum of 70V, while rotation around the MEMS scanner inner axis (V3 and V4) is driven at 180° phase difference in the DC operational mode (5 Hz) with a unipolar sawtooth waveform at a maximum of 200 V (AgilOptics, Inc). The unipolar sawtooth waveform is smoothed at the transition edges to mitigate higher frequency ringing from the inner axis. The step size and depth scan range of the piezoelectric actuator (vertical translation) can be adjusted to optimize the acquisition of the 3D datasets. The PMT gain is synchronously adjusted to compensate for reduced light collected at increased tissue depths. Automated frame averaging and display can be performed to reduce noise and improve image quality during imaging. 2D en face images from the analog input channel are acquired and displayed in real time to enable continuous monitoring or visualization of the sample. All images are acquired in 16-bit data format. Volumetric 3D data can be rendered by post-processing using Amira software (Visage Imaging, Inc).

7 Prototype Systems

7.1 Handheld Instrument

We first developed a 10 mm diameter handheld instrument, schematic shown in Figure 23(a) [14, 29]. A semiconductor laser delivers 25 mW of light ($\lambda = 785\text{nm}$) into a single mode fiber (SMF, Fibercore Limited, SM750). The fiber terminates in a 1.8 mm diameter gradient index (GRIN) collimator (GRINTECH, GmbH). The output beam diameter ($1/e^2$) from the collimator is 0.9 mm. The half angle between the input (illumination) and output (collection) beams is 24.3° . The input beam is focused by an aluminum coated parabolic mirror (PM) with the focal length of 4.6 mm (Anteryon BV) and reflects off the first mirror surface of the MEMS scanner. The center-to-center distance between the two collimators is 3.7 mm. The focused beam continues through a fused silica SIL (hemispheric lens) until it reaches the focal plane below the tissue surface. The SIL has a refractive index (1.47) that is similar to that of the tissue and this material was chosen for index matching. The beams enter the air-silica interface at normal incidence to minimize aberrations as the focal point is scanned. Scattered light from the overlapping focal volume is collected through the optical window provided by the SIL and reflected off the MEMS mirror to the opposite surface of the parabolic mirror. The collected light is then focused onto the output fiber collimator for delivery to the PMT.

As the MEMS mirror raster scans the overlapping beams, the 2D en face image is continuously displayed on a computer monitor using a frame grabber and image acquisition software. Intensity mapping of each 2D en face image is performed by reading the MEMS scanner driving voltages and estimating focal beam trajectory. A 3D volumetric stack is created with post-processing and rendering a series of 2D en face images. Each 3D volumetric image is obtained by translating the MEMS scanner with the piezoelectric micro-motor in the z-direction under computer-control. Imaging can be performed in reflectance or fluorescence mode by inserting a 790 nm long pass optical filter (LP-02-785RU-25, Semrock, Inc.) in the collection path for the latter case. The maximum output laser power on the sample is 2 mW. A photograph of a fully-packaged miniature dual axes confocal microscope is shown in Figure 23(c).

7.2 Endoscope-Compatible Instrument

We scale down the basic design of the 10 mm diameter handheld instrument to develop the 5.5 mm endoscope-compatible version, shown in Figure 24 [36]. This prototype uses the same replicated parabolic focusing and MEMS mirrors as that employed in the larger prototype. A pair of smaller (1 mm) diameter fiber-coupled GRIN collimator lenses is used in the smaller version. Alignment is provided by a pair of 1 mm diameter rotating wedges (Risley prisms), which are inserted into

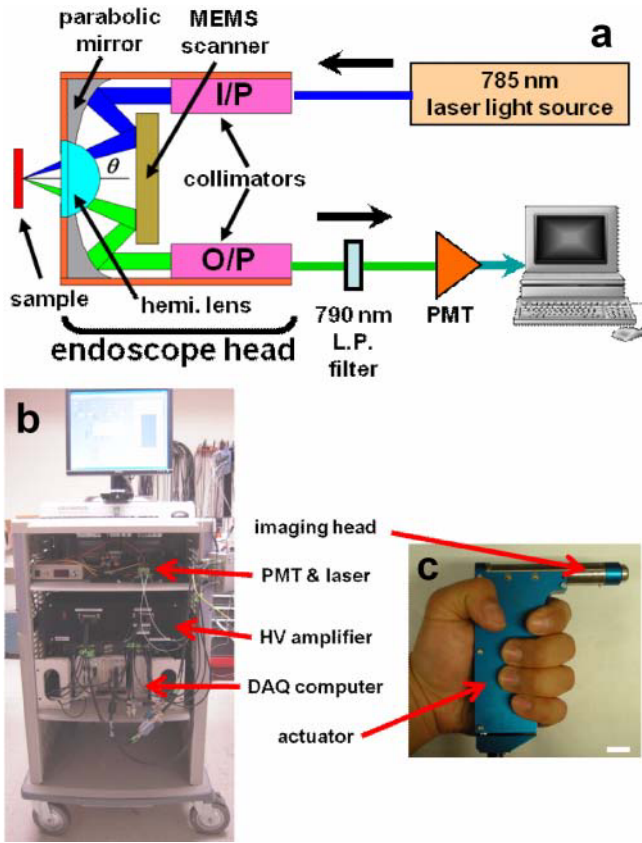


Fig. 23 Handheld prototype system. a) Schematic of complete instrument. b) Portable system demonstrated. c) Packaged handheld (10 mm diameter) dual axes confocal microscope with piezoelectric actuator in the handle, scale bar 10 mm.

the path of one of the collimated beams. The collimators and Risley prisms are both located by precision wire-EDM machined v-grooves and epoxied into place with UV curing glue. As with the larger prototype, the combined precision of the v-grooves and the pointing accuracy of the pre-assembled fiber collimators allow for the collimated beams to become parallel to each other to within $\sim 0.05^\circ$ accuracy. The alignment wedges have a small (0.1°) angle, which allows for steering of a collimated beam over a range of about 0.05° in any direction as each wedge is rotated.

This smaller package design also accommodates a slider mechanism, which is used for axial (z-axis) scanning of the MEMS chip to provide a variable imaging depths within the tissue and for generating 3D volumetric images. This smaller slider mechanism comprises a single rod, which moves within a precision hole drilled through the housing. The MEMS chip is mounted by an adhesive to a

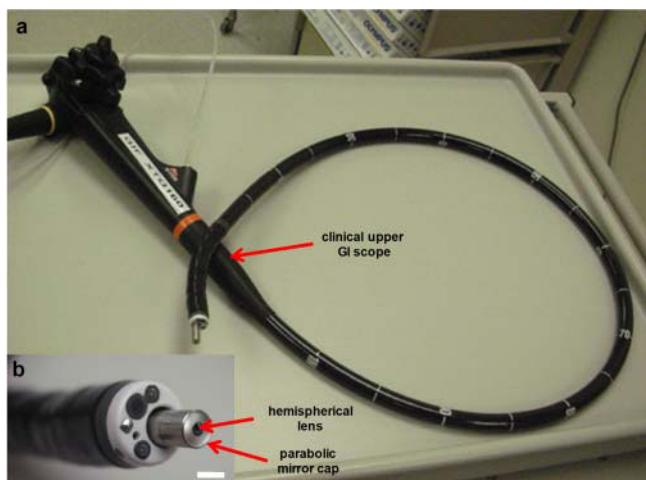


Fig. 24 Endoscope-compatible dual axes confocal microscope. a) Microscope passes through the instrument channel of an Olympus XTQ 160 therapeutic upper endoscope that has a 6 mm diameter instrument channel. b) Distal end of endoscope shows the protruding dual axes microendoscope.

PCB, which is in-turn mounted onto the slider. The PCB provides bondpads to accommodate wire bonding to the MEMS chip and also to provide soldering terminals for the external control wires that power the scan mirror. In Figure 24(a), the endoscope-compatible dual axes confocal microscope is shown inserted through the 6 mm diameter instrument channel of a therapeutic upper endoscope (Olympus GIF XTQ160). A magnified view of the distal tip is shown in Figure 24(b).

8 Imaging Results

8.1 Reflectance Imaging

Instrument characterization is performed in reflectance mode by imaging a chrome surface of a standard (USAF) resolution target. It is also used as a sample to measure the image resolution and FOV. The transverse resolution was measured by the knife-edge method, defined by 10 % to 90 % of maximum intensity points, and found to be $5 \mu\text{m}$ [36]. The axial resolution, defined by FWHM, is measured by translating a plane mirror in the z-direction and was found to be $7 \mu\text{m}$.

Figure 25 shows a reflectance image collected with the handheld confocal microscope that reveals clear visualization of group 7 of the USAF resolution target. The measured values are slightly larger than the theoretical resolutions of $4.5 \mu\text{m}$ for the transverse dimensions, and $6.0 \mu\text{m}$ for the axial dimension. This is mainly due to the decrease in effective NA of the imaging system from the truncation of both input and output collimated beams by the width dimension of the MEMS scanner die. All

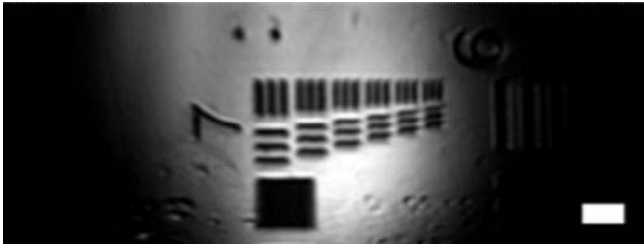


Fig. 25 Reflectance image of standard (USAF) resolution target collected with handheld dual axes confocal microscope, scale bar 20 μm .

acquired images are captured at 5 frames/second with the largest FOV of $800 \times 450 \mu\text{m}^2$ ($900 \times 506 \text{ pixels}^2$). This FOV is much larger than that most other miniature confocal instruments, and is achieved with use of post-objective scanning.

8.2 *Ex Vivo Fluorescence Imaging*

8.2.1 Handheld Dual Axes Confocal Instrument

The 3D volumetric fluorescence imaging capability of the handheld dual axes confocal instrument is shown in Figure 26. Excised tissue specimens of normal and dysplastic colonic mucosa are soaked in 0.5 mg of LI-COR IRDye 800 CW NHS Ester (LI-COR Biosciences, Inc) diluted in 10 ml of phosphate-buffered saline (PBS) at neutral pH for 5 minutes and then rinsed with water to remove excess dye. After imaging, the specimens are fixed in 10 % buffered formalin, cut into 5 μm sections, and processed for histology with hematoxylin and eosin (H&E). All ex vivo images are obtained from freshly excised human tissues (obtained with informed consent at the VA Palo Alto Health Care System).

Figure 26(a, b, and c) and Figure 26(d, e, and f) show the en face image, histology (H&E), and 3D volumetric images of normal and adenomatous (dysplastic) colonic mucosa, respectively, scale bar 100 μm [36]. Features of colonic crypts, including colonocytes and crypt lumens, are clearly resolved. Figure 26(c) and 24(f) show three extracted en face planes at 50, 170, and 230 μm below the tissue surface. The gain is increased with depth to compensate for the lower signal levels.

8.2.2 Endoscope-Compatible Dual Axes Confocal Instrument

A 2D en face fluorescence image of normal colonic mucosa collected ex vivo with the 5.5 mm diameter endoscope-compatible dual axes confocal prototype is shown in Figure 27, scale bar 100 μm . ICG was topically applied to enhance contrast, and

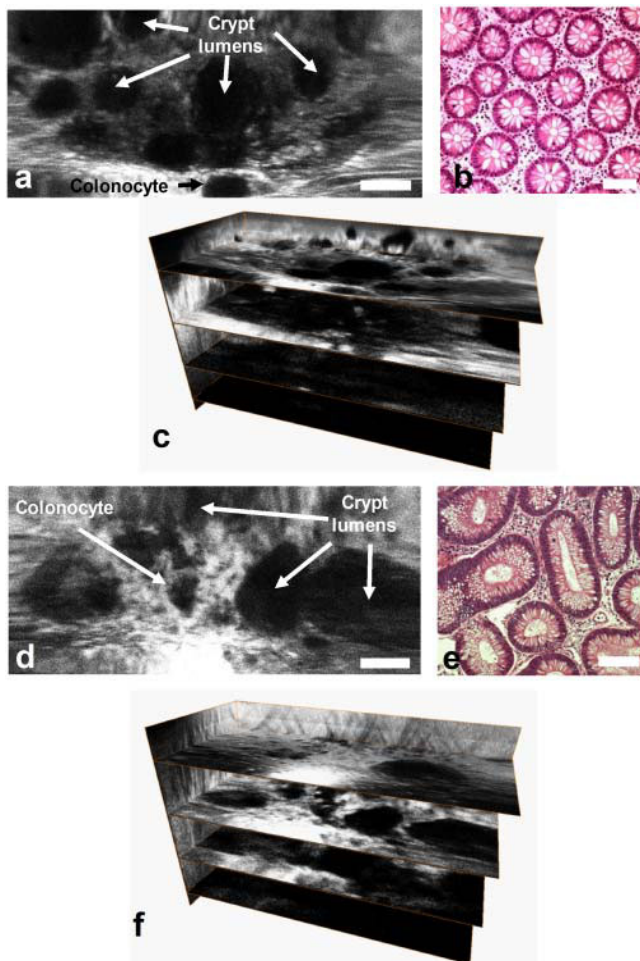


Fig. 26 Ex vivo images. En face dual axes confocal images of a) normal, d) dysplastic colonic mucosa. Corresponding histology (H&E) of b) normal and e) dysplasia. 3D volumetric images of c) normal and f) dysplasia, scale bar 100 μ m.

the pseudocolor image shows dye enhancement in the lamina propria surrounding the circular shaped crypts.

9 In Vivo Fluorescence Imaging

In vivo imaging with the handheld dual axes confocal microscope has also been demonstrated. A mouse was anesthetized, and 10 mg of indocyanine green (Sigma-Aldrich, Corp) diluted in 10 ml of PBS was injected into the retro-orbital plexus of the mouse. Imaging was performed by resting the mouse on a translational stage and

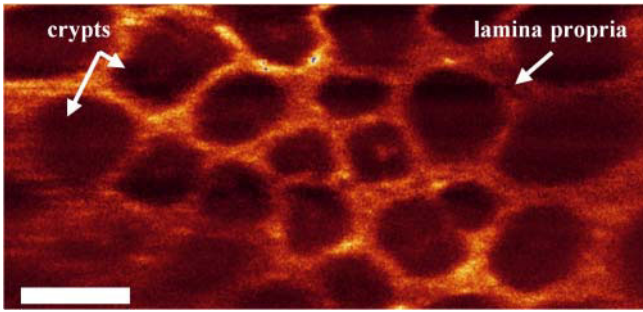


Fig. 27 En face fluorescence image of normal colonic mucosa collected with endoscope-compatible dual axes confocal prototype *ex vivo* using topically applied ICG to enhance contrast shows regular crypt pattern, scale bar $100\ \mu\text{m}$.

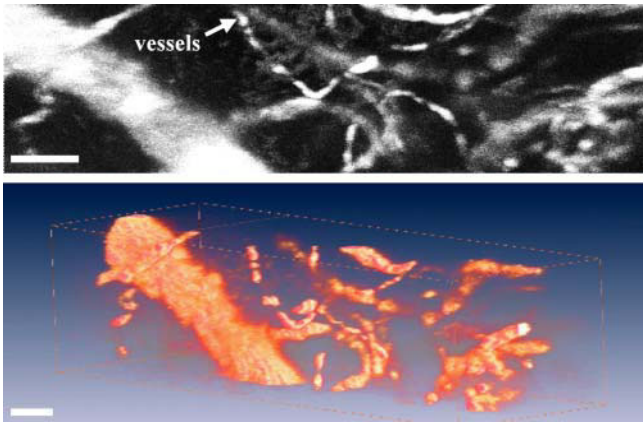


Fig. 28 a) A maximum intensity projected *in vivo* image of blood vessels in an intact mouse ear collected with handheld prototype. b) A 3D volumetric image of blood vessels, scale bar $100\ \mu\text{m}$.

placing its ear intact on the SIL window of the microscope. Figure 28(a) shows an *in vivo* image of blood vessels en face with a maximum intensity projection. Figure 28(b) shows a 3D volumetric rendering of the image stack obtained by scanning from the surface to $150\ \mu\text{m}$ deep into the intact ear. The images were collected in $3\ \mu\text{m}$ intervals along the z -axis by using the piezoelectric actuator. All images were taken at $5\ \text{Hz}$ with 5 frames averaging (1 second per image). Each full 3D volumetric image was acquired in 50 seconds, scale bar $100\ \mu\text{m}$. In addition, *in vivo* images of human skin collected with the handheld dual axes confocal microscope are shown in Figure 29. A sequence of approximately 300 individual en face images of human skin were collected at a fixed depth of $60\ \mu\text{m}$ below the tissue surface (stratum corneum) with a speed of $5\ \text{Hz}\ \mu\text{m}$ [36]. Topically applied indocyanine green was used for contrast. Image stitching or mosaicing was performed to enlarge the FOV

and to increase the signal-to-noise ratio in real time with custom mosaicing software, shown in Figure 29(a). The white rectangle box in Figure 29(a) represents an individual en face image (100 400 m²) obtained with the dual axes confocal microscope. The images were mosaiced by first correcting the image borders for scanning distortions. Then, each new image was registered and blended before proceeding to the next. Figure 29(b) and 29(c) demonstrate how image mosaicing can increase the signal to noise ratio and dramatically improve image quality by tuning the amount of image overlap. The maximum input frame rate that our computer acquisition can process with the real-time mosaicing algorithm is 15 frames/second.

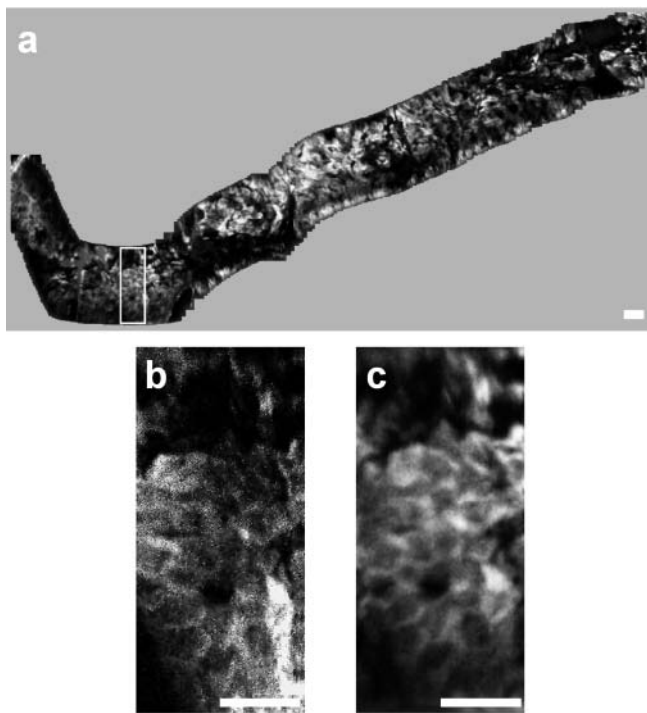


Fig. 29 a) Image mosaic of human skin acquired in vivo at a depth of 60 μm composed of roughly 300 images. The white box shows the corresponding location of individual images, b) A single input image; c) the corresponding area of the mosaic with improved signal-to-noise ratio, scale bars 50 μm .

10 Conclusions and Future Directions

Rapid progress is being made in the development of novel microendoscope for performing real-time optical sectioning in vivo. This technique can collect images with high spatial resolution and contrast in living tissue, and prototype instruments are

now transitioning from the laboratory into the clinic as a result of the significant technological advances being made in micro-optics, flexible fibers, and scanning mechanisms. These tiny imaging instruments are being used to help physicians guide tissue biopsy as an adjunct to medical endoscopes by rapidly assessing tissue for the presence of disease in a nondestructive manner prior to biopsy. Confocal techniques generate image contrast using linear light-tissue interactions and perform optical sectioning using the core of the fiber to spatially filter out-of-focus light. Two commercialized single-axis confocal microendoscopes have been developed to date, and have been demonstrated in the clinic to collect high-quality images in horizontal cross-sections using fluorescein as a nonspecific contrast agent. The dual-axes design is a novel approach that uses off-axis illumination and collection of light to achieve high dynamic range and the ability to collect vertical cross-sectional images, achieving the preferred view of pathologists. This instrument has recently been used to collect clinical images. Future technological advancements in this field are also expected with improved scanning and actuation mechanisms. Galvos are very reliable scanners; however, their large size requires use with optical fiber bundles that have limited spatial resolution and sensitivity. Moreover, their location in the proximal position prevents axial scanning of the focal volume into the tissue for imaging with depth. Cantilever mechanisms have demonstrated high-fidelity images at relatively slow speeds of 1-2 Hz, and faster frame rates are needed to image dynamic events *in vivo*. Spiral scanners can achieve very high scan rates in a tiny package, but suffer from image distortions that can limit their clinical use. MEMS is an alternative approach that provides scanning with high dynamic bandwidth and small package dimensions and is likely to become the preferred choice for *in vivo* microendoscopes. Progress with use of this mechanism will require streamlined fabrication processes, higher device yields, and simplified integration methods. As this novel approach matures, we will be able to use this high resolution imaging instrument to perform clinical investigation in human subjects and longitudinal studies in small animal models. Molecular specificity can be achieved by combining this microendoscope with use of affinity probes that bind to over expressed cell surface targets. This integrated imaging methodology will provide the ability to visualize molecular features of tissue micro-structures in the vertical plane with sub-mucosal axial depths. This powerful capability has tremendous potential to unravel previously unknown molecular mechanisms about important disease processes, such as cancer and inflammation.

In addition, advancements in microendoscope technology are being coupled to development of molecular probes. The growth of imaging as a useful clinical tool requires not only novel instruments with improved spatial resolution and higher scan speeds but also new contrast agents with higher disease specificity and clinically relevant targets. Greater impact will be achieved by visualizing molecular expression patterns in addition to microarchitectural changes. Both confocal and two-photon methods are well suited for this application because of the subcellular resolution and real-time speeds that they can achieve. Novel contrast agents that provide greater sensitivity and higher target-to-background ratio are needed so that smaller volumes of diseased tissue can be evaluated. Furthermore, labels for these

probes must be compatible with the light sources and detectors being used in the design of novel microendoscopes. Promising molecular probes that are currently in development are based on dequenching, antibody, peptide, and small-molecule platforms. To date, the use of peptides has been demonstrated in the clinic for detecting precancer in colon with confocal microendoscopy. We expect that future clinical use of imaging probes will require significant regulatory oversight and monitoring of safety, representing an important administrative hurdle. Despite these numerous challenges, the future for clinical use of *in vivo* microendoscopy is extremely bright and promising. The ability to visualize biological behavior and pathophysiology with subcellular resolution and molecular specificity in real time *in vivo* represents a new frontier in imaging science. Its potential impact on clinical medicine for early diagnosis, image-guided therapy, and monitoring of disease is beyond imagination.

Acknowledgements. We thank Thomas D Wang, Christopher H Contag, Shai Friedland, Gordon S Kino, Jonathon TC Liu, Michael J Mandella, Hyejun Ra, Roy M Soetikno, Olav Solgaard, and Larry K Wong for their technical support. This work was supported in part by grants from the National Institutes of Health (U54 CA105296, R33 CA109988, K08 DK67618, P50 CA93990, and U54 CA136429), the Higher Education Research Promotion and National Research University Project of Thailand, Office of the Higher Education Commission (1166, 1162), and the National Electronics and Computer Technology Center. W. Piyawattanametha is with the National Electronics and Computer Technology Center, Pathumthani 12120, Thailand, the Faculty of Medicine, Chulalongkorn University, Pathumwan 10330, Thailand and also with the Departments of Applied Physics, Biology, Electrical Engineering, Microbiology & Immunology, and Pediatrics, Stanford University, CA 94305 USA (e-mail: wibool@gmail.com).

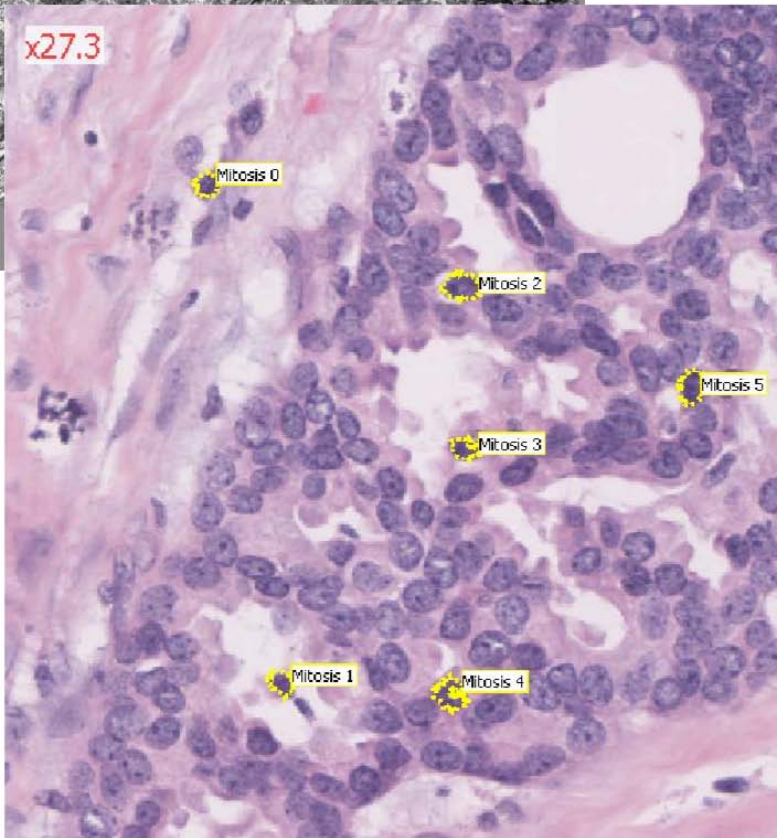
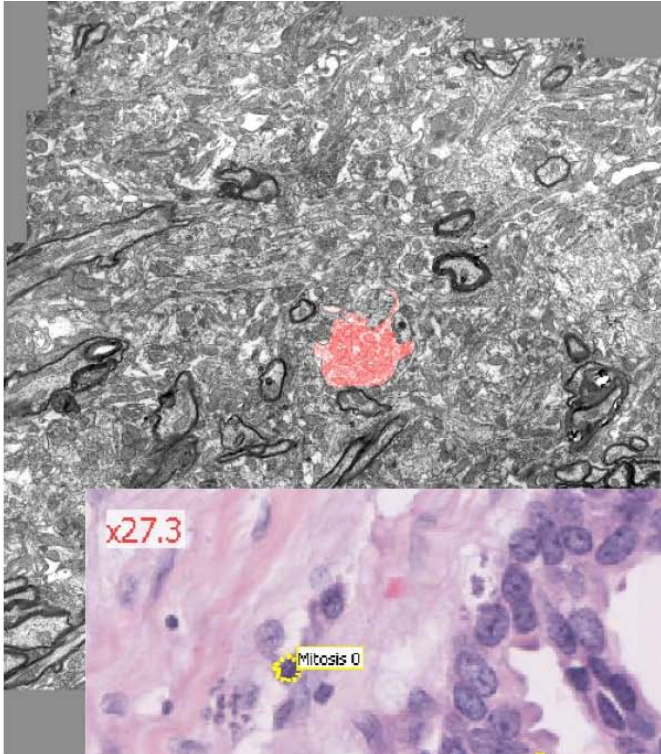
References

1. Cotran, R.S., Kumar, V., Collins, T.: Robbins Pathologic Basis of Disease, 6th edn., pp. 781–787. W. B. Saunders Company, Philadelphia (1999)
2. Pawley, J.: Handbook of biological confocal microscopy, 3rd edn. Plenum Press, New York (1996)
3. Corle, T.R., Kino, G.S.: Confocal Scanning Optical Microscopy and Related Imaging Systems. Academic Press, Boston (1996)
4. Laemmel, E., Genet, M., Le Goualher, G., Perchant, A., Le Gargasson, J.F., Vicaut, E.: Fibered confocal fluorescence microscopy (Cell-viZio) facilitates extended imaging in the field of microcirculation. A comparison with intravital microscopy. *Journal of Vascular Research* 41, 400–411 (2004)
5. Carlson, K., Chidley, M., Sung, K.-B., Descour, M., Gillenwater, A., Follen, M., Richards-Kortum, R.: *In vivo* fiber-optic confocal reflectance microscope with an injection-molded miniature objective lens. *Applied Optics* 44, 1792–1796 (2005)
6. Thekkekk, N., Richards-Kortum, R.: Optical imaging for cervical cancer detection: solutions for a continuing global problem. *Nat. Rev. Cancer* 8, 725–731 (2008)
7. Delaney, P.M., Harris, M.R., King, R.G.: Fiber-optic laser scanning confocal microscope suitable for fluorescence imaging. *Applied Optics* 33, 573–577 (1994)

8. Wang, T.D., Friedland, S., Sahbaie, P., Soetikno, R., Hsiung, P.-L., Liu, J.T.C., Crawford, J.M., Contag, C.H.: Functional Imaging of Colonic Mucosa With a Fibered Confocal Microscope for Real-Time In Vivo Pathology. *Clinical Gastroenterology and Hepatology* 5, 1300–1305 (2007)
9. Dickensheets, D.L., Kino, G.S.: A scanned optical fiber confocal microscope. In: *SPIE Symposium on Electronic Imaging Science & Technology*, San Jose, CA, pp. 39–47 (1994)
10. Dickensheets, D.L., Kino, G.S.: Silicon-micromachined scanning confocal optical microscope. *Journal of Microelectromechanical Systems* 7, 38–47 (1998)
11. Piyawattanametha, W., Toshiyoshi, H., LaCosse, J., Wu, M.C.: Surfacemicromachined confocal scanning optical microscope. In: *Conference on Lasers and Electro-Optics (CLEO 2000)*, San Francisco, CA, USA, May 7–12, pp. 447–448 (2000)
12. Murakami, K., Murata, A., Suga, T., Kitagawa, H., Kamiya, Y., Kubo, M., Matsumoto, K., Miyajima, H., Katashiro, M.: A miniature confocal optical microscope with MEMS gimbal scanner. In: *IEEE International Solid-State Sensors and Actuators Conference*, Boston, MA, USA, June 8–12, vol. 1, pp. 587–590 (2003)
13. Piyawattanametha, W., Fan, L., Hsu, S., Fujino, M., Wu, M.C., Herz, P.R., Aguirre, A.D., Chen, Y., Fujimoto, J.G.: Two-dimensional endoscopic MEMS scanner for high resolution optical coherence tomography. In: *On Lasers and Electro-Optics (CLEO)*, San Francisco, CA, USA, May 16–21, vol. 1, p. 3 (2004)
14. Piyawattanametha, W., Patterson, P.R., Hah, D., Toshiyoshi, H., Wu, M.C.: Surfaceandbulk- micromachined two-dimensional scanner driven by angular vertical combactuators. *Journal of Microelectromechanical Systems* 14, 1329–1338 (2005)
15. Thiberville, L., Moreno-Swirc, S., Vercauteren, T., Peltier, E., Cave, C., Bourg Heckly, G.: In Vivo Imaging of the Bronchial Wall Microstructure Using Fibered Confocal Fluorescence Microscopy. *Am. J. Respir. Crit. Care Med.* 175, 22–31 (2007)
16. Wang, T.D., Mandella, M.J., Contag, C.H., Kino, G.S.: Dual-axis confocal microscope for high-resolution in vivo imaging. *Optics Letters* 28, 414–416 (2003)
17. Wang, T.D., Contag, C.H., Mandella, M.J., Chan, N.Y., Kino, G.S.: Dual-axesconfocal microscopy with post-objective scanning and low-coherence heterodyne detection. *Optics Letters* 28, 1915–1917 (2003)
18. Born, M., Wolf, E.: *Principles of Optics*, 7th edn. Cambridge University Press, Cambridge (1999)
19. Liu, J.T.C., Mandella, M.J., Friedland, S., Soetikno, R., Crawford, J.M., Contag, C.H., Kino, G.S., Wang, T.D.: Dual-axes confocal reflectance microscope for distinguishing colonic neoplasia. *Journal of Biomedical Optics* 11 (September–October 2006)
20. Wong, L.K., Mandella, M.J., Kino, G.S., Wang, T.D.: Improved rejection of multiply scattered photons in confocal microscopy using dual-axes architecture. *Optics Letters* 32, 1674–1676 (2007)
21. Henyey, C.: *Diffuse radiation in the Galaxy* (2000)
22. Mehta, K.T., Shah, H.S.: Correlating Parameters of The Henyeygreensteinphase Function Equation With Size and Refractiveindex of Colorants. *Applied optics-OT* 24, 892–896 (1985)
23. Pavlos, K.: Scattering, Absorption, and Emission of Light by Small Particles. *Bulletin of the American Meteorological Society* 84, 494 (2003)
24. Prah, M.K.S.A., Jacques, S.L., Welch, A.J.: Dosimetry of Laser Radiation in Medicine and Biology. In: *Proc. SPIE*, vol. 5, pp. 102–111 (1989)
25. Wang, T.D., Contag, C.H., Mandella, M.J., Chan, N.Y., Kino, G.S.: Confocal fluorescence microscope with dual-axis architecture and biaxial postobjective scanning. *J. Biomed. Opt.* 9, 735–742 (2004)

26. Wang, T.D., Contag, C.H., Mandella, M.J., Chan, N.Y., Kino, G.S.: Confocal fluorescence microscope with dual-axis architecture and biaxial postobjective scanning. *Journal of Biomedical Optics* 9, 735–742 (2004)
27. Liu, J.T.C., Mandella, M., Crawford, J., Contag, C., Wang, T., Kino, G.: Efficient rejection of scattered light enables deep optical sectioning in turbid media with low-numerical-aperture optics in a dual-axis confocal architecture. *Journal of Biomedical Optics* 13, 34020 (2008)
28. Dickensheets, D.L., Kino, G.S.: Micromachined scanning confocal optical microscope. *Optics Letters* 21, 764–766 (1996)
29. Piyawattanametha, W., Barretto, R.P.J., Ko, T.H., Flusberg, B.A., Cocker, E.D., Ra, H.J., Lee, D.S., Solgaard, O., Schnitzer, M.J.: Fast-scanning two-photon fluorescence imaging based on a microelectromechanical systems two-dimensional scanning mirror. *Optics Letters* 31, 2018–2020 (2006)
30. Timoshenko, S.P., Goodier, J.N.: *Theory of Elasticity*, 3rd edn. McGraw-Hill, New York (1970)
31. Piyawattanametha, W., Patterson, P.R., Hah, D., Toshiyoshi, H., Wu, M.C.: Surface and bulk-micromachined two-dimensional scanner driven by angular vertical comb actuators. *Journal of Microelectromechanical Systems* 14, 1329–1338 (2005)
32. Ra, H., Taguchi, Y., Lee, D., Piyawattanametha, W., Solgaard, O.: Two-dimensional MEMS scanner for dual-axes confocal in vivo microscopy. In: *Proceedings of the 19th IEEE International Conference on Micro Electro Mechanical Systems (MEMS)*, Istanbul, Turkey, pp. 862–865 (2006)
33. Ra, H., Piyawattanametha, W., Taguchi, Y., Lee, D., Mandella, M.J., Solgaard, O.: Two-dimensional MEMS scanner for dual-axes confocal microscopy. *Journal of Microelectromechanical Systems* 16, 969–976 (2007)
34. Ataman, C., Urey, H.: Nonlinear Frequency Response of Comb-Driven Microscanners. In: *Proceedings of SPIE - The International Society for Optical Engineering MOEMS Display and Imaging Systems II*, San Jose, CA, United States, vol. 5348, pp. 166–174 (2004)
35. Liu, J.T.C., Mandella, M.J., Ra, H., Wong, L.K., Solgaard, O., Kino, G.S., Piyawattanametha, W., Contag, C.H., Wang, T.D.: Miniature near-infrared dual-axes confocal microscope utilizing a two-dimensional microelectromechanical systems scanner. *Optics Letters* 32, 256–258 (2007)
36. Siegman, A.E., Sasnett, M.W., Johnston, T.F.: Choice of Clip Levels for Beam Width Measurements Using Knife-Edge Techniques. *IEEE Journal of Quantum Electronics* 27, 1098–1104 (1991)

Part III
Digitized Histopathology



Ontology-Enhanced Vision System for New Microscopy Imaging Challenges

Nicolas Lomenie and Daniel Racoceanu

Abstract. Artificial intelligence and computer vision have long been separate fields basically because the data structures to work with and to reason about were rather distinct and non permeable. Ontology-driven systems may have the ability to build a bridge between these two fundamental topics involved in intelligent system design. We provide preliminary insights about this powerful synergy in the field of digitized pathology as a brand new topic in which, like currently for satellite imaging, the amount of raw data and high-level concepts to handle give no other choice but to innovate about the low-level image image processing machine and the knowledge modeling framework integration. Above all, the end-user who is most of the time naive about signal, image and algorithmic issues can thence play the key role in the design of such enhanced vision system.

1 Introduction

Along the same lines as satellite imaging current challenges, digitized pathology raises new major issues both from technological and scientific points of view. On the more technological side of the research scope, storage and networking is dramatically challenging since, unlike mammograms for instance, the amount of data easily scales up to eight gigabytes of pixels for a single biopsy patient case. At a more fundamental level, the high number of meaningful biological concepts to be handled, sometimes implicitly, calls for innovative ways to handle information in huge visual data.

The design of such enhanced vision system can only benefit from an ontology-driven strategy. The ontology paradigm in information science constitutes the mainstream current tool to make people from various backgrounds work together. In

Nicolas Lomenie · Daniel Racoceanu
IPAL CNRS UMI 2955 (I2R/A*STAR, NUS, UJF,
TELECOM, UPMC/Sorbonne)
e-mail: lomenie@mi.parisdescartes.fr

addition, ontology-based interfaces are a key component of an ergonomic, adaptive computer system, specially in biological/clinical fields for which concepts and standards are constantly shifting. Furthermore, reasoning capabilities embedded in the logical framework on which the ontology softwares are built up constitute a definite bridge between computer vision scientists and knowledge engineers. Even though still brittle and limited, reasoning inferences out of visual data may as well enhance the vision system global experience.

In this work, we prove that image processing at the signal level embedded with high-level interfaces to interact with the system can improve not only the ease of use of such systems for the end-user but also the robustness of the results in daily practice, above all in fields wherein, paradoxically, subjective decision can be taken like in the case of breast cancer grading [Schnorrenberg 1996]. Few attempts to bridge the gap between knowledge modeling and medical image analysis outcomes have been carried out so far [Hudelot et al. 2008, Mechouche et al. 2009] and mostly about highly atlas-based or informed anatomical structures like the brain. Works on microscopy images with an intrinsically higher content of either explicit or implicit biological objects are much fewer [Roux et al. 2009].

The paper is organized as follows. Section 2 overviews the challenges in breast cancer grading not only from a purely clinical point of view but also from the digitized pathology new paradigm. Section 3 describes the low-level image processing algorithms while Section 4 elaborates on the high-level, ontology-based interface capabilities we embedded in the system in order to improve the overall performances of the grading process as assessed in Section 5. Last, Section 6 draws meaningful conclusions about the interactions between the ontology paradigm and the computer vision toolbox achieved so far, leading to major perspectives for the intelligent system designer community.

2 Breast Cancer Grading

2.1 Digitized Pathology

The European Virtual Physiological Human ¹ project is an ambitious program to build up a holistic *in silico* functional model of the human biology system. To do so the design of inter-operable formats for biology system modeling or bio-engineering workflows are of utmost importance. Multi-scale modeling of the human body functions as well is an expected outcome of this scheme. The recent advances in microscopy image acquisition constitutes a definite asset to fulfill this goal. Digitized pathology in particular has been recently standardized at the DICOM ² level and will provide a bunch of valuable visual insights about the way biological phenomena proceed by boosting the modeling at the cellular level. In this perspective, the

¹ <http://www.vph-noe.eu/>

² <http://medical.nema.org/>

ontological framework coming from the computer science community should be a key player to share models in this framework.

Even for clinical daily practice, computer vision systems involving knowledge management are the only way to make them really usable at a large scale and sustainable in terms of design, maintenance and usability. Moreover, reasoning capabilities can leverage image analysis ones to improve the final diagnosis process. Grading breast cancer out of histo-pathological images is the gold-standard for clinicians drawing prognosis reports of such diseases and is known to be still challenging: in terms of reproducibility mostly but also in terms of training and legal assessment due to the lack of traceability and archiving features.

From a learning standpoint as well as from a training perspective, the clinician uses a “mental database” of visual cases that helps him/her to go straight to the relevant Region of Interest (ROI) over the microscope screening, then to switch to the optimal magnification and then to perform the standard computation of scores following the Nottingham Grading System (NGS) for breast cancer grading. The grade is a combination of three scores:

- Nuclear Pleomorphism: if uniform cells (minimal or no nuclear enlargement, long axis diameter $\sim 10\mu m$, minimal or no darkening of chromatin) then score=1; if moderate nuclear size and variation (long axis diameter $\sim 15\mu m$), then score=2; if marked nuclear variation (long axis diameter $\geq 20\mu m$), then score=3;
- Tubular Formation: if $\geq 75\%$ of the invasive area is forming tubules, then score=1; if 10 – 75% of the cancer is forming tubules, then score=2, else if $\leq 10\%$ of the cancer is forming tubules then score=3. (Only structures exhibiting clear central lumina are counted);
- Mitotic Count: if 0 – 9 mitoses/10 hpf, then score=1; if 10 – 19 mitoses/10 hpf, then score=2; if ≥ 20 mitoses/10 hpf, then score=3; where hpf stands for high power field (40X objective lens); (Field selection for mitotic scoring should be from the peripheral leading edge of the tumor; If there is heterogeneity, regions exhibiting a higher frequency of mitoses should be chosen; Field selection is done by random meander through the chosen area; Only fields with a representative tumor cell burden should be assessed³).

Then, the final grading mark is a linear combination of the three previous scores: Grade=Score tubule + Score mitoses + Score nuclear pleomorphism. Low grade (I) breast cancers correspond to a sum of 3-5, Intermediate grade (II) to 6-7 and High grade (III) to 8-9. The grading is computed out of what is called a Whole Slide Image (WSI) that corresponds to up to eight gigabytes of pixel data (see Figure II) and about 50 000 x 40 000 pixels size image at high x40 magnification. An ontology

³ Hyperchromatic and pyknotic nuclei are ignored since they are more likely to represent apoptosis than proliferation. Pyknosis = the irreversible condensation of chromatin in the nucleus of a cell undergoing apoptosis. It is followed by fragmentation of the nucleus. Apoptosis = the process of programmed cell death: loss of membrane asymmetry and attachment, cell shrinkage, nuclear fragmentation, chromatin condensation, chromosomal DNA fragmentation. These definitions are given in order to stress out the complexity of numerical modeling of the biological concepts.

support to the cross-design of a clinical system is almost an inescapable requirement to handle such a broad scope of evolving concepts. To start, we designed a breast cancer ontology both anatomical and clinically operational [Tutac et al. 2008].

2.2 Anatomical and Workflow Ontology: OWL

An ontology is a system of knowledge representation of a domain in the form of a structured set of concepts and relationships between these concepts. An ontology is expressed in the form of a XML graph and produces reasoning through a rule language. Our Breast Cancer Ontology (BCO) is based on two languages: OWL-DL (Web Ontology Language Description Logics) to describe the ontology and SWRL (Semantic Web Rule Language) to write and manage rules for the reasoning part. Technically, OWL and SWRL are specifications of the W3C⁴, OWL is an extension of RDF (Resource Description Framework) used in the description of classes and types of properties, SWRL combines OWL and RuleML (Rule Markup Language) to produce the rules for the reasoning. The annotated images are described with the Wide Field Markup Language (WFML)⁵ specific to the histopathology field. Finally, the query language SPARQL (Simple Protocol And RDF Query Language) is used for querying in Java. SPARQL has been chosen for its ease of use and the very good integration of the API in Java. A thorough description of this ontology-based platform can be found in [Tutac et al. 2008, Roux et al. 2009].

3 Low-Level Signal Processing

The image processing machine provides *a priori* visual landmarks related to ontological biological concepts like nucleus, mitosis, tubule. As this low-level processing machine is not the core of our current contribution, technical details will be skipped over while snapshot illustrations of the resulting visual landmarks population over the WSI are provided.

Invasive Area Segmentation

As a pre-attentive image processing, the invasive Region Of Interest (ROI) detection is casted as a classification problem whereby we leverage the relationship between human vision and neurosciences [Miikkulainen et al. 2005]. An illustration of this focusing step in our platform is provided in Figure 1. All subsequent biological objects like nucleus, mitosis, lumina will be searched over this ROI.

⁴ World Wide Web Consortium.

⁵ An XML language produced by the company TRIBVN for its platform ICS Framework <http://www.tribvn.com>

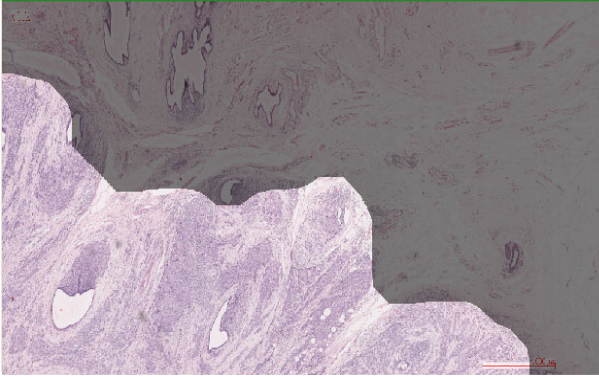


Fig. 1 Invasive area pre-attentive detection step at low-magnification x1.2 over the WSI

Nuclei, Mitoses and Lumina Extraction

The nuclei detection module is the core image analysis module of the system in the sense that it should be the more robust low-level process due to a quite standardized staining process in clinical daily practice. The nuclei detection proceeds following two steps as presented in [Dalle et al. 2009] and the results are illustrated in Figure 2. As the metric scale is known, most image processing is related to the mathematical morphology toolbox using shape and size criteria. Then geometric and radiometric features can be extracted over each detected nucleus.

The low-level mitosis detection module proceeds by machine learning based on radiometric and geometric features computed out of a ground truth database. Results are illustrated in Figure 3.

The lumina are void parts in the tissue that let fluid or air pass going through. The low-level algorithm for lumina detection uses mathematical morphology tools (see Figure 4) to detect bright blob areas in the WSI. They can be confused with fat matter zone or tubular formation.

4 High-Level Processing

Once all these visual landmarks have been potentially computed by database-dependent signal processing formalization, learning and numerical implementation of visual characteristics, more generic high-level knowledge representation and handling enhance the efficiency of the virtual microscope system insofar as the extraction of all the biological concepts by an exhaustive search is not possible in an interactive time.

By designing vision systems through the ontology framework, our research work objectives are threefold:

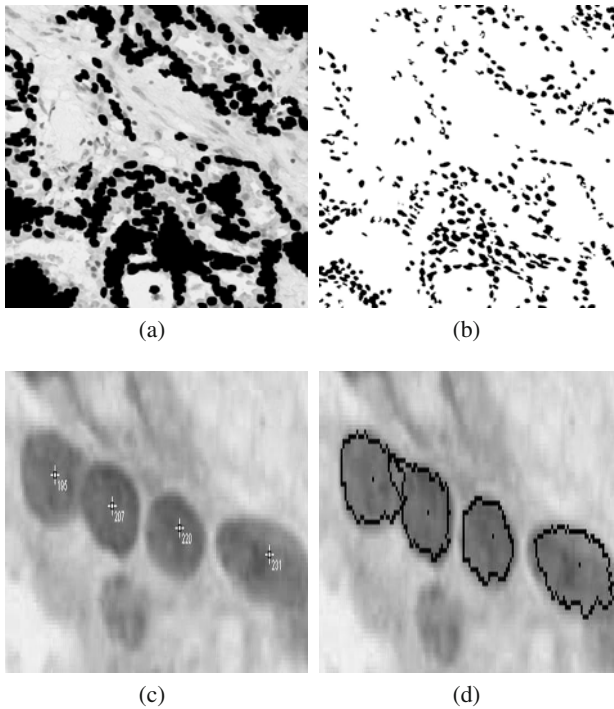
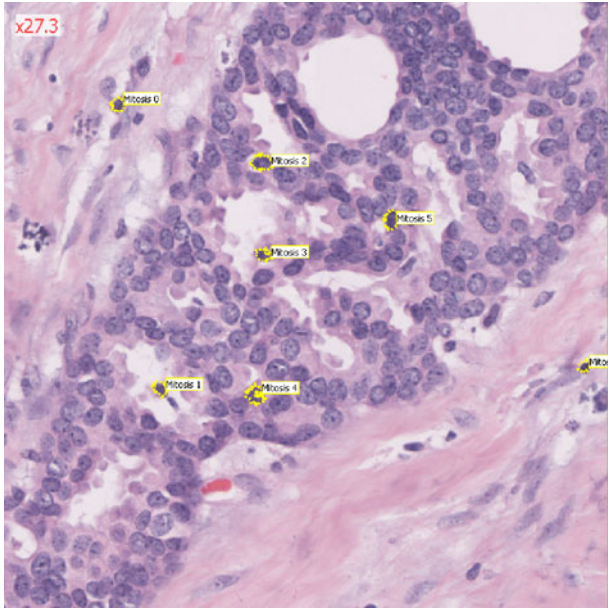


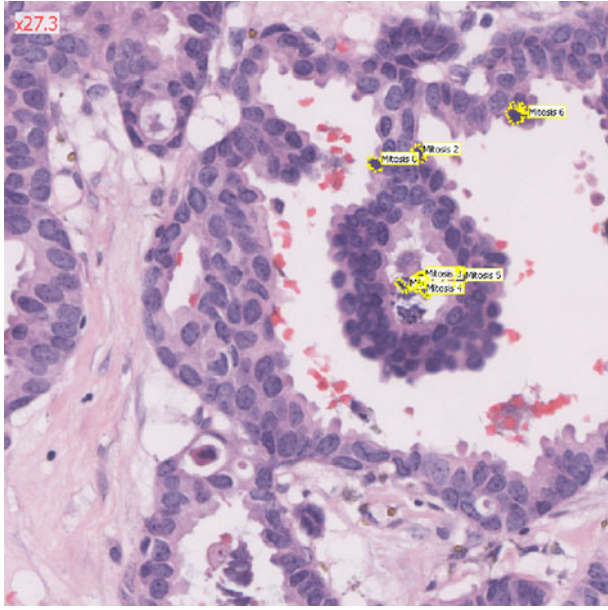
Fig. 2 Nuclei identification - (a) Regions of interest detection by automatic thresholding and morphological filtering, (b) nuclei identification (coarse nuclei separation), (c) Nuclei identification based on a distance map, the furthest points from the boundaries are identified as the nuclei seeds, (d) Nuclear boundaries extracted using a snake-based method [Dalle et al. 2009]. Processing in (c) and (d) being done at high magnification x40 over sample image (1024x1024 pixels size images).

- Consistency checking annotation: to improve the specificity rate;
- Image analysis engine triggering control: to improve the sensitivity rate within a limited response time;
- Smart and adaptive interfacing: Consider the end-user (usually the clinician) as a key player of the system design and functionality in relation with the two previous objectives.

We leverage both on the knowledge formalization features and the reasoning capabilities of platforms like *ProtégéTM* to achieve higher level of interoperability, usability and potentially robustness of the system as described in the following part of the paper.



(a)



(b)

Fig. 3 Mitosis detection by machine learning based on geometric and radiometric features

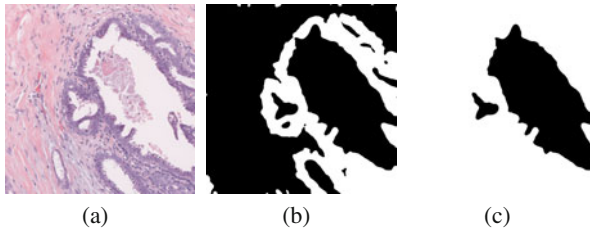


Fig. 4 Lumina detection

4.1 Rules and Reasoning

The core numerical object of the cognitively enhanced system is the XML-like file that stores the annotations of the WSI in the WFML format. The WFML files are translated into OWL file formats both related to the XML technology [Othmani et al. 2010]. Then, we can use the first order logic machine inference within the *Protégé*⁶ environment. For each WSI, the system is able to generate complementary annotation outputs: \mathcal{R}^{signal} (see Section 3) and $\mathcal{R}^{knowledge}$ as described in the current section. We study hereafter the articulation $\mathcal{R}^{signal \times knowledge}$ between the two sets of annotation outputs and illustrate how high-level processing can improve the overall behavior of the virtual microscope system through the three previously mentioned objectives.

4.1.1 User-Based Consistency Checking Annotation: Mitosis Detection

In histopathology, the biological concepts are usually expressed as high-level concepts while image analysis modules provide actually implicit definitions of these concepts. Ideally, a fully-fledged smart vision platform should provide a way of checking the consistency of the low-level numerical annotations with their high-level ontological definitions: the famous semantic gap. Thus anchoring the histopathological concepts in the digitized WSI can benefit of a cross validation between (a) the low-level, implicit, signal-based extraction providing a set of results \mathcal{R}^{signal} , usually by statistical learning and tedious numerical modeling and (b) the explicit high-level description corresponding to a SWRL rule like the one expressed in the Protégé platform in Figure 5 and potentially providing a set of results $\mathcal{R}^{knowledge}$.

Our platform implements these two kinds of mitosis detection: the $\mathcal{R}_{mitosis}^{signal}$ as slightly described in Section 3 and the $\mathcal{R}_{mitosis}^{knowledge}$ that relies on the $\mathcal{R}_{nucleus}^{signal}$ set of results. The whole annotation updating workflow for the mitosis detection is described in Figure 6 and in Figure 7 for the WFML-based annotated resulting images⁷: the

⁶ <http://protege.stanford.edu/>

⁷ In the ICSTM Technology interface from TRIBVN S.A., the image format is a SVS format involving both a pyramidal TIFF multiscale description and WFML description file for the annotations currently available in the database.

```

→ Nucleus(?x) ∧ hasIntensity(?x, ?value) ∧ swrlb:lessThan(?value, 110.0) ∧ hasCircularity(?y, ?cir)
∧ swrlb:lessThan(?cir, 0.75) ∧ hasRound(?z, ?round) ∧ swrlb:lessThan(?round, 0.65) → Mitosis(?x)

```

Fig. 5 A SWRL rule for mitosis description in our BCO (Breast Cancer Ontology) within the Protégé platform where Circularity and Roundness are the standard shape features.

step 2 in the workflow provides $\mathcal{R}_{nucleus}^{signal}$, the step 8 yields $\mathcal{R}_{mitosis}^{knowledge}$ and the step 2' outputs $\mathcal{R}_{mitosis}^{signal}$. Section 5 elaborates on the synergy between the two interaction modes in order to achieve the $\mathcal{R}_{mitosis}^{signal \times knowledge}$ final objective.

4.1.2 Spatial Relationship Modeling

Spatial Configuration Consistency Checking: Tubule Detection

Along the same line, tubule detection can be achieved by high-level spatial configuration reasoning or constraint checking. Let us assume that a sound definition of a tubule is a lumina surrounded by two lines of cells as reported in academic books about pathology. This definition permits among others to discriminate between mere fat areas and tubular configurations that both correspond to large bright blob zones in the WSI. From an image analysis point of view, we need to formalize spatial relationship concepts like *Surrounded by* in a sound theoretical way. That is achieved by resorting to the mathematical morphology toolbox like in [Hudelot et al. 2008] (see Figure 8).

Image Analysis Engine Triggering Control: Mitosis Detection

Interactive time is a fundamental issue in current image processing systems to really comply with user requirements. In particular in digitized histopathology, we must fit within a ten-minute response time frame to be on a par with the daily practice clinician time scores. Thence, being able to control the image analysis triggering over the WSI can help to improve the sensitivity rate of the platform under the time constraint. Referring to pathologists' explicit knowledge, the rule stating that mitoses should be first searched at the periphery of invasive areas can be expressed in the first order Protégé logic (see Figure 9). The spatial relationship *Around* is closely related to the previous one *Surrounded by* and its modeling relies on the same mathematical morphology tools. When applicable, the system was able to save between five and ten-fold processing time which is of dramatic importance for WSI exploration. In addition, this kind of spatial relationship rule can help to check the consistency of \mathcal{R}^{signal} .

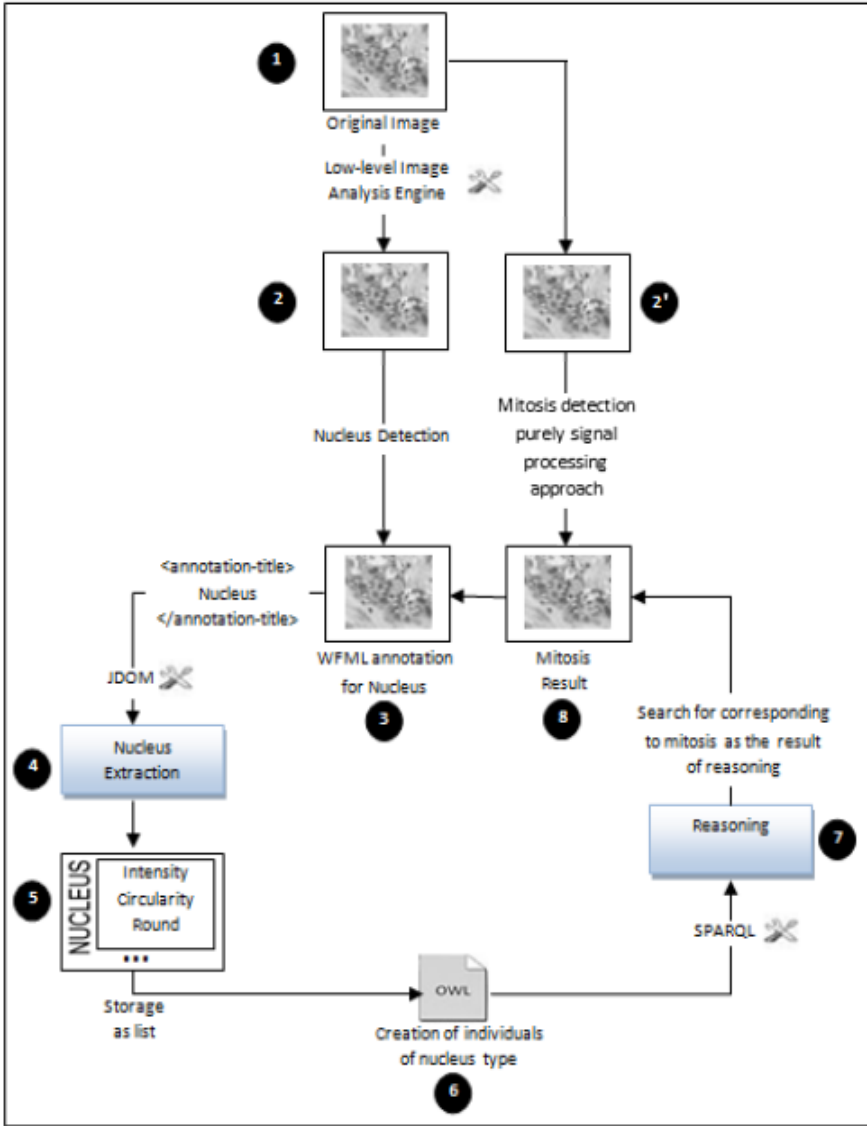


Fig. 6 The mitosis detection process.

5 Results

Mitosis Detection

We chose to thoroughly assess our methodology on the mitosis detection problematic which is determinant according to pathologists. Tables 123 sum up major recognition rates for their detection respectively with ontological intensity and

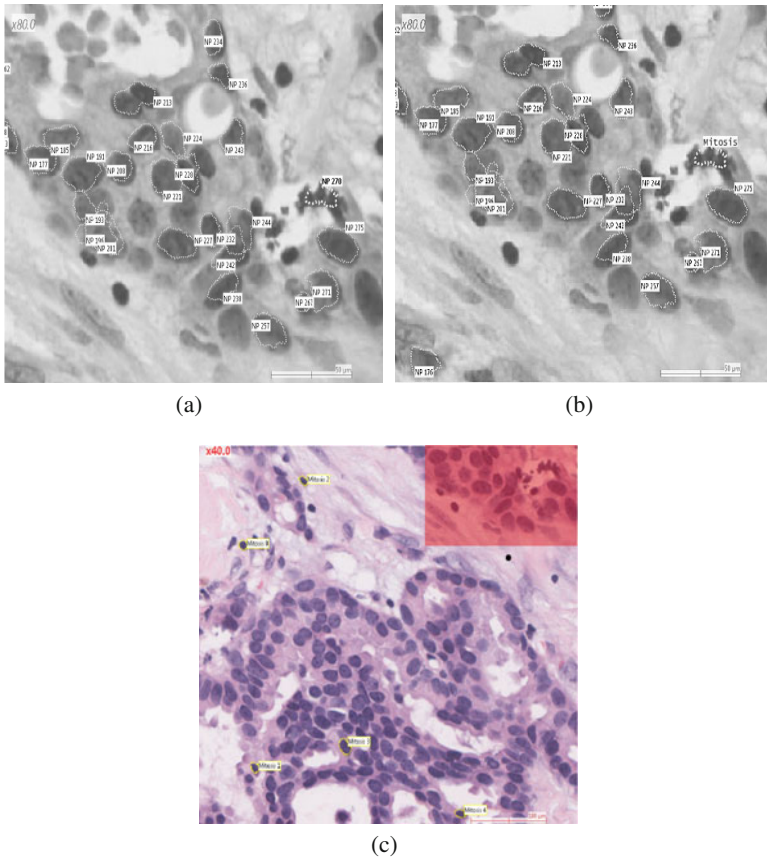


Fig. 7 (a) WFML before Mitosis Detection corresponding to step 3 in Figure 6 (b) WFML after Rule-based Mitosis Detection corresponding to step 8 (c) WFML after low-level based Mitosis Detection corresponding to step 2': the highlighted zone at the top-right corner focuses on the zone in (a) and (b) and no mitosis is detected inside it. Mitoses detected by the low-level engine are annotated in the rest of the image.

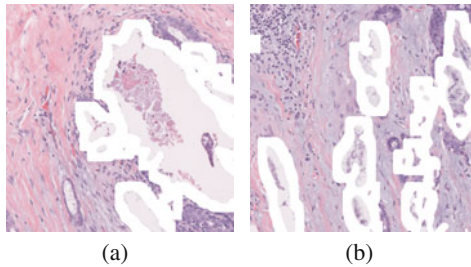


Fig. 8 Formalization of the surrounding area for lumina.

```
→ Mitosis(?x) ∧ Neoplasm(?y) ∧ hasNeoplasmPeriphery(?y, ?x) → sqwrl:select(?x, ?y)
```

Fig. 9 A SWRL rule for the expression of the spatial relationship constraint within the Protégé platform

geometrical criteria for the first two ones and with the purely signal processing approach for the last one.

The \mathcal{R}^{signal} processing results overdetect the mitoses over the ten frames with 50 detections against 20 for the $\mathcal{R}^{knowledge}$ ones. The ontology-driven detection increases the specificity of the system by dramatically reducing the false alarm rate. \mathcal{R}^{signal} outperforms $\mathcal{R}^{knowledge}$ in the case of nuclear pleomorphism score 3 images that correspond to cases wherein the segmentation process is by far less robust and reliable because of treacherous deformations within the cells (for instance specificity rate of score 3 image IMG001 in comparison with score 1 image IMG002). On the contrary, $\mathcal{R}^{knowledge}$ overcomes \mathcal{R}^{signal} in the case of nuclear pleomorphism score 1 images. The better the low-level segmentation process is, the better the ontology-driven approach behaves.

Table 1 Preliminary quantitative assessment for the ontology-driven mitosis detection approach: query with intensity

| Image | Frame | Number of cells | Correct Nb of mitoses | Nb of mitoses detected | TP | TN | FP | FN | Specificity | Sensitivity |
|---------|-------|-----------------|-----------------------|------------------------|----|------|----|----|-------------|-------------|
| NB19413 | f001 | 257 | 3 | 6 | 3 | 251 | 3 | 0 | 0.988 | 1.000 |
| NB19413 | f003 | 314 | 2 | 4 | 2 | 310 | 2 | 0 | 0.994 | 1.000 |
| NB19413 | f008 | 296 | 2 | 3 | 2 | 293 | 1 | 0 | 0.997 | 1.000 |
| NB7824 | f001 | 244 | 0 | 8 | 0 | 236 | 8 | 0 | 0.967 | 1.000 |
| NB7824 | f004 | 242 | 0 | 18 | 0 | 224 | 18 | 0 | 0.926 | 1.000 |
| NB7824 | f002 | 297 | 2 | 4 | 2 | 293 | 2 | 0 | 0.993 | 1.000 |
| NB19271 | f002 | 261 | 0 | 6 | 0 | 255 | 6 | 0 | 0.977 | 1.000 |
| NB19271 | f003 | 214 | 0 | 1 | 0 | 213 | 1 | 0 | 0.995 | 1.000 |
| NB19271 | f011 | 229 | 0 | 5 | 0 | 224 | 5 | 0 | 0.978 | 1.000 |
| NB19271 | f016 | 234 | 0 | 5 | 0 | 229 | 5 | 0 | 0.979 | 1.000 |
| | | 2588 | 9 | 60 | 9 | 2528 | 51 | 0 | 0.980 | 1.000 |

Tubule Detection

As for tubule detection, as more complex and versatile objects, first results based on spatial relationship sound modeling and appropriate triggering in the field of visual reasoning provide clear insights about applications for exploration of huge images like WSIs. Figure 10 shows how it is possible to annotate regions like tubular formations against fat matter zones or simple lumina over the WSI. In addition, Table 4 provides preliminary quantitative assessments of the ontology-driven tubule detection.

Table 2 Preliminary quantitative assessment for the ontology-driven mitosis detection approach: query with intensity and geometrical constraints.

| Image | Frame | Number of cells | Correct Nb of mitoses | Nb of mitoses detected | TP | TN | FP | FN | Specificity | Sensitivity |
|---------|-------|-----------------|-----------------------|------------------------|----|------|----|----|-------------|-------------|
| NB19413 | f001 | 257 | 3 | 2 | 2 | 255 | 0 | 1 | 1.000 | 1.000 |
| NB19413 | f003 | 314 | 2 | 3 | 2 | 311 | 1 | 0 | 0.997 | 1.000 |
| NB19413 | f008 | 296 | 2 | 3 | 2 | 293 | 1 | 0 | 0.997 | 1.000 |
| NB7824 | f001 | 244 | 0 | 0 | 0 | 244 | 0 | 0 | 1.000 | 1.000 |
| NB7824 | f004 | 242 | 0 | 0 | 0 | 242 | 0 | 0 | 1.000 | 1.000 |
| NB7824 | f002 | 297 | 2 | 3 | 2 | 294 | 1 | 0 | 0.997 | 1.000 |
| NB19271 | f002 | 261 | 0 | 5 | 0 | 256 | 5 | 0 | 0.981 | 1.000 |
| NB19271 | f003 | 214 | 0 | 1 | 0 | 213 | 1 | 0 | 0.995 | 1.000 |
| NB19271 | f011 | 229 | 0 | 3 | 0 | 226 | 3 | 0 | 0.997 | 1.000 |
| NB19271 | f016 | 234 | 0 | 0 | 0 | 234 | 0 | 0 | 1.000 | 1.000 |
| | | 2588 | 9 | 20 | 8 | 2568 | 12 | 1 | 0.995 | 1.000 |

Table 3 Preliminary quantitative assessment for the pure signal analysis mitosis detection approach.

| Image | Frame | Number of cells | Correct Nb of mitoses | Nb of mitoses detected | TP | TN | FP | FN | Specificity | Sensitivity |
|---------|-------|-----------------|-----------------------|------------------------|----|------|----|----|-------------|-------------|
| NB19413 | f001 | 257 | 3 | 5 | 3 | 252 | 2 | 0 | 0.992 | 1.000 |
| NB19413 | f003 | 314 | 2 | 3 | 2 | 311 | 1 | 0 | 0.997 | 1.000 |
| NB19413 | f008 | 296 | 2 | 3 | 1 | 293 | 1 | 0 | 0.997 | 1.000 |
| NB7824 | f001 | 244 | 0 | 7 | 0 | 237 | 0 | 0 | 0.971 | 1.000 |
| NB7824 | f004 | 242 | 0 | 7 | 0 | 235 | 7 | 0 | 0.971 | 1.000 |
| NB7824 | f002 | 297 | 2 | 3 | 1 | 294 | 1 | 0 | 0.997 | 1.000 |
| NB19271 | f002 | 261 | 0 | 5 | 0 | 256 | 5 | 0 | 0.981 | 1.000 |
| NB19271 | f003 | 214 | 0 | 5 | 0 | 209 | 5 | 0 | 0.977 | 1.000 |
| NB19271 | f011 | 229 | 0 | 11 | 0 | 218 | 11 | 0 | 0.952 | 1.000 |
| NB19271 | f016 | 234 | 0 | 1 | 0 | 233 | 1 | 0 | 0.996 | 1.000 |
| | | 2588 | 9 | 50 | 7 | 2538 | 41 | 0 | 0.984 | 1.000 |

Table 4 Preliminary quantitative assessment for the ontology-driven tubule detection approach.

| Frame | Number of | Correct number | Number of detected | TP | TN | FP | FN | Specificity | Sensitivity |
|-----------|-----------|----------------|--------------------|----|----|----|----|-------------|-------------|
| Slide 001 | 10 | 7 | 5 | 5 | 3 | 2 | 2 | 0.600 | 0.714 |
| Slide 002 | 25 | 6 | 5 | 5 | 19 | 1 | 1 | 0.950 | 0.833 |
| Slide 003 | 16 | 12 | 13 | 9 | 3 | 4 | 3 | 0.429 | 0.692 |
| Slide 004 | 9 | 5 | 7 | 4 | 2 | 2 | 1 | 0.500 | 0.800 |
| Slide 005 | 17 | 15 | 11 | 10 | 2 | 1 | 5 | 0.667 | 0.667 |
| | 77 | 45 | 41 | 33 | 29 | 10 | 12 | 0.744 | 0.733 |

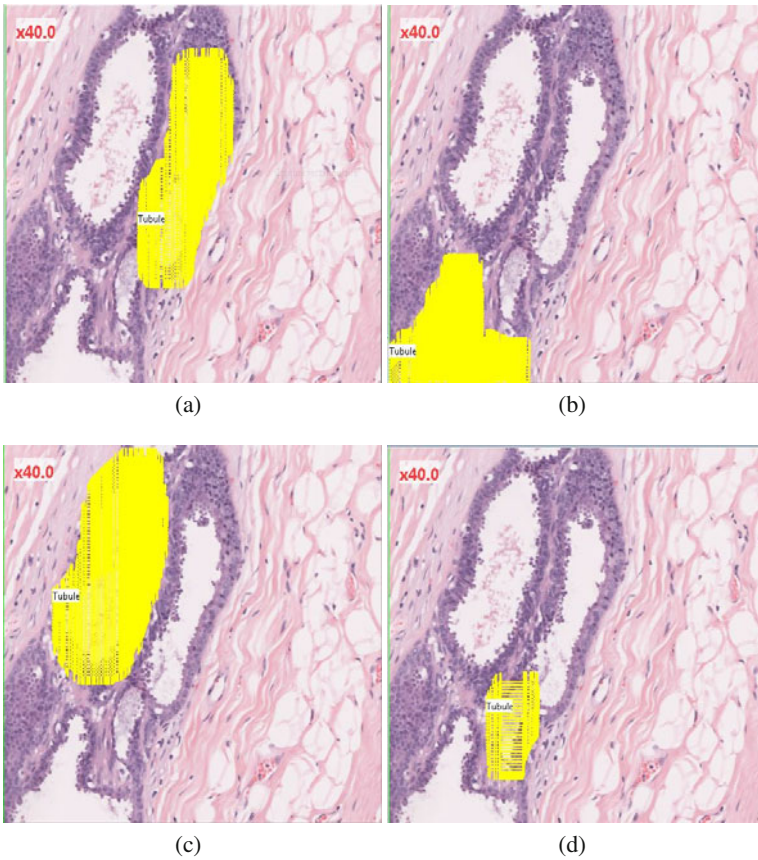


Fig. 10 Examples of tubular detection against mere fat and lumina zones by involving visual reasoning procedure.

Discussion

From a formal point of view, hypothesizing that the nuclei detection is the basic axiom of our system (that is we exclude it from the \mathcal{R}^{signal} set of results) or not, the tubular formation module in our system can be considered either as purely a $\mathcal{R}_{tubule}^{knowledge}$ result or actually a $\mathcal{R}_{tubule}^{signal \times knowledge}$. But as any vision system will need a basic detection module, we consider that the tubule detection module is purely a $\mathcal{R}_{tubule}^{knowledge}$ result. If a low-level, implicit, signal processing was able to provide a $\mathcal{R}_{tubule}^{signal}$ (which might be very challenging according to our experience) then a collaborative synergy between the two approaches could help improve the interaction with and the robustness of the system. This general discussion applies to the mitosis detection case, and in general to all complex biological concepts to be extracted, even discovered, over biological visual material. Thence, the global formalization

of $\mathcal{R}_{object}^{signal \times knowledge}$ extends itself to any kind of complex, versatile object detection over huge image like in current high-resolution satellite images database.

6 Conclusion

While developing a new paradigm of virtual cognitive microscope for the exploration of high-content microscopy images, we proved that articulating knowledge management capabilities with low-level image analysis modules can not only improve the design of the system but as well increase the performance of the system. In particular, when the high-level reasoning module can rely on fair low-level segmentation outcomes, the knowledge - and so the user - in the loop can increase the specificity rate of the system for mitosis detection for instance. In addition, high-level semantic queries are made available by the formalization of spatial relationships between biological objects. This kind of spatial reasoning is a definite asset to discriminate structures from a structural point of view much more than from a purely radiometric one like tubular against fat zones or, as a perspective, subtle differences related to Ductal Carcinoma in Situ.

References

- [Dalle et al. 2008] Dalle, J.-R., Leow, W.-K., Racoceanu, D., Tutac, A.E., Putti, T.C.: Automatic breast cancer grading of histopathological images. In: IEEE Engineering in Medicine and Biology Society, Vancouver, BC, Canada, pp. 3052–3055 (2008)
- [Dalle et al. 2009] Dalle, J.-R., Li, H., Huang, C.-H., Leow, W.-K., Racoceanu, D., Putti, T.C.: Nuclear Pleomorphism Scoring by Selective Cell Nuclei Detection. In: IEEE Workshop on Applications of Computer Vision, Snowbird, Utah, USA (2009)
- [Frkovic-Grazio et al. 2002] Frkovic-Grazio, S., Bracko, M.: Long term prognostic value of Nottingham histological grade and its components in early (pT1N0M0) breast carcinoma. *Journal of Clinical Pathology* 55(2), 88–92 (2002)
- [Gianni et al. 2010] Gianni, D., McKeever, S., Yu, T., Britten, R., Delingette, H.: Sharing and reusing cardiovascular anatomical models over the Web: a step towards the implementation of the virtual physiological human project. *Philosophical Transactions of The Royal Society A* 368, 3039–3056 (2010)
- [Hudelot et al. 2008] Hudelot, C., Atif, J., Bloch, I.: A spatial relation ontology using mathematical morphology and description logics for spatial reasoning. In: ECAI Workshop on Spatial and Temporal Reasoning, pp. 21–25 (2008)
- [Klipp et al. 2010] Klipp, J., Kaufman, J.: Adoption trends in digital pathology. *Laboratory Economics* 5(6), 3–10 (2010)
- [Lomenie 2010] Lomenie, N.: Reasoning with spatial relations over high-content images. In: IEEE World Congress on Computational Intelligence - International Joint Conference on Neural Networks, Barcelona, Spain (2010)
- [Mechouche et al. 2009] Mechouche, A., Morandi, X., Golbreich, C., Gibaud, B.: A hybrid system using symbolic and numeric knowledge for the semantic annotation of sulcogyral anatomy in brain MRI images. *IEEE Transactions on Medical Imaging* 28(8), 1165–1178 (2009)
- [Miikkulainen et al. 2005] Miikkulainen, R., Bednar, J.A., Choe, Y., Sirosh, J.: *Computational Maps in the Visual Cortex*. Springer, Heidelberg (2005)

- [Othmani et al. 2010] Othmani, A., Meziat, C., Lomenie, N.: Ontology-driven Image Analysis for Histopathological Images. In: ISVC 2010, International Symposium on Visual Computing, Las Vegas, USA, p.12 (December 2010)
- [Roux et al. 2009] Roux, L., Tutac, A., Lomenie, N., Balensi, D., Racoceanu, D., Leow, W.-K., Veillard, A., Klossa, J., Putti, T.C.: A Cognitive Virtual Microscopic Framework for Knowledge-based Exploration of Large Microscopic Images in Breast Cancer Histopathology. In: IEEE Engineering in Medicine and Biology Society, Minneapolis, Minnesota, USA (September 2009)
- [Schnorrenberg 1996] Schnorrenberg, F.: Comparison of manual and computer-aided breast cancer biopsy grading. In: Proceedings of the 18th IEEE International Conference of Engineering in Medicine and Biology Society, pp. 1166–1167 (1996)
- [Tutac et al. 2008] Tutac, A.E., Racoceanu, D., Leow, W.K., Dalle, J.R., Putti, T., Xiong, W., Cretu, V.: Translational Approach for Semi-Automatic Breast Cancer Grading Using a Knowledge-Guided Semantic Indexing of Histopathology Images. In: MIAAB-MICCAI Workshop, New-York, USA (2008)
- [Wu et al. 2006] Wu, C., Aghajan, H.: Using Context with Statistical Relational Models - Object Recognition from Observing User Activity in Home Environment. In: Workshop on Use of Context in Vision Processing (UCVP), ICMI-MLMI (November 2009)

Computational Approaches for the Processing of Cerebral Histological Images of Small Animals

Julien Dauguet

Abstract. Histological sections of tissue have been studied for many decades and constitute one of the most prevalent means of information on biological processes and functions for animals. With the introduction of digital images in medicine, image processing techniques derived from medical imaging were adapted to scanned histological sections in order to improve their visualization and analysis. More recently, the introduction of virtual microscopy yet increased the interest of analyzing histological sections on a computer screen and opened up a whole branch of biomedical image processing dedicated to the extraction of information contained in histological sections at very high magnification. In this work we present three novel approaches to study histological sections of the brain in small animals: 1) the alignment of histological sections to create a 3D image, 2) the processing of very large microscopy sections and 3) the correlation of histological sections with 3D *in vivo* images acquired on medical imaging devices.

1 Introduction

1.1 *Brief History of Histology*

The observation of organs and tissues is one of the most ancient ways of studying life mechanisms. The histology is the scientific discipline associated with the observation of tissues, and has been for a long time one of the only ways to understand the processes underlying the function of animals and plants, as well as the most reliable way of characterizing pathological states. Classically, tissue samples are prepared on a thin glass slide so as to be observed through a microscope. Samples have to be cut in very thin slices (a few tens of microns maximum) because light needs to

Julien Dauguet
CEA-CNRS, MIRCen, Route du Panorama,
92265 Fontenay-aux-Roses, France
e-mail: julien.dauguet@cea.fr

pass through the sample to get a clear image of it via the lens of the microscope. Besides, at high magnification, getting a sharp focus everywhere is not possible if too many layers of cells superimpose. The raw thin section is however not easy to study since the enormous number of micro structures observable at high resolution are all mixed together and difficult to differentiate one from another. This is the reason why Golgi's discovery of gold staining (called *reazione nera*: the black reaction) that marked the nervous cells nucleus ([18]) at the end of the XIXth century, can be considered as the starting point of the histology for neuroscience as we understand it today. Shortly after, Ramon y Cajal ([33]) used Golgi's staining to describe the main components of the brain microanatomy.

After the discovery of Golgi's gold staining to mark neurons, many other stains have been developed and used to selectively highlight a specific population of cells, receptors, neurotransmitters, organelles or almost any biological structures that can be of interest to understand brain functions or to characterize a pathological state. There are many stains commonly used in neuroscience histology laboratories, like Nissl staining, acetylcholinesterase, hematoxylin and eosin (*H&E*) to cite a few. Staining can be obtained simply by using a dye which will colorate the section after immersion, but it can also be a more complex process, called immunohistochemistry. This process detects specific antigens by using corresponding antibodies conjugated with an enzyme or tagged with fluorophore in order to observe the binded antibodies. This technique not only detects specific structures (cells, proteins), but can also detect specific states of cells like proliferation, death, or some biomarkers specific to a particular disease, such as the protein aggregates for neurodegenerative diseases.

The microscope classically used to observe a histological section is the optical microscope. There exists several types of optical microscopes, the most common one being the bright field microscope. Another optical microscope commonly used today is the fluorescent microscope with which fluorophores can be excited and observed. For the visualization of 3D processes, the confocal microscope uses a special technique to select successively specific planes of focus within a thick slice, so that to eventually produce a 3D representation of objects. The optical microscope is a powerful tool to observe microorganisms but it has limitations in terms of resolution due to the wavelength in the optical range: the maximum resolution than can be achieved is approximately 0.2 microns. Some micro-particles of interest in the brain are actually much smaller, like the neurotransmitters between synapses.

Another class of microscopy technique is the electron microscopy. In this technique, photons are replaced by a beam of electrons, and this overcomes the resolution limitation, since electron microscopy resolution can be up to a thousand times higher than optical microscopy resolution. Electron microscopy is thus well adapted to the observation of very fine processes in the brain. However, the experimental setup and the preparation of the sample is more complex than it is for optical microscopy.

1.2 From Sections to Images

Originally, observations done on histological slices were shared with peers by making drawings of them. For instance, Golgi and Ramon y Cajal were known for their famous drawings of the architecture of the brain that they made from their observations using the microscope (see **Figure 1**).

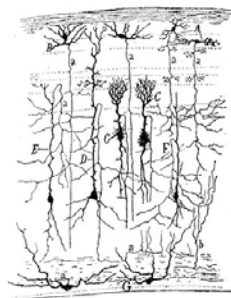


Fig. 1 Drawing of a section through the optic tectum of a sparrow, from "Structure of the nervous centres of the birds", by Santiago Ramon y Cajal, 1905.

The *camera lucida*, or light room, is an optical device that can be attached to a microscope or directed towards a histological slice and which superimposes the scene on the paper sheet to make the drawing easier to complete. This technique has been used for many decades and is still used today to facilitate illustrations. In parallel, photographs of the slice, and the technique of the micrograph attached to the microscope eyepiece, were used to get a picture of the tissue. These images were mostly used for illustration purpose and rarely used for the analysis itself, as the quality of the image was not as good as that which could be achieved directly on the microscope or on the actual slice.

It is only recently that histological images have started to be digitized, either by high quality scanners or by directly using a camera linked to a computer. For a long time, it was common to get either a gross picture of the whole slice acquired with a flatbed scanner, or a high resolution image of a particular sub region inside the slice with the camera attached to the microscope.

The digitization of the images opened the door to the computational image processing techniques that were already in use in medical imaging with Magnetic Resonance Imaging (MRI), Computer Tomography (CT), Positron Emission Tomography (PET) scans, or ultrasound (US) images, all of which are intrinsically digital images, obtained by mathematical reconstruction of a physical signal. When studying whole slices, the digital analysis remained performed at relatively low scale, because of the somehow limited resolution (tens of microns) of the slice scanners at the time. When one needed to perform a high resolution analysis of the section, a microscope was used and the analysis was usually limited to one or multiple small regions corresponding to the field of view at the chosen magnification. Local results had then to be extrapolated to the whole slice using models such as stereology.

1.3 *Virtual Microscopy, Digital Microscopy*

The rather recent introduction of devices capable of acquiring a whole section at very high resolution has greatly increased the power of analysis of histology. There exists at least two ways of acquiring whole slice high resolution scans.

One way is called mosaicing, which consists of montaging several high resolution sub images (each of them covering a small field of view) so as to form a large high resolution image covering the whole slice (see **Figure 2**). This technique has the advantage of being rather inexpensive since it uses a classical microscope with a motorized platine, and the final reconstructed field of view is virtually unlimited. However, some issues can occur from assembling the images.

Another way of proceeding is to use a whole slice high resolution scanner, which is similar in its use to a classical flatbed scanner except that it has a special optical system which offers high resolution scans (magnification $\times 20$, even $\times 40$) comparable in terms of quality of image to that which can be obtained with a microscope.

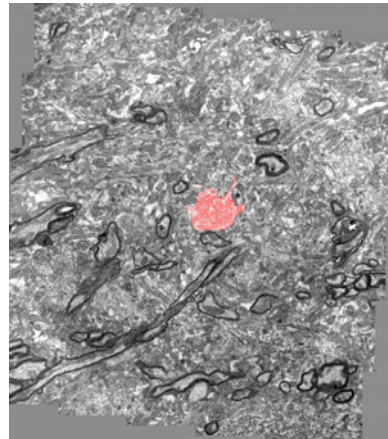


Fig. 2 A large electron microscopy image acquired in mosaic mode (source [11]).

The direct benefit of these new scanning methods for the anatomico-pathologist is to avoid the necessity of his having to keep his eyes on the microscope, to facilitate the study of the slice (especially the navigation within the slice, or from one slice to another, the change of the magnification, of the contrast, the elimination of photobleaching due to repeated exposure of fluorescent slides, the recording of measurements, the saving of snapshots). With digital microscopy whole slice acquisition, one is also able to study the section remotely from anywhere in the world, and share the image with people via the internet, hence the name virtual microscopy ([28]).

In terms of image processing and analysis, the great benefit of these large image digital microscopy devices is that they offer the opportunity to use computational

techniques to address new questions, based on the high resolution information of whole histological sections.

The goal of this chapter is to present some of the new computational approaches to studying histology which emerged with the digitization of whole histological slices, either at low resolution or potentially at very high resolution, and to discuss the new challenges they raise.

2 3D Reconstruction of Series of Histological Slices

The first new approach of studying histology is the 3D reconstruction of a histological volume from a series of sections. This consists of performing the alignment of the series of slices by estimating the transformation that best superimposes one slice onto the next one, and by propagation, obtaining a spatially consistent volume after direct stacking of the registered images.

This technique assumes that a series of successive histological slices (whole slices or a consistent subregion through the series) spanning the whole brain or a big part of it, is available. The slice is not necessarily acquired at very high resolution with a microscope or a high resolution scanner, but the scanning resolution has to be good enough to perform tracing of structures of interest or provide informative measurements (volume, density of staining, activity on autoradiographs), which typically means of the order of 10 microns.

This technique adds another dimension to the study of successive slices. Its main contribution is that it becomes possible, first, to virtually reslice the brain in any desired plane different from the cutting plane, and second, to consider the series of histological slices as a 3D volume, thus enabling 3D analysis.

The early methods to perform 3D reconstruction of histological slices were manual ([23], [34]). Then, automated methods were developed, either relying on linear transformations to perform the alignment ([19], [2], [35], [30], [26], [4]) or piecewise affine ([3], [32], [9]), or using non linear transformations ([22], [27], [36], [6]).

The applications described here rely on the 3D properties of a histological volume.

2.1 3D Region of Interest

The direct application of the creation of a histological 3D volume is the tracing of 3D regions of interest. This has several advantages, namely:

- helping the delineation of an accurate region: when one needs to draw a specific structure of interest which is a spatial object, it is difficult to apprehend it from the only 2D cutting plane projection. With the reconstructed 3D histological volume, one can switch from one view to another orthogonal view, or potentially any oblique view, as can be done with an MRI scan. This is of great help in order

to render the 3D configuration of the object. This technique is a good way to consolidate the segmentation.

- finding the real counterpart of a specific region: it is often useful in neurobiological studies involving histology to compare a region in one hemisphere to the symmetrical region in the other hemisphere. Classically, the brain is then cut in coronal incidence with each section perpendicular to the antero-posterior axis of the brain. The symmetrical region traced on a 2D slice is then obtained by doing the 2D symmetry in the slice. However, the actual cutting plane is often slightly tilted relatively to the antero-posterior axis, resulting in an inaccurate definition of the symmetrical region. When working with a 3D histological volume, it becomes possible to apply the real symmetry to a 3D region with respect to the mid sagittal plane, thus obtaining the accurate symmetrical region.

An example that illustrates this 3D delineation of region of interest can be found in [16]. Note that in this example, the segmentation of the colliculus region is made on the histological slices stained with cresyl violet, and then used on the autoradiographs to measure glucose consumption.

2.2 Using 3D Atlases

The previous subsection was dealing with one, or a few manually segmented region(s) of interest. We will describe here how a fully automated and complete segmentation of histological slices can be performed thanks to the 3D properties of the histological volume. This is again inspired by the use of 3D atlases as it is done in medical imaging (MRI, CT scans). If a 3D atlas is created based on one specific subject, or a template subject (average of many subjects), the atlas can be warped to fit another given subject providing it is somehow similar (species, age, pathological state). The warping transformation is a 3D transformation that deforms the different regions of the template image - and therefore of the atlas - so that they match the structures of the given image. Such a transformation can not be estimated in 2D between a template slice and a particular slice of the given subject. In fact, because of the differences in the cutting planes, the interindividual particularities, and the mechanical deformations due to the histological processing, none of the slices from the template subject can be matched precisely with one particular slice of the given subject using a 2D transformation only.

An example of the use of a 3D atlas to segment more than 30 anatomical structures of a mouse brain can be found in [24]. Note that in this study, the atlas was not created on a histological volume but on a high resolution post mortem MRI.

When possible, photographs of the brain during the cutting process are taken. They are often referred to as blockface photographs, or cryosections when the brain is frozen. Each photograph is taken prior to cutting, and corresponds exactly to the section about to be sliced, which at the time of the photograph, is still attached to the brain block. The tissue deformations are much smaller on the photographs than on the histological slice, and when taken in good conditions, the direct stacking of the photographs leads to a photographic volume with no need for alignment. It

then serves as a shape reference to build the histological volume. The series of photographs is also very useful because it can serve as a reference image to estimate the warping transformation of the atlas to the given subject. As a consequence, there is no need for staining and mounting on glass slides the complete series of histological slices spanning the whole brain, which can be a very time consuming work. Indeed, once the 3D atlas is warped into the geometry of the photographic volume, there is a direct correspondence between the histological slices and the resampled slices of the atlas. Any isolated histological slice, or group of slices, can then benefit from the estimated transformation (see **Figure 3**), and thus be segmented. This is of particular interest when only a subregion of the brain is to be studied.

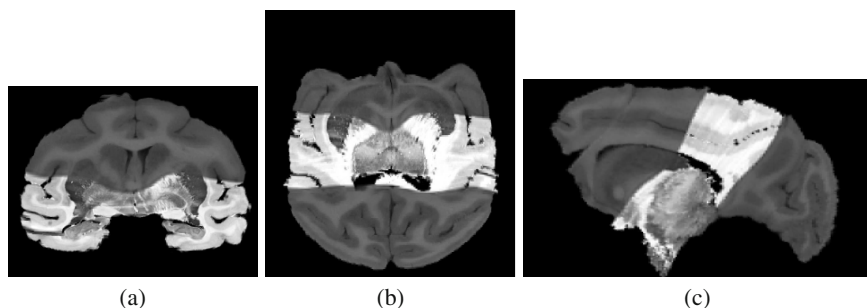


Fig. 3 Macaque brain hybrid histological volume made of stained histological slices (in the center of the brain), and blockface photographs (posterior and anterior part) in coronal (a), axial (b) and sagittal (c) views. The volume has been warped to match the MRI scan.

This technique of using 3D atlases makes the extensive comparison of populations of subjects in multiple anatomical regions possible in a rapid and automated fashion.

2.3 *Voxel-Wise Statistical Comparison*

The previous subsection described how it became possible to segment automatically anatomical structures on one or a series of 2D histological slices in order to compare different specific regions between groups. We will now consider another kind of analysis which is commonly performed in studies involving functional Magnetic Resonance Imaging (fMRI) or PET images *in vivo*. The idea is to compare two populations of subjects which have been spatially normalized (registered to a template image) beforehand with no *a priori* assumption on the region where differences could occur. The series of signals measured in each location (or voxel) for each subject of one population is statistically compared to the corresponding series at the same location for the other population. Voxels showing significant differences are gathered into clusters, which are eventually displayed in the geometry of the

template. This method is very interesting for exploring a whole volume since it automatically detects places of differences, potentially in areas that were a priori not suspected of being involved in the experiment. It is possible to lead voxel wise statistical comparisons on histological volumes and therefore automatically detect with no a priori subtle differences between populations in terms of: intensity of staining (representing a particular density of microorganisms), glucose consumption on autoradiographs, and even potentially morphometry (differences in the average size of some regions). A study based on a voxel wise statistical comparison performed using the Statistical Parametric Mapping software (SPM) and histological volumes can be found in [17].

This section closes the non-exhaustive list of new possibilities offered by the 3D reconstruction of a histological volume from a series of digital slices scanned at macroscopic resolution. In the next section we will consider not only digital slices but very high resolution scans with microscopic quality as well.

3 Large Dimensions Microscopy Images

As mentioned in the introduction, many microscopes now have the ability to produce large images in mosaic mode, which means that they can produce a very large image from an assemblage of small field of view images stitched together. High performance whole slide scanners can produce very high magnification scans of histological slices and are usually faster and easier to use than motorized microscopes. These large image microscopy techniques have developed greatly thanks, in part, to the drop in storage prices, the increase of the computer *Read Only Memory* (RAM), the common use of clusters of CPUs, and high speed network communication. The information enclosed in these high dimension microscopy images is tremendous and gives access to the global micro-organization inside the brain. Whereas studying small subregions of the brain under a microscope is time consuming but remains doable *manually*, the fine analysis of this type of large images is hard to envision without resorting to computational approaches.

The goal of this subsection is to briefly describe some of the new computational approaches that have been developed, or are still in active development, to deal with the study of large microscopy images.

3.1 Viewing Large Images

Most classical biomedical image viewers are not adapted to display very large images, one of the main reasons being that they usually have to load the whole image in the computer RAM, which is often not big enough. Similar problems have arisen in other scientific domains (e.g. satellite images, <http://iipimage.sourceforge.net/>),

so that the same strategies can be used and some large histological image viewers are already available, either associated with scanners or microscopes from private companies (*NDP.view* from Hamamatsu Photonics, Hamamatsu, Japan, *Olyvia* from Olympus, Tokyo, Japan, *ImageScope* from Aperio, Vista, USA, to cite a few) or from academia (e.g. the V3D viewer, [31]). The challenges are multiple since each 2D microscopy slice is huge, but neurobiologists are interested in viewing a series of slices at several levels, and possibly comparing two or more different stainings. The visualization problems then become quite complex, especially because real time navigation is needed as well.

3.2 Processing Large Images

Most image processing algorithms will not work properly with very large microscopy images: they can either just fail, because for example they need to invert a matrix that becomes too large for the solver capacity, or they can be very slow because memory access becomes an issue, or because they have to process serially the data. We will present a few methods that overcame some of the difficulties of processing large images.

3.2.1 Registration

Two major situations will be considered: registering a pair of slices, or having to deal with the alignment of a series of slices for 3D reconstruction. We will not discuss here the registration or alignment of large 3D images (or even nD images), nor the methods to perform the assemblage of the tile images to create the large image.

Pair of Slices

Estimating a spatial transformation to correlate the signal of two histological slices - also called registering - is essential prior to some types of cross analysis. The two slices to register can be the same physical section scanned in different conditions (e.g. two different fluorescence wavelengths), in that case a simple rigid or affine registration can usually be used to superimpose both signals together. However, slices can be two different physical sections (e.g. one section and the immediate next one), or they can be the same physical section but the several staining processes and the scanning procedure may have introduced mechanical distortions to one of the images (e.g. two different microscopes were used with different stitching methods). In that case, non-linear distortions have to be corrected using non-linear registration methods.

Several strategies for the registration of very large microscopy images can be chosen.

One simple strategy consists of downsampling the two images to some manageable size images, and performing registration with regular algorithms. However, this still implies that some resample algorithms able to deal with large images are available. Moreover, the registration performed using down sampled versions of the original images obviously lacks precision since it does not use the original information.

Another strategy consists of dividing the images into smaller images that are easier to deal with, then performing the registration of each pair of sub images, and then working on the global transformation to make it continuous. This idea was developed in [11] for large Electron Microscopy images.

Finally, another strategy consist of extracting a reasonable number of corresponding salient region from both images and trying to match them ([11]). This strategy has the advantage of being almost independent of the resolution of the images, but on very large images, the number of necessary salient regions can potentially become a problem.

Series of Slices

To get a general understanding of the micro organization of the brain, knowing the 3D configuration of structures, such as axons or synapses, is a great asset. Creating a histological volume out of very large images is theoretically feasible, similarly to what is done on *regular size* images, or macroscopic images, providing strategies to deal with very large images are used. This has actually already been done to some extents using strategies described in the previous paragraph (see **Section 4**). The new challenge that scientists are facing is related to the size of the stack. Since we are considering very high resolution images, the in-plane resolution of each slice is very fine (typically smaller than 1 micron in optical microscopy, closer to the nanometer for electron microscopy), so that in order to be spatially consistent, the thickness of each section and/or the inter slice spacing should be of the same order of magnitude, thus very small. As a consequence, the number of slices to consider in the stack becomes very big as well. For instance, to capture a still relatively small volume of contiguous electron microscopy slices of size $50 \times 50 \times 50 \mu\text{m}^3$ with an in plane resolution of $5 \times 5 \text{nm}^2$ and a slice thickness of 50nm , the dimensions of the final volume are $10,000 \times 10,000 \times 1,000$. The alignment of such a number of slices with no reference becomes problematic because of the composition of numerous transformations (in this example up to 1,000 transformations) and the unavoidable propagation of error.

3.2.2 Segmentation

The section above discussed techniques to superimpose different types of information together, or to create a 3D histological block, which is the preliminary step before analysis. Analysis of histological sections is usually performed manually by

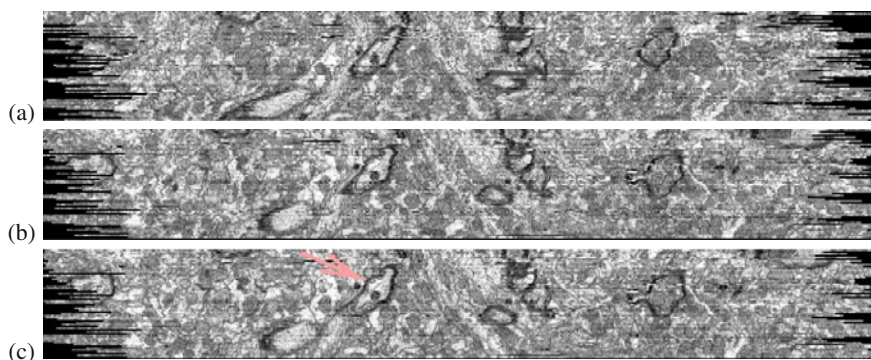


Fig. 4 Orthogonal views of a aligned stack of electron microscopy images of the lateral geniculate nucleus of a ferret using manual (a), affine (b) and elastic (c) transformations. The Arrow indicates structures which appear smoother on the elastic alignment. Each 2D image is 100 Mpixels.

a neuroanatomist expert looking at the sections at very high resolution. Yet, as we said, the tremendous amount of data that new microscopic acquisition devices can produce requires automated analysis. One of the first steps leading to automated analysis consists of identifying objects of interest and segmenting them in order to evaluate meaningful statistics. Quantitative values such as relative densities of cells, morphometric parameters, correlation of the presence of objects can be derived from segmentations. The segmentation problem appears less difficult than the registration problem since it can be turned into multiple local segmentations problems. However, once again, the continuity of the results especially for objects belonging to multiple regions of analysis, is problematic. In this field, the methods can be very specific to the desired application: it is quite a different problem to extract activated astrocytes in a series of histological images acquired in light microscopy compared to segmenting synapses and myelinated axons in electron microscopy images. Even if some efficient methods are available (see for instance [25] and [29]) for 3D segmentation on confocal images), most of them were not used on very large images, and there is still a lot of efforts to be put into this research area.

4 In Vivo / Post Mortem Correlation

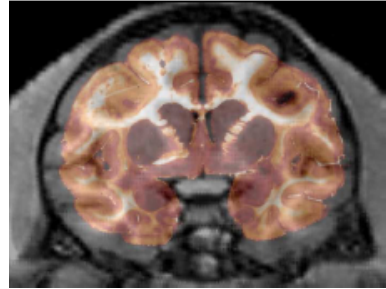
Correlating and comparing the signal from histological slices to the signal from in vivo imaging techniques such as MRI is fundamental in neurodegenerative diseases research and in neuroscience in general. In fact, histological slices are usually considered as the richest and the most reliable source of biological information as far as anatomy and architecture of the brain are concerned (as opposed to functional and behavioral information which is usually better evaluated in vivo). Consequently, histological signal is then used to check the validity and the accuracy of what can be

measured with in vivo imaging, or it is used to provide the information about what can not yet be seen in vivo. Whereas in most studies a simple somehow approximative comparison with one or a few histological slices is sufficient to establish the correlation, some studies require a more global, accurate and quantitative level of correlation.

4.1 *Estimation of a 3D Warping Transformation to Correct the Deformations*

As classified in [9], the brain undergoes two types of deformations during histological preparation: the primary and the secondary deformations. The latter are 2D deformations and include the loss of spatial consistency due to cutting. We saw in the first section how to deal with these secondary deformations using techniques for the 3D reconstruction of a consistent volume out of series of histological slices. The primary deformations are 3D deformations that occur between the time of the sacrifice and before the brain is cut. Primary deformations are mainly due to: the loss of irrigation, the fixation, the mechanical deformations resulting from the manual handling of the brain, and the freezing or paraffin embedding. The main effect of these primary deformations is a global shrinkage of the histological brain compared to the in vivo brain (see **Figure 5**).

Fig. 5 Fusion of a baboon brain stained histological slice (false color orange) and an in vivo MRI of the same animal. The shrinkage of the post mortem brain due to histological processing is clearly visible (source [8]).



The use of a 3D non-linear deformation is necessary to correct the primary deformations. Quite a few techniques have been proposed to achieve this matching between the histological and the MRI of the same subject (3D affine transformations: [30], [26], [4]; 3D non-linear transformations: [7], [36], [9], [5]). Most correlations were performed for primates since the relative resolution of in vivo imaging was not good enough for rodents till rather recently. High field MRI being more and more common, in vivo/ post mortem correlation for rodents is now performed rather commonly. Rodent's brains are from an anatomical point of view considered simpler than primates', essentially because of the almost lack of cerebral convolutions, inducing deformations of smaller magnitude. However, the contrast and the signal

of in vivo images are still of inferior quality compared to those of primates. This makes the estimation of the matching transformation more difficult, due to the big differences in terms of geometry, resolution, contrast and type of signal compared to the histological slices. Some work has explicitly been done to directly tackle these issues, adding control and a priori information to help estimate the warping transformation ([13]). The correction of the primary deformations is the necessary step to matching the histological volume to the in vivo volume, and then being able to correlate the two imaging modalities.

4.2 Correlation for Comparison

We will consider in this subsection the use of the histological signal as a gold standard for comparison with in vivo imaging techniques.

4.2.1 Validation of Signal

A natural question when using an in vivo imaging technique is how to interpret the signal. The signal of most of the classical imaging techniques is well known (e.g. grey/white matter in MRI, bones in CT) and it is used in clinical routine to diagnose diseases. However, thanks to the biological and technical progresses, imaging protocols are constantly evolving in order to study a particular disease in more details, requiring new validations of the acquired signal. For instance, in neurodegenerative disease research, finding and validating a way to detect amyloid plaques in Alzheimer disease (AD) patients using T1 and T2 weighted MRI is an active research field ([15]). The validation of the in vivo imaging signal by the information derived from histological slices is a big application of the in vivo / post mortem matching.

4.2.2 Validation of an Imaging Marker

Imaging markers represent another large category of imaging studies where there is an important need of validation. Imaging markers are agents injected to the subject to enhance the signal of a particular population of cells, receptors, or proteins. They are similar to stainings for histology. However, the difficulty in vivo is that it is very difficult to predict the behavior of the marker in living physiological conditions, especially in the brain, because of the blood brain barrier. The comparison between the signal obtained in vivo with this marker on one hand, and a known histological staining with the same target on the other hand, is thus necessary for a complete validation (e.g. validation of a AD PET marker, [20]). This can be achieved much more accurately thanks to the 3D vivo/post mortem matching compared to a 2D slice to in vivo volume comparison.

4.2.3 Validation of Models

A last application of *in vivo* / post mortem matching is the validation of computational models, such as simulations or image reconstruction techniques. An important area of research in this field concerns the tractography of white matter bundles based on Diffusion Weighted Imaging (DWI) signal. Based on a measure of the diffusion coefficient of water estimated using diffusion weighted MRI, many algorithms have been proposed to reconstruct the underlying fibers, and thus gain access to the white matter connectivity of the brain in a non-invasive way. However, these techniques have not yet been completely validated, and because of the intrinsically 3D configuration of fibers, the correlation of histological and MRI volumes for comparison is particularly well suited. Some efforts to propose a validation of tractography techniques are pursued using classical histological neural marker ([10]).

4.3 Correlation for Improved Information

Finally, histological slices can be used to add information that can not be obtained from *in vivo* imaging. An example of this use of histology is the use of anatomical atlases, superimposed on MRI images to delineate fine structures that can not be seen *in vivo*. Here again, working in 3D with an accurate matching is absolutely necessary. For instance, we can cite the segmentation of the subnuclei of the thalamus to drive PET measurements (see **Figure 6**).

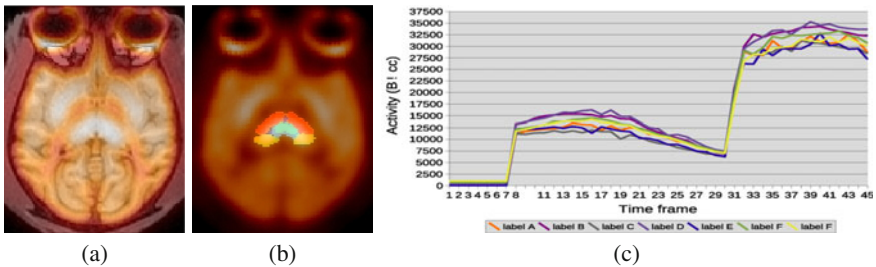


Fig. 6 Matching of a PET FDG A85 scan with the MRI data for a baboon (a), a thalamus atlas made on the histology mapped onto the PET FDG A85 scan (b) and individual kinetics of the thalamus nuclei derived from the atlas (c) (irregular temporal frame spacing: inter-frame spacing approximately 5min)(source [12]).

Another information of great interest (to locate fMRI activation for example) is the cortex layers and cortex areas of the brain. The layers are surfaces and the areas are complex 3D regions, and they can only be identified on the histology so far. In [5], area 46 and layer I of VI are identified on histological slices and mapped onto the MRI of the same monkey.

5 Conclusion

It is possible today to make very precise *in vivo* observations of the brain, and of the body in general, thanks to the development of non-invasive or minimally invasive imaging techniques (e.g. Magnetic Resonance Histology, MRH, [21]). These high performance *in vivo* imaging devices are powerful tools to understand the development of the brain and ultimately diagnose neurodegenerative diseases earlier.

However, histology is the oldest form of imaging and still remains the essential reference for brain research on neurodegenerative diseases. In this chapter we described novel approaches to the use of histology for neurodegenerative disease research, based either on macroscopic slices, or microscopic slices potentially in combination with *in vivo* imaging for translational research. These new approaches extend the information that can be derived from histology, and help make experiments more efficient and reliable.

Future work will include the macro to nano correlation so as to understand the influence of the micro-organization of the brain on the macroscopic *in vivo* imaging signal.

The interpretation of the series of digitized histological sections might be hampered by:

- The loss of the 3D spatial consistency compared to the intrinsically 3D images acquired with medical imaging devices like MRI;
- The difference of geometry and shape between the brain acquired *post mortem* and the *in vivo* images as illustrated in Figure 5;
- The difference of signal and resolution between the stained histological slices and the medical images such as MRI.

Acknowledgements. The author would like to thank people at MIRCen for the scientific collaborations.

References

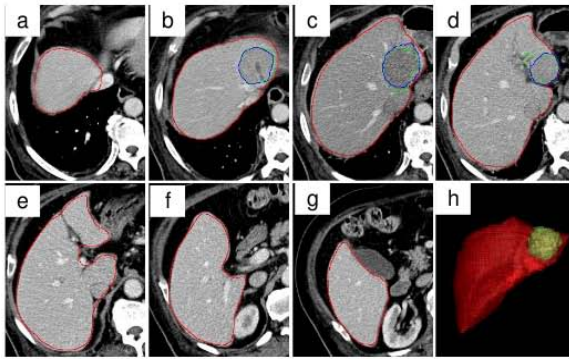
1. Akselrod-Ballin, A., Bock, D., Reid, R.C., Warfield, S.K.: In: Proceedings of IEEE International Symposium on Biomedical Imaging (ISBI 2009), Improved registration for large electron microscopy images, Boston, MA, USA, pp. 434–437 (2009)
2. Andreasen, A., Drewes, A.M., Assentoft, J.E., Larsen, N.E.: Computer-assisted alignment of standard serial sections without use of artificial landmarks. A practical approach to the utilization of incomplete information in 3-D reconstruction of the hippocampal region. *Journal of Neuroscience Methods*, 45(3),199–207 (1992)

3. Arsigny, V., Pennec, X., Ayache, N.: Medical Image Analysis, Polyrigid and Polyaffine Transformations: a Novel Geometrical Tool to Deal with Non-Rigid Deformations - Application to the registration of histological slices 6(9), 507–523 (2005)
4. Bardinet, E., Bhattacharjee, M., Dormont, D., Pidoux, B., Malandain, G., Schupbach, S., Ayache, N., Ornu, P., Agid, Y., Yelnik, J.: A three-dimensional histological atlas of the human basal ganglia. II. Atlas deformation strategy and evaluation in deep brain stimulation for Parkinson disease. *Journal of Neurosurgery* 2, 208–219 (2009)
5. Ceritoglu, C., Wang, L., Selemon, L.D., Csernansky, J.G., Miller, M.I., Ratnanather, J.T.: Large deformation diffeomorphic metric mapping registration of reconstructed 3D histological section images and in vivo MR images. *Frontiers in Human Neuroscience* 5, 12 (2010)
6. Chakravarty, M.M., Bertrand, G., Hodge, C.P., Sadikot, A.F., Collins, D.L.: The creation of a brain atlas for image guided neurosurgery using serial histological data. *NeuroImage* 30(2), 359–376 (2006)
7. Christensen, G., Joshi, S., Miller, M.: Volumetric transformation of brain anatomy. *IEEE Trans. Med. Imaging* 16, 864–877 (1997)
8. Dauguet, J.: École Centrale de Paris. L'imagerie post mortem tridimensionnelle cérébrale: constitution et apport pour l'analyse conjointe de données histologiques anatomo-fonctionnelles et la mise en correspondance avec l'imagerie in vivo (2005)
9. Dauguet, J., Delzescaux, T., Condé, F., Mangin, J.-F., Ayache, N., Hantraye, P., Frouin, V.: Three-dimensional reconstruction of stained histological slices and 3D non-linear registration with in-vivo MRI for whole baboon brain. *Journal of Neuroscience Methods* 164(1), 191–204 (2007)
10. Dauguet, J., Peled, S., Berezovskii, V., Delzescaux, T., Warfield, S.K., Born, R., Westin, C.-F.: Comparison of fiber tracts derived from In-Vivo DTI tractography with 3D histological neural tract tracer reconstruction on a macaque brain. *NeuroImage* 37(2), 530–538 (2007)
11. Dauguet, J., Dock, D., Reid, R.C., Warfield, S.K.: Alignment of large image series using cubic B-splines tessellation: Application to transmission electron microscopy data. In: Ayache, N., Ourselin, S., Maeder, A. (eds.) *MICCAI 2007, Part II*. LNCS, vol. 4792, pp. 710–717. Springer, Heidelberg (2007)
12. Dauguet, J., Condé, F., Hantraye, P., Frouin, V., Delzescaux, T.: Generation of a 3D atlas of the nuclear division of the thalamus based on histological sections of primate: intra- and inter-subject atlas-to-MRI warping. In: *IRBM*, vol. 30(5-6), pp. 281–291 (2009)
13. Dauguet, J., Hérard, A.-S., Declerck, J., Delzescaux, T.: Locally constrained cubic B-spline deformations to control volume variations. In: *Proceedings of IEEE International Symposium on Biomedical Imaging (ISBI 2009)*, Boston, MA, USA (2009)
14. Dauguet, J., de Primatologie, R.: Three-dimensional histological imaging of primate brain and correlation with in vivo medical device images 4, 2 (2010), <http://primatologie.revues.org/>
15. Dhenain, M., El Tannir El Tayara, N., Wu, T.D., Guégan, M., Volk, A., Quintana, C., Delatour, B.: Characterization of in vivo MRI detectable thalamic amyloid plaques from APP/PS1 mice. *Neurobiol. Aging* 1, 41–53 (2009)
16. Dubois, A., Dauguet, J., Hérard, A.-S., Besret, L., Duchesnay, E., Frouin, V., Hantraye, P., Bonvento, G., Delzescaux, T.: Automated three-dimensional analysis of histological and autoradiographic rat brain sections: application to an activation study. *J. Cereb. Blood Flow Metab.* 10(27), 1742–1755 (2007)

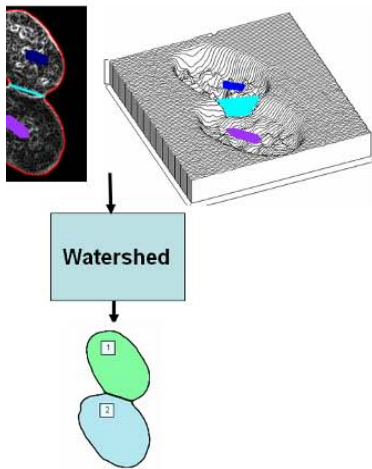
17. Dubois, A., Hérard, A.-S., Delatour, B., Hantraye, P., Bonvento, G., Dhenain, M., Delzescaux, T.: Detection by voxel-wise statistical analysis of significant changes in regional cerebral glucose uptake in an APP/PS1 transgenic mouse model of Alzheimer's disease. *NeuroImage* 51(2), 586–598 (2010)
18. Golgi, C.: On the structure of the brain grey matter. *Gazzetta Medica Italiana lombarda* 6, 244–246 (1873)
19. Hibbard, L.S., Hawkins, R.A.: Objective image alignment for three-dimensional reconstruction of digital autoradiograms. *J. Neurosci. Methods* 26(1), 55–74 (1988)
20. Ikonomic, M.D., Klunk, W.E., Abrahamson, E.E., Mathis, C.A., Price, J.C., Tsopelas, N.D., Lopresti, B.J., Ziolko, S., Bi, W., Paljug, W.R., Debnath, M.L., Hope, C.E., Isanski, B.A., Hamilton, R.L., DeKosky, S.T.: Post-mortem correlates of in vivo PiB-PET amyloid imaging in a typical case of Alzheimer's disease. *Brain* 131(6), 1630–1645 (2008)
21. Johnson, G.A., Cofer, G.P., Fubara, B., Gewalt, S.L., Hedlund, L.W., Maronpot, R.R.: Magnetic resonance histology for morphologic phenotyping. *J. Magn. Reson. Imaging* 16(4), 423–429 (2002)
22. Kim, B., Boes, J.L., Frey, K.A., Meyer, C.R.: Mutual information for automated unwarping of rat brain autoradiographs. *Neuroimage* 5(1), 31–40 (1997)
23. Laan, A., Lamers, W., Huijsmans, D., Kortschot, A.T., Smith, J., Strackee, J., Los, J.: Deformation-corrected computer-aided three-dimensional reconstruction of immunohistochemically stained organs: application to the rat heart during early organogenesis. *The Anatomical Record* 224, 443–457 (1989)
24. Lebenberg, J., Herard, A.-S., Dubois, A., Dauguet, J., Frouin, V., Dhenain, M., Hantraye, P., Delzescaux, T.: Validation of MRI-based 3D digital atlas registration with histological and autoradiographic volumes: an anatomofunctional transgenic mouse brain imaging study. *Neuroimage* 51(3), 1037–1046 (2010)
25. Lin, G., Bjornsson, C.S., Smith, K.L., Abdul-Karim, M.-A., Turner, J.N., Shain, W., Roysam, B.: Automated image analysis methods for 3-D quantification of the neurovascular unit from multichannel confocal microscope images. *Cytometry* 66A, 9–23 (2005)
26. Malandain, G., Bardinet, E., Nelissen, K., Vanduffel, W.: Fusion of autoradiographs with an MR volume using 2-D and 3-D linear transformations. *NeuroImage* 23(1), 111–127 (2004)
27. Mega, M.S., Chen, S.S., Thompson, P.M., Woods, R.P., Karaca, T.J., Tiwari, A., Vinters, H.V., Small, G.W., Toga, A.W.: Mapping histology to metabolism: coregistration of stained whole-brain sections to premortem PET in Alzheimer's disease. *Neuroimage* 5(2), 147–153 (1997)
28. Mikula, S., Trotts, I., Stone, J.M., Jones, E.G.: Internet-enabled high-resolution brain mapping and virtual microscopy. *Neuroimage* 35(1), 9–15 (2007)
29. Indhumathi, C., Cai, Y., Guan, Y., Opas, M.: An automatic segmentation algorithm for 3D cell cluster splitting using volumetric confocal images. *Journal of Microscopy* (in Press)
30. Ourselin, S., Roche, A., Subsol, G., Pennec, X., Ayache, N.: Reconstructing a 3D Structure from Serial Histological Sections. *Image and Vision Computing* 19(1-2), 25–31 (2001)
31. Peng, H., Ruan, Z., Long, F., Simpson, J.H., Myers, E.W.: V3D enables real-time 3D visualization and quantitative analysis of large-scale biological image data sets. *Nat. Biotechnol.* 28(4), 348–353 (2010)
32. Pitiot, A., Bardinet, E., Thompson, P.M., Malandain, G.: Piecewise Affine Registration of Biological Images for Volume Reconstruction. *Medical Image Analysis* 10(3), 465–483 (2006)
33. Ramon y Cajal, S.: *Manual de Histologia normal y Tecnica micrografica* (1889)

34. Rydmark, M., Jansson, T., Berthold, C.H., Gustavsson, T.: Computer-assisted realignment of light micrograph images from consecutive section series of cat cerebral cortex. *J. Microsc.* 165(1), 29–47 (1992)
35. Schormann, T., Dabringhaus, A., Zilles, K.: Statistics of deformations in histology and application to improved alignment with MRI. *IEEE Trans. Med. Imaging* 14(1), 25–35 (1995)
36. Schormann, T., Zilles, K.: Three-Dimensional Linear and Nonlinear Transformations: An Integration of Light Microscopical and MRI Data. *Human Brain Mapping* 6, 339–347 (1998)

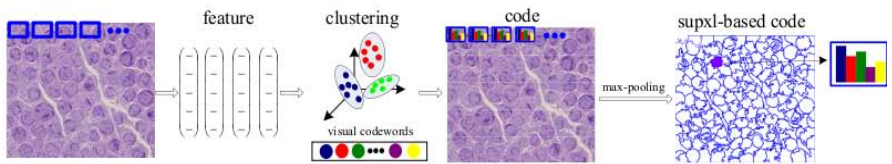
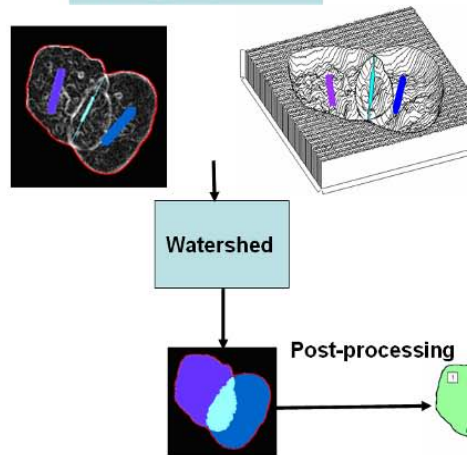
Part IV
Image Analysis



Aggregated Nuclei



Overlapping Nuclei



Liver Workbench: A Tool Suite for Liver and Liver Tumor Segmentation and Modeling

Jiayin Zhou, Wei Xiong, Feng Ding, Weimin Huang, Tian Qi, Zhimin Wang, Thiha Oo, and Sudhakar Kundapur Venkatesh

Abstract. Robust and efficient liver and tumor segmentation tools from CT images are important for clinical decision-making in liver treatment planning and response evaluation. In this work, we report recent advances in an ongoing project *Liver Workbench* which aims to provide a suite of tools for the segmentation, quantification and modeling of various objects in CT images such as the liver, its vessels and tumors. Firstly, a liver segmentation approach is described. It registers a liver mesh model to actual image features by adopting noise-insensitive flipping-free mesh deformations. Next, a propagation learning approach is incorporated into a semi-automatic classification method for robust segmentation of liver tumors based on liver ROI obtained. Finally, an unbiased probabilistic liver atlas construction technique is adopted to embody the shape and intensity variation to constrain liver segmentation. We also report preliminary experimental results.

1 Introduction

The liver is the largest solid organ in the abdomen and is one of the most frequently involved by tumors. Liver failure due to cirrhosis and liver cancers, both primary and secondary, is prevalent in the Eastern countries and accounts for about one million deaths worldwide annually [1]. The treatment for liver tumors includes

Jiayin Zhou · Wei Xiong · Weimin Huang · Tian Qi · Zhimin · Thiha Oo

Institute for Infocomm Research, A*STAR, Singapore

e-mail: {jzhou,wxiong,wmhuang,tian,}@i2r.a-star.edu.sg

{zwang,othiha}@i2r.a-star.edu.sg

Feng Ding

Department of Diagnostic Radiology, School of Computing,
National University of Singapore, Singapore

Sudhakar Kundapur Venkatesh

Department of Diagnostic Radiology,
National University of Singapore, Singapore

radiofrequency ablation (RFA), transarterial chemo-embolization (TACE), selective internal radiation therapy (SIRT), resection and even liver transplantation. During treatment, it is important to preserve as much liver tissue as possible for normal liver function especially in those with cirrhotic livers; however inadequate resection or treatment will be ineffective. Hence information about the volume of healthy liver parenchyma and tumor burden is important for clinical decision-making in treatment planning and response evaluation.

The efficacy of volume quantification highly depends on robust and reliable segmentation methods which are able to extract the desired organs/structures from medical images. Besides the robustness of segmentation algorithms, segmentation results can be improved by incorporating a probabilistic atlas, which encodes probabilities of anatomic variability while retaining both spatial and densitometric variances. In addition, probabilistic atlases provide valuable information for medical image interpretation, registration as well as group variation studies.

A project named *Liver Workbench* is being conducted by our institutions, with the aim to develop an image analysis platform with 3D liver objects (including the whole liver, liver tumors and vessels) segmentation, modeling, visualization and quantification toolkits for liver surgical planning and tumor treatment evaluation. By combining image database with associated ground truth created by radiologists, the *Liver Workbench* will also work as a performance benchmarking platform for segmentation methods. In this paper, the segmentation and modeling methods developed for the *Liver Workbench* are presented, including the algorithms, experiments and results.

2 System Overview

Multi-detector computer tomography (MDCT) is the imaging modality of choice for the comprehensive assessment of liver diseases, due to the fast imaging capability and the excellent spacial resolution up to 0.5 mm. However high spacial resolution will cause the decrease of signal-to-noise ratio (SNR), hence some image segmentation algorithms are not able to achieve satisfying performance under a low SNR environment. The contrast of a CT image comes from the differentiation of density, however in a lot of cases, there is no obvious difference in density between liver lesion and surrounding healthy liver parenchyma. In addition, high spacial resolution also leads to the decrease of resolution in density. These factors make the low contrast in lesion and the fuzziness of the lesion contour. The liver is the largest organ in human body, with very large variations in size, shape and hepatic vascular structure. These problems should be addressed in algorithms developed for the *Liver Workbench*.

This system has four modules: liver segmentation, tumor segmentation, segmentation performance validation, and the construction of probabilistic liver atlas, as shown in Fig. 1. Segmentation ground truth data are included for performance benchmarking, algorithm training and probabilistic atlas construction. The whole liver volume is segmented by a flipping-free mesh deformation model, with the aid

from the liver atlas to be a strong spatial constraint. The segmented liver volume is treated as a region of interest (ROI) and liver tumors are segmented using the support vector machines (SVMs)-based classification from the ROI. After the segmentation, results are fed into the performance validation module, where quantitative evaluation metrics are computed with the comparison to segmentation ground truth. Moreover an iterative landmark-free method based on dense volumes has been developed for the construction of a linear unbiased diffeomorphic probabilistic liver atlas from CT images. The whole system is integrated in 3D Slicer [2] which is an ITK/VTK [3,4]-based open-source platform.

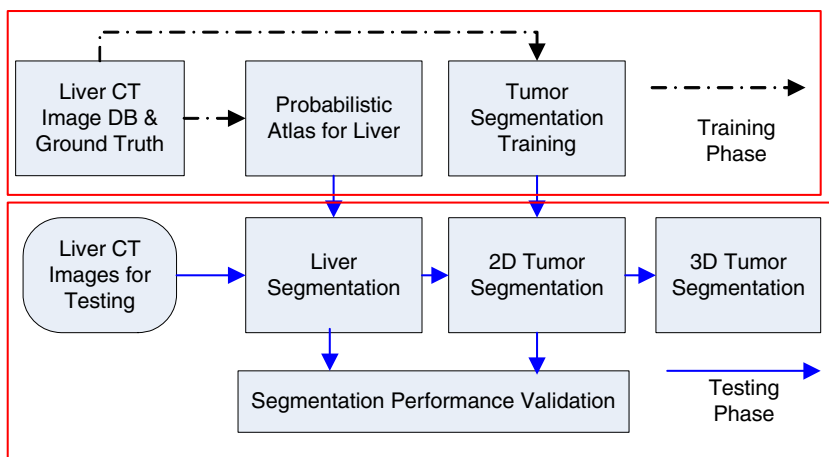


Fig. 1 System overview of the segmentation and modeling part of the Liver Workbench.

3 Segmentation of Liver and Liver Tumors

3.1 Flipping-Free Mesh Deformation for Liver Segmentation

Deformable models have been widely used for medical image segmentation [5]. Segmentation methods using implicit models such as the level set method and the fast marching method represent a 3D surface as an implicit function discretized into voxels, resulting in computationally expensive algorithms. The level set method can change the topology of the evolving surface to match highly complex object surface. However, it often leaks out of the object boundaries, producing undesired segmentation. In contrast, segmentation methods using explicit models represent a 3D surface as a mesh, which significantly reduce the space complexity of the algorithms. Deformation is accomplished by displacing the mesh vertices. The problem of mesh-based methods is that the displacements of vertices may cause self-intersections

of the mesh, which can be categorized as flipping or non-flipping. Flipping self-intersection occurs locally if the displacement vectors of neighboring mesh vertices cross in space. As a result, the directions of some surface normals flip after deformation. This problem cannot be solved by simply reducing the deformation step size. Non-flipping self-intersection occurs globally without flipping the surface normals but causes penetration of different parts of the mesh.

In this study, a flipping-free mesh deformation approach [6] has been developed to segment the 3D liver volume from the input CT data volume by iteratively deforming a 3D mesh model to register it to extracted image features. It searches for possible correspondence between mesh vertices and image features over long distances in iterations. The detected correspondence is refined before deformation to avoid flippings. The registration procedure of finding correspondences, flipping detection and avoidance and mesh deformations is iterated until convergence. The major components of the method are detailed as follows.

3.1.1 Image Feature Extraction

We extract the density distribution of all voxels in a volume within a mesh surface, as the liver volume may have heterogeneous voxel densities and some object boundaries are indistinct. Densities of the liver are modeled as a mixture of Gaussians $g(x) = \sum_i a_i f_i(x)$, where x is the voxel density, a_i are coefficients, such that $\sum_i a_i = 1$, and $f_i(x)$ are Gaussian distributions with parameters (μ_i, σ_i) . The number of Gaussians is determined by the input images. Parameters a_i , μ_i and σ_i can be estimated by expectation maximization (EM). To smooth out noise, the anisotropic filtering is applied to the input image as a pre-processing step.

3.1.2 Finding Correspondence

A 3D cubical quadrilateral mesh M consists of a set of cubes whose sides are aligned with the axes x -, y - and z - axis of a rectangular coordinate system. It is defined by three groups of orthogonal and closed contours that are parallel to the xy -, yz - or zx - plane respectively. Each vertex u_i in M is an intersection of two contours from different groups and with exactly four connected neighboring vertices.

To find the correspondence between the mesh model M and the target T (the image feature), for each vertex u_i in M , we search along the projection line $P(u_i)$, which can be defined as the surface normal at u_i , for a possible corresponding point v_i on the surface of T . The point v_i is the intersection of $P(u_i)$ and the face of a feature voxel on the surface of T . Each v_i serves as a target location for u_i . In general, $P(u_i)$ may be defined along other appropriate directions. u_i is labeled as a solitary vertex if its corresponding point cannot be found. Hence corresponding u_j to u_i along $P(u_i)$ is to find the minimum j such that

$$\sum_{i=j}^{j+N} h(u_i) = 0, \quad h(u_i) = \begin{cases} 0 & g(x_i) < \Gamma \\ 1 & \text{otherwise} \end{cases}, \quad (1)$$

where x_i is the density of u_i , Γ is a pre-defined threshold and $g(x_i)$ is the image feature. The vertex u_j that satisfies Eq. (1) is likely on the boundary of the target object, since $(N + 1)$ consecutive voxels along $P(u_i)$ starting from u_j all have low probabilities of belonging to the foreground. In the current study, $N = 3$.

3.1.3 Flipping Detection

The flipping of a mesh cell after mesh deformation occurs at least at one of its edges. Therefore, surface flipping can be identified by detecting edge flipping. Let u_i and u_j denote two non-solitary neighbors on a closed contour, and v_i and v_j denote their respective corresponding points on the target. Then, edge flipping occurs when the orientations of the edges $u_i - u_j$ and $v_i - v_j$ differ significantly such that $(u_i - u_j) \cdot (v_i - v_j) \leq \tau \|u_i - u_j\| \|v_i - v_j\|$, where $\tau \in [0, 1]$ is a predefined threshold. The vertices u_i and u_j that form a flipping edge are labeled as flipping vertices; otherwise they are non-flipping vertices. As each vertex u_i is an intersection of two orthogonal closed contours on mesh M , its flipping-free on one contour does not guarantee its flipping-free on the other contour. Therefore, each u_i will undergo the flipping detection along two closed contours when the algorithm iterates.

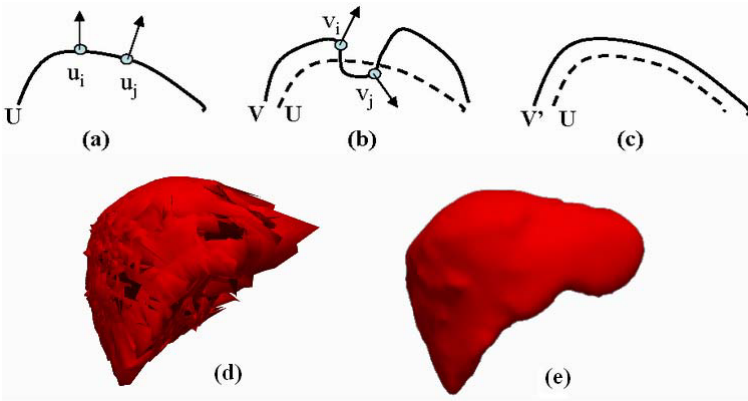


Fig. 2 (a) Two non-solitary neighbors u_i and u_j on a closed curve U; (b) After U deforms to V, u_i and u_j deform to v_i and v_j , the orientation of the edges $u_i - u_j$ and $v_i - v_j$ differ significantly; (c) Flipping avoidance by discarding the point correspondences; (d) A liver segmentation result without flipping detection and avoidance; (e) The corresponding result with flipping detection and avoidance.

3.1.4 Flipping Avoidance

We discard the point correspondences involving flipping. Let u_i, u_{i+1}, \dots, u_n denote a consecutive sequence of flipping vertices on a closed contour, excluding solitary vertices, such that u_{i-1} and u_{n+1} are non-flipping. The method identifies the middle flipping vertex u_m of the sequence, labels it as non-flipping, and labels the other flipping vertices as solitary, i.e., discarding their correspondences. After repeating this process for every closed contour, only non-flipping vertices have point correspondences. Thereafter, deforming the mesh according to these correspondences does not result in flipping. The procedure of flipping detection and avoidance is illustrated in Fig. 2.

3.1.5 Mesh Deformation

During mesh deformation, if non-flipping vertices are displaced to their target locations while solitary vertices remain unchanged, as shown in Fig. 3(a), the mesh may fold around solitary vertices, as shown in Fig. 3(b). In an extreme case, it results in non-flipping self-intersections, as shown in Fig. 3(c). To tackle this problem, the displacement vectors of non-flipping vertices are propagated to neighboring solitary vertices, turning them into non-flipping vertices by iterative local averaging of displacement vectors. This process is analogous to the diffusion of gradient vectors [7]. In the meanwhile, it can also smooth the variation of displacement vectors among neighboring non-flipping vertices, thus improving noise resilience. In this study, the Laplacian method [8] is adopted for mesh deformation because it is very efficient, easy to use, and easy to incorporate geometric constraints. During the deformation, non-flipping vertices are displaced towards their target locations, which are regarded as positional constraints. The other mesh vertices are displaced according to geometric constraints including the preservation of Laplacians (i.e., curvature normals) and uniform vertex distribution.



Fig. 3 Folding problem: (a) Displacing non-flipping vertices (dots) around solitary vertices (circle) may cause (b) folding of the mesh, and in an extreme case, (c) non-flipping self-intersection.

3.2 SVMs-Based Voxel Classification and Propagational Learning for Liver Tumor Segmentation

The major idea of this semi-automatic scheme is to utilize the similarities of lesion location, shape and signal intensities among the neighboring slices. Targeted tumor region is first extracted from one single 2D slice in the intermediate part of a tumor using supervised learning-based voxel classification. Then the extracted tumor contour, after some morphological operations, is mapped to its neighboring slices for automated sampling, learning and further voxel classification in the neighboring slices. This scheme is constructed on the important basis that scan is performed on multi-sliced CT and the slice thickness is no more than 3 mm such that there are only slight changes in both structural shapes and density properties among consecutive slices. The proposed segmentation scheme, illustrated in Fig. 4, has three main steps:

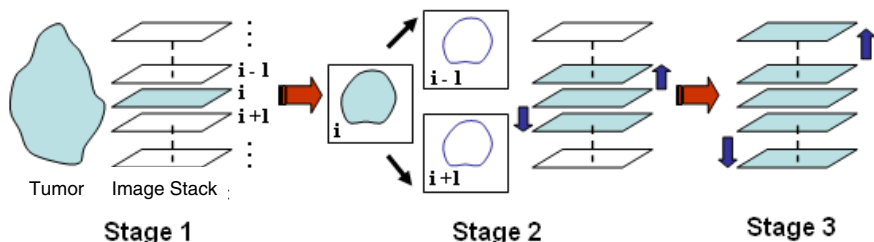


Fig. 4 Three main steps for the liver tumor segmentation scheme.

1. **Step A1** Targeted tumor region in 2D slice i at the intermediate part of the tumor is first segmented out by supervised learning-based voxel classification. In this procedure, tumor samples and non-tumor tissue (healthy liver tissue and other non-liver tissue) samples are manually selected to train a two-class SVMs-based classifier. Then the trained SVM classifier is imposed to a ROI in slice i for voxel classification such that tumor region in the ROI is extracted [9,10].
2. **Step A2** Let C_i be the contour of extracted tumor region from slice i , C_i^D and C_i^E be the contours after morphological dilation and erosion operations are performed on C_i , respectively. As slice thickness of 1-3 mm was employed for these data, it can be assumed with a high confidence level that the targeted tumor contours and image features vary slightly among neighboring slices. Hence both C_i^D and C_i^E are projected to slices $i-1$ and $i+1$. In slices $i-1$ and $i+1$, voxels enclosed by C_i^E are used as the new tumor samples for heuristic learning to train the SVM classifier, then the updated SVMs classifier is imposed to the area enclosed by C_i^D for tumor region extraction in the two propagating slices. This step is the first propagation procedure.

- Step A3** Similarly the propagation procedure including contour projection, SVMs classifier training and voxel classification is further applied to upper and lower slices for tumor region extraction till all tumor-bearing slices are processed.

3.3 Implementation

In the implementation, the liver segmentation was initialized by a 3D spherical mesh totally inside the target liver (Fig. 5(a)). Voxels inside the sphere are used to build a Gaussian mixture model (GMM) of the density probability distribution of the target liver (foreground). Voxels with low probability are regarded as background feature voxels. Transitions from consecutive foreground voxels to consecutive non-liver voxels along searching directions suggest the presence of boundary points of the target organ. After liver segmentation, the segmented liver contour (Fig. 5(b)) was treated as the ROI for further tumor segmentation. During the SVMs-based voxel classification in tumor segmentation, voxel density and the median of the densities of the voxel's eight-neighbors in the same slice were used as input features. They represent the information for the voxel and its neighborhood, respectively. In addition, a Gaussian radius basis function (RBF) $K(x, y) = \exp\left(\frac{-\|x-y\|^2}{\sigma}\right)$ was adopted as the learning kernel in the SVM classifier used, where σ was set by the variations of tumor samples. In the first step of tumor segmentation, tumor samples were picked by mouse click while non-tumor samples were selected by a rectangular box (Fig. 5(c)). If the amount of non-tumor samples is more than twice of tumor samples, a random re-sampling would be performed on non-tumor samples to balance sample populations, which is important in the training of SVM classifier. After voxel classification for tumor region extraction, the whole propagation procedure including contour projection, SVM classifier training and voxel classification was further applied to upper and lower slices till all tumor-bearing slices were processed. Fig. 5(d) shows the segmented tumor.

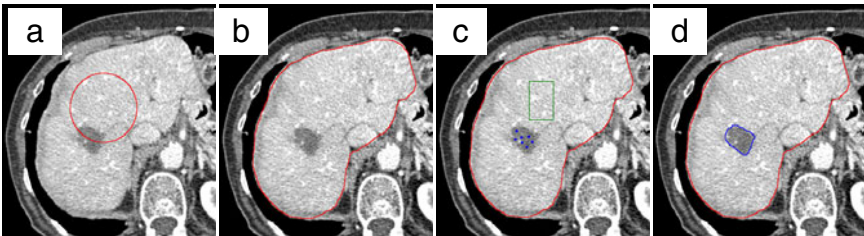


Fig. 5 (a) A 2D slice of a 3D spherical mesh for the initialization of liver segmentation; (b) the contour of the segmented liver in one slice; (c) the selected tumor samples (blue dots) and non-tumor samples (green rectangular box) and (d) the segmented liver tumor (blue contour).

3.4 Experiments and Evaluation Metrics

Twenty sets of multi-detector CT data for abdominal scan (slice thickness, 1-3 mm; image matrix, 512×512 pixels; and in-plane resolution, 0.6-0.9 mm) were used to test the algorithms. The liver boundaries were manually traced out by an experienced body radiologist. For the 20 data sets, 12 are with healthy livers (no focal lesion found) and 11 isolated focal lesions are found in the remaining 8 data sets. The outlines of the 11 tumors identified were also manually traced out by the same radiologist. They will be used as the reference standard (RS) for the comparison with the computerized segmentation results. In this study, three quantitative measures covering both volume and voxel levels were used to evaluate the algorithms' performance, with the comparison to liver and tumor reference segmentation RS [11].

1. Relative absolute volume difference (RAVD, %)

$$RAVD = \frac{|Vol_{seg} - Vol_{RS}|}{Vol_{RS}} \times 100\%, \quad (2)$$

where Vol_{seg} denotes segmented liver/tumor volume, Vol_{RS} denotes the volume of RS. Note that the perfect value of 0 can also be obtained for a non-perfect segmentation, if the volume of that segmentation is equal to the volume of RS.

2. Volumetric overlap error (VoE, %)

$$VoE = \left(1 - \frac{Vol_{seg} \cap Vol_{RS}}{Vol_{seg} \cup Vol_{RS}}\right) \times 100\%, \quad (3)$$

where $Vol_{seg} \cap Vol_{RS}$ is the number of voxels in the overlap or intersection of the two volumes, $Vol_{seg} \cup Vol_{RS}$ is the number of voxels in the union. This value is 0 for a perfect segmentation and the value of 100 means that there is no overlap at all between segmentation and RS.

3. Average symmetric surface distance (ASSD, mm)

$$ASSD = \frac{\sum_{a \in A} [\min_{b \in B} \{\text{dist}(a, b)\}] + \sum_{b \in B} [\min_{a \in A} \{\text{dist}(b, a)\}]}{N_A + N_B}, \quad (4)$$

where A and B denote the surfaces of segmented and RS volumes respectively, a and b are mesh points on A and B respectively, $\text{dist}(a, b)$ denotes the distance between a and b . N_A and N_B are the number of points on A and B . For each voxel along the border of a surface, the closest voxel along the border of another surface is determined and the distance between the two voxels is computed. All these distances are stored, for border voxels from both RS and segmentation. The average of all these distances gives the ASSD which tells us how much on average the two surfaces differ. This value is 0 for a perfect segmentation.

4 Probabilistic Liver Atlas Modeling

Existing liver probabilistic atlases are built based on registrations of landmarks [12, 13, 14], which are sensitive to the choice, the accurate localization and the placements of the landmarks. As the liver shape is highly variable and the texture is almost homogeneous in CT images, automatic localization of the landmarks inside the liver is difficult. Recent developments in constructing statistical atlases of shape variation, and non-rigid registration focus on building models of diffeomorphic deformation fields with a dense voxel correspondence [15, 16]. This can avoid the difficulties of sparse correspondence of landmarks. Hence we build an atlas based on all liver voxels. Registration involves wrapping moving subjects to the space of a *target* image. Bias may be introduced into the registration results towards to the chosen target image if it is arbitrarily chosen [15]. Minimizing or even removing such bias is thus highly desirable. Here we build unbiased atlases by using the classical pairwise deformation approach to construct a linear unbiased diffeomorphic probabilistic atlas of liver. For each pair of registrations, an efficient non-parametric image registration method, called diffeomorphic demons [16] is adopted. A more detailed description of this algorithm was presented in [17] and we outline it here for completeness.

The construction of a probabilistic atlas comprises two phases: find the optimal representative of group of images and statistically summarize the spatial and intensity variations. The first phase is to estimate a template image that is the best representative for the population on the infinite dimensional space of diffeomorphisms. Generally this can be considered as a registration optimization problem involving multiple images. Formally, given N image intensity images $\{x_i\}_{i=1}^N$ defined in a very large Euclidian vector space R^q (with q being the maximum number of voxels), we want to find $\hat{\mu}$ such that

$$\hat{\mu} = \underset{x \in R^q}{\operatorname{arg\,min}} \sum_{i=1}^N d(x, x_i)^2, \quad (5)$$

where d is a distance metric. If we choose the simple Euclidean distance, then the unbiased estimation is the *algebraic* mean of the population, i.e.,

$$\mu = \frac{1}{N} \sum_{i=1}^N x_i. \quad (6)$$

Now considering the possible deformation h_i for each image x_i with respect to the target, we have, at each iteration j ,

$$\mu^{(j)} = \frac{1}{N} \sum_{i=1}^N I_i^{(j)} = \frac{1}{N} \sum_{i=1}^N I_i(h_i^{(j)}(x_i)). \quad (7)$$

Here for the original training images, $j = 0$. Further, we use

$$\omega(h_i^{(j)}(x), \mu^{(j)}) \rightarrow h_i^{(j+1)}(x) \quad (8)$$

to denote the i th image x deformed by h_i for each iteration j to the space of $\mu^{(j)}$ and result in a new warped image $h_i^{(j+1)}(x)$, derived from x . The algorithm initializes by setting $j = 0$, followed by the following three steps.

1. **Step B1:** Compute $\mu^{(j)}$ using the Procrustes method, i.e., superposition of all sets of points. If $j = 0$, use Eq. (6), else use Eq. (7).
2. **Step B2:** For each image $I_i^{(j)} = I_i(h_i^{(j)}(x_i))$, find the optimal diffeomorphic deformation $\tilde{h}_i^{(j)}$ to warp $I_i^{(j)}$ to $\mu^{(j)}$: $\omega(\tilde{h}_i^{(j)}(x), \mu^{(j)}) \rightarrow \tilde{h}_i^{(j+1)}(x)$.
3. **Step B3:** Let $j = j + 1$; go to Step B2 until convergence or the maximum number of iterations is achieved.

Having found the optimal representative group mean image, we check whether there is a liver point instance at each voxel of the registered image space. If there is, the number of instances is incremented by one. After scanning all the space, the higher the number of liver instances found, the higher the probability. In this way we construct the liver probabilistic atlas.

5 Experiments and Results

5.1 Liver and Tumor Segmentation Results

The algorithm segmented out 19 liver volumes while it failed in one data set with health liver. Among the 19 segmented liver volumes, some are with minor errors at the border of the liver while some have considerable errors. Fig. 6 shows slices from one data set with good liver segmentation result that minor errors of under-segmentation occur at the marginal part. Fig. 7 shows results from another data set with moderate errors. Besides the under-segmentation errors at the marginal places with high curvatures, the algorithm could not well separate liver from the abdominal wall or the neighboring organs when they have similar density values and are in close contact to each other. Some examples of liver tumor segmentation results are also shown in Figs. 6 and 7. Overall computerized segmentation results are close to the interpretation from radiologist, but large errors occur where blurry transition exists between tumor and normal liver parenchyma. As shown in Table 1, for the 19 livers segmented, the mean *RAVD*, *VOE* and *ASSD* are 7.1%, 12.3%, and 2.5 mm, respectively. For the segmentation of 11 liver tumors, as shown in Table 2, the median *RAVD*, *VOE* and *ASSD* achieved are 7.3%, 18.4%, and 1.7 mm, respectively.

It is observed that the major errors in liver segmentation come from two types: The under-segmentation at some marginal part of the liver where the shape is with high curvatures and the over-segmentation that the liver contour leaks to the abdominal wall and other neighboring organs. The first type is due to the strong shape constraints from the global 3D mesh to keep the shape smoothness. Therefore it is difficult for the contour to deform to some places with high curvature, though there is strong image feature as the object boundary. On the other hand, the second type comes from the weak image feature as the object boundary. The leakage of the liver

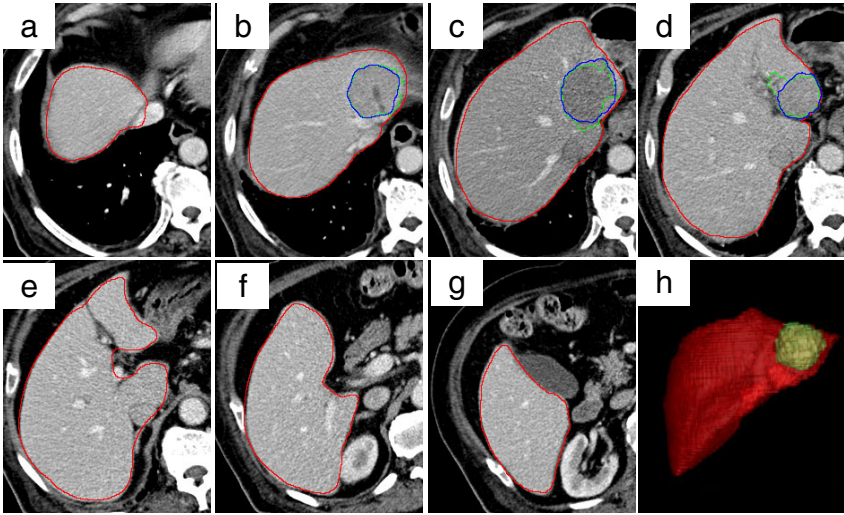


Fig. 6 (a)-(g) Slices from a well segmented liver volume (red contours), with outlines of the segmented liver tumor (green) in the left lobe and the tumor RS (blue); (h) 3D view (coronal) of the segmented liver with the tumor.

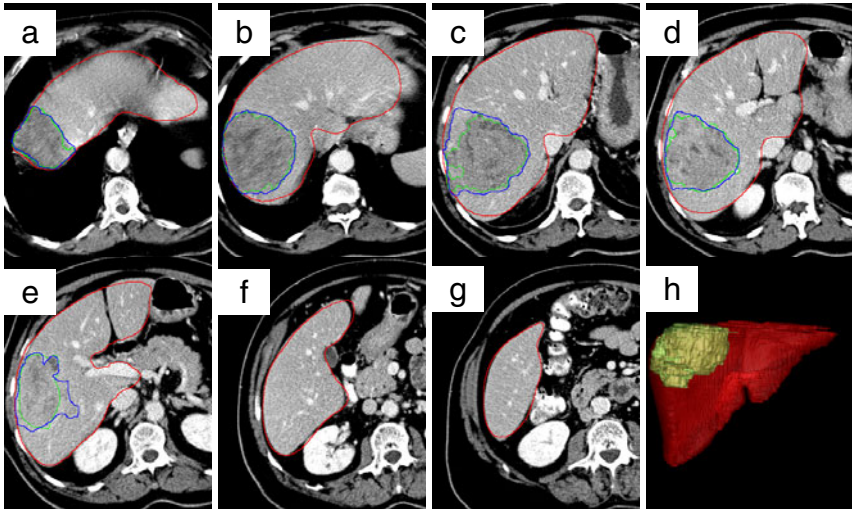


Fig. 7 (a)-(g) Slices from another segmented liver volume (red contours), with outlines of the segmented liver tumor (green) in the right lobe and the tumor RS (blue); (h) 3D view (coronal) of the segmented liver with the tumor.

Table 1 Quantitative evaluation of liver segmentation results.

| | Min. | Max. | Mean | STD. | Median |
|------------------|------|------|------|------|--------|
| <i>RAVD (%)</i> | 0.0 | 30.8 | 7.1 | 8.7 | 3.5 |
| <i>VOE (%)</i> | 6.6 | 36.3 | 12.3 | 7.1 | 9.9 |
| <i>ASSD (mm)</i> | 1.1 | 10.5 | 2.5 | 2.1 | 1.8 |

Table 2 Quantitative evaluation of liver tumor segmentation results.

| Tumor Subject | 1 | 2 | 3 | 4 | 5 | 6 | 7 | 8 | 9 | 10 | 11 | Median |
|------------------|------|------|------|------|------|------|------|------|------|------|------|--------|
| <i>RAVD (%)</i> | 2.8 | 19.6 | 8.4 | 6.7 | 14.2 | 8.9 | 6.5 | 5.9 | 7.3 | 5.8 | 16.1 | 7.3 |
| <i>VOE (%)</i> | 12.8 | 30.4 | 20.0 | 16.3 | 20.5 | 24.7 | 16.7 | 17.5 | 11.1 | 18.4 | 24.2 | 18.4 |
| <i>ASSD (mm)</i> | 1.0 | 2.5 | 1.7 | 1.3 | 2.1 | 2.2 | 0.8 | 1.2 | 0.7 | 1.1 | 2.1 | 1.7 |

contour to the abdominal wall and other neighboring organ does not cause a significant change of the property of the GMM which was previously learned. Hence it will be very interesting to study the combination of this method with a probabilistic liver atlas, which is able to give a strong shape prior to guide the mesh deformation.

5.2 Probabilistic Liver Atlas Modeling Results

We use $N = 25$ CT liver datasets of varying spacings and sizes. They are first normalized to give a common size of $441 \times 441 \times 48$ voxels with voxel size $1 \times 1 \times 5$ mm³. Registration performance is measured by using the mean square metric and the mutual information between the registered image and the fixed image. The mean square metric between the intensity difference of two images A and B is given by $MSE(A, B) = \frac{1}{q} \sum_{i=1}^q (a_i - b_i)^2$, where a_i , b_i is the intensity of the i th pixel of A and B , respectively, and q is the total number of pixels considered. We denote the marginal probability density functions of the intensities of A and B by p_1 and p_2 , respectively, and their joint probability density function by p_{AB} . The entropy of an image is defined by $H_i = -\sum_k p_i(k) \log_2(p_i(k))$, $i = 1, 2$. Similarly, we can define the joint entropy $H_{1,2}$ by using p_{AB} . Now the mutual information MI can be defined by $MI = H_1 + H_2 - H_{1,2}$.

We have implemented our method using liver expert-labeled CT image datasets in 10 iterations. For each cycle of iterations j , $j = 1, \dots, 10$, we record the performance indexes (MSE and MI) between each registered image $\tilde{h}_i^{(j)}(x)$ and the mean $\mu^{(j)}$. The respective averages of the MSE and MI measures of all datasets for this iteration are also computed as performance indexes. We have used $N = 5, 10, 15, 20, 25$ datasets to construct 5 respective probabilistic atlases. Of all the datasets involved, their average of MSEs and that of MIs for $N = 10$ are denoted by MSE10 and MI10, respectively. Similarly, we can define the measures for other cases, say, MSE25 and MI25 are for $N = 25$.

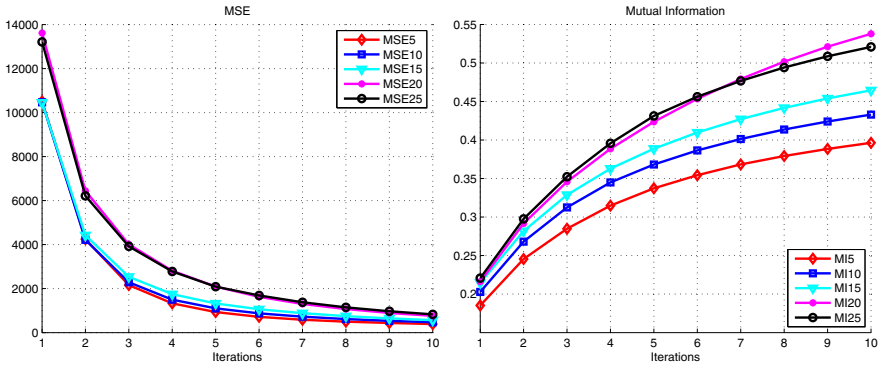


Fig. 8 Performance index curves against the number of iterations: When iterating more times MSEs decrease while MIs increase.

Fig. 8 presents these performance indexes against the number of iterations. As we iterate more times for the optimization, the MSEs decrease monotonically while MIs increase monotonically. Hence, given enough cycles, the iterations will converge. In particular, for MSE5, MSE10 and MSE15, their curves tend to be horizontal for cycles 7 to 10, i.e., already converged. Furthermore, the more datasets we use, the higher their MIs are. Hence with more and more datasets for training, we can obtain more information and more representative liver atlases.

Fig. 9 illustrates the mean images $\mu^{(j)}$, $j = 1, 5, 10$, for $N = 25$, and the corresponding probabilistic atlases in upper, middle and lower rows, respectively. In each of the figures, the left three columns are the mean images and the right three columns are their respective probabilistic atlases in order. Each column is for a

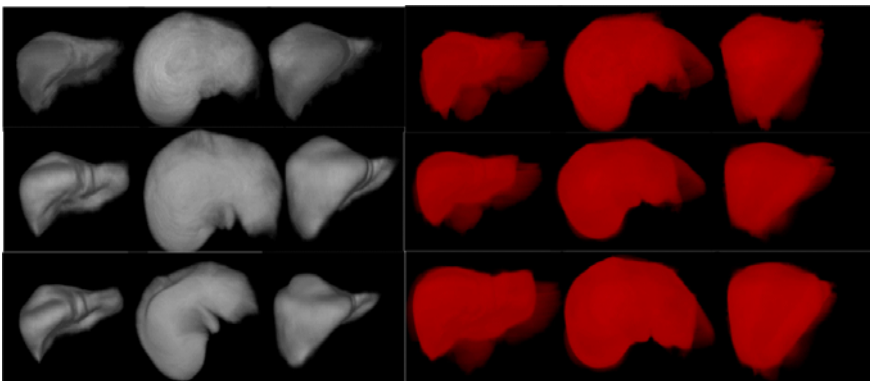


Fig. 9 The mean images (left three columns) and respective probabilistic atlases (right three columns) of the liver using 25 datasets for iteration 1 (upper row), 5 (middle row) and 10 (lower row) iterations. Three views are shown in different columns.

particular view of observations. When visualizing the atlases, we render the image with brightness proportional to the probability of each voxel at which it might be a liver point so that the higher the probability the brighter it appears. We notice that, with more iterations, the fine parts of the liver become more apparent.

6 Conclusions

We have described methods in an ongoing project *Liver Workbench* which aims at providing tools for segmentation and measuring the liver, its tumor and vessels from CT images. They are liver and liver tumor segmentation and unbiased probabilistic liver modeling. Liver segmentation is based on the iterative flipping-free mesh deformations to register the mesh model to image features in 3D volumes. In most situations, it works well, though there are errors in handling liver boundaries with high curvatures. Based on liver ROI obtained, a semi-automatic SVMs-based classification method is introduced to delineate liver tumor contours with an acceptable accuracy. A probabilistic liver atlas is built to confine the shape and intensity variation. The integrations of the techniques are still being investigated.

References

1. Teo, E.K., Fock, K.M.: Hepatocellular carcinoma: an Asian perspective. *Dig. Dis.* 19, 263–268 (2001)
2. <http://www.slicer.org> (cited March 15, 2011)
3. ITK: The Insight ToolKit, <http://www.itk.org> (cited March 15, 2011)
4. VTK: The Visualization ToolKit, <http://www.vtk.org> (cited March 15, 2011)
5. Suri, J., Farag, A.: *Deformable Models II: Theory and Biomaterial Applications*. Springer, New York (2007)
6. Ding, F., Yang, W., Leow, W.K., Venkatesh, S.: Segmentation of soft organs by flipping-free mesh deformation. In: *Proc. IEEE Workshop Application Comput. Vis.* (2009)
7. Xu, C., Prince, J.L.: Snakes, shapes, and gradient vector flow. *IEEE Trans. Image Process.* 7, 359–369 (1998)
8. Sorkine, O., Lipman, Y., Cohen-Or, D., Alexa, M., Rössl, C., Seidel, H.P.: Laplacian surface editing. In: *Proc. 2004 Eurographics*, pp. 179–188 (2004)
9. Cristianini, N., Shawe-Taylor, J.: *An Introduction to Support Vector Machines and Other Kernel-based Learning Methods*. University of Cambridge, Cambridge (2000)
10. Zhou, J., Chan, K.L., Xu, P., Chong, V.F.: Nasopharyngeal carcinoma lesion segmentation from MR images by support vector machine. In: *Proc. 3rd IEEE Int. Symp. Biomed. Imaging*, pp. 1364–1367 (2006)
11. Gerig, G., Jomier, M., Chakos, M.: Valmet: A new validation tool for assessing and improving 3D object segmentation. In: Niessen, W.J., Viergever, M.A. (eds.) *MICCAI 2001*. LNCS, vol. 2208, p. 516. Springer, Heidelberg (2001)
12. Park, H., Bland, P.H., Meyer, C.R.: Construction of an abdominal probabilistic atlas and its application to segmentation. *IEEE Trans. Med. Imaging* 22, 483–492 (2003)
13. Park, H., Bland, P.H., Hero III, A.O., Meyer, C.R.: Least biased target selection in probabilistic atlas construction. In: Duncan, J.S., Gerig, G. (eds.) *MICCAI 2005*. LNCS, vol. 3750, pp. 419–426. Springer, Heidelberg (2005)

14. Zhou, X., Kitagawa, T., Okuo, K., et al.: Construction of a probabilistic atlas for automated liver segmentation in non-contrast torso CT images. *Int. Congress Series*, vol. 1281, pp. 1169–1174 (2005)
15. Joshi, S., Davis, B., Jomier, M., Gerig, G.: Unbiased diffeomorphic atlas construction for computational anatomy. *NeuroImage* 23 (suppl.), S151–S160 (2004)
16. Vercauteren, T., Pennec, X., Perchant, A., Ayache, N.: Non-parametric diffeomorphic image registration with the demons algorithm. In: Ayache, N., Ourselin, S., Maeder, A. (eds.) *MICCAI 2007, Part II*. LNCS, vol. 4792, pp. 319–326. Springer, Heidelberg (2007)
17. Xiong, W., Ong, S.H., Xu, G., et al.: Construction of an unbiased diffeomorphic probabilistic liver atlas based on CT images. In: *Proc. Int. Conf. Image Process.*, pp. 1773–1776 (2009)

A Bag-of-Words Model for Cellular Image Segmentation

Li Cheng, Ning Ye, Weimiao Yu, and Andre Cheah

Abstract. Cellular segmentation in microscopy images is an important step in modern biological research. Microscopy image segmentation is known to be a difficult problem, as illustrated in the paper, in many scenarios the microscopic images become a real challenge for existing methods to accurately segment these cellular objects of interest. In this paper we propose a learning based approach using a bag-of-words model and dedicated feature design to deal with this problem. By introducing the recent machine learning and computer vision techniques including sparse coding, superpixel representation, our approach is shown to achieve good performance in practice.

1 Introduction

Cellular segmentation in microscopy images is an indispensable step for modern biological research, and this is greatly facilitated by the recent development of fluorescence dyes. It is highly desirable to automate this process in order to enable many follow-up applications such as high-throughput screening in drug discovery [16] and automated tracking of cell population in time-lapse microscopy [19]. Microscopy

Li Cheng · Ning Ye

BioInformatics Institute, A*STAR, Singapore

e-mail: chengli,yening@bii.a-star.edu.sg

Weimiao Yu

IMCB, A*STAR, Singapore

e-mail: wmyu@imcb.a-star.edu.sg

Andre Cheah

NUHS, Singapore

e-mail: Andre_EJ_Cheah@nuhs.edu.sg

image segmentation is known to be a difficult problem [27,2], partly due to the variations of specimen types, staining techniques, and imaging hardware. As examples, some of the image data used during experiments are displayed in Figure 1.

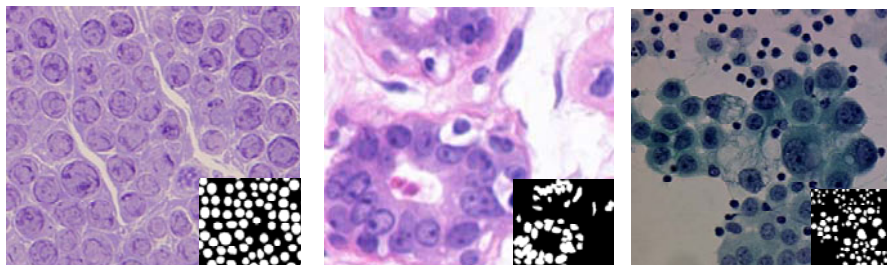


Fig. 1 Example images of the three datasets. From Left to Right: Hand, Breast cancer, Serous datasets.

A number of unsupervised segmentation methods, such as thresholding, region growing, watershed methods, as well as edge-based methods, have been widely used in microscopic image segmentation where the foreground objects and background regions have distinct statistical properties. Recently, an increased number of learning-based algorithms are developed to accommodate more difficult cases, including supervised levelset [26], support vector machines (SVMs) [22], as well as conditional random fields and variants [6,25,39]. However, there are many scenarios where it remains difficult to segment out cellular objects from the microscopic images, such as the examples presented in Figure 1. Moreover, it is a challenging task to devise a general purpose segmentation system that performs well with different type of cellular images.

In this paper we propose a systematic learning-based approach to examine the problem of segmenting cellular objects from images. The proposed framework is able to segment cellular foreground objects by nicely integrating information from both local and global contexts from pixel as well as superpixel representations along the process pipeline, as illustrated in *e.g.* Figure 2 where a novel superpixel-based coding scheme is presented to incorporate higher-order scene context. In addition, we analyze the effect of sparse coding schemes of [21,43]. Concerning feature design, Beside color feature, a new detection score feature is devised to exploit the strength of object detection developed over the years in computer vision and machine learning communities to deal with the cellular image segmentation problems.

Finally, two evaluation criteria are proposed, one is for measuring the pixel-level performance, and the other is for the object-level performance.

2 Our Approach

The flowchart of our approach is visually depicted in Figure 2, as well as summarized below. We follow an often used assumption that an image object can be sufficiently characterized by features describing its complementary aspects, including *e.g.* its shape and appearance. As a result, each pixel of an object is represented by a set of such features. Previous research work such as [18, 26] directly supply these features to classifiers. Inspired by the work of [31], we advocate in this paper the usage of coding or vector quantization scheme, where a codebook with a number of codewords is applied to turn a feature into a code representation. This procedure is further extended by pooling the set of codes from local pixels inside one superpixel [28] together to form a superpixel code. By passing through a learned classifier, a prediction of image segmentation is then delivered providing a combination of the features. In addition, an object-level segmentation can also be produced via a dedicated postprocessing procedure.

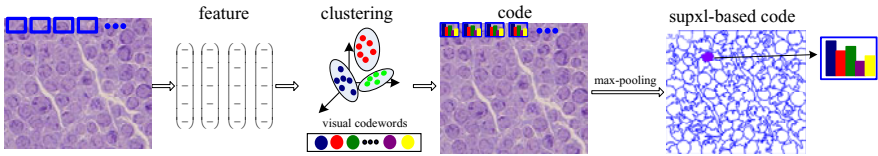


Fig. 2 Flowchart of the proposed approach. From an input image, a set of features is extracted to characterize its various aspects at pixel level: *e.g.* appearance, shape, contexture information. This is followed by a coding or vector quantization process using *e.g.* k-means clustering method, then each feature is mapped to a code representation. A superpixel (or over-segmentation) coding scheme is devised here to provide a more compact signature of local visual information, as well as to incorporate higher-order scene context. Then they are passed to a learned predictor to produce labeling prediction.

2.1 Features

In general, the features in our framework can be any set of domain-specific features that capture complementary aspects of the observed image. In this paper, we choose to utilize the color feature to capture the appearance aspect and a newly devised detection score feature to capture the context of the pixel of interest.

Color Feature

For a pixel in color images, its RGB color values is used together with its YUV color space values, which give a 6 dimensional feature. For grayscale images, 1D intensity

feature is used directly. Meanwhile the detection score feature, as described below, aims to capture local shape and context information.

Detection Score Feature

Object detection [10] is usually regarded as a separate problem from image segmentation, and is thus dealt with by substantially different techniques. Nevertheless, detection outputs possess important information about the location and size of the foreground objects that can be utilized to help segmentation. In addition, as generated through top-down scheme the detection scores carry context information over to pixel level. We construct a novel detection score feature that takes as input the detection location, bounding box size, and score – the commonly used triplet output of many object detectors. As shown in Figure 3(b), these bounding box detections are overlaid onto a two dimensional space with each assigning its score. This gives our context feature. By feeding through our multiple superpixel-based quantization pipeline with local models, the corresponding pixel probability maps are obtained as *e.g.* displayed in Figure 3(c).

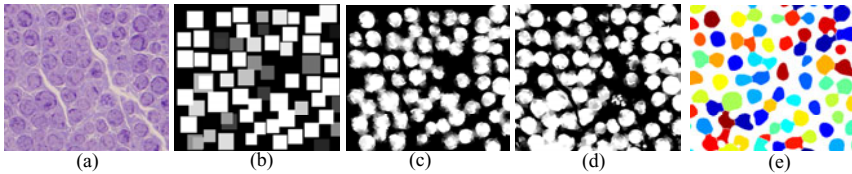


Fig. 3 (a) The input image of Figure 2. (b) Its detection score feature. (c) The resulting prediction map of this feature. Similar, the prediction map of the color features (d) is also displayed. (e) Final segmentation result.

2.2 A Bag-of-Words Model: Code, Superpixel-Based Code

Vector Quantization and Sparse Coding

Vector quantization (*i.e.*, Bag-of-words) has been a popular method to obtain a succinct representation of local information for object recognition problems [33]. Moreover, sparse coding is recently proposed in *e.g.* [21, 12] to obtain an over-complete basis set for image classification, which resembles the receptive fields of neurons in the visual cortex [24]. In this paper, we adopt a variant [43, 12] that preserves the locality property and the induced optimization problem can be solved analytically.

From this coding process, a pixel feature is mapped to a code describing its projection onto the bases. In what follows, we propose an extension of this process using superpixels.

Superpixel-Based Coding Scheme: Incorporating Higher-Order Scene Context

An image is usually represented as a two-dimensional lattice graph where each node corresponds to a pixel. However a pixel by itself contains very limited amount of information. Alternatively, an image can be expressed as a general planar graph, and each node is now a superpixel or oversegmentation [28] containing a set of nearby pixels, usually obtained using an unsupervised segmentation. In particular, the unsupervised method of [17] is adopted in this paper to partition an image into superpixels. Although the superpixel representation naturally incorporates higher-order scene context (e.g. [1]), it heavily relies on the quality of the initial unsupervised segmentation, which may result in dramatic labeling errors.

In our approach, after sparse coding, the codes in a superpixel that each represents a pixel are pooled spatially to form a higher-level code that describes the superpixel. Specifically we adopt the max-pooling strategy as it has been shown as being more robust and biologically plausible [29,41].

The Classifier

In fact, the learning model can be any existing classifiers. In this paper we use the LIBSVM library [5] with RBF kernels. As individual feature can be turned into a prediction map by means of learned classifier, as illustrated in Figure 3(c) and (d), we use a combination of color and detection score features, which is able to produce a visually appealing final prediction result in Figure 3(e).

Postprocessing

Our postprocessing step involves separating touching objects and forming object-level segments from pixel-level segmentation. The process starts with seed finding [45,46,44] to obtain the object centers. This is obtained by a distance transform based on the pixel segmentation result. Then object centers are detected as the local maximum locations in both spatial and scale domains. Two loops of iteration are therefore applied: The outer loop is to gradually reduce the thresholding on the distance function and to encourage the segments growing. The inner loop is the Evolving Generalized Voronoi Diagrams algorithm [44] to preserve topological dependence and to avoid unnecessary under/over segmentations.

3 Datasets and Performance Evaluation

3.1 The Datasets

The proposed framework is evaluated on three microscopic datasets with some example images presented in Figure 1. Below we examine in more detail these datasets.

Hand Dataset

This is a dataset of nerve ending specimen images harvested from fresh frozen adult human cadavers, which are preserved in glutaraldehyde and refrigerated. The specimens are processed the next day starting with dehydration of the specimen with increasing concentrations of alcohol and finally infusion with xylene. They then are stained with methylene blue and photographed using a light microscope to facilitate the process of histomorphometry, and are further partitioned into 24 smaller images of similar size.

Breast Cancer Dataset

This breast cancer dataset is prepared by [11]. There are 58 stained histopathology images (with binary ground truth masks) containing breast cancer cells, where routine histology uses the stain combination of hematoxylin and eosin, commonly referred to as H&E. These images are stained since most cells are essentially transparent, with little or no intrinsic pigment. Certain special stains, which bind selectively to particular components, are used to identify biological structures such as cells.

Serous Dataset

This database [18] contains 10 color microscopic images from serous cytology. The ground truth is prepared by [18] that contains two classes of pixels: nucleus pixels and others. The overall class distributions are 7% for the nuclei pixels and 93% for the other pixels. As emphasized in [18], the spatial configuration varies significantly, and similarly for the color of cells, which ranges from very dark to very pale blue. This observation suggests the need of a robust supervised segmentation system.

3.2 Performance Evaluation

The performance of a cellular segmentation method are usually quantitatively assessed by two types of metrics: those of pixel based and those of object-level based. We follow the PASCAL VOC evaluation criteria of image segmentation task [9] for pixel-based evaluation. The metric for object-level evaluation is an adaptation of the criteria used in the object segmentation task [9] of PASCAL VOC challenges.

Pixel-Based Evaluation

A common pixel-based evaluation scheme is the percentage of pixels being correctly classified. This metric however can be misleading when class distribution is unbalanced, *e.g.* when the dataset contains fewer foreground object pixels and a larger percentage of background pixels. To rectify this issue, in PASCAL VOC image segmentation challenge the results of competing methods are instead compared by the following criteria (Eq.(4) of [9]):

$$\text{pxl. score} = \frac{\text{true pos.}}{\text{true pos.} + \text{false neg.} + \text{false pos.}}. \quad (1)$$

Object-Level Evaluation

In object detection, a bounding box is utilized to delineate the location and scale of a foreground object. Object-based image segmentation can be considered as a closely related task, where in addition to location and scale, it also demands the detailed shape of a foreground object.

Following the scheme adopted by the object detection challenge of PASCAL [9], we also use an intersection/union ratio to determine a true correct object level match. Given a pair of objects consisting of a prediction O_p and a ground-truth O_{gt} , there exists a match if the overlap ratio,

$$r_o = \frac{\text{area}(O_p \cap O_{gt})}{\text{area}(O_p \cup O_{gt})}, \quad (2)$$

exceeds a threshold t . In the equation above, \cap denotes the intersection, and \cup the union. t is also set to 0.5 as in [9]. Similar to Eq.(1), we can also define object-level accuracy as

$$\text{obj. score} = \frac{\text{true pos.}}{\text{true pos.} + \text{false neg.} + \text{false pos.}}. \quad (3)$$

4 Experiments

For all datasets, half are retained for training the model, and the rest are used for testing and final evaluation. Besides, the unsupervised method of [17] is used to partition an image into superpixels.

A series of experiments are conducted on each of the datasets, where different components are intentionally turning on or off to examine their importance. One observation is that at different scenarios, color features turns to be more salient than detection features. As they are very complementary features, the combination of both appears to give better performance. Meanwhile the design of superpixel-based code improves the performance. Throughout all datasets, we observe that the proposed method, denoted as M6, have demonstrated to perform the best, as highlighted in the last row of Tables 1, 2, and 3. Some of the results of the hand, serous, and breast cancer datasets are displayed in Figures 4, 5 and 6 respectively.

Table 1 Comparisons of pixel classification rate on hand dataset.

| Method | Brief Description | Pixel Score | Obj. Score |
|--------|---|-------------|------------|
| M1 | color feature, pixel-based | 74.33% | 71.10% |
| M2 | color feature, superpixel-based | 77.08% | 80.93% |
| M3 | detection score feature, pixel-based | 70.88% | 81.06% |
| M4 | detection score feature, superpixel-based | 71.89% | 82.49% |
| M5 | color & det. score features, pixel-based | 76.23% | 81.82% |
| M6 | color & det. score features, superpixel-based | 81.82% | 86.68% |

Table 2 Comparisons using pixel classification rate on Breast Cancer dataset.

| Method | Brief Description | Pixel Score | Obj. Score |
|--------|---|-------------|------------|
| M1 | color feature, pixel-based | 65.17% | 39.15% |
| M2 | color feature, superpixel-based | 68.01% | 40.31% |
| M3 | detection score feature, pixel-based | 53.79% | 37.22% |
| M4 | detection score feature, superpixel-based | 55.42% | 39.83% |
| M5 | color & det. score features, pixel-based | 66.46% | 40.59% |
| M6 | color & det. score features, superpixel-based | 69.64% | 42.23% |

5 Outlook and Discussion

In this paper, we propose to study cellular image segmentation problem from a supervised learning viewpoint. In particular, a novel segmentation framework is devised that utilizes a bag-of-words model, and incorporates complementary feature

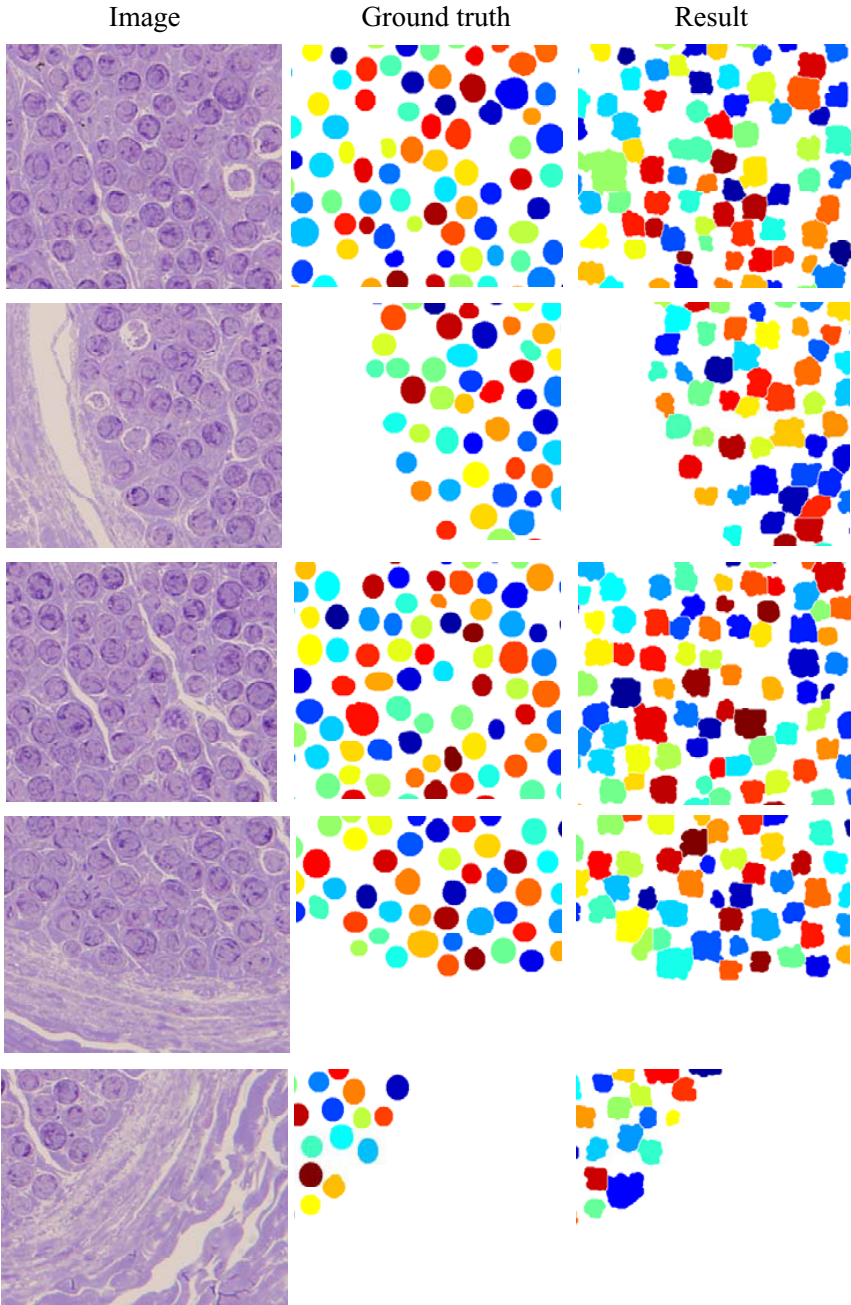


Fig. 4 Exemplar results for the hand dataset. First column: inputs. Second column: ground truths. Third column: object-level segmentation results using color & det. score features, and superpixel-based code.

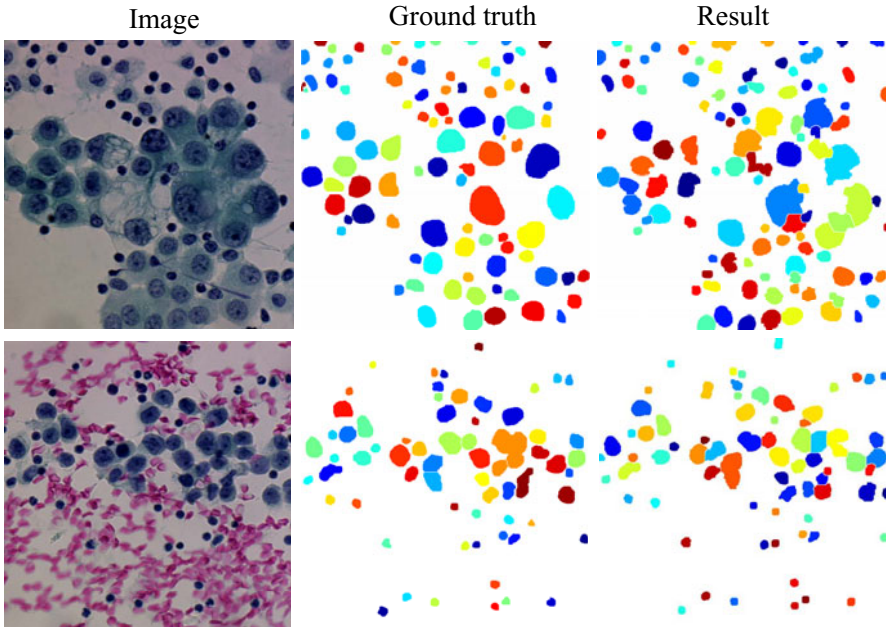


Fig. 5 Exemplar results for the Serous dataset. First column: inputs. Second column: ground truths. Third column: object-level segmentation results using color & det. score features, and superpixel-based code.

Table 3 Comparisons of pixel classification rate on Serous dataset.

| Method | Brief Description | Pixel Score | Obj. Score |
|--------|---|-------------|------------|
| M1 | color feature, pixel-based | 80.79% | 74.29% |
| M2 | color feature, superpixel-based | 81.14% | 75.47% |
| M3 | detection score feature, pixel-based | 59.37% | 48.32% |
| M4 | detection score feature, superpixel-based | 62.42% | 48.95% |
| M5 | color & det. score features, pixel-based | 81.49% | 77.10% |
| M6 | color & det. score features, superpixel-based | 82.71% | 78.99% |

patterns, as well as considers a superpixel representation with sparse coding. Extensive experiments are conducted on three difficult microscopic image datasets, where our approach is shown to achieve good performance.

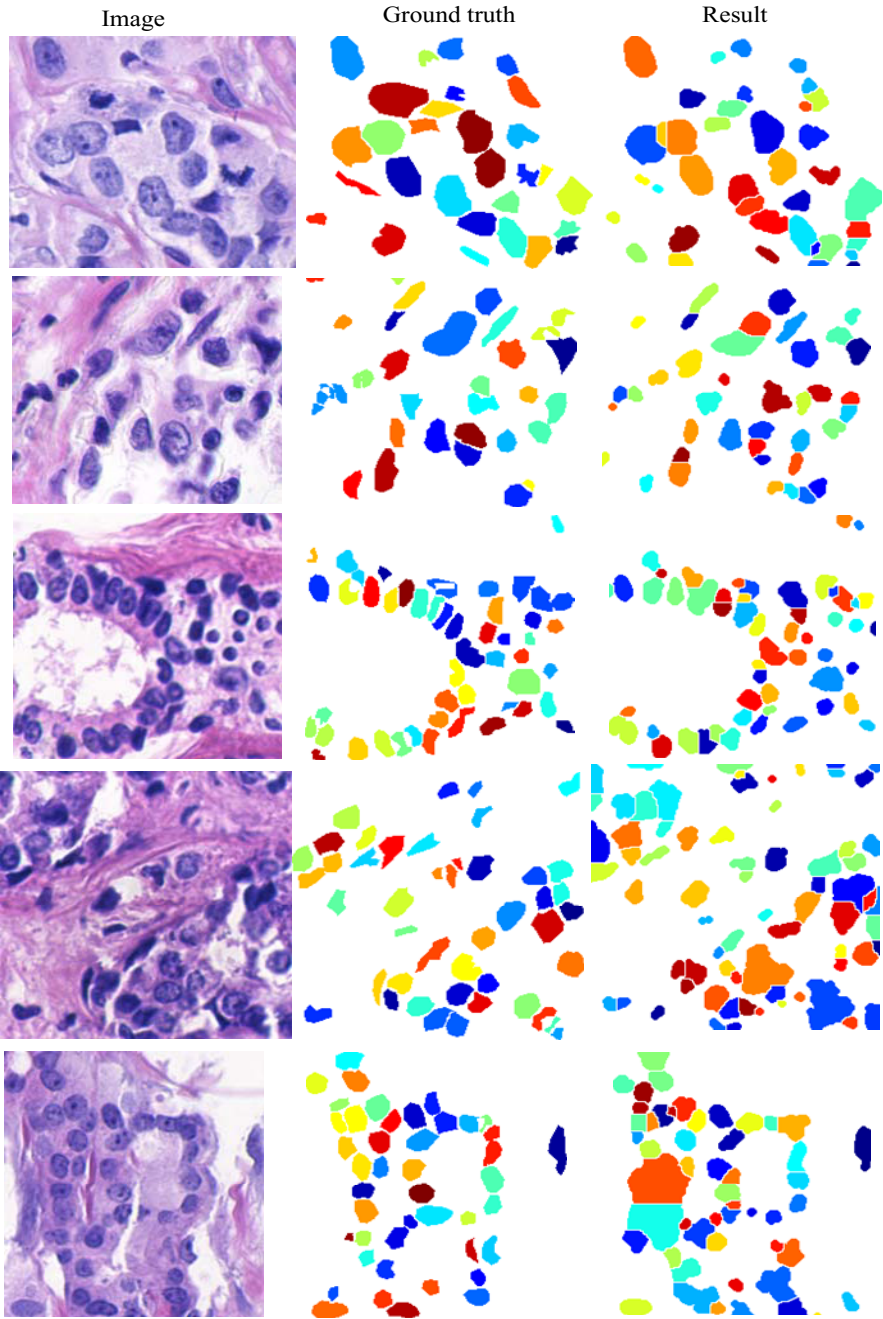


Fig. 6 Exemplar results for the Breast cancer dataset. First column: inputs. Second column: ground truths. Third column: object-level segmentation results using color & det. score features, and superpixel-based code.

References

1. Batra, D., Sukthankar, R., Chen, T.: Learning Class-Specific Affinities for Image Labelling. In: *Int. Conf. Computer Vision and Pattern Recognition* (2008)
2. Bengtsson, E., Wahlby, C., Lindblad, J.: Robust Cell Image Segmentation Methods. *Pattern Recognition and Image Analysis* 14(2), 157–167 (2004)
3. Boykov, Y., Veksler, O., Zabih, R.: Fast approximate energy minimization via graph cuts. *IEEE TPAMI* 23(11), 1222–1239 (2001)
4. Cardona, A., Saalfeld, S., Preibisch, S., Schmid, B., Cheng, A., Pulokas, J., Tomancak, P., Hartenstein, V.: An Integrated Micro- and Macroarchitectural Analysis of the Drosophila Brain by Computer-Assisted Serial Section Electron Microscopy. *PLoS Biol.* 8(10) (2010)
5. Chang, C.-C., Lin, C.-J.: LIBSVM: a library for support vector machines (2001)
6. Chen, S., Gordon, G., Murphy, R.: Graphical Models for Structured Classification, with an Application to Interpreting Images of Protein Subcellular Location Patterns. *J. Mach. Learn. Res.* 9, 651–682 (2008)
7. Cheng, L., Vishwanathan, S., Schuurmans, D., Wang, S., Caelli, T.: Implicit Online Learning with Kernels. *Neural Information Processing Systems* (2007)
8. Cortes, C., Vapnik, V.: Support Vector Networks. *Machine Learning* 20(3), 273–297 (1995)
9. Everingham, M., Van Gool, L., Williams, C., Winn, J., Zisserman, A.: The Pascal Visual Object Classes (VOC) Challenge. *International Journal of Computer Vision* 88(2), 303–338 (2010)
10. Felzenszwalb, P., McAllester, D., Ramanan, D.: A Discriminatively Trained, Multiscale, Deformable Part Model. In: *Int. Conf. Computer Vision and Pattern Recognition* (2008)
11. Gelasca, E., Obara, B., Fedorov, D., Kvilekval, K., Manjunath, B.: A biosegmentation benchmark for evaluation of bioimage analysis methods. *BMC Bioinformatics* 10, 386 (2009)
12. Gonfaus, J., Boix, X., Weijer, J., Bagdanov, A., Serrat, J., Gonzalez, J.: Semantic Texton Forests for Image Categorization and Segmentation. In: *Int. Conf. Computer Vision and Pattern Recognition* (2010)
13. Hunter, D., Moradzadeh, A., Whitlock, E., Brenner, M., Myckatyn, T., Wei, C., Tung, T., Mackinnon, S.: Binary imaging analysis for comprehensive quantitative histomorphometry of peripheral nerve. *Journal of Neuroscience Methods* 166(1), 116–124 (2007)
14. Kohli, P., Ladicky, L., Torr, P.: Robust Higher Order Potentials for Enforcing Label Consistency. *Int. J. Comput. Vision* 82(3), 302–324 (2009)
15. Ladicky, L., Russell, C., Kohli, P., Torr, P.: Associative Hierarchical CRFs for Object Class Image Segmentation. In: *Int. Conf. on Computer Vision* (2009)
16. Lang, P., Yeow, K., Nichols, A., Scheer, A.: Cellular imaging in drug discovery. *Nat. Rev. Drug. Disco.* 5(4), 343–356 (2006)
17. Levinshtein, A., Stere, A., Kutulakos, K., Fleet, D., Dickinson, S., Siddiqi, K.: TurboPixels: Fast Superpixels Using Geometric Flows. *IEEE Trans. Pattern Anal. Mach. Intell.* 31(12), 2290–2297 (2009)
18. Lezoray, O., Cardot, H.: Cooperation of color pixel classification schemes and color watershed: a study for microscopical images. *IEEE Transactions on Image Processing* 11(7), 783–789 (2002)
19. Li, K., Chen, M., Kanade, T., Miller, E., Weiss, L., Campbell, P.: Cell Population Tracking and Lineage Construction with Spatiotemporal Context. *Medical Image Analysis* 12(1), 546–566 (2008)

20. Lindeberg, T.: Edge Detection and Ridge Detection with Automatic Scale Selection. *International Journal of Computer Vision* 30(2), 117–154 (1998)
21. Mairal, J., Bach, F., Ponce, J., Sapiro, G., Zisserman, A.: Discriminative Learned Dictionaries for Local Image Analysis. In: *International Conf. of Computer Vision and Pattern Recognition, CVPR* (2008)
22. Marcuzzo, M., Quelhas, P., Campilho, A., Maria Mendonca, A., Campilho, A.: Automated Arabidopsis plant root cell segmentation based on SVM classification and region merging. *Comput. Biol. Med.* 39(9), 785–793 (2009)
23. Martin, D., Fowlkes, C., Malik, J.: Learning to Detect Natural Image Boundaries Using Local Brightness, Color, and Texture Cues. *IEEE Trans. Pattern Anal. Mach. Intell.* 26(5), 530–549 (2004)
24. Olhausen, B., Field, D.: Emergence of simple-cell receptive field properties by learning a sparse code for natural images. *Nature* 381, 607–609 (1996)
25. Pan, J., Kanade, T., Chen, M.: Heterogeneous Conditional Random Field: Realizing Joint Detection and Segmentation of Cell Regions in Microscopic Images. In: *IEEE Conf. on Computer Vision and Pattern Recognition* (2010)
26. Paragios, N., Deriche, R.: Geodesic Active Regions and Level Set Methods for Supervised Texture Segmentation. *Int. J. Comput. Vision* 46(3), 223–247 (2002)
27. Prewitt, J., Mendelsohn, M.: The analysis of cell images. *Ann. NY Acad. Sci.* 128(3), 1035–1053 (1966)
28. Ren, X., Malik, J.: Learning a classification model for segmentation. In: *Int'l. Conf. Computer Vision*, vol. 1, pp. 10–17 (2003)
29. Serre, T., Wolf, L., Poggio, T.: Object Recognition with Features Inspired by Visual Cortex. In: *International Conference on Computer Vision and Pattern Recognition* (2005)
30. Shalev-Shwartz, S., Singer, Y., Srebro, N.: Pegasos: Primal Estimated sub-Gradient Solver for SVM. In: *International Conference on Machine Learning*, pp. 807–814 (2007)
31. Shotton, J., Johnson, M., Cipolla, R.: Semantic Texton Forests for Image Categorization and Segmentation. In: *Int. Conf. Computer Vision and Pattern Recognition* (2008)
32. Shotton, J., Winn, J., Rother, C., Criminisi, A.: TextonBoost for Image Understanding: Multi-Class Object Recognition and Segmentation by Jointly Modeling Appearance, Shape and Context. *International Journal on Computer Vision* 81(2) (2009)
33. Sivic, J., Russell, B., Efros, A., Zisserman, A., Freeman, W.: Discovering object categories in image collection. In: *ICCV* (2005)
34. Szummer, M., Kohli, P., Hoiem, D.: Learning cRFs using graph cuts. In: Forsyth, D., Torr, P., Zisserman, A. (eds.) *ECCV 2008, Part II. LNCS*, vol. 5303, pp. 582–595. Springer, Heidelberg (2008)
35. Taskar, B., Guestrin, C., Koller, D.: Max-Margin Markov Networks. In: *NIPS*, pp. 25–32. MIT Press, Cambridge (2004)
36. Tsochantaridis, I., Joachims, T., Hofmann, T., Altun, Y.: Large Margin Methods for Structured and Interdependent Output Variables. *J. Mach. Learn. Res.* 6, 1453–1484 (2005)
37. Vapnik, V.: *The nature of statistical learning theory*. Springer, Heidelberg (1995)
38. Wang, J., Yang, J., Yu, K., Lv, F., Huang, T., Gong, Y.: Locality-constrained Linear Coding for Image Classification. In: *CVPR* (2010)
39. Wu, X., Shah, S.: A bottom-up and top-down model for cell segmentation using multi-spectral data. In: *IEEE International Symposium on Biomedical Imaging* (2010)
40. Yang, Y., Hallman, S., Ramanan, D., Fowlkes, C.: Layered Object Detection for Multi-Class Segmentation. In: *Int. Conf. Computer Vision and Pattern Recognition* (2010)
41. Yang, J., Yu, K., Gong, Y., Huang, T.: Linear spatial pyramid matching using sparse coding for image classification. In: *CVPR*, pp. 1794–1801 (2009)

42. Yin, Z., Bise, R., Chen, M., Kanade, T.: Cell Segmentation in Microscopy Imagery using a Bag of Local Bayesian Classifiers. In: IEEE International Symposium on Biomedical Imaging, ISBI (2010)
43. Yu, K., Zhang, T., Gong, Y.: Nonlinear learning using local coordinate coding. In: Neural Information Processing Systems, NIPS (2009)
44. Yu, W., Lee, H.K., Hariharan, S., Bu, W., Ahmed, S.: Evolving Generalized Voronoi Diagrams of Active Contours for Accurate Cellular Image Segmentation. *Cytometry Part A* 77A(4), 379–386 (2010)
45. Yu, W., Lee, H.K., Hariharan, S., Bu, W., Ahmed, S.: Quantitative Neurite Outgrowth Measurement Based on Image Segmentation with Topological Dependence. *Cytometry Part A* 75(4), 289–297 (2009)
46. Yu, W., Lee, H.K., Hariharan, S., Sankaran, S., Vallotton, P., Ahmed, S.: Segmentation of neural stem/Progenitor cells nuclei within 3-D neurospheres. In: Bebis, G., Boyle, R., Parvin, B., Koracin, D., Kuno, Y., Wang, J., Wang, J.-X., Wang, J., Pajarola, R., Lindstrom, P., Hinkenjann, A., Encarnaç o, M.L., Silva, C.T., Coming, D. (eds.) ISVC 2009. LNCS, vol. 5875, pp. 531–543. Springer, Heidelberg (2009)

Knowledge Based and Statistical Based Approaches in Biomedical Image Analysis

Florence Cloppet and Thomas Hurtut

Abstract. Biomedical Imaging has grown significantly for the past twenty years, as it is considered as a unique method for visualizing biological processes within living organisms in a non-invasive manner. Although works in biomedical image analysis rely on underlying biological problems, scientists are just beginning to embrace the idea that these works will benefit from multidisciplinary interactions. Moreover, within the computer vision community, time has come for a more holistic and integrated approach in order to articulate statistical/machine learning and knowledge-based approaches. In this paper we present studies based on these two classic approaches and show how their complementarity may benefit biomedical imaging.

1 Introduction

Over the past twenty years, the field of biomedical imaging has been developing rapidly with the advent of new physical imaging systems, a wide range of new probes or contrast agents, and image analysis. The challenge of this field cannot boil down to *taking pretty images*, but lie in extracting information from them, in order to understand the complex relationships between genes, proteins, cellular components, organs and physiological systems, and finally whole organisms.

As biomedical imaging methods develop, their effectiveness and impact rely more and more on scientists who have specific skills in physics, biochemistry, biology-medicine and mathematics-computer sciences. Therefore there is a growing interest for interdisciplinary curricula¹ that will help scientists to effectively

Florence Cloppet · Thomas Hurtut
Laboratoire d'Informatique de Paris Descartes (LIPADE),
Paris Descartes University,
45, Rue des Saints Pères, 75006 Paris
e-mail: florence.cloppet@mi.parisdescartes.fr
e-mail: thomas.hurtut@parisdescartes.fr

¹ Examples of interdisciplinary Bioimaging curricula.

collaborate with experts of these different domains, and the quality of this relationship will undoubtedly accelerate and benefit biomedical research and development.

Biomedical image analysis has to address many difficult challenges, both in terms of developing image analysis software dedicated to biomedical scientists, and of developing theoretical advances in computer vision. Although works in biomedical image analysis rely on underlying biological problems (analysis of normal structure or function, abnormal/pathological states), scientists are just beginning to embrace the idea that these works will benefit from multidisciplinary interactions. What has been observed for the last two decades is that bio-imaging software are more and more powerful, but are not *plug and play*. Often, they must be adapted for specific experimental conditions and that is why it is so important to have an effective collaboration between computer scientists and biomedical scientists.

However, the role of the computer scientist is not only to tune or adapt existing programs for the biomedical community, but also to find new methods to solve problems that are particularly difficult to address. Within the computer scientist community, works using biomedical images used to be considered as *works of applications*, which was somewhat derogatory. Times are changing and the community is beginning to embrace the idea that interesting and fundamental algorithmic strategies, proved useful to tackle more general computer vision problems, have come out of the biomedical image analysis field.

From the biomedical point of view, computer-based image analysis provides methods of scoring visual content in a way that yields both quantitative and objective data, while being potentially more sensitive, more consistent, and more accurate. These automatic techniques are of considerable interest to help biomedical scientists understanding and quantifying the phenomena they observe, as the increasing quantity and complexity of images render manual analysis unreasonably time consuming.

From the computer vision point of view, biomedical images involve problems that are quite difficult to address due to the complexity and variability of the observed objects. We have chosen to work on three kinds of problems:

- Segmentation, which refers to the task of detecting boundary objects;
- Characterization of morphometric changes;
- Search of patterns or interactions between elements.

-
- *Biomedical Engineering Master*, Paris Descartes University - ParisTech Engineering Schools (France)
 - *Biomedical Engineering Master*, Imperial College London (Great Britain)
 - *Master in Biomedical Engineering*, Swiss Federal Institute of Technology Zurich (Switzerland)
 - *Master in Biomedical Engineering*, Linköping University (Sweden)
 - *Master in Biomedical Engineering*, RWTH Aachen (The Netherlands)
 - *Master in Biomedical Engineering*, Delft University of Technology (The Netherlands)
 - *Master of Engineering in Biomedical Engineering*, Harvard-MIT Health Sciences and Technology (USA)

In computer vision the developed methodologies to tackle these problems are based on two classic approaches: the statistical/learning machine-based approach, and the knowledge-based approach. Our works have been mostly oriented towards object detection/segmentation, and to higher-level processing that can deal with the estimation of specific parameters about the extracted objects (shape parameters, relationships between objects), pattern recognition (classification of a detected object or pattern into different categories), image registration (comparing and/or combining different views of the same object/pattern). The latter topic involves studies about integrating different forms of image-derived information. Images can be acquired from the same imaging modality but at two different points in time, which is the case for the developed methodology [2] to register soft tissues, or from disparate imaging modalities (functional/anatomical) (see p. 67 *infra* [7]). These studies about registration will not be discussed in this paper, as we decided to focus on biological images where both knowledge-based and statistical-based approaches were developed. The paper is organized as follows: Section 2 highlights the challenges of the BioImaging field. Section 3 will show the interest of introducing experts' knowledge, while Section 4 will describe studies that explore the power of statistical-based or learning machine methods. In the last section, we will discuss how making these two approaches interact may be even more effective.

2 Challenges

The major challenges that we have to face are related to the variability of observed biological structures. They can be stained (see Figure 1) or not (see Figure 2). If they are unstained, the separation between background and biological structures is quite difficult. Furthermore, the separation of the biological structures may be hampered by the fuzziness of their contours due to

- the similarity of the observed tissue radiometry,
- a low signal-to-noise ratio due to the dynamic of the observation.

These problems can be encountered even if the biological structure are stained, as the staining may be non-uniform throughout the image. The density of the observed structures can also be very high, so they may be involved in complex configurations such as networks, aggregating or overlapping structures.

There is no universal methodology to deal with biological images. The methodology depends on the type of images (2D, 2D+Time, 3D, 3D+Time, stained/unstained cells or biological structures), and on the type of structures that need to be extracted and measured. In BioImaging, one way of taking such variability into account would be to rely on statistics or on expert knowledge. Thus redundancies could be used, models could be learned in order to help the system dealing with complex configurations.

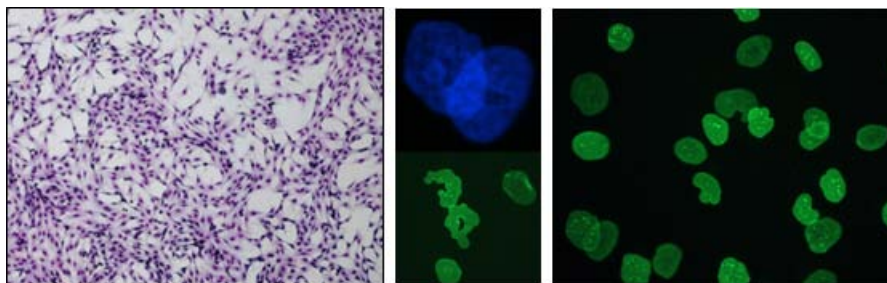


Fig. 1 Stained biological structures

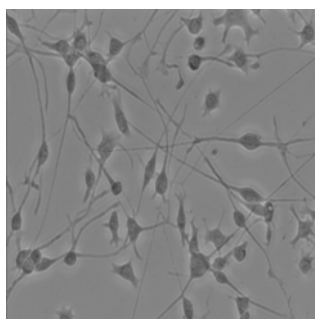


Fig. 2 Unstained biological structures

3 Knowledge-Based Approaches for Cell Extraction

Cell morphology is a pressing research issue in biology. The development of large scale quantitative biological research or high throughput drug screens can lead to greater understanding of the mechanisms that underlie cell or nuclear morphometric changes and thus might help to find a treatment. To deal with such large screening tests, it is important to develop methods of segmentation that allow highly reliable shape description and characterization [5,4]. To do so, efficient solutions in computer vision have to be found especially for extracting the contour of each cell or nucleus in a highly precise way, even if the nuclei are aggregated or overlapping, or if the cells involved in a cell network. The two following sub-sections are dedicated to segmentation methods, using prior information or expert knowledge at different levels. The first segmentation method is developed for nucleus segmentation, where prior information based on nucleus shape is used at the lower level of the method, in order to begin the segmentation process with the right information. In the second segmentation method, the objects to be extracted are much more complicated, as they are cells with neurites embedded in a network. In that case, the developed method is a two-step segmentation method. The first one deals with the extraction of cells from the background. In the second one, information from extracted shapes

at the previous level and rules modeled from expert knowledge help to separate each neural cell of the network.

3.1 Segmentation of Complex Nucleus Configurations

Biological object segmenting methods are mainly divided into two categories: energy-driven segmentation [12,21,3,15] and watershed-based segmentation [18,1]. In the first category, the segmentation is obtained as a result of the minimization of an energy function, composed of a data driven term and a regularization term. They have proved efficient to segment objects, especially when the boundaries are weak. Some recent advances were proposed to deal with object of complex topologies [15], or to prevent the contours that are in contact from merging [22,20]. These methods are very useful in applications related to isolated cells tracking. The major drawbacks of these methods are the parameter value evaluation, and the computation time that is quite high. These drawbacks are a handicap for high throughput drug screens.

In the second category, the image is processed as a height function that describes a landscape. The watersheds are the lines that separate the catchment basins when *rain is falling* on the relief represented by the height function. It has shown many interesting properties among which simplicity, speed and complete partition of the image, and has proven useful especially on blurred gray level images with low contrast and weak boundaries. However there are some drawbacks too, such as over-segmentation or great sensitivity to noise. Some recent works [8,14] have shown that the segmentation result can be highly improved by selecting good region markers from which the flooding will be done. The former one uses a statistical anatomical atlas, the latter one needs a rough manual initialisation and a supervised pixel classification from which the knowledge used to select the best markers is built.

The method developed in [4] to segment overlapping or aggregated nuclei is a watershed- based method where prior information based on geometrical properties via configuration nucleus templates and gray level criterion yields a semantic understanding of these configurations. (see Figure 3).

Once these different nuclei configurations are identified, marker regions, from which the flooding will be done, are selected and positioned approximately at the middle of each region located on both sides of the validated segment of separation in case of aggregating nuclei. In case of overlapping nuclei, one more marker is positioned in the overlapping area along the validated separating segment(see Figure 4).

The results show that 88.76% of the aggregated nuclei and 77.14% of the overlapping nuclei are well segmented with this method. The global rate of well-segmented nuclei in terms of number of nuclei is 97.47%. The selection of good markers from which the flooding is done yields a very low rate of over segmentation (0.28%). This

² This project is developed in collaboration with N. Levy, P. Cau, C. Navarro, S. Perreira of the Unity Inserm U910 - Génétique Médicale et Développement - Faculté de Médecine de La Timone - Marseille (France)

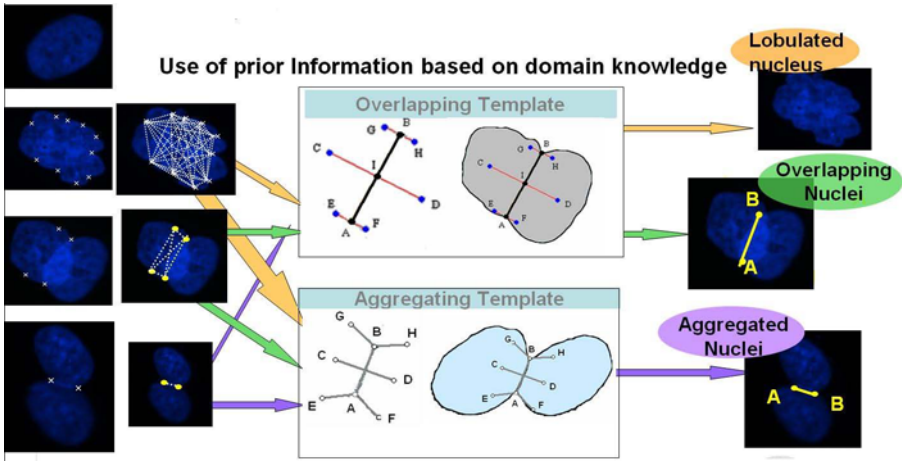


Fig. 3 Use of templates and gray level criterion along the potential separating segment, to give a semantic understanding of nucleus configuration with high concavity points

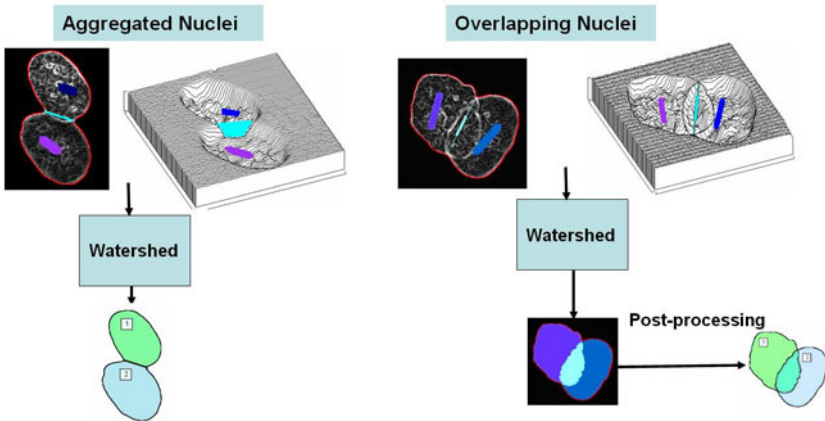


Fig. 4 Selection of good markers from which the flooding is done during the watershed process in case of overlapping or aggregated nucleus configurations

shows that it is pertinent to introduce prior information in watershed-based segmentation, a powerful and fast technique for contour extraction. To improve these results we think that it would be interesting to introduce a learning step in order to extract information useful to build the templates in a less empirical way (even if this step is based on expert knowledge).

3.2 *Extraction of Neurons Embedded in a Network*

Unstained neuronal cells are very difficult to segment because of their intersecting neurites³. The cells cannot be individualized using only gray level intensity as they have approximately the same mean gray level. Even if edge information is combined with gray level intensity, the obtained results are shapes that contain several cells (see Figure 5A). Therefore, this first step of segmentation has to be completed in order to extract each cell (see Figure 5B). At this step, using information based on a shape descriptor has proved to be efficient. The designed shape descriptor [5] shares some properties with the Generalized Voronoi Diagram (GVD). It is a partition of a polygonal space, which reflects the topology and the general morphology of the shape (skeleton features), and it is a planar graph with linear algebraic complexity. From this shape descriptor called the angular bisector network, some typical points can be extracted, namely

- extremal points, which reflect end points of a shape;
- branching points, which reflect bifurcations (fork, odd or even branching areas) in a shape;
- gem points, which represent the center of body cells;

The extraction of these typical points allows shape characterization and, when combined with the use of splitting rules driven by experts' knowledge, it yields 83.6% of processed branching areas (100% for synthesized neuron shapes, see Figure 7). Among them 72.3% are well-processed branching areas. The non-valid connections and/or the non-processing of some branching areas are due to two major factors: artefacts of segmentation (consequently the method of splitting is not questioned), or a lack of non-ambiguous information in the neighborhood of branching areas. Developing more rules and integrating more global information, that is to say information that is farther away from the processed branching area, thus appear interesting to get rid of ambiguous local information.

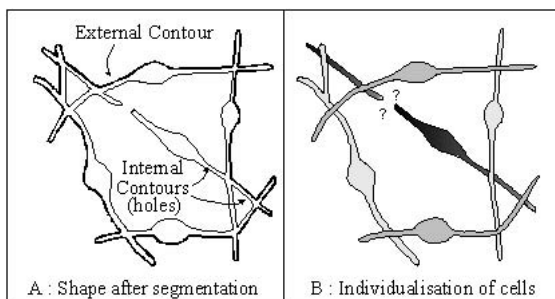


Fig. 5 Extracting five cellular entities whose neurites cross over from polygonal shape

³ This project was developed in collaboration with biologists of the INSERM-Unit 339, directed by W. Rostène

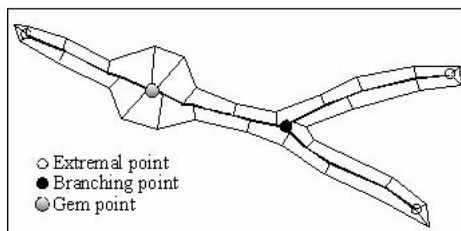


Fig. 6 Typical points of Angular Bisector Network

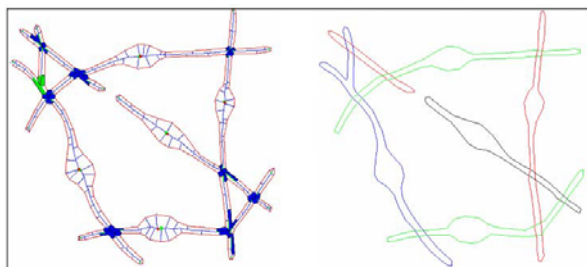


Fig. 7 Example of results on a synthesised shape

4 Statistical Modeling and Synthesis of Element-Based Biomedical textures

Expert knowledge or diagnosis habits may sometimes be very challenging. Sets of rules that may be fuzzy or unformalized and strongly based on both intuition and a high level of experience and expertise, are often at stake in biomedical issues dealing with diagnosis or complex recognition tasks. In these situations, purely knowledge-based approaches such as the one presented in the previous section may be too limited and unable to fully model rules that cannot be made clearly explicit or disambiguated. This is why, such research topics in biomedical images should be studied from a purely mathematical point of view. In fact, several methods are based on statistics, optimization or geometry, and aim to model information from images. This information may be used for medical diagnosis tasks, characterization or comprehension of biological phenomena. In this section, we focus on the issues of having to decide whether two patterns are similar or different and to quantify this difference. The patterns may be a spatial arrangement of medical elements, such as cells or vascular vessels over a rather homogeneous background. When the observation window is much larger than the element's scale, and when these arrangements are somehow stationary, the images may be considered as textures (see Figure 9 for instance). This type of texture occurs in various types of images such as fluoroscopic, retinal OCT, histological, or hematology images. In these contexts, the modeling of images strongly overlaps with the texture modeling research area, a

key fundamental research problem in computer vision and computer graphics. The goal of this section is to show how some statistical models that we previously studied in a hand-drawing context [10] are able to capture and synthesize the spatial arrangement of elements in this type of stationary textures.

Recently, several approaches have investigated the use of stochastic models to extract elements in element-based images. These approaches are grounded in the spatial statistics active domain [11] where methods implement spatial relationship models. Basically, these approaches let a dynamic population of simple geometric shapes (rectangles, circles, etc.) evolve and converge through a Monte-Carlo Markov-Chain sampling procedure until the population sticks to the underlying elements, see e.g. [9, 6, 19, 13]. The optimization constraint is based first on a priori interaction constraints (repulsive, thus forbidding overlaps). Secondly, a data-driven term forces the geometric elements to converge on the elements in the input image. Such approaches are quite robust for detection or counting tasks.

Considering the spatial distribution of elements (once they have been detected) as a sample of some specific statistical model is an alternative solution. For instance, Strauss hard-core models which are able to represent a population of similar elements have been studied in the same medical context as the one we target in this section [16, 17]. We studied in an artistic texture synthesis context a sophisticated version of this model, called multitype Strauss hard core models [10]. These models make it possible to describe and sample populations of different kind of elements that may interact one with the others. We propose to show here how it performs on biomedical element-based textures.

Strauss Hard-Core Model

We make use of a spatial marked point process relying on a Hard Core Strauss pairwise interaction model. It models first-order statistics (element appearance likelihood) and second-order statistics of the distances between elements. Let $\|x_i - x_j\|$ be the Euclidean distance between two elements x_i and x_j . In the Hard Core Strauss model, the interaction probability of two elements at a relative distance $\|x_i - x_j\|$ is given by a three-step piecewise function. A first zero-valued piece indicates an interval $[0, h]$ of relative distances that cannot be observed between elements. In other words, two elements cannot be closer than h . A second interval $[h, r]$ delimits the relative distance space where the occurrence probability value is γ . In order to be mathematically sound, the interaction model ends up almost surely in a third interval $[h, +\infty[$. Two elements can be considered as randomly arranged when distant to more than r . This simple model enables to synthesize spatial arrangements of elements that goes from rather regularly spaced to strongly random. This model can be refined into a multitype Strauss hard-core model, embedding different types of elements (different categories of cells for instance).

This pairwise interaction distance is combined with a first-order probability density under a Gibbs probability density function (PDF). Such Gibbs models offer a big advantage for the texture synthesis context. Indeed, a Monte Carlo Markov Chain sampling strategy is able to easily and surely resample the model at any

given scale. It is also able to sample unstationary textures by fixing any first-order mapping. The third section in [10] gives all the technical details according to this methodology, the estimation of the model’s parameters and the resampling procedure.

We focus on the illustration of how such statistical synthesis approach is able to capture the spatial relationships in element-based textures. For the sake of simplicity, we thus rely here on a manual segmentation and annotation of the elements. Some automatic methods could be investigated here, for instance based on the techniques presented in Section 3. Figure 8 presents the partial histological section we used⁴. On the lower left corner, sane cells (nuclei and cytoplasm) are visible whereas a tumor region dominates the right half of the image. This tumor region is recognizable because of the dense accumulation of cell nuclei and of some chemically marked dark cells that are sparsely arranged. We manually annotated these three types of elements on two windows (Figure 8b).

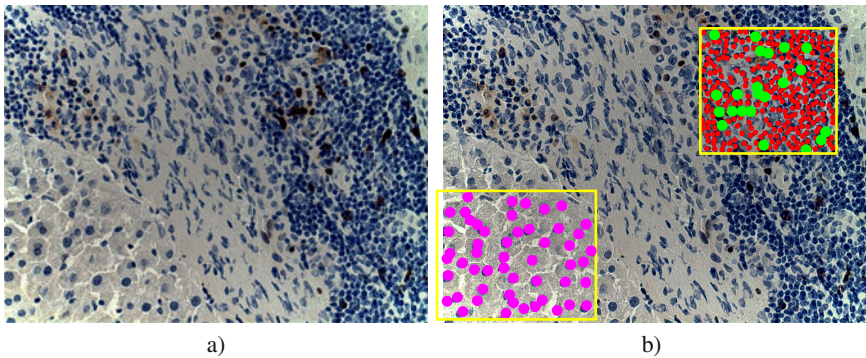


Fig. 8 a) The original plate on which several spatial arrangements of cells are visible. The lower left corner exhibits some sane cells whereas a partial tumor is visible on the right of the image. This tumor contains two kind of elements: small dense nuclei, darker and bigger nuclei. b) On two small observation windows, we manually annotated these three types of elements. Our model parameters are then learned on these two annotated windows.

Once our model is learned on these annotations, we can resample it at any given scale and shape. Let us stress that both the learning and sampling of the model are based on a (x_i, y_i, c_i) triplet population where (x_i, y_i) is the location of the i^{th} element and c_i indicates its category. On the first observation window (sane cells) of Figure 8, all elements belong to the same category. Two categories are used on the second window (small blue nuclei and darker nuclei). During re-synthesis, for the sake of illustration, we make use of a small dictionary of segmented element thumbnails. It contains around 10 examples per category. During the synthesis loop, we simply paste a random c_i element of this dictionary on a (x_i, y_i) position.

⁴ This project is developed in collaboration with biologists of the INSERM-Unit 1022 directed by Daniel Scherman.

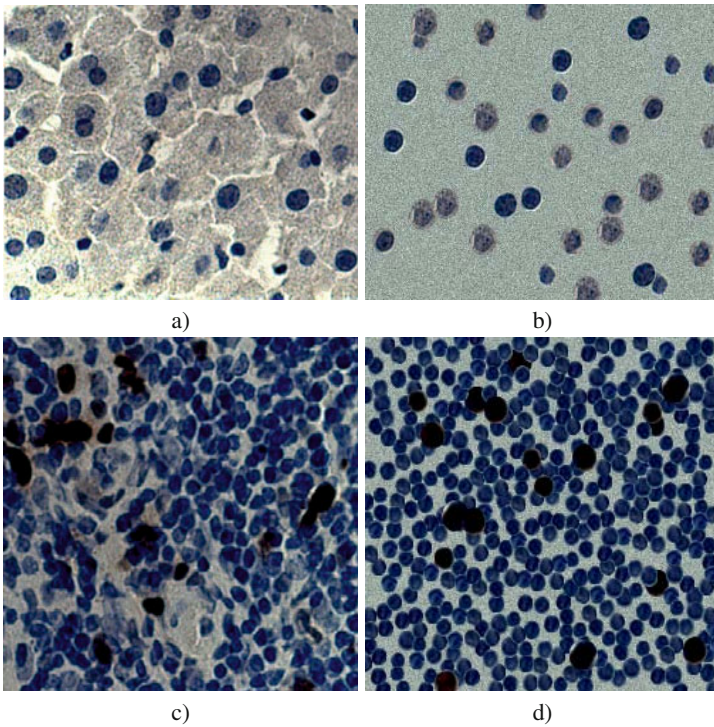


Fig. 9 The left column shows two sub-images cropped from Figure 8a. The right column shows 1:1 scale re-synthesis using the presented method. Our model only produces a list of (x,y) positions. Therefore, for the sake of illustration, a few segmented elements are pasted at these locations over a synthetic noisy background. On the top row, a unique category of elements has been learnt whereas on the bottom row, two categories are used (small blue nuclei, bigger and darker nuclei).

Figure 9 shows two comparative results. Both these examples illustrate how our model is able to capture the spatial relationships of the elements at stake. Sane cells tend to be sparsely and randomly arranged with very few overlaps. Conversely, tumoral cells tend to aggregate with strong overlapping. Considering the tumor cells, the two different types of spatial arrangement are also well captured. Small blue nuclei are very dense whereas dark marked cells are much more random and sparse. Figure 10 illustrates how efficient our model is to synthesize larger scales, for instance by simulating larger tumor regions. These synthesis results suggest that such statistical models are efficient to capture spatial relationships involving several types of elements.

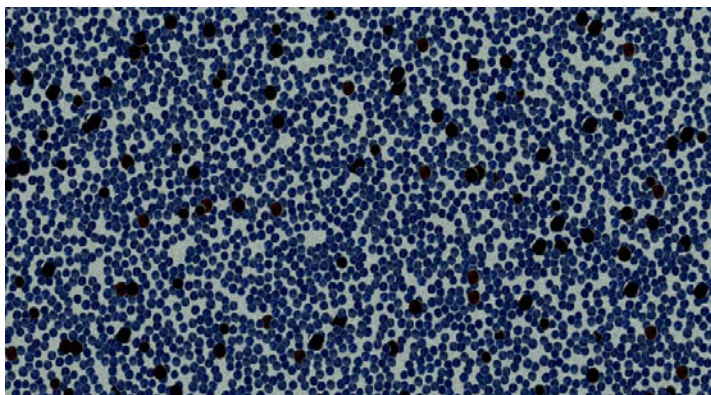


Fig. 10 A 1:8 scale synthesis illustrating our model at a larger scale.

5 Conclusion

Interdisciplinary exchanges between the biomedical field and computer vision have proved fruitful for both fields. Biomedical image analysis plays a major role in biomedical research as it yields objective and quantitative data useful for computer-aided diagnosis or biomedical mechanism understanding.

Besides fundamental advances in computer vision are necessary to obtain efficient solutions in order to process biomedical images. In the past, the classic approaches were subdivided in two categories: knowledge-based and statistical/learning machine approaches. We think that time has come for a more holistic and integrated approach. In fact, what counts is that knowledge is important to build methods that can deal with such complex images, no matter how this knowledge is obtained: information extracted by using statistics or thanks to learning machine methods, or even modeled from the expert knowledge domain. The presented works show how complementary these approaches are, and how much they would benefit from being articulated in the same methodology. In the next decade, ontology will probably provide a good methodological framework to develop systems where knowledge-management is articulated with low-level image analysis methods in order to make systems perform better.

References

1. Beucher, S., Meyer, F.: In: Dougherty, E. (ed.) *Mathematical Morphology in Image Processing*, Marcel Dekker, New York (1992)
2. Boucher, A., Cloppet, F., Vincent, N., Jouve, P.: Visual Perception Driven Registration of Mammograms. In: *Proceedings of International Conference on Pattern Recognition (ICPR)*, pp. 2374–2377 (2010)

3. Caselles, V., Kimmel, R., Sapiro, G.: Geodesic active contours. *International Journal of Computer Vision* 22(1), 61–69 (1997)
4. Cloppet, F., Boucher, A.: Segmentation of complex nucleus configurations in biological images. *Pattern Recognition Letters* 31, 755–761 (2010)
5. Cloppet, F., Oliva, J.M., Stamon, G.: Angular Bisector Network, a simplified generalized Voronoi diagram: application to processing complex intersections in biomedical images. *IEEE Transactions on Pattern Analysis Machine Intelligence* 22(1), 120–128 (2000)
6. Descombes, X., Kruggel, F., Willny, G., Gertz, H.J.: An object-based approach for detecting small brain lesions: application to Virchow-Robin spaces. *IEEE Trans. on Pattern Analysis and Machine Intelligence* 23(2), 246–255 (2004)
7. Frapart, Y.: In Vivo Electron Paramagnetic Resonance and Imaging in Biomedical Science, p. 7
8. Grau, V., Mewes, A., Alcañiz, M., Kkinis, R., Warfield, S.: Improved watershed transform for medical image segmentation using prior information. *IEEE Transactions on Medical Imaging* 23(4), 447–458 (2004)
9. Guo, C.E., Zhu, S.C., Wu, Y.N.: Modeling visual patterns by integrating descriptive and generative methods. *Int. Journal of Computer Vision* 53(1), 5–29 (2003)
10. Hurtut, T., Landes, P.-E., Thollot, J., Gousseau, Y., Drouilhet, R., Coeurjolly, J.-F.: Appearance-guided Synthesis of Element Arrangements by Example. In: NPAR: Proc. of the 7th International Symposium on Non-photorealistic Animation and Rendering (2009)
11. Illian, J., Penttinen, A., Stoyan, H.: Statistical analysis and modelling of spatial point patterns. Wiley Interscience (2008)
12. Kass, M., Witkins, A., Terzopoulos, D.: Snakes: active contours models. *International Journal of Computer Vision* 4(1), 321–331 (1997)
13. Lafarge, F., Gimel'farb, G., Descombes, X.: Geometric Feature Extraction by a Multi-Marked Point Process. *IEEE Trans. on Pattern Analysis and Machine Intelligence* 32(9), 1597–1609 (2010)
14. Lefèvre, S.: Knowledge from markers in watershed segmentation. In: Kropatsch, W.G., Kampel, M., Hanbury, A. (eds.) CAIP 2007. LNCS, vol. 4673, pp. 579–586. Springer, Heidelberg (2007)
15. Luminata, A., Vese, L.A., Chan, T.F.: A multiphase level set framework for image segmentation using the Mumford and Shah model. *International Journal of Computer Vision* 50(3), 271–293 (2002)
16. Mattfeldt, T., Eckel, S., Fleischer, F., Schmidt, V.: Statistical modelling of the geometry of planar sections of prostatic capillaries on the basis of stationary Strauss Hard-core processes. *Journal of Microscopy*, 272–281 (2007)
17. Mattfeldt, T., Eckel, S., Fleischer, F., Schmidt, V.: Statistical analysis of labelling patterns of mammary carcinoma cell nuclei on histological sections. *Journal of Microscopy*, 106–118 (2009)
18. Vincent, L., Soille, P.: Watershed in digital spaces, an efficient algorithm based on immersion simulation. *IEEE Transactions on Pattern Analysis Machine Intelligence* 13(6), 583–598 (1991)
19. Wirjadi, O., Kim, Y.-J., Breuel, T.: Spatial Statistics for Tumor Cell Counting and Classification. In: Denzler, J., Notni, G., Süße, H. (eds.) *Pattern Recognition*. LNCS, vol. 5748, pp. 492–501. Springer, Heidelberg (2009)

20. Zhang, B., Zimmer, C., Olivo-Marin, J.C.: Tracking fluorescent cells with coupled geometric active contours. In: Proceedings of IEEE International Symposium on Biomedical Imaging, vol. 1, pp. 476–479 (2004)
21. Zhu, S.C., Yuille, A.: Region competition: unifying snakes, region growing and Bayes/MDL for multiband image segmentation. *IEEE Transactions on Pattern Analysis Machine Intelligence* 18(9), 884–900 (1996)
22. Zimmer, C., Olivo-Marin, J.C.: Coupled Parametric Active Contours. *IEEE Transactions on Pattern Analysis Machine Intelligence* 27(11), 838–1842 (2005)

Glossary

2-photon microscopy Also known as multiphoton microscopy. A relatively new imaging technique, whereby fluorescence is emitted after the simultaneous absorption of two photons (or more) by a fluorophore. This is achieved by using a high-powered femtosecond pulsed laser that is focused through the objective lens to concentrate photons temporally and spatially, respectively. The major advantage of this technique is that excitation is confined to around the focal point, thereby minimizing photobleaching/phototoxicity and enabling a greater depth of penetration.

Acoustic cavitations are small bubbles or voids in a medium, created by the propagation of an acoustic wave through a medium. Often the cavities are formed when the pressure in the medium drops so low that the elastic limit of the medium is surpassed and the material pulls apart.

Adrenergic/noradrenergic system Part of the autonomic nervous system that uses adrenaline (epinephrine) and noradrenaline (norepinephrine) as neurotransmitters. One of its most well-known effects is the fight-or-flight response.

Amino-PLNP Persistent luminescence nanoparticles displaying amine functions on their surface.

Biomarker In medicine, a biomarker is a term often used to refer to a protein measured in blood whose concentration reflects the severity or presence of some disease state. More generally, a biomarker is anything that can be used as an indicator of a particular disease state or some other physiological state of an organism.

Brightfield microscopy The simplest microscopy technique, in which a sample is illuminated using white light from below and then observed from above. Darker regions are observed where light has been absorbed by structures in the sample.

CD11c-YFP mouse A mouse that has been genetically engineered to express yellow fluorescent protein (YFP) in dendritic cells (CD11c+ cells).

Colloidal stability Physico-chemical state in which nanoparticle are well dispersed in the solvent, stable in time (ergo without any trend toward aggregation, or sedimentation).

Confocal laser scanning microscopy: An imaging technique that enables the optical sectioning of a sample. This is achieved by using a pinhole to capture fluorescence that is emitted only from the focal plane i.e. light is focused onto the sample, emitted fluorescence is focused back through the objective lens and fluorescence emitted from the focal plane is allowed to pass through the pinhole for detection. The pinhole also excludes any light emitted from the focal plane that has scattered on its way back through the sample.

Contrast agent: Substance used to enhance the contrast of a region of interest in acquired images. The term is not related to any specific imaging modality, but refers more generally to a way to improve contrast.

Darkfield imaging: is an early method of observing objects with low contrast by observing light that is scattered from them whilst carefully blocking out the incident light that illuminates them.

Dark states: are states of a molecule that do not emit light.

Dendritic epidermal T cells: Specialized immune cells, also known as innate T cells, located in the outermost layer of the skin (the epidermis), which play an important role in regulating skin homeostasis.

Distal location: A located further away from the centre of the body.

Electronically excited state/ vibrationally excited state: An electronically excited state is the state of a molecule in which the electron cloud in its, normally unoccupied molecular orbitals, are occupied by electrons. In other words it is the state of a molecule where excess energy has lead to the redistribution of the electrons in the highest energy (newly) occupied molecular orbital. A vibrationally excited state is the sate of a molecule which is vibrating at higher energy than the lowest possible vibrational energy level of that molecule.

Epidermal Langerhans cells: Specialized immune cells found in the outermost layer of the skin, which defend against pathogens that try to enter the skin

Epidermis: The outermost layer of the skin.

Epifluorescence microscopy: A commonly used imaging technique, whereby a sample is illuminated using light from above that is focused through an objective lens. Emitted fluorescence is then focused back through the same objective for detection.

Formation/deactivation pathways: are the chemical and photophysical steps that result in an excited state of a molecule forming and then decaying back to the ground state of the molecule.

fMRI (functional MRI): MRI methods used to detect neural activity. These methods are based on the hemodynamic changes, including cerebral blood flow, cerebral blood volume, blood oxygenation, etc, induced by neural activation. The most common technique is based on the BOLD.

fcMRI (functional connectivity MRI): An MRI technique that detects the synchrony in fMRI signals across the brain when the subject does not perform a specific task, i.e., during the resting state. It has been suggested it reflects the intrinsic brain network or functional connectivity in the brain.

Heterodyne detection: is a method of detecting radiation by non-linear mixing with radiation of a reference frequency.

Homeostasis: Balanced resting conditions.

Immune cells: Specialized cells that defend the body against invading pathogens. These cells are located within tissues of the body and also circulate in the blood.

Internal conversion: is the iso-energetic conversion of the excitation energy of a higher electronic state in its lower vibrational state into vibrational energy in the next lowest electronic state.

Keratinocyte: The predominant cell type that is present in the outermost layer of the skin.

Laser coupling: is the absorption of laser light into a material.

Laser fluence: The energy of a laser, in J/cm^2 or Joules per unit area. In the case of a pulsed laser this is often stated per pulse. In the case of a CW laser it may be expressed per second or as Watts per unit area.

Laser plasma interactions: The way in which the electromagnetic field of incident light affects, or is absorbed by a plasma or expanding cloud of electrons and/or ions.

Laser T-jump: is an increase in the temperature of a medium upon the absorption of laser light.

Light scattering: is a general physical process where some forms of radiation, such as light, sound, or moving particles, are forced to deviate from a straight trajectory by one or more localized non-uniformities in the medium through which they pass.

Luminescent nanocrystal: could be used to describe any crystalline material with luminescence properties and distribution in the nanometer range.

Luminescent silicate Near-synonym of the luminescent nanocrystal.

Model system: An animal model of human disease. (e.g. With reference to the 'intravital skin imaging model'; a set-up that allows the real-time visualization of cells within the skin of a living animal).

Morris water maze: A kind of maze invented by an UK scientist, Richard Morris, to study the place learning and memory in animals.

Neutrophil: One of the first immune cells recruited to an injured or infected tissue. Once recruited, neutrophils help defend against pathogens and amplify the immune response.

Optical sectioning: The aim of the microscopic approaches that allow to visualize a tissue at a well defined depth is to be able to provide the doctor with an image (a virtual slice) that mimics the real histopathologic slice.

PEG chain; PEG chain length: PEG refers to polyethylene glycol, a hydrophilic polymer usually grafted on nanoparticles to ensure colloidal stability and mask residual charges on their surface. Depending on the number of oxyethylene motifs, the PEG chain length is longer or shorter.

Perception gap: The degree of difference between the image-focused researcher and other conventional researchers in the acceptance of the biological relevance of image-based data.

Phosphorescence: is the emission of light from a state of a molecule of one multiplicity accompanied by its conversion to the at ground state with a different multiplicity.

Phase contrast microscopy: is a microscopy illumination technique in which the phase shifts in the light passing through a transparent medium are converted into amplitude or contrast changes in the image.

Photoacoustics: is the generation of a sound wave in a medium caused by the rapid thermal expansion of that medium.

Photochemistry: Any chemistry which is initiated or influenced by the absorption of light.

Photochemically excited state: is any state of a molecule that is electronically excited due to the absorption of a photon.

Photostability: refers to the ability of an optical signal to go on, without significant fainting, for several hours.

Photomechanical effect: Any effects of light that lead to morphological change in a medium or movement of the medium.

Photothermal microscopy: is microscopy where the observation of transmitted or scattered light is attenuated by the presence of a refractive index gradient that results from absorption of light leading to localized heating.

Plasmon resonance: is the resonant interaction of light of a certain frequency with the electron cloud surrounding a metal particle or surface.

Polydisperse sample: Sample that comprises several size distributions, in opposition to monodisperse sample characterized by a size almost narrowed to one unique diameter value.

Pulsed-x-ray laser: A laser which produces pulses of light in the x-ray region of the spectrum.

Pump-probe spectroscopy: is a laser based spectroscopy technique in which one laser generates a change in a sample and a second time synchronized laser probes that change optically or spectroscopically.

Pump-probe Raman spectroscopy: Raman spectroscopy based on the pump-probe spectroscopy technique in which one laser generates a change in a sample and a second time synchronized laser probes that change optically, in this case using Raman spectra.

Quantum yield: Defined as the ratio of the emitted energy on the absorbed energy.

Second harmonic generation (SHG) / third harmonic generation THG: A non-linear optical process whereby two photons (or three, in the case of THG) combine together to produce a photon with double the energy i.e. the emitted light has double the frequency and therefore half the wavelength of the incoming light. SHG occurs during multiphoton imaging of biological tissues when the femtosecond pulsed laser hits repetitive symmetrical biological structures such collagen fibres. THG is much weaker than SHG, but can be used to detect lipid bodies. SHG and THG imaging can be used at the same time as multiphoton imaging of fluorescence, thereby enabling the co-visualization of native, unstained structures within tissues.

Segmentation: With reference to imaging, the process of identifying and separating structures within an image.

Silicate phosphor Material from silicate host displaying persistent luminescence properties.

Singlet state/triplet state These describe the multiplicity of a molecule - $M = 2|S| + 1$ where S is the sum of the spins of the electrons in the molecular orbitals of a molecule which can have values of $+1/2$ or $-1/2$ depending on whether the electrons spin is up or down. Singlets have one electron up and one down so $|S| = 0$ and $M = 1$, whereas triplets have two electrons up or two electrons down, so for triplets $|S| = 1$ and $M = 3$.

Sparse coding Sparse coding refers to these coding schemes that favors sparse code representations from a given codeword basis.

Stoichiometrically functionalized is the functionalization of a particle or molecule with an exact and controlled ratio of function number / particle.

Stratum lucidum A layer of hippocampus area CA3 lying superficial to the pyramidal cell layer that contains mossy fiber axons projecting from the dentate gyrus.

Stratum oriens A region in CA3 deep to the CA3 pyramidal cell layer.

Superpixel code A code provides a compact representation of an object, based on a finite set of codewords. A superpixel refers to a segment after oversegmentating an image. A superpixel code is an representation of an entire superpixel from the given codeword basis.

Surface functionalization Chemical modification of the surface of the particle.

Thermal lens is a lensing effect caused by gradients of refractive index due to local thermal expansion of a medium.

Thiolated ligand is a molecule with an S-H group on it. The S-H group assists the bonding or liganding to a surface.

Time-lapse imaging Imaging that is performed with a predefined time delay between each acquisition.

Transient grating Is a grating generated in a material caused by refractive index changes that result from transient states of a molecule or from transient events.

Vibrational cascade Is the loss of vibrational energy of a molecule through sequentially lower energy excited vibrational levels within an electronic state of the molecule

Vibrational level A molecule can vibrate at various discrete quantized frequencies, with the atoms acting as small masses and the bonds vibrating like springs. Each level is quantized the energy of each successive level is higher than the last.

Zeta potential Potential value, calculated from the electrophoretic mobility of the particle, representative of the global surface charge of the probe.

Index

- 2-photon microscopy, [4](#)
- adrenergic, [22](#) [23](#)
- amino-PNLP, [44](#) [48](#)
- biomarker, [37](#)
- brightfield microscopy, [3](#)
- CD11c-YFP mouse, [8](#)
- colloidal stability, [46](#)
- confocal, [3](#) [11](#) [29](#) [57](#) [77](#) [78](#)
- contrast agent, [17](#) [18](#) [37](#) [77](#)
- dendritic epidermal cells, [5](#)
- epifluorescence, [3](#)
- fcMRI, [18](#)
- fMRI, [17](#) [22](#)
- histological, [77](#)
- histopathology, [IX](#) [80](#)
- light scattering, [42](#) [43](#)
- luminescent nanocrystal, [38](#)
- luminescent silicate, [39](#) [46](#)
- model, [3](#) [4](#) [6](#) [8](#) [18](#) [20](#) [23](#) [50](#) [51](#) [58](#) [61](#) [62](#)
- nanoparticle, [37](#) [38](#) [41](#) [48](#) [50](#) [51](#)
- noradrenergic, [22](#)
- optical sectioning, [4](#) [77](#)
- phosphorescence, [38](#) [40](#)
- photostability, [38](#)
- polydisperse sample, [42](#)
- quantum yield, [38](#)
- segmentation, [11](#) [12](#) [21](#) [32](#)
- silicate phosphor, [39](#)
- surface functionalization, [41](#) [44](#) [50](#) [51](#)
- time-lapse imaging, [9](#) [13](#)
- zeta potential, [44](#) [45](#)